INVESTIGATION ON THE FUNCTIONAL COORDINATION POLYMERS: SYNTHESIS, STRUCTURE AND POTENTIAL APPLICATIONS

Thesis Submitted for the Degree of
Doctor of Philosophy in the Faculty of
Science

By

CHHATAN DAS

DEPARTMENT OF CHEMISTRY

JADAVPUR UNIVERSITY

JADAVPUR, KOLKATA-700032

INDIA

August, 2024

JADAVPUR UNIVERSITY

Department of Chemistry

Kolkata 700032, India

Dr. Partha Mahata

Assistant Professor

Email: parthachem@gmail.com

CERTIFICATE FROM THE SUPERVISOR

This is to certify that the thesis entitled **"INVESTIGATION ON THE FUNCTIONAL COORDINATION POLYMERS: SYNTHESIS, STRUCTURE AND POTENTIAL APPLICATIONS"** submitted by Mr. **Chhatan Das**, who got his name registered on 17th September, 2019 for the award of Ph.D. (Science) degree of Jadavpur University, is absolutely based upon his own work under the supervision of Dr. Partha Mahata and that neither this thesis nor any part of it has been submitted for either any degree/diploma or any other academic award anywhere before.

August, 2019

Jadavpur

Partha Mahata 30/08/24

(Dr. Partha Mahata)

(Signature of the supervisor date with official seal)

Dr. Partha Mahata
Assistant Professor
Department of Chemistry
Jadavpur University
Kolkata-700 032

Dedicated to

Baba, Maa, and Kabita

Acknowledgements

As I reach the culmination of my Ph.D. journey, I find myself reflecting on the numerous people who have played an integral role in this achievement. To all those who have supported, guided, and encouraged me along the way, I extend my deepest gratitude. Though I will try my best to mention everyone who has been part of this journey, I ask for forgiveness if I unintentionally overlook anyone.

The first person who comes to mind is my supervisor, Dr. Partha Mahata, from the Department of Chemistry at Jadavpur University. His unwavering encouragement throughout my research has been invaluable. Dr. Mahata's ability to elucidate even the most challenging concepts with clarity greatly expanded my knowledge, particularly in Single Crystal X-Ray Diffraction, Powder X-Ray Diffraction, Fluorescence Spectroscopy, Solid State Chemistry and Sensing. His approachable nature and the nurturing environment he provided for healthy discussions in the lab helped me navigate the inevitable challenges of research. I am deeply indebted to him for both the academic guidance and personal support he offered throughout this journey.

I would also like to express my heartfelt thanks to my lab-mates, Sourav Sarkar, Priyanka Manna, Sayani Hui, and Akash Chandra. Their collaboration, shared insights, and emotional support were instrumental in sustaining my momentum, even during difficult times. I feel truly fortunate to have worked in such a warm and encouraging environment. I also extend my gratitude to my senior lab members, Dr. Debal Kanti Singha, Dr. Debamalya Ghosh, and Dr. Prakash Majhi, for their valuable advice and guidance whenever I sought it.

My sincere thanks go to my collaborators, Dr. Dhritiman Gupta, Dr. Anjan Banerjee, Dr. Mohabul Alam Mondal, Dr. Ayan Dutta, Mr. Vishwas D. Patel, Mr. Pappu Naskar, Mr. Subhrajyoti Debnath, and Mr. Arunava Mishra, for their contributions and partnership. I am especially grateful to Dr. Saurabh Das, Dr. Manas Panda, and Dr. Bibhuti Bhushan Shaw for their steadfast support and encouraging words throughout my research career.

I would also like to extend my sincere appreciation to Prof. Subrata Mukhopadhyay, Prof. Debajyoti Ghoshal, Prof. Chittaranjan Sinha, Prof. Samaresh Bhattattacharya, Prof. Arup Gayen, Prof. Sujoy Kumar Baitalik, Prof. Shouvik Chattapadhyay, Prof. Kajal Krishna Rajak, Prof. Amrita Saha, and Prof. Partha Roy for their continuous encouragement and invaluable suggestions. My thanks also go to the other faculty members of the Department of Chemistry, as well as the Office of the HOD and the Dean, for their timely assistance.

I am deeply grateful to Srikanta da, Subhasish da, Chandan da, Mona da, Sushanta, Samit, Gopal, Sunanda di, Soumi, Abhimunya, Suvamay, Jayanta da, Pravat da, Mou, Ravi, Sudip, Tamal da, Rahul da, Anmol, Ruchi, Deepak, Akshay, and Abhishek. Their support, whether direct or indirect, has been crucial to my success, and I cannot thank them enough.

I also acknowledge with gratitude the financial assistance provided by the CSIR, India, and the infrastructure and laboratory facilities provided by Jadavpur University, which were vital in the completion of my thesis.

My deepest appreciation goes to my beloved parents, whose unwavering love, support, and encouragement have been my guiding light throughout this journey. The moral values they instilled in me from childhood have been the foundation of my life, and their emotional and inspirational support has sustained me through every challenge. I am profoundly thankful to my brother-in-law, Arabinda Das, my elder sister, Prarthana Das, and my younger sister, Pritilata Das, for their constant love and support throughout my academic career.

Lastly, but certainly not least, I wish to express my heartfelt thanks to my would-be wife and dear friend, Kabita. She has been my oxygen, my constant companion, and the anchor for my often-scattered moods. Her unwavering mental support has been instrumental in helping me overcome the many challenges of my research career. I am also deeply grateful to my parents for respecting my decision to pursue a Ph.D. and for standing by me every step of the way.

Department of Chemistry
Jadavpur University
Kolkata 700032

(Chhatan Das)

CONTENTS

CONTENTS

CONTENTS

CONTENTS

CONTENTS

CONTENTS

Chapter 1

General Introduction and Summary of Research Works

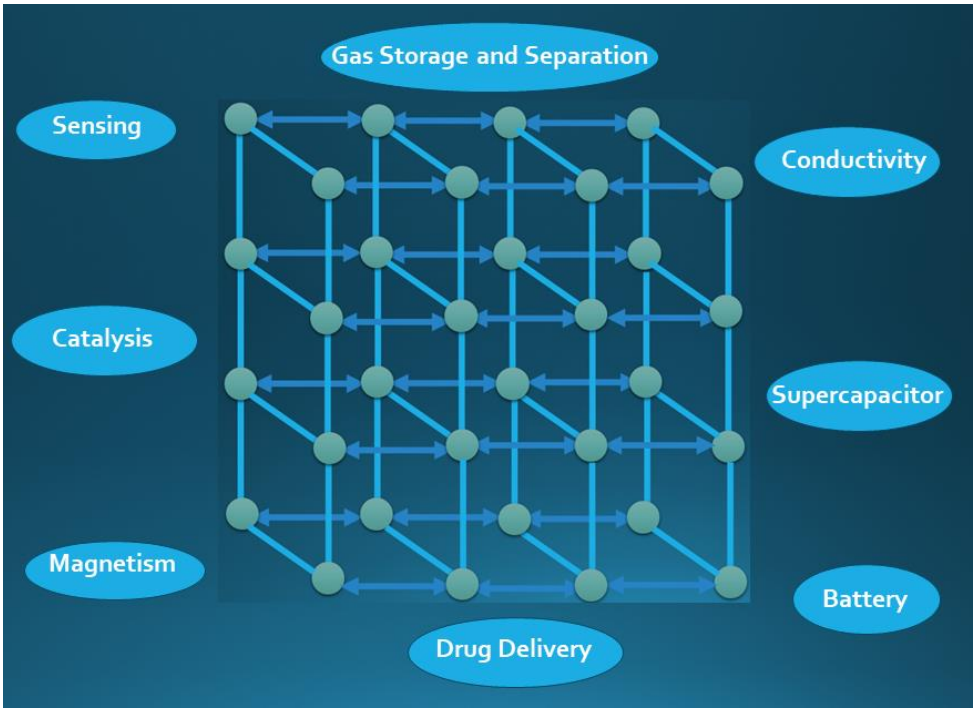

Section A:

A Short Survey on Coordination Polymers and Their Functional Nature

Section B:

Summary of Research Works

CHAPTER-1: Section A

A Short Survey on Functional Coordination Polymers (CPs)

1A.1. INTRODUCTION

1A.1.1. Definition of Coordination Polymers (CPs)

Coordination polymers (CPs) represent an exciting category of hybrid materials, blending inorganic vertices (metal ions or clusters) with organic ligands.[1] In this hybrid, the metal component acts as a "node," while the organic ligand serves as a "linker" or "rod." These organic linkers form infinite structures via coordination bonds with the metal ions, resulting in frameworks spanning one, two, or three dimensions.[2] Notably, CPs' single-crystal nature enables precise structural determination through single-crystal X-ray analysis. Today, the synthesis of CPs are crucial not only for generating diverse structural topologies but also for their extensive applications in gas storage and separation[3], electrical/proton conduction,[4] magnetism,[5] sensing,[6] anion exchange,[7] catalysis,[8] drug delivery[9] and more (Figure 1).

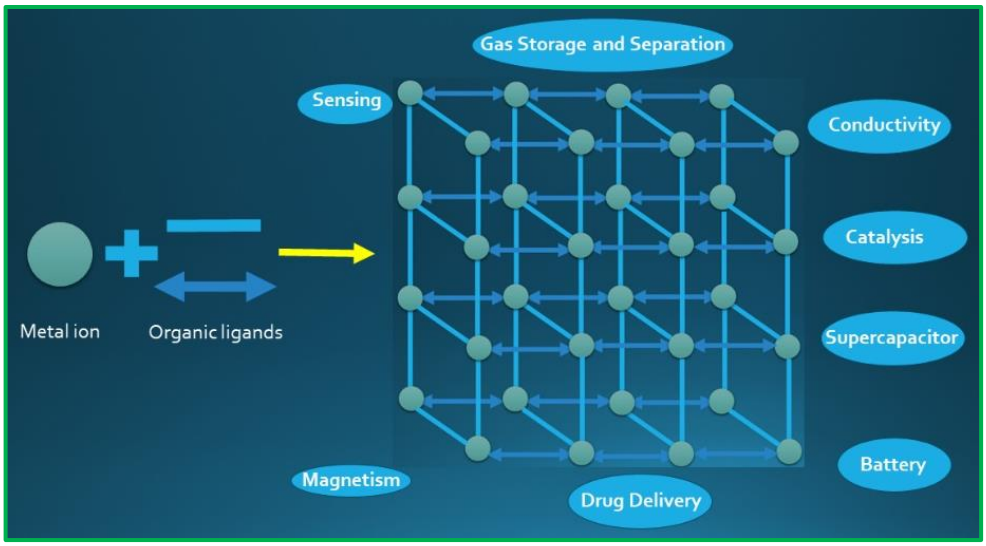

Figure 1. General scheme of synthesis of CPs and potential applications in different fields.

These functionalities are finely tuned by modulating the CPs' structures through variations in organic ligands, including their size, shape, and functional groups.[10] CPs with solvent-accessible voids, maintaining robust structures after solvent removal, are termed porous coordination polymers (PCPs) or metal-organic frameworks (MOFs).[1] While other porous materials like zeolites, activated carbon, and molecular sieves exhibit porosity,[11, 12] they often

lack the structural organization and stability of PCPs. PCPs stand out for their ordered, thermally stable structures with customizable pore size, volume, and functional surfaces, making them highly effective for gas storage and separation. Consequently, contemporary research has seen extensive synthesis of CPs with tailored functionalities achieved through careful selection of organic ligands and metal ions.

1A.1.2. Historical Evolution and Terminology

The term "coordination polymers (CPs)" first gained significant attention from researchers in the 1960s.[13] In contrast, the term "metal-organic frameworks (MOFs)" emerged in the late 1990s to describe a specific subset of coordination polymers.[14] Statistical data indicates a marked increase in the use of these terms between 2001 and 2017, reflecting the burgeoning interest in this area of research.[15] A fundamental distinction between organic polymers and CPs lies in their structure. Organic polymers consist of macromolecules formed from monomers or oligomers linked by covalent bonds, with defined molecular weights. Conversely, coordination polymers are infinite networks of metal-ligand coordination's formed through various non-covalent interactions, resulting in at least one-dimensional frameworks.[16] The concept of "coordination polymers" was first introduced by J. C. Bailar in 1964 to compare organic polymers with inorganic polymeric species.[17] Bailar outlined specific properties that inorganic polymeric structures must possess to be classified as CPs. In 1977, Buser et al. reported the first X-ray structure of a coordination polymer, which was Prussian blue.[18] This structural analysis revealed a three-dimensional framework with mixed-valent Fe(II)/Fe(III) states. Over time, the term "coordination polymers" became somewhat ambiguous as it encompassed all extended structures of metal-ligand coordination without specifying a definitive structure or morphology.[19] In contrast, "metal-organic frameworks" referred specifically to three-dimensional structures with porosity or gas storage capabilities. This led to a preference among inorganic chemists for the term "CPs," while solid-state chemists favored "MOFs." The use of multiple terminologies in this field has sometimes caused confusion among researchers.

To clarify, CPs are now defined as extended structures of metal-ligand coordination forming infinite one-dimensional chains, two-dimensional sheets, or three-dimensional frameworks. In contrast, MOFs are considered only those porous three-dimensional frameworks,

excluding one- or two-dimensional networks.[1] However, O. M. Yaghi, who first coined the term "MOF" for a copper bipyridine complex,[20] argued that the term should not be limited to three-dimensional structures with porosity or gas storage properties, noting the difficulty in consistently identifying porosity in crystals.[21] Recently, new terminologies such as "porous coordination polymers (PCPs),"[22] "metal-organic coordination networks,"[23] "metal-organic hybrids,"[24] and "metal-organic rotaxane frameworks (MORFs)"[25] have also become prevalent in this field.

1A.2. Evolution and Design Principles of Functional Coordination Polymers: From Metal Nodes to Bridging Linkers.

Initially, pioneering researchers like Robson,[14] Fujita,[26] and various other groups[27] synthesized coordination polymers by combining metal centers (acting as metal nodes) with organic donors, commonly referred to as organic linkers. This approach was rooted in classical coordination chemistry, focusing solely on the coordination number of metal ions. To create infinite polymeric materials, known as coordination polymers (CPs), metal ions were combined with non-chelating multidentate organic ligands, referred to as bridging linkers (Figure 2).

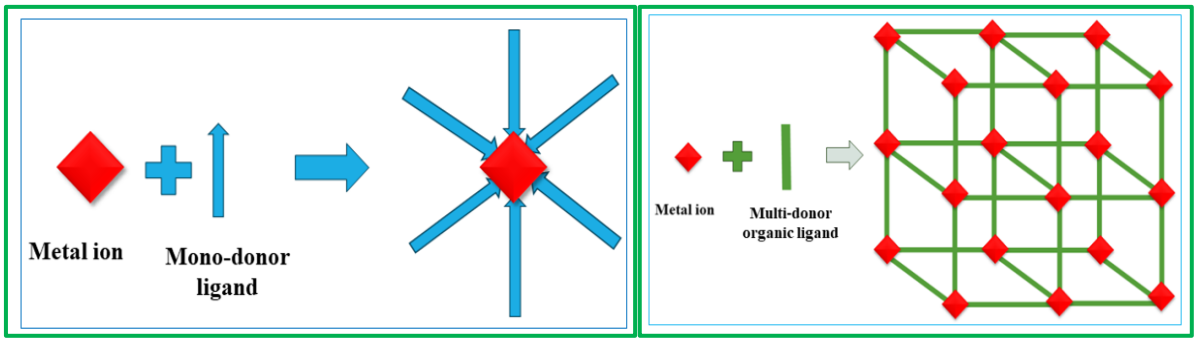

Figure 2. A schematic diagram showing the development of infinitely extended coordination polymers (CPs) from mono-donor to multi-donor ligand.

In the structure of polymeric materials, metal nodes are typically generated in situ through the combination of metal salts, or by using metal clusters or metal-oxo clusters, along with a variety of organic linkers.[28] These linkers vary in their structural features and the number of

donor centers, which can include bi-, tri-, or multi-dentate linkers with N-donor, O-donor, or hetero-donor groups.[29] These organic linkers can readily produce diverse dimensionalities (e.g., 1D, 2D, or 3D) and intriguing topologies (e.g., linear, ladder, zig-zag, square grid, hexagonal, honeycomb, adamantoid, etc.) in the structure of CPs (Figure 3).[30] The specific coordination number or geometry of the metal or metal cluster, along with the bridging capabilities of the organic linkers, dictates these structures.

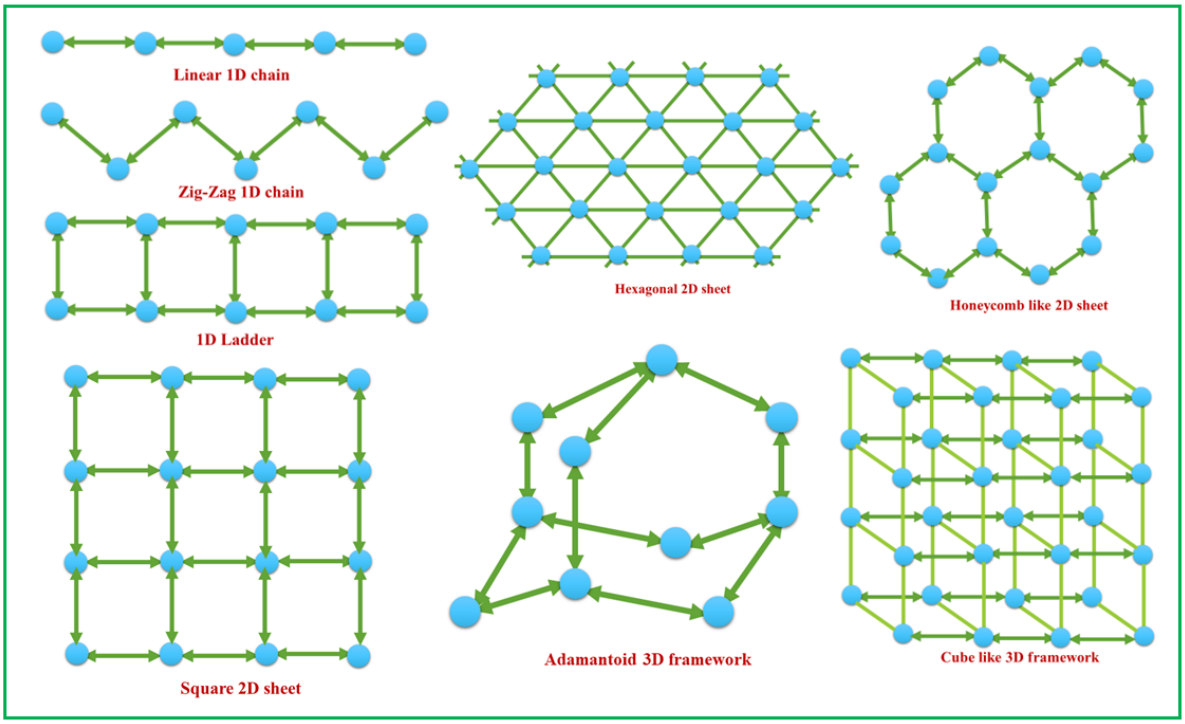

Figure 3. Various topology observed in one-, two- and three-dimensional coordination polymers.

Various chemical interactions, such as ionic, coordinate, π–π, C–H···π, and hydrogen bonding, including both intra- and intermolecular interactions, play crucial roles in designing the diverse dimensionalities and stability of the polymeric network in CPs.[31] Additionally, several key parameters-such as solvent effects, temperature, pH, and the stoichiometry of the ligand and metal are vital in achieving the desired structural topology and functionality of CPs.[32, 33] By carefully selecting organic ligands and metal centers, it is possible to tune the pore size, volume, surface area, and functionality of CPs, as discussed in the following.

1A.2.1. Influence of Metal Centers on the Synthesis and Structure of Coordination Polymers.

Metal centers, or nodes, play a crucial role in the synthesis of coordination polymers (CPs) by bonding to linkers at well-defined angles, influenced by factors like size, hardness, coordination number, geometry, and ligand field stabilization energy. Transition metals are favored due to their partially filled d-orbitals, which offer versatile coordination numbers and effective size for bonding with organic ligands. In contrast, lanthanides, with large sizes and high coordination numbers (7-10), present challenges due to unpredictable coordination environments. Common transition metal salts used in CP synthesis include nitrates, chlorides, and acetates, among others. Transition metals also form metal clusters or secondary building units (SBUs) with diverse geometries. Alkali and alkaline earth metals are less commonly used due to their undefined coordination numbers, geometries, and the tendency to form solvated, aquated centers, leading to organic-inorganic ionic layers. Thus, CPs based on these metals have been less explored.[34, 35]

1A.2.2. The Crucial Role of Organic Ligands in Shaping Coordination Polymers

From the above discussion, it is clear that various factors contribute to the diverse dimensionality and topology in coordination polymers (CPs). However, organic ligands play the most critical role in this process. These ligands, which bridge metal centers to form infinite polymeric structures known as CPs or metal–organic frameworks (MOFs), must be bi-dentate or multi-dentate. The linkers vary in charge (neutral or ionic), donor atoms (N, O, S, or a combination of N and O), and in their shapes and sizes. Additionally, they differ in terms of functional groups, the presence of aliphatic or aromatic rings, and saturated or unsaturated components. The following section will discuss these aspects in detail.

1A.2.2.1 Role of N-donor Ligands.

Since the 1990s, N-donor ligands have been predominant among organic ligands used for the synthesis of coordination polymers (CPs). These ligands typically function in their neutral form, where the lone pairs of nitrogen atoms in amine groups or pyridyl, imidazole, triazole, and tetrazole rings coordinate with metal centers to form infinite CP structures. Generally, the nitrogen atoms in pyridyl or imidazole/triazole rings coordinate more readily with metal

centers compared to those in amine groups. Although metal-N bonds are more labile than the more stable metal-O bonds, this lability facilitates structural variation in CPs through easy rearrangements during self-assembly, often resulting in supramolecular isomerism. Researchers have extensively utilized N-donor ligands for CP synthesis,[36, 37] with some examples depicted in Figure 4. As N-donor ligands bind with cationic metal centers, the resulting metal-ligand complexes are also cationic. To neutralize these complexes, counter anions are present in the framework, preventing the formation of interpenetrated networks. The size of N-donor ligands can also influence the structures of the resulting CPs. Smaller N-donor ligands, such as thiazole (thz), pyrazole (pyz), imidazole (imz), pyrazine (pyz), piperazine, 1,10 phenanthroline (phen) and 4,4′-bipyridine (bpy), typically form robust, non-flexible structures with small pores, which are generally non-interpenetrated. Conversely, N-donor ligands with long flexible chains, such as 1,2-bispyridylethane (bpe), 1,3-bispyridylpropane (bpp), and bisimidazolepropane (bip), often form interpenetrated structures and exhibit structural dynamicity.

Additionally, azo/azine group-based N-donor ligands, such as 4,4′-azobispyridine (azbpy), 1,4-bis-(4-pyridyl)-2,3-diaza-1,3-butadiene (4-bpdb), 2,5-bis-(4-pyridyl)-3,4-diaza-2,4-hexadiene (4-bpdh) and 2,4,5-tri-4-pyridyl-1H-imidazole, contain Lewis basic nitrogen atoms in the azo/azine groups, enhancing the CO_2 adsorption capacity of CPs. Thus, N-donor ligands significantly impact the structural modulation and functionality of CPs.

Long et al. reported a novel porous coordination polymer (PCP) based on the tritopic N-donor ligand 1,3,5-benzenetristetrazolate (BTT^{3-}). The compound, synthesized hydrothermally at 70°C using a DMF and MeOH solvent mixture, is $[Mn(DMF)_6]_3[(Mn_4Cl)_3(BTT)_8(H_2O)_{12}]_2 \cdot 42DMF \cdot 11H_2O \cdot 20CH_3OH$. This PCP exhibited an intriguing three-dimensional cubic structure where square-planar $[Mn_4Cl]^{7+}$ clusters were connected through BTT^{3-} ligands to form an anionic framework. The nitrogen atoms of the tetrazolate rings on the BTT^{3-} ligands bridged Mn^{2+} ions along the edges of a square, with each $[Mn_4Cl]^{7+}$ unit surrounded by eight BTT^{3-} ligands. Each BTT^{3-} ligand further bridged three $[Mn_4Cl]^{7+}$ units, forming a truncated octahedron reminiscent of a sodalite cage of $[Mn(DMF)_6]^{2+}$. Interestingly, immersion in distilled MeOH produced a different CP with the formula $[Mn(CH_3OH)_6]_3[(Mn_4Cl)_3(BTT)_8(CH_3OH)_{12}]_2 \cdot 42CH_3OH$.[38]

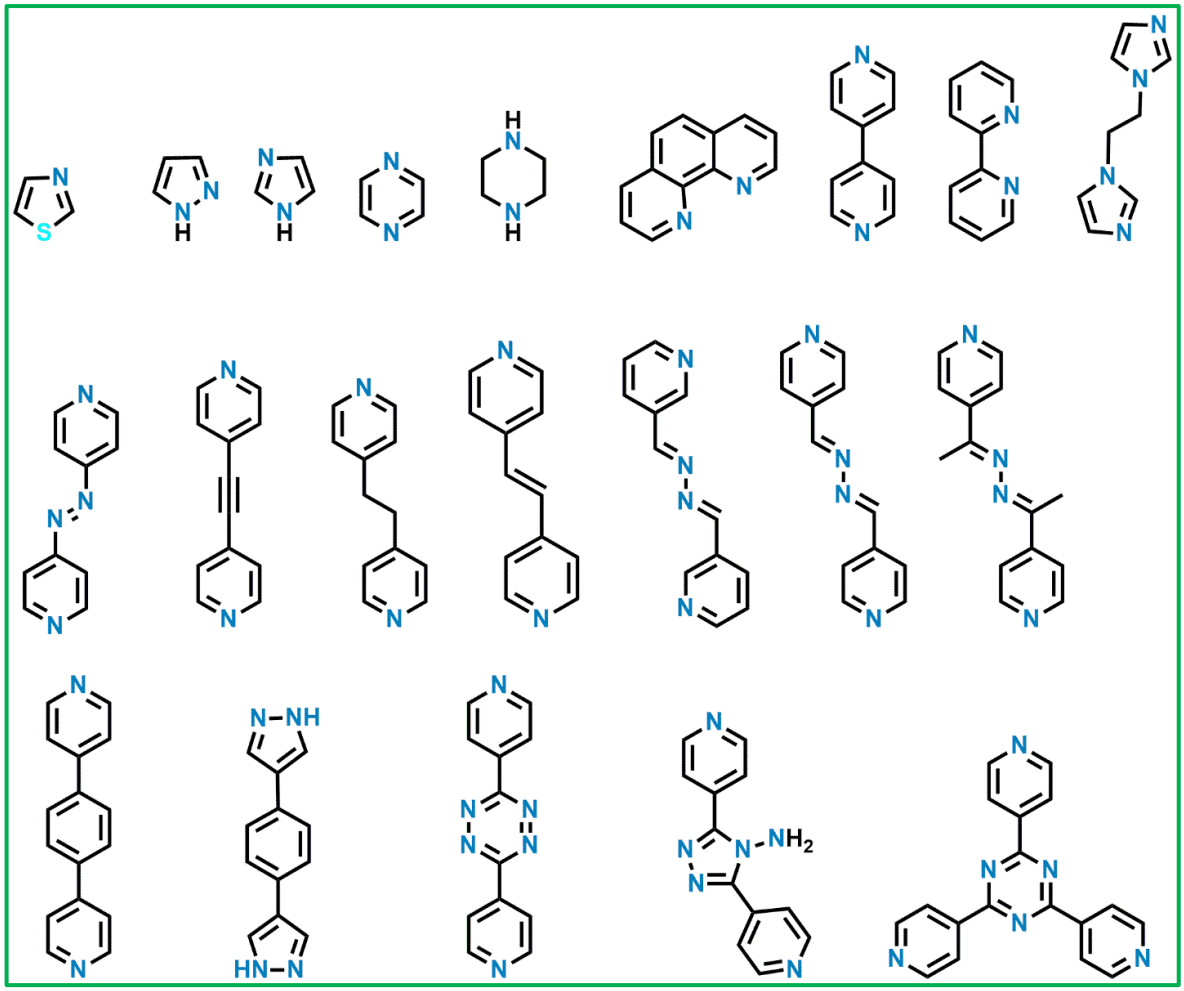

Figure 4. Some N, N′-donor ligands to prepare the MOFs.

1A.2.2.2. The function of O-donor ligands

Another commonly used class of organic ligands in the construction of coordination polymers are O-donor ligands, which primarily function in their anionic forms such as alkoxides, carboxylates, sulfonates, nitrates, and phosphates. Among these, carboxylate O-donors, particularly bi-dentate or multi-dentate ones, are extensively employed in the synthesis of MOFs due to their effectiveness in producing significant results.[39-41] Carboxylates, with their multi-dentate anionic donor sites, are highly efficient at bridging with cationic metal centers, leading to the formation of various dimensional MOFs. Consequently, a wide range of O-donor poly-carboxylates are used in materials science, as

illustrated in Figure 5. These poly-carboxylates vary in size, shape, rigidity, flexibility, and the presence of functional groups, among other characteristics. Similar to N-donor ligands, poly-carboxylates play a crucial role in influencing the structural diversity of MOFs. For example, small-sized dicarboxylates like oxalate, malonate, or fumarate typically result in non-interpenetrated MOFs due to the formation of smaller cavities, whereas larger aliphatic dicarboxylates like glutarate or adipate tend to form interpenetrated frameworks because of their larger cavities.[42-44] Aromatic dicarboxylates often produce robust MOFs due to their structural rigidity. Both aliphatic and aromatic dicarboxylates, depending on their functional groups, generate a variety of functional MOFs suitable for different applications.[45] Carboxylates, known as hard ligands, form strong bonds with hard metal centers,

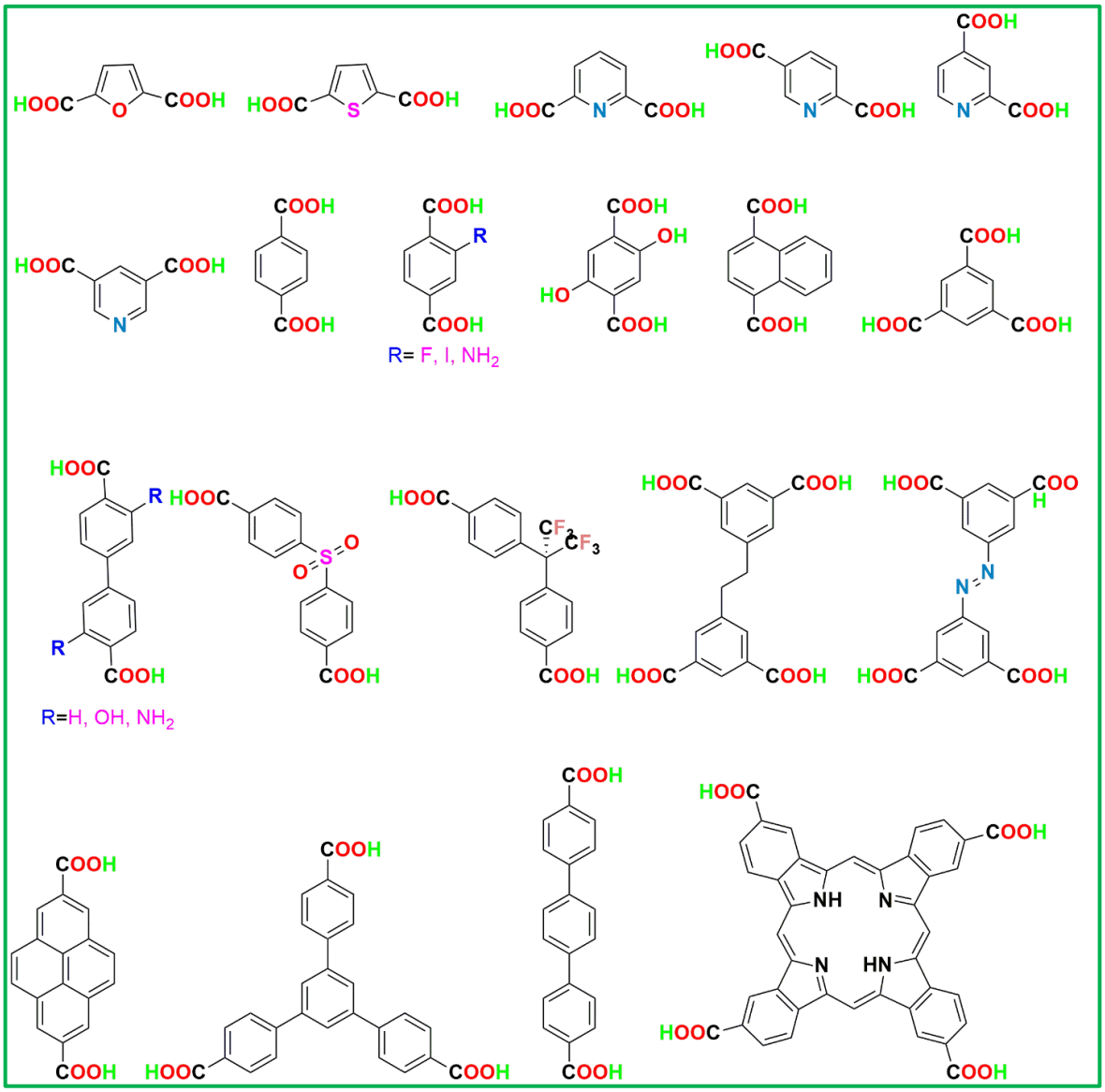

Figure 5. Some O-donor ligands to prepare the MOFs.

with transition metals being the preferred choice due to their ability to form diverse coordination geometries, leading to varied network architectures. Polycarboxylate ligands exhibit multiple bridging modes when coordinating with cationic metal centers such as monodentate, bis-monodentate, mono-chelatate, bis-chelatate, mono-bidentate, bis-bidentate, chelating-monodentate, chelating-bidentate, and various oxo-bridging modes, as shown in the example of terephthalic acid in Figure 6.

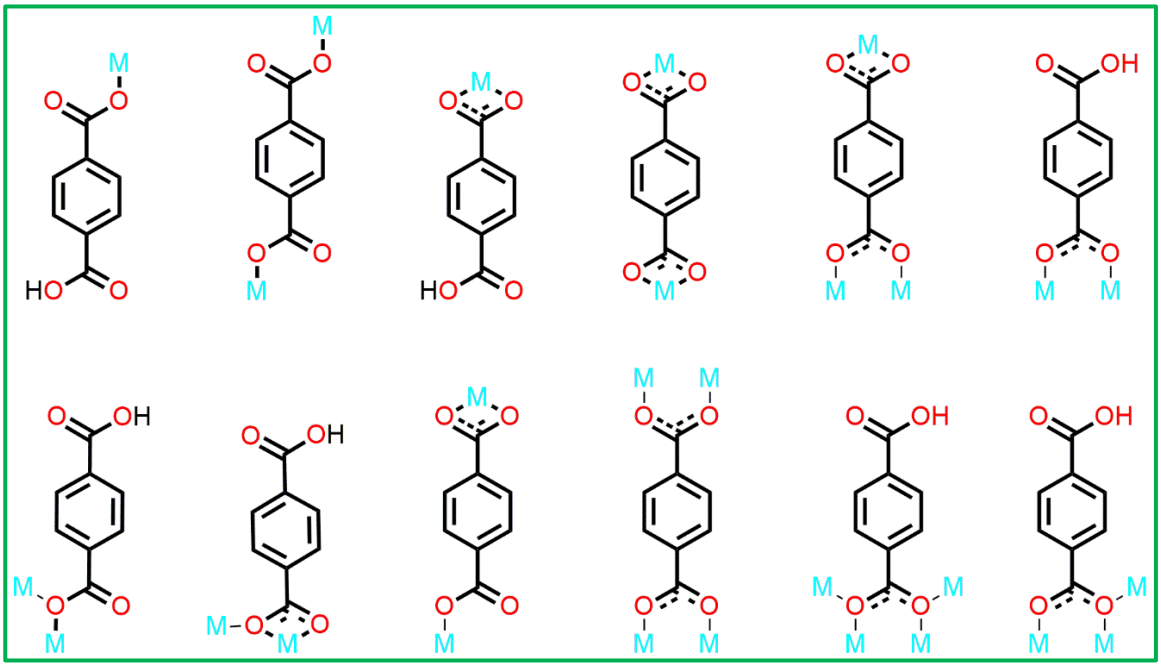

Figure 6. Various bridging fashion of terephthalic acid/terephthalate

1A.2.3. Role of Solvent Used for the Synthesis of CPs

Solvents play a crucial role in generating diverse dimensionalities and fascinating topologies in coordination polymers (CPs) due to their varying coordination capabilities with metal centers, influenced by the Lewis acidity of the metals. Numerous studies have demonstrated the synthesis of different dimensional CPs by altering the solvent.[46-50]

The study by Nithi Phukan et al. investigated how solvents influence the coordination symmetries and properties of dysprosium(III) based coordination polymers.[46] Six new

Dy(III)-based coordination polymers were synthesized using different solvents, and their structures, thermal stability, and luminescent properties were characterized. The solvents significantly directed the formation of the Dy(III) coordination sphere, affecting the polymers' dimensionality, stability and emission properties. The compounds exhibited diverse symmetries: $[Dy_2(L)_2(HCOO)_3(DMF)\cdot Me_2NH_2\cdot H_2O]_n$(1): D_{2d} symmetry; $Dy_4(L)_6(DMA)_2(H_2O)_4\cdot 4DMA\cdot 4H_2O]_n$ (2) : C_{2v} and D_{4d} symmetries; $[Dy_2(L)_3(DMSO)_3(H_2O)_2\cdot 2DMSO\cdot 2H_2O]_n$ (3): C_{4v} and Cs symmetries; $[\{Dy(L)(DEF)\}_2(\mu_2\text{-}OH)]_n$ (4): C_{5v} symmetry; $[Dy_2(L)_3(phen)_2\cdot DMA\cdot 7H_2O]_n$ (5): D_{4d} symmetry; $[Dy(L)(NO_3)(py)_2\cdot py]_n$ (6): D_{2d} symmetry. These structural variations significantly affected the emission properties of the compounds, with emission maxima ranging from the blue to the yellow region depending on the coordination symmetry and the type of solvent used.

1A.2.4. Role of pH in Reaction Medium for the Construction of CPs

Indeed, the pH of the reaction medium plays a crucial role in the synthesis of CPs, as evidenced by various studies in the literature.[51-53] For instance, Yang et al. conducted experiments where they varied the pH of the reaction medium to synthesize a variety of CPs.[54] Yang et al.'s study underscores the importance of pH in the synthesis of metal-organic frameworks (MOFs). The ability to tune structural features through pH manipulation opens pathways for designing materials with specific properties, crucial for applications in catalysis, gas storage, and photonics. The study effectively demonstrated how pH modulates the deprotonation of the H_4ODPT ligand, influencing the coordination environment and resulting in diverse structural frameworks. The findings contribute valuable insights into the field of crystal engineering, highlighting how subtle changes in synthesis conditions can lead to significant variations in material properties.

1A.2.5. The Influence of Counter Ions on the Structural Design and Functionality of Coordination Polymers

Counter ions significantly influence the synthesis and structural design of coordination polymers (CPs).[34, 55] Researchers have extensively explored the synthesis of various CPs by simply varying the counter ions of metal salts.[56] The diversity in the shape, size, coordination sites, and coordination capabilities of different counter ions makes them powerful tools for creating CPs with varied dimensionality and fascinating topologies.[57] Moreover, CPs

incorporating counter ions within their lattice structures can exhibit intriguing functionalities, such as anion exchange.

The study by Yan Xu *et al.* explored how counter anions influence the crystal growth and properties of one-dimensional homochiral coordination polymers. Four pairs of enantiomeric dysprosium(III) phosphonates were synthesized using different counter anions: NO_3, Cl, Br, and CF_3SO_3.[58] The research revealed that counter anions significantly affect crystal morphology and aspect ratios in the order: $NO_3^- > Cl^- > Br^- > CF_3SO_3$, reflecting decreasing interchain interactions.

The study also showed that variations in coordination geometries of the Dy(III) ions, induced by different counter anions, lead to distinct magnetic properties. Specifically, compounds with Cl^- and Br exhibited dual relaxation processes under zero DC field, indicative of single molecule magnet behavior. This research highlights the critical role of counter anions in determining the structural and functional characteristics of homochiral coordination polymers, providing valuable insights for designing materials with specific magnetic and luminescent properties. These findings advance the understanding of crystal engineering and the development of advanced functional materials.

1A.2.6. Role of Temperature for the Fabrication of CPs

Temperature is a critical parameter in the synthesis of coordination polymers, impacting nucleation and growth rates, structural variations, solubility, and reactivity of precursors, as well as the morphology and functional properties of the resulting materials.[59-61] Controlling the synthesis temperature allows researchers to tailor the properties of coordination polymers for specific applications as well as help to synthesize versatile structures.[62, 63]

Mahata *et al.* have been synthesized three new three-dimensional zinc-triazolate-oxybis (benzoate) compounds via a hydrothermal reaction, and the compounds are identified as $[\{Zn_3(H_2O)_2\}\{C_{12}H_8O(COO)_2\}_2\{C_2H_2N_3\}_2]\cdot 2H_2O$ (I), $[Zn_7\{C_{12}H_8O(COO)_2\}_4\{C_2H_2N_3\}_6]\cdot H_2O$ (II), and $[\{Zn_5(OH)_2\}\{C_{12}H_8O(COO)_2\}_3\{C_2H_2N_3\}_2]$ (III). Compound I exhibit an interpenetrated diamond structure, while compounds II and III feature pillared-layer related structures. The formation of the hydrated phase I at lower temperatures and the dehydrated

phase III at higher temperatures underscores the significance of thermodynamic factors in the synthesis of these compounds.[64] In another study by Mahata et al. (2008) investigated the impact of temperature and time on the formation of metal-organic frameworks (MOFs) in manganese oxybis(benzoate) and manganese trimellitates. The researchers identified six phases in the oxybis(benzoate) system and three in the trimellitate system. Their findings reveal that low-temperature phases consist of Mn_4 clusters linked by carboxylate ligands, whereas high-temperature phases form three-dimensional structures with Mn-O-Mn linkages. The study emphasizes the thermodynamic control of MOF formation, with some evidence of kinetic control under moderate conditions, underscoring the critical role of temperature and time in determining the final structure.[65] Another pioneering work by Mahata et al. investigated the influence of temperature on the structure and dimensionality of manganese oxy-bis(benzoate) compounds, revealing a pathway driven by entropy that leads to the formation of different phases. By synthesizing three distinct manganese oxy-bis(benzoate) structures at varying temperatures (100°C, 160°C, and 220°C), they observed a progression from one-dimensional to three-dimensional frameworks, accompanied by a decrease in Mn-Mn distances. Their findings underscore the role of thermodynamic factors, particularly dehydration, in the formation of metal-organic frameworks (MOFs). This research highlights the significant impact of synthesis conditions on the structural evolution of MOFs and suggests avenues for further exploration of other variables such as reaction time and pH.[66]

1A.3. CONTEMPORARY STRATEGIES FOR THE SYNTHESIS OF FUNCTIONAL COORDINATION POLYMERS.

Designing functional coordination polymers (CPs) involves selecting ligands with specific functional groups, employing mixed ligands for structural diversity, and choosing metal ions based on coordination preferences and desired properties. Controlling network topology through the coordination environment and utilizing supramolecular interactions, along with careful adjustment of synthetic conditions. Post-synthetic modifications and defect engineering can further enhance functionality, while host-guest chemistry allows for dynamic behavior and incorporation of guest molecules.

1A.3.1. Mixed Ligand Strategies

Mixed-linker CPs/MOFs, a significant subclass of MTV-MOFs, offer a unique approach to functionalizing MOFs by selectively generating pore environments and structural defects. These mixed-linker systems incorporate linkers of varying lengths and geometries during one-pot synthesis or through post synthetic modification to achieve desired functionalities as illustrated in Figure 7.

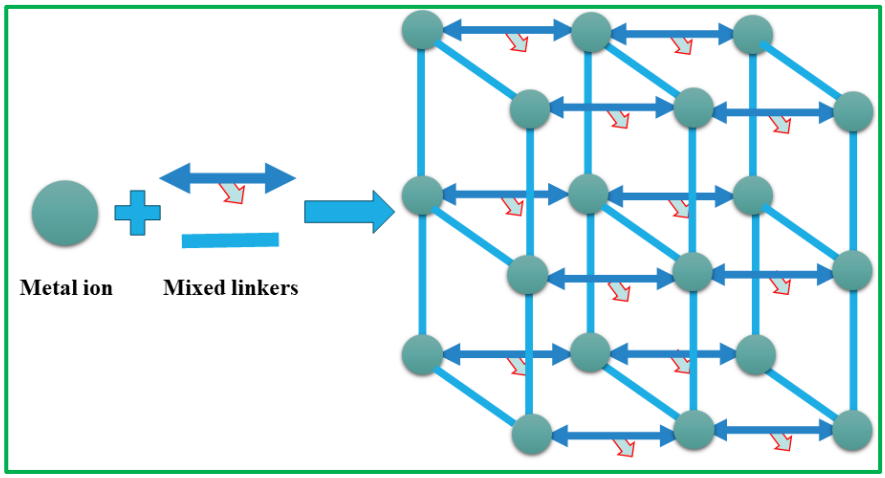

Figure 7. Schematic representation of mixed ligand CPs/MOFs synthesis.

In 2010, Yaghi et al. reported early examples of mixed-linker MOFs, specifically MTV-MOF-5, which incorporated eight distinct functionalities (-NH_2, -NO_2, -Br, -Cl_2, -$(CH_3)_2$, -$(OC_3H_5)_2$, -C_4H_4, and -$(OC_7H_7)_2$) within a singular crystalline network, resulting in a 400% enhancement in selectivity for CO_2 over CO.[67] Similarly, the Zhou group synthesized a UiO-66 based multivariate MOF incorporating 2-connected BDC and 4-connected TCPP linkers into a disordered, yet ordered, structure.[68] Despite the advantages, targeted incorporation of linkers remains challenging due to the thermodynamic nature of MOF assembly. Metals within clusters can influence linker positioning, allowing some control over the final structure. Fully connected mixed-linker MOFs can be achieved through a combination of linkers, although this often results in structural disorder.[69] Efforts to minimize this disorder include the strategy by Tefel et al., who synthesized mixed-linker Zn MOFs in a modular quaternary system, introducing three distinct linkers into a preformed porous framework.[70] This approach has been applied to other MOFs, such as PCN-133 and PCN-134. While

traditional one-pot synthesis techniques are common, they require precise control to avoid undesired phases. Post synthetic modification methods, particularly linker exchange, offer more controllable design options for mixed-linker MOFs, utilizing the reversible nature of metal-ligand bonds to achieve ordered structures under mild conditions.

1A.3.2. Mixed Metal Strategies

Mixed-metal coordination polymers, incorporate more than two kinds of metal species in a single metal cluster as illustrated in Figure 8, offering several advantages such as enhanced stability, customizable electronic properties, and improved catalytic activity. These CPs/MOFs exhibit structural diversity beneficial for various applications, including water splitting, gas storage and separation processes. The choice and combination of metals are crucial in shaping the properties and performance of these MOFs.

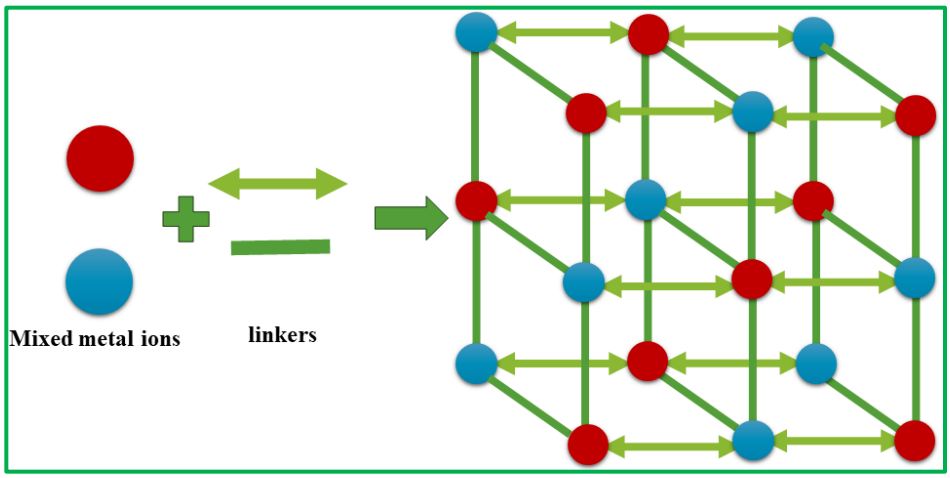

Figure 8. Schematic representation of mixed metal CPs/MOFs synthesis.

Solvothermal synthesis of mixed-metal MOFs typically produces mixed MOF phases rather than pure mixed-metal MOFs. In 2014, Yaghi and coworkers reported a series of microcrystalline MOF-74 variants containing divalent metal clusters (Mg, Ca, Sr, Ba, Mn, Fe, Co, Ni, Zn, and Cd) obtained through one-pot solvothermal reactions. Energy-dispersive X-ray spectroscopy indicated that the metal ions were heterogeneously arranged within each crystalline MOF sample.[71] Subsequent studies, such as those by Qi and coworkers, have deciphered the spatial distribution of metals in mixed-metal MOFs. They found that these MOFs could exist as either domain structures, where each cluster contains only one type of

metal, or well-mixed structures, where clusters contain two or more metals per cluster. Well-mixed clusters are rarer and more challenging to synthesize than domain structures.[72] An example of well-mixed clusters is the alkaline-resistant MOF [{$Fe_3(\mu_3$-O)$(BDC)_3\}_4\{Co_2(NA)_4(LT)_2\}_3$], exhibited remarkable catalytic activity in the oxygen evolution reaction (OER) with a low overpotential of 225 mV at a current density of 10 mA cm^{-2}.[73] Another example is the heterometallic Ni–Co MOF [$CoNi(\mu_3$-$BDC)_2(\mu_2$-$PYZ)_2$], which has shown potential in supercapacitor development.[74]

1A.3.3. Isoreticular expansion

Isoreticular expansion, also known as scale chemistry or isoreticular synthesis, involves enlarging the pore sizes and surface areas of metal-organic frameworks (MOFs) by using ligands of increasing length while maintaining the same framework topology.[75] This method allows for tuning pore surface functionalities and requires that the reaction conditions produce the same inorganic cluster to preserve the coordination geometry and topology of the parent MOF.[76]

In isoreticular series, the original MOF retains its name, while subsequent structures are often labeled with "IRMOF" to indicate their derivation through isoreticular expansion, though this naming convention is not universally applied.[77] For example, the HKUST-1 series can be expanded using different metals such as Zn^{2+}, Fe^{2+}, Cr^{2+}, and the original Cu^{2+}.[78, 79] A pioneering example of an isoreticular MOF series by Yaghi et al. was based on MOF-5, with variations in BDC linkers leading to different pore sizes.[80] Another significant study by Wang et al. synthesized Zr-MOFs (NU-1101 to NU-1104), achieving surface areas between 4422 m^2/g and 5646 m^2/g.[81] However, increasing linker size can also increase the likelihood of interpenetration (catenation), which reduces surface area, pore volume, and active site availability, though it can be advantageous for applications involving small molecules like hydrogen.[82]

A common challenge in isoreticular synthesis is interpenetration or catenation, which reduces surface area, pore volume, and active sites, though it may be beneficial for applications involving small molecules like hydrogen. Researchers focus on topology-guided design to mitigate interpenetration issues.

1A.3.4. Post Synthetic Modification

MOFs are highly versatile materials known for their high surface area, porosity, and structural flexibility, making them suitable for various applications such as catalysis, gas storage, separation, sensors, drug delivery, and more. However, the inherent limitations of direct synthesis methods often restrict the optimization of MOF properties for specific applications. Post Synthetic Modification emerges as a robust strategy to address these limitations by allowing targeted modifications of MOF structures post-synthesis.[83]

1A.3.4.1. Metal Exchange.

Trans metalation involves replacing the metal ions in the MOF's framework with different metal ions. This process requires breaking the existing coordinate bonds between the metal ions and organic ligands and forming new bonds with the incoming metal ions (Figure 9). For example, the replacement of Zn(II) ions with Cu(II) ions in a Zn-based MOF can lead to improved thermal stability due to the Jahn-Teller effect associated with Cu(II) ions.[84] The effectiveness of trans metalation depends on factors such as the lability of the metal ions, coordination preferences, solvent effects, and the stability of the resultant MOF. In one study, Cu(II) ions replaced Zn(II) ions in the MOF PUM-210, resulting in enhanced framework stability and modified magnetic properties.[85]

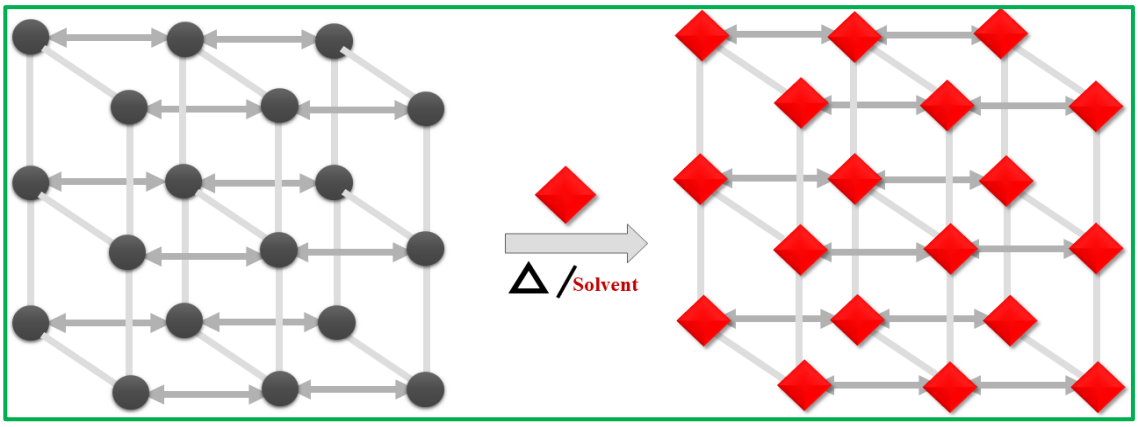

Figure 9. Schematic representation of metal exchange via post synthetic modification.

A.3.4.2. Ligand Exchange.

Ligand exchange involves replacing the organic ligands in the MOF structure with different ligands (Figure 10). This method can significantly alter the chemical environment within the MOF, thereby introducing new functionalities. The exchange process often retains the

original topology of the MOF while enabling the introduction of ligands that confer additional properties. A series of mesoporous bio-MOFs were successfully synthesized by utilizing dicarboxylic acid ligands of varying sizes through a linker replacement strategy.

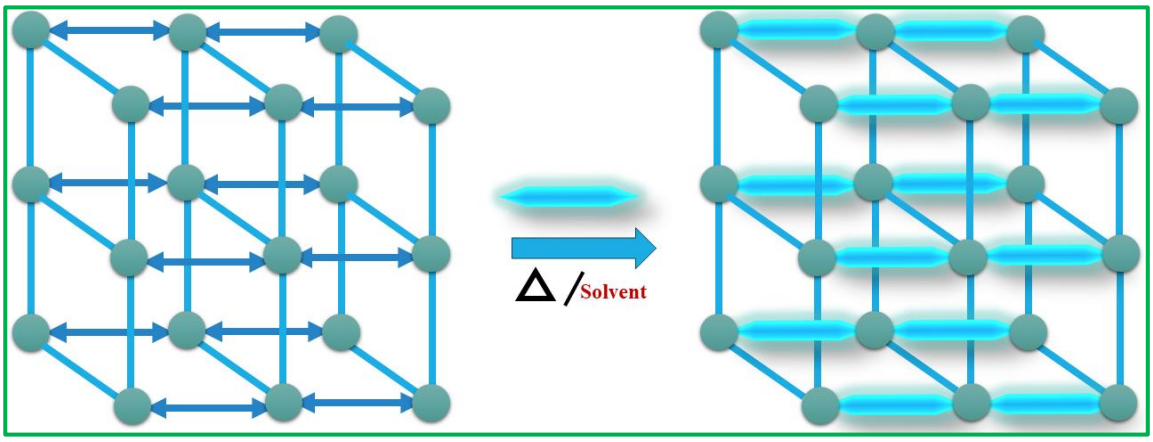

Figure 10. Schematic representation of post synthetic ligand exchange in CPs or MOFs.

The bio-MOFs created were heteroleptic, featuring zinc-adeninate clusters ($Zn_8Ad_4O_{28}^+$; Ad = adeninate) that were periodically connected to dicarboxylate groups to form the three-dimensional structure. This transformation occurred in a single-crystal-to-single-crystal (SC-SC) manner, and with each step using a larger dicarboxylate ligand, the resulting MOFs were more robust and exhibited increased pore volume. During the synthesis process, MOF crystals were isolated and analyzed, revealing a decreasing pore size from the periphery to the core of the single crystal. This observation confirms the absence of a dissolution–recrystallization pathway.[86]

1A.3.4.3. Guest Exchange.

Guest exchange involves the introduction or replacement of guest molecules within the MOF's pores. This approach can enhance the MOF's properties without altering its overall structure. Guest exchange can be achieved by simply soaking the MOF in a solution containing the desired guest molecules.[87] The replacement of aqua ligands with pyridine molecules in HKUST-1 resulted in the formation of a new MOF with increased thermal stability. The guest exchange method also allows for the introduction of metal nanoparticles, such as palladium or platinum, into the MOF structure, enhanced its catalytic activity. [78]

PSM is a transformative approach that addresses the limitations of conventional MOF synthesis. By allowing precise modifications at the metal, ligand, and guest levels, PSM enables the creation of MOFs with tailored properties that meet the specific demands of various applications.

1A.4. DETAILED METHODOLOGIES OF COORDINATION POLYMER SYNTHESIS.

Currently, there are several prominent approaches for fabricating coordination polymers (CPs) in the fields of material science and synthetic chemistry. Some of these key methods were described below.

1A.4.1. Stirring Method.

Traditionally, scientists employ a standard procedure to synthesize CPs. Initially, they blend a concentrated solution of the reactants through stirring for several hours at ambient temperature to achieve homogeneity. Following this, the meticulously mixed solution is allowed to evaporate in a dry environment, promoting the growth of high-quality single crystals suitable for analysis via single crystal X-ray diffraction.

1A.4.2. Solvothermal Method.

Solvothermal synthesis is the most common method for synthesizing coordination polymers (CPs). It involves crystallizing substances from high-temperature solutions of reactants in solvents like water, dimethylformamide, dimethylacetamide, acetonitrile, methanol, or their mixtures. Key factors include reactant concentration, stoichiometry, pH, reaction time, and temperature. Samples are placed in durable, non-corrosive Teflon cups, sealed in an autoclave, and heated to 80–180 ºC under autogenous pressure. After the reaction, the mixture is slowly cooled, forming crystals in-situ. At high temperatures, lattice particles vibrate vigorously and can leave their positions, melting the crystal. Dynamic equilibrium is achieved if the solid and liquid phases stay in contact, with crystal growth governed by kinetic factors and thermal randomization countering molecular ordering.

1A.4.3. Slow Diffusion Method.

This method focuses on meticulously blending reactants to maximize the chances of obtaining the desired crystal structure. The technique involves setting up separate solutions

containing different reactants (metal and ligand) within a layered tube, separated by a buffer solution created by carefully mixing two solvents used for metals and ligands at specific ratios. Through the gradual diffusion process, the distinct solutions slowly intermingle, leading to the formation of crystals at their interface over time. Moreover, in addition to this method, there are several other well-established techniques, such as reflux and ultrasonic methods, which synthetic chemists frequently employ. These methods offer controlled and convenient approaches for the synthesis of coordination polymers, enhancing the versatility and efficiency of CP fabrication in the laboratory.

1A.4.4. Reflux Method.

Chemists utilize this approach to yield single crystals. Initially, reactant solutions are combined and subjected to reflux at a precise temperature for several hours. Following this, the mixture is transferred into a beaker, where, over a designated period, high-caliber single crystals ideal for single-crystal analysis develop.

1A.4.5. Microwave or Ultrasonic Reaction.

While this technique is not extensively utilized for generating single crystals of MOFs because of its limitations in achieving rapid synthesis, it remains a valuable method for precisely regulating the size and morphology of the resultant products.

1A.5. STRUCTURAL CHARACTERIZATIONS OF CPS.

Understanding the complete structure of synthesized coordination polymers (CPs) is essential, and various methods are employed for structural characterization, with X-ray crystallography taking precedence. Both single crystal and powder forms of crystallography are indispensable for precisely determining CPs. Single crystal X-ray diffraction (XRD) reveals crystallographic parameters, unveiling the entire structure, crystal packing, and weak forces. Conversely, powder X-ray diffraction confirms phase purity by comparing patterns with simulated data from single crystal XRD. Software tools aid in deducing crystallographic parameters from powder XRD patterns. Fundamental spectroscopic techniques like Fourier transform infrared (FT–IR), UV–vis, and nuclear magnetic resonance (NMR) spectroscopy are used for primary characterization of ligands and synthesized frameworks. FT–IR identifies functional groups by correlating with theoretical frequencies, while UV–vis

spectroscopy elucidates electronic transitions. NMR spectroscopy probes nuclear spin state interactions. Additionally, complementary methods like scanning electron microscopy (SEM) provide morphological information and particle size distribution, while energy-dispersive X-ray spectroscopy (EDX) determines elemental composition. Thermogravimetric analysis evaluates thermal stability and decomposed products at different temperatures, offering valuable insights into synthesized CPs.

1A.5.1. Fourier Transform Infrared (FT–IR) Spectroscopy.

Fourier transform infrared (FT-IR) spectroscopy is a fundamental technique widely used in both organic and inorganic chemistry to analyze samples by directing infrared radiation through them. Traditionally, this involves preparing samples with KBr to form a homogeneous mixture, allowing the detector to measure the energy of transmitted radiation and reveal absorption at different wavelengths. This information helps identify structural characteristics and functional groups based on their characteristic frequencies. An alternative, simpler method for FT-IR analysis is the Attenuated Total Reflectance (ATR) technique. In ATR, the sample is placed directly onto an ATR crystal, with solids making firm contact and liquids forming a thin, even layer. Gentle pressure is applied using the ATR accessory to ensure optimal contact. The FT-IR spectrometer then captures the spectrum, showing how infrared radiation is absorbed as it reflects off the crystal and interacts with the sample. ATR spectra are generally easier to interpret and require less preparation, offering a straightforward way to identify functional groups and structural features.

1A.5.2. Nuclear Magnetic Resonance (NMR) Spectroscopy.

Nuclear magnetic resonance (NMR) spectroscopy is a widely utilized absorption technique in chemistry. Samples are subjected to a strong magnetic field, causing nuclei in the atoms to absorb energy from radio waves. This technique is effective in both liquid and solution states, relying on interactions between nuclei and the magnetic field to facilitate transitions between nuclear spin states. Its importance lies in offering valuable chemical and structural insights into samples. NMR spectroscopy is versatile, allowing for the prediction of structural information in different states, including solutions and solid forms.

1A.5.3. Scanning Electron Microscopy (SEM) and Energy Dispersive X-ray Spectroscopy.

SEM works by scanning a focused beam of electrons across the surface of a specimen. When the electrons interact with the atoms in the specimen, various signals are generated, including secondary electrons, backscattered electrons, and characteristic X-rays. These signals are then detected and used to create high-resolution images of the specimen's surface. SEM can produce images with extremely high resolution, typically ranging from nanometers to micrometers. This allows to visualize surface features, morphology, and microstructure of materials at very small scales. In addition to imaging, SEM can also perform elemental analysis using techniques such as energy-dispersive X-ray spectroscopy (EDS) or wavelength-dispersive X-ray spectroscopy (WDS). These techniques allow researchers to identify and quantify the elements present in a specimen based on the characteristic X-rays emitted during electron interaction. Overall, SEM is a versatile tool that provides detailed insights into the structure and composition of a wide range of materials and samples, making it indispensable in scientific research and various industries.

1A.5.4. Elemental Analysis.

Elemental analysis entails determining the proportions of elements such as carbon (C), hydrogen (H), and nitrogen (N). By focusing on these elements, this analysis aids in corroborating the probable empirical formula of the structures being investigated.

1A.5.5. Single Crystal X-ray Diffraction Analysis.

Single crystal X-ray diffraction analysis serves as a comprehensive technique, furnishing intricate insights into the crystal structure of a compound. It offers a plethora of details including crystal symmetry, unit cell parameters, space group, structural dimensions, site-ordering specifics, and atomic positions. The derived unit cell parameters can ascertain whether the structures are novel or already documented in databases like the Cambridge Structural Database (CSD). This method relies on the utilization of graphite-monochromated X-rays of Mo-Kα radiation (λ= 0.71073Å) and a crystalline sample. These X-rays, emanating from a sealed tube source and refined to produce monochromatic radiation, are directed onto the sample. The interaction between the incident rays and the sample induces constructive

interference and diffracted rays, adhering to Bragg's Law ($n\lambda = 2d \sin\theta$). This law correlates the wavelength of electromagnetic radiation, diffraction angle, and lattice spacing within a crystalline sample. The resultant diffracted X-rays are detected, processed, and enumerated. By manipulating the incident ray geometry, crystal orientation, and detector placement, access to all feasible diffraction directions of the lattice is achieved. The collected data is subsequently processed, correcting for absorption using various software tools. Following data collection, integration, and solution, successive Fourier and difference Fourier synthesis techniques are employed. Full matrix least-squares refinements are then applied to F_2 values for all non-hydrogen atoms utilizing diverse refinement software.

1A.5.6. X-ray Powder Diffraction.

The X-ray powder diffraction pattern depicts the intensity of scattered radiation from a sample, illustrating incident and scattered angles, polarization, and wavelength or energy. This pattern serves as a distinctive "fingerprint" for crystalline materials, facilitating their identification based on unique characteristics. Moreover, it assists in validating phase transformations within a solid sample by comparing unit cell parameters before and after analyses. To conduct this study, solid samples synthesized initially are homogenously ground into bulk form. Subsequently, X-ray powder diffraction patterns of these samples are captured using Cu-Kα radiation (λ = 1.5406 Å) with a suitable powder diffractometer set in Bragg–Brentano (reflection) mode.

1A.5.7. Thermogravimetric Analysis (TGA).

Thermogravimetric analysis (TGA) is a crucial technique that monitors the changes in weight of a solid material as temperature varies under controlled atmospheric conditions. It offers a quantitative evaluation of weight loss associated with material transitions and thermal degradation. This approach is instrumental in assessing the thermal stability of a substance and discerning its decomposition products.

1A.5.8. UV–Vis Spectroscopy.

This form of absorption spectroscopy unveils electronic transitions such as π–π^*/n–π^* or d–d transitions, illustrating intra-ligand (ILCT) or metal-to-ligand (MLCT) charge transfers within the UV or visible range during experiments on solid samples. Coordination polymers typically exhibit insolubility in conventional organic solvents, necessitating structural

characterization in their solid state. UV-VIS spectroscopy is conducted using diffuse reflectance spectra (DRS) on powdered samples, employing a diffuse reflectance accessory, thus termed diffuse reflectance UV-VIS spectroscopy.

1A.5.9. Nitrogen Gas Adsorption.

Determining the surface area and pore volume of synthesized structures is essential in coordination chemistry. Coordination polymers, formed by combining metals and ligands, often exhibit high surface areas and porosities, crucial for various applications. Manipulating the surface area is vital for the practical use of these materials. Expanding organic linkers is a common strategy to create microporous coordination polymers (MCPs) with increased surface areas. However, challenges such as framework collapse, incomplete guest removal, or non-optimal linkers can reduce surface areas or result in nonporous structures.[88, 89] Theoretical calculations, including Grand Canonical Monte Carlo (GCMC) simulations, help predict the optimal surface area, which is then compared to experimental BET surface area analysis using nitrogen gas adsorption.[90] BET is considered more reliable than other methods like Langmuir. Recent studies also explore the separation of nitrogen from gas mixtures, showcasing the wide-ranging applications of these materials.[91]

1A.6. VARIOUS POTENTIAL APPLICATIONS OF CPS.

1A.6.1. Gas and Solvent Sorption

Coordination polymers have a wide range of applications, with gas and solvent adsorption being particularly well-studied due to their versatile industrial and practical uses.[92, 93] These materials often feature frameworks with significant voids, which enable their multifunctional applications. These frameworks can accommodate specific adsorbates based on properties such as kinetic diameter, polarity, and shape, making them suitable for a variety of molecules. Determining the pore size of synthesized coordination polymers is essential for understanding their adsorption capabilities, and this is typically accomplished by analyzing their nitrogen adsorption isotherms.

1A.6.1.1. Carbon Dioxide Adsorption

The combustion of fossil fuels is leading to progressively rising atmospheric CO_2 levels, significantly contributing to dramatic climate changes such as global warming. To address this issue, capturing the emitted CO_2 is crucial, given the essential role of energy in sustaining civilization. Most flue gases contain substantial amounts of nitrogen (N_2), making it critical to achieve selectivity in the absorption process to ensure that the capturing material exclusively traps CO_2 from the nitrogen-carbon dioxide gas mixture. While carbon capture and sequestration (CCS) technologies, such as amine scrubbing and membrane separation, have been widely used for CO_2 capture, they often face issues related to economic durability.[94] However, zeolites have gained prominence in CO_2 separation due to their well-defined structures and stability. Recently, researchers have focused on metal-organic frameworks (MOFs) as porous solids for CO_2 separation. Numerous groups have reported thousands of porous CPs/MOFs due to their capacity for selective CO_2 adsorption.[95, 96]

Gan et al. synthesized mCB-MOF-1, a MOF characterized by its hydrophobicity and high thermal and chemical stability, leveraging the unique properties of icosahedral carboranes. This study explores the performance of mCB-MOF-1 for the adsorptive separation of CO_2 under humid conditions. The results demonstrated that mCB-MOF-1 exhibits superior CO_2 adsorption capacity and selectivity compared to traditional MOFs, especially under humid conditions. The MOF maintained high CO_2 uptake and selectivity for CO_2:N_2 mixtures, even in the presence of water vapor, highlighting its potential for real-world CCS applications. The study concludes that mCB-MOF-1 is a promising candidate for CCS applications due to its high CO_2 selectivity, stability under humid conditions, and ease of regeneration. This work significantly contributes to the field of MOFs and CO_2 capture technologies, offering a viable solution for mitigating CO_2 emissions from industrial processes.

1A.6.1.2 Hydrogen Adsorption

The petroleum fuel crisis and substantial CO_2 emissions from combustion necessitate alternative energy sources for automotive transportation. Battery and fuel-cell technologies are strong candidates to replace gasoline and diesel engines. Hydrogen is particularly attractive as an energy carrier due to its carbon-free nature, abundant availability from water, and exceptional mass energy density. However, effective hydrogen storage remains a significant challenge, hindering the commercialization of fuel-cell vehicles. This difficulty

arises from hydrogen's high fugacity and associated safety concerns. Coordination polymers (CPs) and metal-organic frameworks (MOFs) possess several key features that make them promising for hydrogen storage.[97] These materials exhibit open metal sites, catenation/interpenetration, high specific surface area, suitable pore sizes, and structural flexibility, all of which contribute to enhanced H_2 uptake capacity under optimal conditions.[98] [99]

Barman et al. introduced two zinc-based metal-organic frameworks (MOFs), designated as MOF-645 and MOF-646. These MOFs, synthesized from 1,3-azulenedicarboxylate ligands, demonstrate significant hydrogen adsorption capabilities. MOF-646, in particular, exhibited strong MOF-H_2 interactions, underscoring the potential of azulene-based frameworks in hydrogen storage applications.[100]

1A.6.1.3. Solvent Adsorptions

Activated carbon is commonly used in solvent recovery due to its effectiveness in adsorbing organic solvents from diluted gas streams. However, its high adsorption capacity can increase gas humidity during the treatment process. Metal-organic frameworks (MOFs) have emerged as viable alternatives for adsorbing solvent vapors, aiding in applications such as separation and solvent recovery. The adsorption process for solvents in MOFs is often complicated by the presence of water. Research has highlighted how both pre-adsorbed and co-adsorbed water impact adsorption equilibrium, particularly in small fixed bed systems. Unlike many hybrid materials, MOFs typically do not have a distinct pressure threshold because their hydrophilic sites result in a strong affinity for water.

The study by Jeremias *et al.* investigated the water adsorption/desorption capabilities of the porous MOFs 3D-$\{M_3O(X)(H_2O)_2[btc]_2.nH_2O\}$ specifically MIL-100 (M = Al, Fe; X = OH, F; btc = benzene-1,3,5-tricarboxylate, trimesate). These MOFs exhibited significant water uptake of up to 0.75 g per gram of MOF at low relative pressures ($P/P_0 < 0.4$) with minimal hysteresis. This, coupled with excellent cycle stability, positions MIL-100(Al and Fe) as promising candidates for thermally driven heat pumps and adsorption chillers.[101] Similarly, Tang *et al.* developed a novel in-situ polymerization technique to incorporate poly(N-isopropylacrylamide) (PNIPAM) chains within the one-dimensional (1D) pores of a zinc-

based MOF. This innovative approach produced MOF-based composites that demonstrated selective adsorption for water and methanol over ethanol, particularly in equimolar mixtures of methanol-ethanol and water-ethanol.[102]

1A.6.2. Photoluminescence

Luminescence is a complex phenomenon where radiation is emitted from an excited state. This can be caused by various excitations, such as photonic, mechanical, chemical, or electrochemical processes. The fundamental mechanism involves an electron transitioning from the ground state to an excited state upon photon absorption, followed by emission as it returns to the ground state. Fluorescence and phosphorescence are two types of luminescence. In fluorescence, the electron transitions from a singlet excited state (S_1) to the ground state (S_0), resulting in a short-lived emission (1–100 ns). Phosphorescence involves intersystem crossing from the singlet excited state (S_1) to a triplet state (T_1), followed by a forbidden transition to the ground state (S_0), resulting in longer emission lifetimes (1 µs or more).[103]

Coordination polymers (CPs) exhibit diverse luminescence mechanisms due to their complex structures, which include metal-centered (MC) emission, ligand-centered (LC) emission, and various charge-transfer (CT) emissions, such as ligand-to-metal (LMCT), metal-to-ligand (MLCT), ligand-to-ligand (LLCT), and metal-to-metal (MMCT)(Figure 11).[104] Guest molecules can also contribute to luminescence through guest-centered emission and guest-sensitization. The luminescence in CPs can be enhanced by immobilizing ligands within the crystal lattice, which restricts molecular rotation and introduces the heavy atom effect, shifting luminescence from fluorescence to phosphorescence. Metal ions with closed-shell configurations (e.g., alkali and alkaline earth metals, d^0 or d^{10} transition metals) are typically used for LC-based CPs, while lanthanides and actinides are used for MC-based CPs. This property's significance has spurred substantial interest among researchers, driving a heightened focus on synthesizing luminescent CPs tailored for diverse purposes. Numerous applications are actively under discussion and exploration, tapping into the potential of these materials.[105]

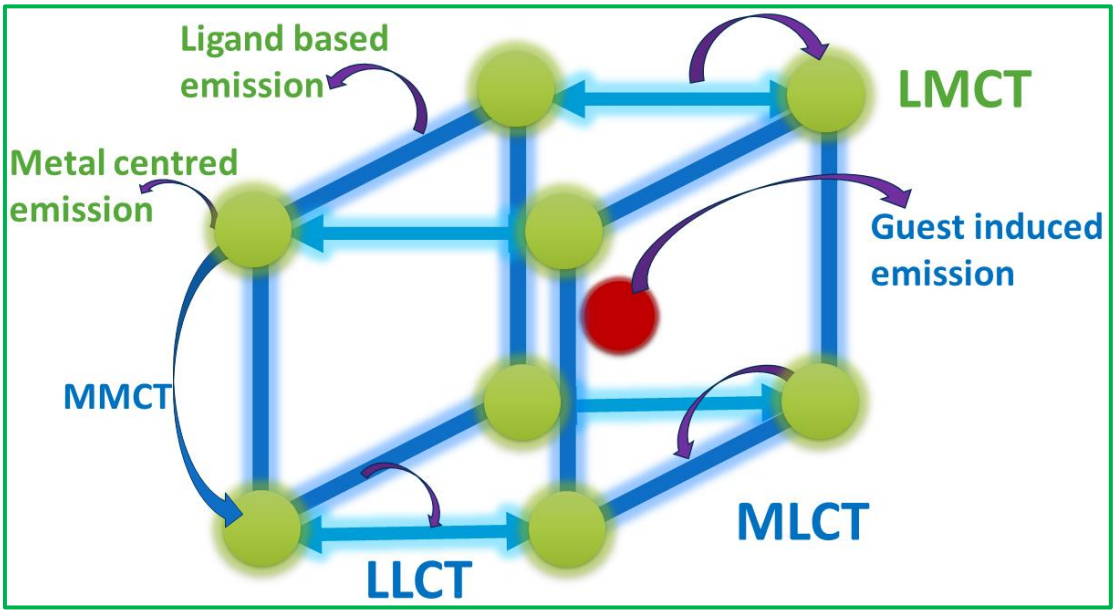

Figure 11. Key transitions in CPs indicating pathways for luminescence.

1A.6.2.1. VOCs and Explosive Sensing

Luminescent coordination polymers (LCPs) combine the advantages of MOFs, such as porosity and tailorability, with intrinsic luminescent properties, making them ideal for sensing applications. These applications rely on host-guest interactions between analyte molecules and LCPs, leading to changes in luminescent intensity (e.g., turn-on and turn-off effects) or shifts in peak positions.[6]

In 2020, Liu et al. developed a rigid Cu(I)-based MOF, $[Cu_4I_4(Py_3P)_2]n$ (Py_3P = tris(2-pyridyl)phosphine), that exhibited guest-induced luminescence enhancement. Exposure to chlorinated VOC vapors (CH_2Cl_2, $CHCl_3$, and $C_2H_4Cl_2$) resulted in a significant increase in luminescence intensity, unlike other VOC vapors such as benzene, methanol, acetone, and DMF. This enhancement was attributed to weak host-guest interactions reducing molecular vibrations within the MOF.[106]

In the same year, Olorunyomi et al. reported enhanced fluorescence in self-assembled colloidal crystal films by incorporating the fluorescent dye Nile Red (NR) into ZIF-8 colloidal crystals. These dye-functionalized MOF particles were then assembled into

colloidal crystal films via dip-coating. The NR~ZIF-8 films exhibited a 186-fold increase in fluorescence compared to disordered samples. These films also demonstrated selective fluorescent quenching in response to various organic vapors (acetone, methanol, toluene, and xylenes), with the highest response to toluene and the lowest to xylene isomers. The selectivity was due to molecular size and shape exclusion, highlighting the importance of porosity in colloidal crystal assemblies for fluorescent sensing.[107]

Singha et al. (2014) presented the synthesis and characterization of two isomorphous metal-organic phosphor compounds, $[Y_2(PDA)_3(H_2O)]\cdot 2H_2O$ and $[Y_{1.8}Tb_{0.2}(PDA)_3(H_2O)]\cdot 2H_2O$, designed for the optical detection of nitro explosives at sub micromolar levels. The study highlights the use of the dehydrated form of the Tb-doped compound, Tb@1', which exhibited high sensitivity and efficiency in detecting nitro explosives such as TNP, DNB, and DNT through luminescence quenching. The reported quenching constants (K_{SV}) are among the highest recorded for metal-organic materials, underscoring the potential of these materials in explosive detection applications.[108]

1A.6.2.2. Anion Sensing

Coordination polymers (CPs) or Metal-organic frameworks (MOFs) have emerged as promising materials for sensing toxic anions due to their tunable structures and functional properties. Recent advancements highlight their application in detecting hazardous anions like cyanide (CN^-), fluoride (F^-), and bisulfite (HSO_3^-), which pose significant environmental and health risks.[109] Cyanide detection with MOFs is notably rare. A study by incorporating 3,6-diaminoacridinium cation (DAAC) into bio-MOF-1 showcased a significant fluorescence enhancement in the presence of CN^- ions, achieved a detection limit of 5.2 ppb and effective sensing within MCF-7 cells.[110]

Singha et al. reported a terbium-doped yttrium-based metal-organic framework (MOF) synthesized via hydrothermal methods, designed for the luminescent detection of toxic oxoanions in aqueous environments. The framework, identified as $[Tb_{0.2}Y_{0.8}(FDA)(Ox)_{0.5}(H_2O)_2]\cdot H_2O$, demonstrates high sensitivity to anions such as chromate, permanganate, and phosphates, with significantly low limits of detection. The MOF's large Stokes shift and minimal luminescence self-quenching enhance its detection

capabilities, making it a highly effective material for environmental monitoring of hazardous anions.[111]

For fluoride ions detection, MOFs have shown exceptional potential. For instance, Tb-based MOF-76 and NH_2-MIL-101(Al) linked with fluorescein 5(6)-isothiocyanate (FITC) showed turn-on responses upon interaction with F^- ions, even in the presence of other anions.[112] A Eu-based MOF functionalized with boronic acid demonstrated selective fluoride sensing through strong boron-fluoride interactions.[113] Bisulfite (HSO_3^-) sensing was achieved using NH_2-MIL-68(In) modified with glyoxal, which reacts with HSO_3^- to form a stable ring structure, resulting in a turn-on fluorescence response.[114] Similarly, MOF-5-NH_2 showed selective SO_3^{2-} detection with a detection limit of 2.08 μM.[115] Additionally, hypochlorite (ClO^-) sensing was explored using ZIF-90 modified with n-butylamine, which undergoes oxidation in the presence of ClO^-, leading to a detectable response with a limit of 6.25 μM.[116] These studies demonstrated the versatility and efficiency of MOFs in environmental and biological anion detection.

1A.6.2.3. Cation Sensing

Coordination polymers (CPs) or Metal-organic frameworks (MOFs) are highly effective matrices for detecting various cations, which are crucial in many biological systems and can be environmental pollutants posing health risks. The tunable electronic properties and host-guest interactions of MOFs make them particularly adept at sensing a wide range of cations. Fluorometric methods, known for their speed and simplicity, are particularly promising in this regard.[117, 118]

Zhao et al. were among the first to reported the synthesis of two 3d-4f heterometallic coordination polymers {[Ln-$(PDA)_3Mn_{1.5}(H_2O)_3$].3.25H_2O}n (where PDA stands for pyridine-2,6-dicarboxylic acid; Ln represents Eu and Tb). These polymers exhibited a selective turn-on fluorescence response to Zn^{2+} ions. The fluorescence originated from the Ln^{3+} ions, and the presence of Zn^{2+} enhanced the photo-induced energy transfer from the PDA ligand to the Ln^{3+}, increasing emission intensity.[119] In 2017, Bu et al. developed a 3D framework {[Zn_2(O-BTC)(4,4′-BPY)$_{0.5}(H_2O)_3$] ·$(H_2O)_{1.5}$·$(DMA)_{0.5}$}n [O-BTC = 2-hydroxy-benzene-1,3,5-tricarboxylic acid, 4,4′-BPY = 4,4′-bipyridine]. This MOF, initially weakly

fluorescent, exhibited increased emission upon Al^{3+} addition, with a detection limit of 0.10 ppm, one of the lowest for Al^{3+} in MOFs. This was attributed to the formation of a cation-π complex between Al^{3+} and the parallel pyridyl groups of the MOF, promoting electron transfer.[120]

Yan et al. created Uio-66(Zr)-$(COOH)_2$ and incorporated Eu^{3+} within the framework's pores through post-synthetic modification. This improved the quantum yield via energy transfer from the MOF ligands to Eu^{3+}. Adding Cd^{2+} enhanced energy transfer from the ligand to the sensitizer, resulting in a fluorescence turn-on effect.[121]

1A.6.3. Magnetism

Magnetic metal-organic frameworks (MMOFs) are metal-organic frameworks (MOFs) that exhibit magnetism due to paramagnetic 3d transition metal nodes and diamagnetic organic linkers.[122] First-row transition metals like V, Cr, Mn, Fe, Co, Ni, and Cu are commonly used, contributing to the creation of porous molecular magnets with variable spin quantum numbers and magnetic anisotropy.[123] Key factors in their magnetic activity include the framework structure, which often features a layered geometry with short distances between metal clusters, and the use of organic linkers with radicals contributed to their magnetic properties.[124] For instance, $Mn_3(THQ)_2$ (THQ = tetrahydroxyquinone) synthesized via electrostatic gating exhibited high Curie temperatures of 250 K (neutral monolayer) and 300 K (hole-doped monolayer).[125] Another example was the Ni-Glutarate-based MOF, which showed ferromagnetic behavior at a Curie temperature of 4 K due to weak ferromagnetic interactions.[126] Lanthanides can also form magnetic MOFs, as seen in $Dy_2(bpa)_2(H_2O)_3$ and $Er_4(bpa)_4(H_2O)_6.(H_2O)$, which displayed ferromagnetic interactions.[127] Copper(II)/zinc(II)-MOF-74, created using 2,5-dioxido-1,4-benzenedicarboxylic acid (H_4dobdc) as a linker, demonstrated antiferromagnetic intrachain and weaker ferromagnetic interchain interactions.[128] Gd-based MOFs like $[Gd_2(ox)_3(H_2O)_6]_n \cdot 4nH_2O$ demonstrated magnetic relaxation and moderate magnetocaloric efficiency, useful in cryogenic magnetic refrigeration.[129] MOFs can integrate magnetic centers either in functional nodes or in the pores, leading to organized magnetic nanostructures with cooperative exchange interactions via organic linkers. Short linkers, metalloligands, radical organic linkers, and conjugated

bridges enhance magnetic interactions. The incorporation of carboxylate linkers between metal centers, such as M–O–C–O–M or M–O–M bridges, is particularly effective.[5]

In 2008, Mahata et al. introduced a novel metal-organic framework (MOF) with the formula $[Mn_3\{C_6H_3(COO)_3\}_2]$, featuring a distinctive three-dimensional structure. This MOF was constructed from distorted Kagome layers, interconnected by trimellitate anions and comprised two geometrically distinct Mn^{2+} ions. The study emphasized the reduced magnetic frustration in this framework and observed spin-canted long-range ordering, which was attributed to antisymmetric Dzyaloshinsky–Moriya (DM) exchange interactions. These findings provide valuable insights into the magnetic behaviors of MOFs with distorted Kagome lattices.[130]

In a subsequent study in 2009, Mahata et al. reported the synthesis and magnetic characterization of a novel metal-organic framework (MOF) featuring $[Co_4]$ clusters. These clusters were linked by μ_3-OH and μ_2-OH_2 units into a two-dimensional network via pyrazine ligands. This 2D structure was further bridged by oxybisbenzoate (OBA) ligands, resulting in a unique three-dimensional body-centered arrangement of $[Co_4]$ clusters, which has not been observed before. Magnetic characterization revealed a noncollinear frustrated spin structure with a net magnetic moment of 1.4 μB per cluster. The material demonstrated quasi-2D XY magnetic behavior above 32 K, with a stretched-exponential temperature dependence of the correlation length, aligning with the Berezinskii-Kosterlitz-Thouless (BKT) model. Below 14 K, it transitioned to a soft ferromagnetic state with slow relaxation and hysteretic behavior, including a coercive field of up to 5 T at 4 K. This slow relaxation was linked to the dynamics of vortex-antivortex pair formation and annihilation, underscoring the distinctive magnetic properties of this MOF.[131]

Rare-earth-based MOFs showed promise as magnetic refrigerant materials for hydrogen liquefaction due to their high molar magnetic entropy. Additionally, 2D CPs with a kagome lattice structure generate tunable magnetic phases. MOFs' magnetic properties can be tuned by exchanging metal ions or coordination polymers, leading to applications in magnetic switchers, sensors, microelectronics, device fabrication, and clinical therapies. Combining MOFs with magnetic nanoparticles (MNPs) creates magnetic framework composites (MFCs)

with applications in catalysis, environmental remediation, sensing, and separation.[132] Despite their advantages, controlling MOF crystal growth on MNPs poses challenges. Future research should focus on developing simpler, greener methods to prepare these composites, enhancing their potential in innovative applications and information technology.

1A.6.4. Organic Catalysis

Coordination polymers (CPs) represent a promising alternative to heterogeneous catalysts, mimicking the catalytic behaviors observed in homogeneous complexes.[133] Through strategic design and selection of organic linkers, it is feasible to engineer CPs with local structures resembling those found in specific metal coordination compounds with desired catalytic activities. This approach offers precise control over the catalytic environment. CPs can serve as either spectator species, facilitating catalytic reactions, or as active sites that stabilize transition states and orient molecules. Some MOFs exhibit catalytic activity due to the presence of unsaturated metal centers or catalytic species within their pores or inherent sites. A comprehensive examination of CPs' potential applications in catalysis can be found in a review by Kitagawa et al. Gascon et al. and Verpoort and colleagues have more recently explored the versatility of MOFs as heterogeneous catalysts for various organic transformations.[134-136] Notable examples of CP-catalyzed reactions include [Cu(2-pymo)$_2$] and [Co(PhIM)$_2$], both used for the aerobic oxidation of tetralin, yielding α-tetralone as the main product.[137] MOFs were also replaced conventional methods for acidic catalysis; for instance, MOF-199 has proven to be an efficient heterogeneous acid catalyst in the aza-Michael reaction.[138] MIL-101, housing Pd nanoparticles, served as a bifunctional Lewis acid/hydrogenation catalyst in synthesizing methyl isobutyl ketone from acetone and H_2.[139] Similarly, MOF-5 has been employed in the Friedel–Crafts benzylation reaction,[140] while MIL-47 and MOF-48 have been utilized in methane conversion to acetic acid.[141] Various MOFs and Porous Coordination Polymers (PCPs) have been investigated as catalysts for organic species oxidation in the presence of oxidants like tert-butyl hydroperoxide, H_2O_2, and O_2.

1A.6.5. Electrochemical Applications

1A.6.5.1 Supercapacitor

Supercapacitors (SCs) represent a distinct category of energy storage devices known for their high power energy retention, extended cycle life, elevated power density, and remarkable packaging adaptability compared to traditional energy storage solutions.[142] Similar to batteries, supercapacitors consist of two electrodes separated by an ion-permeable membrane. The charging process in a supercapacitor involves the movement of electrons.[143] There are two main types of SCs: Electric Double-Layer Capacitors (EDLCs) and pseudocapacitors. EDLCs store charges through electrostatic adsorption between the electrode surface and the electrolyte, while pseudocapacitors utilize reversible Faradaic reactions, such as redox reactions and intercalation processes, to store charges.[144] SCs have garnered widespread attention across various research domains, leading to continuous efforts aimed at enhancing their performance. Strategies include the development of new electrode materials, modification of electrode surfaces, and the creation of hybrid systems.[145] Metal-Organic Frameworks (MOFs) have emerged as promising candidates for SC applications due to their customizable structures, high surface areas, and ability to absorb guest molecules. However, one of the challenges with MOFs is their low conductivity. This limitation can be addressed by incorporating conducting materials like graphene and polymers.[146] Zhang and colleagues introduced a method for synthesizing a double-shelled Zn-Co-S hierarchical structure, which exhibited superior performance as an electrode for SCs. The optimized structure demonstrated a capacitance exceeding 1266 F/g at 1 A/g, along with excellent cycling stability.[147] Enhancements in supercapacitive performance rely on several key factors, including nanoparticle dispersion, porous frameworks for nanoparticle retention, efficient ion movement channels, improved electrical conductivity through nitrogen doping or other additives, and the presence of conductive networks for electron mobility.[148] Furthermore, ultrathin nanosheets of NiCo-MOFs have shown promise as high-performance supercapacitor electrode materials. By optimizing the molar ratio of Ni to Co ions during synthesis, these nanosheets exhibited a specific capacitance of 1202.1 F/g at 1 A/g, outperformed electrodes based solely on Ni-MOF or Co-MOF.[149] In summary, ongoing research efforts focused on material development and structural optimization continue to propel the advancement of supercapacitor technology, offering promising solutions for various energy storage applications.

1A.6.5.2. Water Splitting

Developing clean and sustainable energy is crucial to address the energy crisis and environmental issues.[150] Hydrogen (H_2) is a promising clean fuel due to its high energy density, environmental friendliness, and abundance. However, current industrial hydrogen production methods, such as steam reforming, consume fossil fuels and emit CO_2. Electrochemical water splitting is a more sustainable alternative, powered by renewable energy sources like solar and wind, to produce highly purified hydrogen.[151] Water splitting involves two reactions: hydrogen evolution reaction (HER) and oxygen evolution reaction (OER). While the theoretical voltage for water splitting is 1.23 V, additional voltage (overpotential) is required in practice, increasing energy consumption.[152] Electrocatalysts are essential to reduce this overpotential and improve efficiency. Noble-metal-based electrocatalysts (e.g., Pt for HER, Ir/Ru for OER) are effective but expensive and scarce. Therefore, developing cost-effective, non-noble metal electrocatalysts is vital.[153] Several electrocatalysts have been developed, including metals, alloys,[154] metal oxides,[155] sulfides,[156] carbides,[157] phosphates,[158] hydroxides,[159] and carbon-based materials. Improving electrocatalytic performance involves increasing active site numbers and intrinsic activity, often through nanostructuring and adjusting the electron structure of catalysts.[160]

Metal-organic frameworks (MOFs) are emerging as promising materials for electrocatalysts due to their tunable porosities, open channels, and high specific surface areas.[161] MOFs can be pyrolyzed to produce various nanostructured materials (metals, oxides, sulfides, etc.), which can enhance electrocatalytic performance.[162] The design of MOF precursors and optimization of synthesis processes are crucial for improving these catalysts. Recent advancements in metal-organic frameworks (MOFs) have shown significant potential in improving electrocatalytic performance for hydrogen evolution reaction (HER) and oxygen evolution reaction (OER). By manipulating the crystal structure and morphology of MOFs, researchers have been able to enhance their catalytic efficiency and stability.[163]

Studies on MOFs such as NENU-500 and NENU-501 revealed their differing electrocatalytic performances. NENU-500, with a Tafel slope of 96 mV dec^{-1}, outperformed NENU-501, which has a Tafel slope of 137 mV dec^{-1} and an HER overpotential of 392 mV at 10 mA cm^{-2}. The reduced activity of NENU-501 is attributed to its nearly pore-free structure, which

complicates the removal of cationic ligands. Despite these differences, both MOFs maintained their activity over 2000 cycles, demonstrated good durability.[164] Adjusting the crystal structure can optimize the electronic properties of MOFs. For instance, a lattice-strained NiFe MOF, created through ultraviolet-light irradiation, exhibits enhanced OER activity. This modification increases the crystal plane spacing, enhanced the Ni-O bond covalency and promoted better adsorption of oxygen species. Consequently, the lattice-strained NiFe MOF achieved a lower overpotential of 210 mV at 200 mA cm^{-2} and a Tafel slope of 68 mV dec^{-1}, outperformed the pristine NiFe MOF and commercial RuO_2.[165] The morphology of MOFs significantly impacts their catalytic performance. Two-dimensional (2D) MOF nanosheets, with high surface areas and numerous exposed active sites, generally exhibited superior catalytic properties compared to bulk structures. Techniques such as electrochemical exfoliation and solvothermal synthesis were used to produce these nanosheets. For example, 2D-Co-NS, derived from a three-dimensional pillared-layer MOF via electrochemical exfoliation, reduces the OER overpotential from 429 mV to 310 mV. Similarly, ultrathin NiFe-MOF nanosheets synthesized through solvothermal methods showed excellent OER performance with an overpotential of 221 mV at 10 mA cm^{-2} and a Tafel slope of 56 mV dec^{-1}.[166]

Optimizing the structure and morphology of MOFs significantly enhances their catalytic performance for HER and OER. Adjusting crystal structures to improve electronic properties and creating 2D morphologies to expose more active sites are effective strategies. Continued research in these areas is crucial for developing advanced MOF-based electrocatalysts for energy applications.

REFERENCES

1. W. L. Leong and J. J. Vittal, *Chemical Reviews*, 2011, **111**, 688-764.
2. O. M. Yaghi, H. Li, C. Davis, D. Richardson and T. L. Groy, *Accounts of Chemical Research*, 1998, **31**, 474-484.
3. C. Jiang, X. Wang, Y. Ouyang, K. Lu, W. Jiang, H. Xu, X. Wei, Z. Wang, F. Dai and D. Sun, *Nanoscale Advances*, 2022, **4**, 2077-2089.
4. Y.-J. Song, S.-Y. Ren, S. Zuo, Z.-Q. Shi, Z. Li and G. Li, *Inorganic Chemistry*, 2024, **63**, 8194-8205.
5. A. E. Thorarinsdottir and T. D. Harris, *Chemical Reviews*, 2020, **120**, 8716-8789.

6. Y. Shen, A. Tissot and C. Serre, *Chemical Science*, 2022, **13**, 13978-14007.
7. S. Thapa, L. Meng, E. Hettiarachchi, Y. K. Bader, D. A. Dickie, G. Rubasinghege, S. A. Ivanov, E. C. Vreeland and Y. Qin, *Chemistry – A European Journal*, 2020, **26**, 13788-13791.
8. J. L. Obeso, J. G. Flores, C. V. Flores, M. T. Huxley, J. A. de los Reyes, R. A. Peralta, I. A. Ibarra and C. Leyva, *Chemical Communications*, 2023, **59**, 10226-10242.
9. I. Abánades Lázaro and R. S. Forgan, *Coordination Chemistry Reviews*, 2019, **380**, 230-259.
10. M. Kalaj and S. M. Cohen, *ACS Central Science*, 2020, **6**, 1046-1057.
11. S. Horike, S. Shimomura and S. Kitagawa, *Nature Chemistry*, 2009, **1**, 695-704.
12. E. Díaz, E. Muñoz, A. Vega and S. Ordóñez, *Chemosphere*, 2008, **70**, 1375-1382.
13. E. A. Tomic, *Journal of Applied Polymer Science*, 1965, **9**, 3745-3752.
14. B. F. Hoskins and R. Robson, *Journal of the American Chemical Society*, 1990, **112**, 1546-1554.
15. E. Loukopoulos and G. E. Kostakis, *Journal of Coordination Chemistry*, 2018, **71**, 371-410.
16. K. Biradha, A. Ramanan and J. J. Vittal, *Crystal Growth & Design*, 2009, **9**, 2969-2970.
17. J. C. J. P. I. R. Bailar Jr, 1964, **1**.
18. H. J. Buser, D. Schwarzenbach, W. Petter and A. Ludi, *Inorganic Chemistry*, 1977, **16**, 2704-2710.
19. J. L. C. Rowsell and O. M. Yaghi, *Microporous and Mesoporous Materials*, 2004, **73**, 3-14.
20. O. M. Yaghi and H. Li, *Journal of the American Chemical Society*, 1995, **117**, 10401-10402.
21. L. J. Barbour, *Chemical Communications*, 2006, DOI: 10.1039/B515612M, 1163-1168.
22. S. Kitagawa and R. Matsuda, *Coordination Chemistry Reviews*, 2007, **251**, 2490-2509.
23. Z. Wang, R.-G. Xiong, B. M. Foxman, S. R. Wilson and W. Lin, *Inorganic Chemistry*, 1999, **38**, 1523-1528.
24. E. A. Nytko, J. S. Helton, P. Müller and D. G. Nocera, *Journal of the American Chemical Society*, 2008, **130**, 2922-2923.
25. S. J. Loeb, *Chemical Communications*, 2005, DOI: 10.1039/B416609D, 1511-1518.
26. M. Fujita, J. Yazaki and K. Ogura, *Journal of the American Chemical Society*, 1990, **112**, 5645-5647.
27. O. Ermer, *Journal of the American Chemical Society*, 1988, **110**, 3747-3754.
28. O. M. Yaghi, M. O'Keeffe, N. W. Ockwig, H. K. Chae, M. Eddaoudi and J. Kim, *Nature*, 2003, **423**, 705-714.
29. X.-L. Zhao and W.-Y. Sun, *CrystEngComm*, 2014, **16**, 3247-3258.
30. V. Guillerm and D. Maspoch, *Journal of the American Chemical Society*, 2019, **141**, 16517-16538.
31. P. Thanasekaran, C.-H. Su, Y.-H. Liu and K.-L. Lu, *Coordination Chemistry Reviews*, 2021, **442**, 213987.

32. R. Seetharaj, P. V. Vandana, P. Arya and S. Mathew, *Arabian Journal of Chemistry*, 2019, **12**, 295-315.
33. V. F. Yusuf, N. I. Malek and S. K. Kailasa, *ACS Omega*, 2022, **7**, 44507-44531.
34. H. He, L. Hashemi, M.-L. Hu and A. Morsali, *Coordination Chemistry Reviews*, 2018, **376**, 319-347.
35. S. M. Humphrey, R. A. Mole, R. I. Thompson and P. T. Wood, *Inorganic Chemistry*, 2010, **49**, 3441-3448.
36. Y.-P. He, Y.-X. Tan and J. Zhang, *Coordination Chemistry Reviews*, 2020, **420**, 213354.
37. B. Manna, A. V. Desai and S. K. Ghosh, *Dalton Transactions*, 2016, **45**, 4060-4072.
38. M. Dincă, A. Dailly, Y. Liu, C. M. Brown, D. A. Neumann and J. R. Long, *Journal of the American Chemical Society*, 2006, **128**, 16876-16883.
39. I. Ahmed, M. M. H. Mondol, M. J. Jung, G. H. Lee and S. H. Jhung, *Coordination Chemistry Reviews*, 2023, **475**, 214912.
40. K. J. Gagnon, H. P. Perry and A. Clearfield, *Chemical Reviews*, 2012, **112**, 1034-1054.
41. R. Ma, X. Guo, Y. Sun, F. Wang, S. Sun, T. Zhou, S. Liu, H. Guo and E. V. Alexandrov, *Inorganica Chimica Acta*, 2019, **496**, 119032.
42. K.-L. Zhang, W. Liang, Y. Chang, L.-M. Yuan and S. W. Ng, *Polyhedron*, 2009, **28**, 647-652.
43. W. Zhao, J. Fan, T.-a. Okamura, W.-Y. Sun and N. Ueyama, *Journal of Solid State Chemistry*, 2004, **177**, 2358-2365.
44. F. J. Teixeira, L. S. Flores, L. B. L. Escobar, T. C. dos Santos, M. I. Yoshida, M. S. Reis, S. Hill, C. M. Ronconi and C. C. Corrêa, *Inorganica Chimica Acta*, 2020, **511**, 119791.
45. J.-S. Hu, Y.-J. Shang, X.-Q. Yao, L. Qin, Y.-Z. Li, Z.-J. Guo, H.-G. Zheng and Z.-L. Xue, *Crystal Growth & Design*, 2010, **10**, 4135-4142.
46. D. Fonseca, A. F. Pérez-Torres, J. Cobo, J. Zapata-Rivera, J. J. Hurtado and M. A. Macías, *CrystEngComm*, 2022, **24**, 2982-2991.
47. M. A. Withersby, A. J. Blake, N. R. Champness, P. A. Cooke, P. Hubberstey, W.-S. Li and M. Schröder, *Inorganic Chemistry*, 1999, **38**, 2259-2266.
48. L. Li, S. Wang, T. Chen, Z. Sun, J. Luo and M. Hong, *Crystal Growth & Design*, 2012, **12**, 4109-4115.
49. N. Phukan, S. Goswami, S. Lipstman, I. Goldberg and B. K. Tripuramallu, *Crystal Growth & Design*, 2020, **20**, 2973-2984.
50. J. Yang, G.-D. Li, J.-J. Cao, Q. Yue, G.-H. Li and J.-S. Chen, *Chemistry – A European Journal*, 2007, **13**, 3248-3261.
51. Z. Guo, R. Cao, X. Li, D. Yuan, W. Bi, X. Zhu and Y. Li, *European Journal of Inorganic Chemistry*, 2007, **2007**, 742-748.
52. Y. Xu, F. Ding, D. Liu, P.-P. Yang and L.-L. Zhu, *Journal of Molecular Structure*, 2018, **1155**, 72-77.
53. Y.-C. He, X. Zhang, Y.-Y. Liu, H.-Y. Liu and J.-F. Ma, *European Journal of Inorganic Chemistry*, 2014, **2014**, 6205-6211.
54. J.-X. Yang, X. Zhang, J.-K. Cheng, J. Zhang and Y.-G. Yao, *Crystal Growth & Design*, 2012, **12**, 333-345.

55. A. Beheshti, V. Nobakht, L. Carlucci, D. M. Proserpio and C. Abrahams, *Journal of Molecular Structure*, 2013, **1037**, 236-241.
56. A. K. Gupta, D. M. Salazar and A. Orthaber, *European Journal of Inorganic Chemistry*, 2019, **2019**, 3740-3744.
57. S. Tripathi, R. Srirambalaji, S. Patra and G. Anantharaman, *CrystEngComm*, 2015, **17**, 8876-8887.
58. Y. Xu, Y.-S. Yu, X.-D. Huang, S.-S. Bao, H.-m. Ding, Y.-q. Ma and L.-M. Zheng, *Inorganic Chemistry*, 2018, **57**, 12143-12154.
59. J. Zhang, L. Wojtas, R. W. Larsen, M. Eddaoudi and M. J. Zaworotko, *Journal of the American Chemical Society*, 2009, **131**, 17040-17041.
60. Y. B. Go, X. Wang, E. V. Anokhina and A. J. Jacobson, *Inorganic Chemistry*, 2005, **44**, 8265-8271.
61. L. Bello, M. Quintero, A. J. Mora, T. González, A. Escalona, R. Añez, E. E. Ávila and A. Briceño, *CrystEngComm*, 2015, **17**, 5921-5931.
62. M.-L. Tong, S. Hu, J. Wang, S. Kitagawa and S. W. Ng, *Crystal Growth & Design*, 2005, **5**, 837-839.
63. Y.-B. Dong, Y.-Y. Jiang, J. Li, J.-P. Ma, F.-L. Liu, B. Tang, R.-Q. Huang and S. R. Batten, *Journal of the American Chemical Society*, 2007, **129**, 4520-4521.
64. P. Mahata, M. Prabu and S. Natarajan, *Crystal Growth & Design*, 2009, **9**, 3683-3691.
65. P. Mahata, M. Prabu and S. Natarajan, *Inorganic Chemistry*, 2008, **47**, 8451-8463.
66. P. Mahata, A. Sundaresan and S. Natarajan, *Chemical Communications*, 2007, DOI: 10.1039/B708060C, 4471-4473.
67. H. Deng, C. J. Doonan, H. Furukawa, R. B. Ferreira, J. Towne, C. B. Knobler, B. Wang and O. M. Yaghi, *Science*, 2010, **327**, 846-850.
68. Y. Sun, L. Sun, D. Feng and H.-C. Zhou, *Angewandte Chemie International Edition*, 2016, **55**, 6471-6475.
69. S. Yuan, J.-S. Qin, L. Zou, Y.-P. Chen, X. Wang, Q. Zhang and H.-C. Zhou, *Journal of the American Chemical Society*, 2016, **138**, 6636-6642.
70. L. Liu, K. Konstas, M. R. Hill and S. G. Telfer, *Journal of the American Chemical Society*, 2013, **135**, 17731-17734.
71. L. J. Wang, H. Deng, H. Furukawa, F. Gándara, K. E. Cordova, D. Peri and O. M. Yaghi, *Inorganic Chemistry*, 2014, **53**, 5881-5883.
72. Q. Liu, H. Cong and H. Deng, *Journal of the American Chemical Society*, 2016, **138**, 13822-13825.
73. W. Zhou, D.-D. Huang, Y.-P. Wu, J. Zhao, T. Wu, J. Zhang, D.-S. Li, C. Sun, P. Feng and X. Bu, *Angewandte Chemie International Edition*, 2019, **58**, 4227-4231.
74. H. Gholipour-Ranjbar, M. Soleimani and H. R. Naderi, *New Journal of Chemistry*, 2016, **40**, 9187-9193.
75. E. R. Parnham and R. E. Morris, *Accounts of Chemical Research*, 2007, **40**, 1005-1013.
76. M. T. Wharmby, J. P. S. Mowat, S. P. Thompson and P. A. Wright, *Journal of the American Chemical Society*, 2011, **133**, 1266-1269.
77. H. Furukawa, Y. B. Go, N. Ko, Y. K. Park, F. J. Uribe-Romo, J. Kim, M. O'Keeffe and O. M. Yaghi, *Inorganic Chemistry*, 2011, **50**, 9147-9152.

78. S. S. Y. Chui, S. M. F. Lo, J. P. H. Charmant, A. G. Orpen and I. D. Williams, *Science*, 1999, **283**, 1148-1150.
79. L. J. Murray, M. Dinca, J. Yano, S. Chavan, S. Bordiga, C. M. Brown and J. R. Long, *Journal of the American Chemical Society*, 2010, **132**, 7856-7857.
80. M. Eddaoudi, J. Kim, N. Rosi, D. Vodak, J. Wachter, M. O'Keeffe and O. M. Yaghi, *Science*, 2002, **295**, 469-472.
81. T. C. Wang, W. Bury, D. A. Gómez-Gualdrón, N. A. Vermeulen, J. E. Mondloch, P. Deria, K. Zhang, P. Z. Moghadam, A. A. Sarjeant, R. Q. Snurr, J. F. Stoddart, J. T. Hupp and O. K. Farha, *Journal of the American Chemical Society*, 2015, **137**, 3585-3591.
82. Y. Bai, Y. Dou, L.-H. Xie, W. Rutledge, J.-R. Li and H.-C. Zhou, *Chemical Society Reviews*, 2016, **45**, 2327-2367.
83. Z. Wang and S. M. Cohen, *Chemical Society Reviews*, 2009, **38**, 1315-1329.
84. S. Mandal, S. Natarajan, P. Mani and A. Pankajakshan, *Advanced Functional Materials*, 2021, **31**, 2006291.
85. D. Balestri, I. Bassanetti, S. Canossa, C. Gazzurelli, A. Bacchi, S. Bracco, A. Comotti and P. Pelagatti, *Crystal Growth & Design*, 2018, **18**, 6824-6832.
86. T. Li, M. T. Kozlowski, E. A. Doud, M. N. Blakely and N. L. Rosi, *Journal of the American Chemical Society*, 2013, **135**, 11688-11691.
87. J. Martí-Rujas, S. Bonafede, D. Tushi and M. Cametti, *Chemical Communications*, 2015, **51**, 12357-12360.
88. G. Lee, D. K. Yoo, I. Ahmed, H. J. Lee and S. H. Jhung, *Chemical Engineering Journal*, 2023, **451**, 138538.
89. X. Hu, Z. Zuhra, S. Ali, Y. Zhou, L. Zhang, X. Duan and Z. Zhao, *New Journal of Chemistry*, 2023, **47**, 3306-3311.
90. K. S. Walton and R. Q. Snurr, *Journal of the American Chemical Society*, 2007, **129**, 8552-8556.
91. K. Koh, A. G. Wong-Foy and A. J. Matzger, *Journal of the American Chemical Society*, 2009, **131**, 4184-4185.
92. K. S. Song, D. Kim, K. Polychronopoulou and A. Coskun, *ACS Applied Materials & Interfaces*, 2016, **8**, 26860-26867.
93. O. K. Farha, A. M. Spokoyny, K. L. Mulfort, S. Galli, J. T. Hupp and C. A. Mirkin, *Small*, 2009, **5**, 1727-1731.
94. R. Sabouni, H. Kazemian and S. Rohani, *Environmental Science and Pollution Research*, 2014, **21**, 5427-5449.
95. J.-R. Li, Y. Ma, M. C. McCarthy, J. Sculley, J. Yu, H.-K. Jeong, P. B. Balbuena and H.-C. Zhou, *Coordination Chemistry Reviews*, 2011, **255**, 1791-1823.
96. D. Danaci, M. Bui, N. Mac Dowell and C. Petit, *Molecular Systems Design & Engineering*, 2020, **5**, 212-231.
97. A. I. Osman, W. Abd-Elaziem, M. Nasr, M. Farghali, A. K. Rashwan, A. Hamada, Y. M. Wang, M. A. Darwish, T. A. Sebaey, A. Khatab and A. H. Elsheikh, *Environmental Chemistry Letters*, 2024, **22**, 1703-1740.
98. A. Ahmed, S. Seth, J. Purewal, A. G. Wong-Foy, M. Veenstra, A. J. Matzger and D. J. Siegel, *Nature Communications*, 2019, **10**, 1568.

99. S. K. Singh, A. T. Sose, F. Wang, K. K. Bejagam and S. A. Deshmukh, *Journal of Chemical Theory and Computation*, 2023, **19**, 6686-6703.
100. S. Barman, H. Furukawa, O. Blacque, K. Venkatesan, O. M. Yaghi and H. Berke, *Chemical Communications*, 2010, **46**, 7981-7983.
101. F. Jeremias, A. Khutia, S. K. Henninger and C. Janiak, *Journal of Materials Chemistry*, 2012, **22**, 10148-10151.
102. Y. Tang, D. Dubbeldam and S. Tanase, *ACS Applied Materials & Interfaces*, 2019, **11**, 41383-41393.
103. J.-Q. Liu, Z.-D. Luo, Y. Pan, A. Kumar Singh, M. Trivedi and A. Kumar, *Coordination Chemistry Reviews*, 2020, **406**, 213145.
104. A. Van Wyk, T. Smith, J. Park and P. Deria, *Journal of the American Chemical Society*, 2018, **140**, 2756-2760.
105. Z. Hu, B. J. Deibert and J. Li, *Chemical Society Reviews*, 2014, **43**, 5815-5840.
106. C.-Y. Liu, X.-R. Chen, H.-X. Chen, Z. Niu, H. Hirao, P. Braunstein and J.-P. Lang, *Journal of the American Chemical Society*, 2020, **142**, 6690-6697.
107. J. F. Olorunyomi, M. M. Sadiq, M. Batten, K. Konstas, D. Chen, C. M. Doherty and R. A. Caruso, *Advanced Optical Materials*, 2020, **8**, 2000961.
108. D. K. Singha, S. Bhattacharya, P. Majee, S. K. Mondal, M. Kumar and P. Mahata, *Journal of Materials Chemistry A*, 2014, **2**, 20908-20915.
109. A. Karmakar, P. Samanta, S. Dutta and S. K. Ghosh, *Chemistry – An Asian Journal*, 2019, **14**, 4506-4519.
110. A. Karmakar, N. Kumar, P. Samanta, A. V. Desai and S. K. Ghosh, *Chemistry – A European Journal*, 2016, **22**, 864-868.
111. D. K. Singha, P. Majee, S. Hui, S. K. Mondal and P. Mahata, *Dalton Transactions*, 2020, **49**, 829-840.
112. B. Chen, L. Wang, F. Zapata, G. Qian and E. B. Lobkovsky, *Journal of the American Chemical Society*, 2008, **130**, 6718-6719.
113. Z.-R. Yang, M.-M. Wang, X.-S. Wang and X.-B. Yin, *Analytical Chemistry*, 2017, **89**, 1930-1936.
114. A. Sen, A. V. Desai, P. Samanta, S. Dutta, S. Let and S. K. Ghosh, *Polyhedron*, 2018, **156**, 1-5.
115. M. Wang, L. Guo and D. Cao, *Analytical Chemistry*, 2018, **90**, 3608-3614.
116. Y. Li, K. Jiang, J. Zhang, T. Xia, Y. Cui, Y. Yang and G. Qian, *Polyhedron*, 2018, **148**, 76-80.
117. Y. Cui, B. Chen and G. Qian, *Coordination Chemistry Reviews*, 2014, **273-274**, 76-86.
118. P. Wang, J.-P. Ma, Y.-B. Dong and R.-Q. Huang, *Journal of the American Chemical Society*, 2007, **129**, 10620-10621.
119. B. Zhao, X.-Y. Chen, P. Cheng, D.-Z. Liao, S.-P. Yan and Z.-H. Jiang, *Journal of the American Chemical Society*, 2004, **126**, 15394-15395.
120. M.-H. Yu, T.-L. Hu and X.-H. Bu, *Inorganic Chemistry Frontiers*, 2017, **4**, 256-260.
121. J.-N. Hao and B. Yan, *Chemical Communications*, 2015, **51**, 7737-7740.
122. M. Kurmoo, *Chemical Society Reviews*, 2009, **38**, 1353-1379.
123. E. Coronado and G. Mínguez Espallargas, *Chemical Society Reviews*, 2013, **42**, 1525-1539.

124. C. N. R. Rao, S. Natarajan and R. Vaidhyanathan, *Angewandte Chemie International Edition*, 2004, **43**, 1466-1496.
125. Q. Yu and D. Wang, *Journal of Materials Chemistry A*, 2023, **11**, 5548-5558.
126. Y.-g. Huang, B.-l. Wu, D.-q. Yuan, Y.-q. Xu, F.-l. Jiang and M.-c. Hong, *Inorganic Chemistry*, 2007, **46**, 1171-1176.
127. M. Chen, H. Zhao, Z.-W. Wang, E. C. Sañudo and C.-S. Liu, *Inorganic Chemistry Communications*, 2015, **56**, 48-52.
128. S. Muratović, V. Martinez, B. Karadeniz, D. Pajić, I. Brekalo, M. Arhangelskis, M. Mazaj, G. Mali, M. Etter, T. Friščić, Y. Krupskaya, V. Kataev, D. Žilić and K. Užarević, *Inorganic Chemistry*, 2022, **61**, 18181-18192.
129. M. Orts-Arroyo, R. Rabelo, A. Carrasco-Berlanga, N. Moliner, J. Cano, M. Julve, F. Lloret, G. De Munno, R. Ruiz-García, J. Mayans, J. Martínez-Lillo and I. Castro, *Dalton Transactions*, 2021, **50**, 3801-3805.
130. P. Mahata, D. Sen and S. Natarajan, *Chemical Communications*, 2008, DOI: 10.1039/B715314G, 1278-1280.
131. P. Mahata, S. Natarajan, P. Panissod and M. Drillon, *Journal of the American Chemical Society*, 2009, **131**, 10140-10150.
132. D. Li, A. Yadav, H. Zhou, K. Roy, P. Thanasekaran and C. Lee, *Global Challenges*, 2024, **8**, 2300244.
133. J. Liu, L. Chen, H. Cui, J. Zhang, L. Zhang and C.-Y. Su, *Chemical Society Reviews*, 2014, **43**, 6011-6061.
134. S. Kitagawa, R. Kitaura and S.-i. Noro, *Angewandte Chemie International Edition*, 2004, **43**, 2334-2375.
135. J. Gascon, A. Corma, F. Kapteijn and F. X. Llabrés i Xamena, *ACS Catalysis*, 2014, **4**, 361-378.
136. A. H. Chughtai, N. Ahmad, H. A. Younus, A. Laypkov and F. Verpoort, *Chemical Society Reviews*, 2015, **44**, 6804-6849.
137. F. X. Llabrés i Xamena, O. Casanova, R. Galiasso Tailleur, H. Garcia and A. Corma, *Journal of Catalysis*, 2008, **255**, 220-227.
138. L. T. L. Nguyen, T. T. Nguyen, K. D. Nguyen and N. T. S. Phan, *Applied Catalysis A: General*, 2012, **425-426**, 44-52.
139. Y. Pan, B. Yuan, Y. Li and D. He, *Chemical Communications*, 2010, **46**, 2280-2282.
140. N. T. S. Phan, K. K. A. Le and T. D. Phan, *Applied Catalysis A: General*, 2010, **382**, 246-253.
141. A. Phan, A. U. Czaja, F. Gándara, C. B. Knobler and O. M. Yaghi, *Inorganic Chemistry*, 2011, **50**, 7388-7390.
142. Z.-X. Cai, Z.-L. Wang, J. Kim and Y. Yamauchi, *Advanced Materials*, 2019, **31**, 1804903.
143. P. Dubey, V. Shrivastav, S. Sundriyal and P. H. Maheshwari, *ACS Applied Nano Materials*, 2024, DOI: 10.1021/acsanm.4c01697.
144. S. Zheng, H. Xue and H. Pang, *Coordination Chemistry Reviews*, 2018, **373**, 2-21.
145. H. Kim, M.-Y. Cho, M.-H. Kim, K.-Y. Park, H. Gwon, Y. Lee, K. C. Roh and K. Kang, *Advanced Energy Materials*, 2013, **3**, 1500-1506.

146. F. Boorboor Ajdari, E. Kowsari, M. Niknam Shahrak, A. Ehsani, Z. Kiaei, H. Torkzaban, M. Ershadi, S. Kholghi Eshkalak, V. Haddadi-Asl, A. Chinnappan and S. Ramakrishna, *Coordination Chemistry Reviews*, 2020, **422**, 213441.
147. P. Zhang, B. Y. Guan, L. Yu and X. W. Lou, *Angewandte Chemie International Edition*, 2017, **56**, 7141-7145.
148. M. H. Yap, K. L. Fow and G. Z. Chen, *Green Energy & Environment*, 2017, **2**, 218-245.
149. Y. Wang, Y. Liu, H. Wang, W. Liu, Y. Li, J. Zhang, H. Hou and J. Yang, *ACS Applied Energy Materials*, 2019, **2**, 2063-2071.
150. D. Millstein, R. Wiser, M. Bolinger and G. Barbose, *Nature Energy*, 2017, **2**, 17134.
151. B. Zhu, R. Zou and Q. Xu, *Advanced Energy Materials*, 2018, **8**, 1801193.
152. H.-S. Park, J. Yang, M. K. Cho, Y. Lee, S. Cho, S.-D. Yim, B.-S. Kim, J. H. Jang and H.-K. Song, *Nano Energy*, 2019, **55**, 49-58.
153. Z. Zhang, G. Liu, X. Cui, B. Chen, Y. Zhu, Y. Gong, F. Saleem, S. Xi, Y. Du, A. Borgna, Z. Lai, Q. Zhang, B. Li, Y. Zong, Y. Han, L. Gu and H. Zhang, *Advanced Materials*, 2018, **30**, 1801741.
154. E. Demir, S. Akbayrak, A. M. Önal and S. Özkar, *ACS Applied Materials & Interfaces*, 2018, **10**, 6299-6308.
155. G. Yan, Y. Lian, Y. Gu, C. Yang, H. Sun, Q. Mu, Q. Li, W. Zhu, X. Zheng, M. Chen, J. Zhu, Z. Deng and Y. Peng, *ACS Catalysis*, 2018, **8**, 10137-10147.
156. D.-Y. Wang, M. Gong, H.-L. Chou, C.-J. Pan, H.-A. Chen, Y. Wu, M.-C. Lin, M. Guan, J. Yang, C.-W. Chen, Y.-L. Wang, B.-J. Hwang, C.-C. Chen and H. Dai, *Journal of the American Chemical Society*, 2015, **137**, 1587-1592.
157. N. Han, K. R. Yang, Z. Lu, Y. Li, W. Xu, T. Gao, Z. Cai, Y. Zhang, V. S. Batista, W. Liu and X. Sun, *Nature Communications*, 2018, **9**, 924.
158. L. Xie, R. Zhang, L. Cui, D. Liu, S. Hao, Y. Ma, G. Du, A. M. Asiri and X. Sun, *Angewandte Chemie International Edition*, 2017, **56**, 1064-1068.
159. X. Zhang, Y. Zhao, Y. Zhao, R. Shi, G. I. N. Waterhouse and T. Zhang, *Advanced Energy Materials*, 2019, **9**, 1900881.
160. H. Zhang, J. Su, K. Zhao and L. Chen, *ChemElectroChem*, 2020, **7**, 1805-1824.
161. O. M. Yaghi, G. Li and H. Li, *Nature*, 1995, **378**, 703-706.
162. M. Zhang, Q. Dai, H. Zheng, M. Chen and L. Dai, *Advanced Materials*, 2018, **30**, 1705431.
163. C. Cao, D.-D. Ma, Q. Xu, X.-T. Wu and Q.-L. Zhu, *Advanced Functional Materials*, 2019, **29**, 1807418.
164. J.-S. Qin, D.-Y. Du, W. Guan, X.-J. Bo, Y.-F. Li, L.-P. Guo, Z.-M. Su, Y.-Y. Wang, Y.-Q. Lan and H.-C. Zhou, *Journal of the American Chemical Society*, 2015, **137**, 7169-7177.
165. W. Cheng, X. Zhao, H. Su, F. Tang, W. Che, H. Zhang and Q. Liu, *Nature Energy*, 2019, **4**, 115-122.
166. J. Huang, Y. Li, R.-K. Huang, C.-T. He, L. Gong, Q. Hu, L. Wang, Y.-T. Xu, X.-Y. Tian, S.-Y. Liu, Z.-M. Ye, F. Wang, D.-D. Zhou, W.-X. Zhang and J.-P. Zhang, *Angewandte Chemie International Edition*, 2018, **57**, 4632-4636.

CHAPTER 1: Section B

Section B: Summary of Research Work

Chapter 1. This chapter comprises two distinct sections: Chapter 1A delves into a concise overview of coordination polymers related with synthesis, structure, characterizations and their functional properties, while Chapter 1B offers a comprehensive overview of the research works carried out.

Section A. The opening of this chapter initiates an exploration into the realm of coordination polymers, introducing readers to their fundamental concepts. Subsequently, it delves into an examination of methodologies aimed at attaining functionality within individual coordination polymers. Concluding this section, the chapter further delves into diverse synthesis approaches, potential applications, and the significance of dynamic coordination polymers concerning these characteristics.

Section B. It elegantly encapsulates the themes explored within each chapter of this thesis.

Chapter 2. A new coordination polymer of formula $[Cd(C_8N_2O_3H_7)_2(H_2O)_2]_n$, **1**, have been synthesized via hydrothermal method using a bio-inspired ligand, N-nicotinoyl glycinate. The compound was characterized by SCXRD, PXRD, FTIR spectra, and thermogravimetric analysis (TGA). Single crystal X-ray diffraction reveals the connectivity between Cd^{2+} ions and N-nicotinoyl glycinates layer in nature and the layers are arranged in *ABAB*…. fashion to give three-dimensional packing arrangement stabilized by inter-layer N-H…O and O-H…O hydrogen bond and π…π interactions. An aqueous dispersion of compound **1** exhibits strong emission centered at 420 nm after excitation at 280 nm. This emission has been used for the selective sensing of p-xylene over other related electron-rich C8 aromatic isomers based on luminescence turn-on. The calculated value of limit of detection (LOD) was 84.55 ppb which is far lower than the safe limit of p-xylene (300 ppb in water). This compound also shows pH dependent luminescence property and stability in the widerange of pH (1-14). In both the cases (p-xylene detection and pH dependence), the time-resolved studies were used to determine the excited state lifetime and understand the mechanism of luminescence behaviour in presence of analytes. DFT based computational studies were also carried out to understand the selectivity of detection of p-

xylene over the other isomers.Schottky diodes fabricated using this material (CP) showed ideal diode like behaviour at the low voltage regime.

Chapter 3. Two new isostructural 2D coordination polymers, denoted as **1**(Mn) and **2**(Fe), have been synthesized using the layer diffusion method. These polymers, {[Mn(PDA)(4-bpdb)(H_2O)$_2$].4-bpdb}n and {[Fe(PDA)(4-bpdb)(H_2O)$_2$].4-bpdb}n, incorporated 1,4-phenylenediacetate (PDA) and 1,4-bis(4-pyridyl)-2,3-diaza-1,3-butadiene (4-bpdb) ligands. Structural analysis through the single-crystal X-ray study revealed that compound **1**(Mn) and compound **2**(Fe) exhibited a one-dimensional connectivity along the *a-axis* between metal ions (Mn(II)/Fe(II)) and 1,4-phenylenediacetate ligands and formed a 2D layered structure interconnected with 4-bpdb. These layers arranged in an *AAA*... pattern along the *b-axis*, forming a three-dimensional supramolecular structure. Non-bonded 4-bpdb molecules occupy voids within this arrangement, stabilized by hydrogen bonds and π···π interactions. The redox-active metal centers (Mn^{2+}/Fe^{2+}) present in the coordination polymers hold promise for electrochemical studies. Supercapacitor assessment revealed an intriguing discrepancy: compound **1**(Mn) demonstrated nearly 2.5 times greater specific capacitance than compound **2**(Fe) in a 1 M H_2SO_4 medium, despite their isostructural nature. However, cyclic stability testing showed a reverse trend, with compound **2**(Fe) exhibiting excellent stability, retaining 98% capacity after 5000 cycles compared to **1**(Mn)'s 78%. Conductivity measurements indicated that compound **1**(Mn) possesses conductivity 10 times superior to that of compound **2**(Fe). Notably, both compounds exhibited potential for Schottky diode fabrication. Overall, this study highlights the influence of specific metal ions on the distinctive supercapacitor characteristics and conductivity within isostructural coordination polymers.

Chapter 4. In this study, we present a new cadmium (II) based two-dimensional coordination polymer [Cd(L)(NA)(H_2O)] (L = Iminol form of N-nicotinoyl glycinate, NA = Nicotinate), **1**, containing two linkers generated from N-nicotinoyl glycine. A comprehensive investigation was carried out during the synthesis of the coordination polymers by varying reaction time interval and temperature and it revealed the formation of three distinct phases. Of which two phases were previously reported and one was new compound (**1**). The structure of compound **1** was determined by single crystal X-ray diffraction and it shows corrugated layer structure with hydrogen bond interactions leading to three dimensional supramolecular *ABABAB*…type

packing arrangement. The compound was characterized by powder X-ray diffraction, FT-IR spectroscopy and thermogravimetric analysis (TGA). The stability of compound **1** in water was found to be excellent, and it exhibited strong blue emission at 420 nm when excited at 260 nm in aqueous medium. The emission behaviour of this compound was used for the detections of various sulfonamide antibiotics sulfadiazine (SDZ), sulfamethazine (SMZ), sulfachloropyridazine (SCP), sulfameter (SM), sulfaquinoxaline (SQX), sulfathiazole (STZ)) in the presence of common water pollutants such as transition and heavy metal ions and volatile organic compounds (VOCs). The luminescence quenching response of compound **1** to sulfonamide antibiotics was significant, ranging from 81% to 94%, and the detection sensitivity reached parts per billion (ppb) levels (226-726 ppb). The compound **1** also used for the fabrication of Schottky diode devices with barrier height 0.86 eV along with excellent ideality factor of 1.24.

Chapter 5. This study presents the synthesis of a Cd(II) based hydrophobic three dimensional crystalline network material (CNM), $[Cd_3(L)_2(LH)_2(bpe)_2]$,{L={4,4'-(hexafluroisopropylidine) bis (benzoate)} and 1,2-di(4-pyridyl) ethylene (bpe)}, **1**(Cd), by employing the slow-diffusion method. The three-dimensional structure of **1**(Cd) was determined by single crystal X-ray diffraction and characterized by powder X-ray diffraction (PXRD), FT-IR spectroscopy and thermogravimetric analysis (TGA). Subsequent, post-synthetic modification of **1**(Cd) with Cu(II) at room temperature led to the formation of isostructural **1**(Cu). This transformation, unattainable through de-novo synthesis, was monitored using energy dispersive X-ray analysis (EDX), PXRD, FT-IR spectroscopy, and through visual observation confirming a single crystal to single crystal metal exchange. The modified material, **1**(Cu), exhibited red-shifted emission with enhanced thermal stability and tenfold increase in N_2 uptake. Furthermore, the catalytic potential of **1**(Cd) in aza-Michael addition reactions of α, β-unsaturated olefins to nucleophilic aromatic/aliphatic amines was demonstrated successfully under ambient conditions. This approach employed a heterogeneous and acid-base free methodology showcasing the versatility and effectiveness of **1**(Cd) as a catalyst.

Chapter 6. This study presents the synthesis of a Ni(II) based three dimensional metal-organic framework (MOF), $[Ni_2(NNG)(NA)_3(\mu_2\text{-}H_2O)]$, {NNG= N-nicotinoyl glycinate and NA= nicotinate} named as Ni-MOF and its bimetallic derivative NiCo-MOF by employing the

hydrothermal method. The three-dimensional structure of Ni-MOF was determined by single crystal X-ray diffraction and characterized by powder X-ray diffraction (PXRD), FT-IR spectroscopy, thermogravimetric analysis (TGA) and energy dispersive X-ray analysis (EDX) and Brunauer-Emmet-Teller (BET) studies. The electrochemical results demonstrates that the bimetallic NiCo-MOF only need 120mV overpotential to drive a current density of 10mAcm^{-2} in acidic medium with a very low Tafel slope value of 39mV/dec for HER electrocatalysis, outperforming single-metal counterparts and surpassing most of the previous Tafel slopes and overpotential values reported by pristine MOFs. Notably, the molecular structure of both MOFs remained intact after 18 hours of electrocatalysis. Our findings underscore the potential of bimetallic MOFs as highly efficient electrocatalysts, crucial role of synergistic interactions between active metal centers in bimetallic systems and paving the way for systematic design approaches in sustainable energy research.

CHAPTER-2

A Cd-based Coordination Polymer using Bio-Inspired Ligand: Studies towards Turn-On Luminescence based Sensing and Schottky Diode Behaviour through Device Fabrication

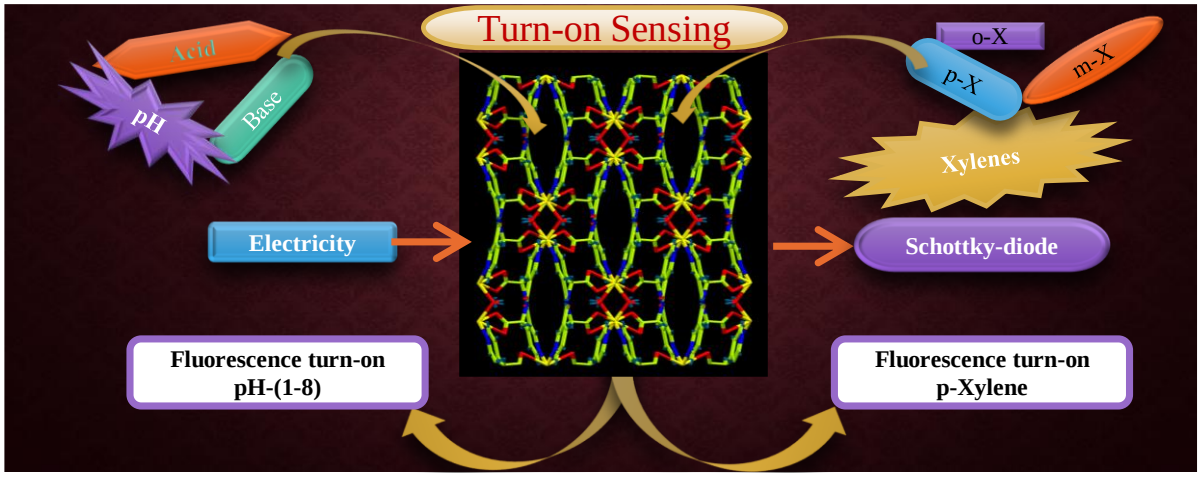

CHAPTER-2

A Cd-based Coordination Polymer using Bio-Inspired Ligand: Studies towards Turn-On Luminescence based Sensing and Schottky Diode Behaviour through Device Fabrication

2.1. INTRODUCTION

Coordination polymers (CPs) are in acontinual stage of research, focusing on an extensive array of potential applications, including heterogeneous catalysis, gas storage, separation, sensing, drug delivery, and proton conductivity due to their structural flexibility, variable pore functionality, and high surface area.[1-14] Throughout these years, luminescent CPs as probes have gained attention in the research community for the detection of circumstantially relevant species.[15-17] Generally, the coordination polymers made of Zn^{2+} and Cd^{2+} ions (d^{10} electronic configuration) and aromatic organic ligands show highly intense visible light emissions. During the crude oil refinement, xylene isomers are extracted and used as chemical intermediates for several valuable products. Among the three isomers (o-,m-,and p-xylene) of xylenes, p-xylene is the most precious intermediate which is the crucial raw material for polybutylene terephthalate (PBT) and polyethylene terephthalate (PET) synthesis. On the other hand, o-xylene as well as m-xylene are mainly used for the production of phthalic anhydride, and isophthalic acid and mixed xylenes are used as a solvent.[18]However, the three xylene isomers (o-, m-, and p-xylene) have similar physical and structural properties as given in table 1.

Table 1. Physical properties of the xylene isomers.

Xylene isomers	Boiling points (K)	Freezing points (K)	Kinetic diameter(Å)
o-xylene	417.6	248	6.8
m-xylene	412.3	222	6.8
p-xylene	411.5	286.4	5.85

So, the detection of xylene isomers from each other is a difficult task.[19-21] Extensive use of solvents in chemical industries, and the wastewater from these factories are the main source of water pollution. To ensure water safety, VOC detection has attracted great attention from the research community as well as the public.[22-24]

At present standard methods for xylene detection and quantification depend on a heavy instrument like gas chromatography, coupled with mass spectroscopy (GC-MS) or flame ionization detection (GC-FID).[25-26] These highly sensitive techniques are time-consuming, laborious, expensive, and complicated. This to a great extent restricts their use for rapid on-site detection and quantification application for xylene isomers. Therefore, it is highly desired to develop new portable devices, which can facilitate fast and favourable on-site measurements.[27] Fluorescence-based sensing techniques may be promising alternatives due to their high sensitivity, quick response, dual applicability, and economic instrumentation.[28] Most of these relevant studies are focused on the chemical separation of xylenes[29-37] and some research works have been done on the detection and discrimination of the xylene isomers based on various materials such as an ambipolar transistor,[38] metal oxide-based chemiresistors ($NiO/NiWO_4$ composite,[39] and Co-doped ZnO nanowires,[40] Surface-Enhanced Raman scattering(SERS)[41] and hydrogen-bonded organic framework (HOF)[42] substrates have also been used.[43-44] A few luminescent compounds have also been reported to sense o-xylene,[45] m-xylene,[46-47] but there is no report of luminescent CP-based aqueous phase selective detection of p-xylene from the pool of other C_8 isomers and investigation on this line remains a more or less unexplored area.

It is also well known that pH is a crucial physicochemical parameter in many fields, which includes human health, biomedicine, environmental monitoring, and industrial production.[48-49] In plants and animals, fluctuation of pH can destroy their activities as well as in organisms have the severe effect of pH change which can lead to several neurological diseases like cancer and stroke.[50-51] Therefore, it is essential to monitor the change of pH to understand the morphology and physiology of living beings. For environmental monitoring, evaluating the standards of discharged wastewater w.r.t pH is an important task otherwise it will cause a serious effect on nature.[52] At present pH measurements are based on the voltammetric, potentiometric method which has disadvantages like impedance, and complicated assembly.[53] Hence it is highly desired to develop a new kind of pH sensor for human health and environmental safety.

Recently Cd-based coordination polymers have been explored for the electrical current conduction properties.[54-57] One of the important behaviour of these materials are Schottky barrier diode properties based on device fabrication.[58-60] There are still lots of possibilities to

develop a device based on the electrical nature of the coordination polymers. Generally, coordination polymer of Cd^{2+} and Zn^{2+} ions show semiconductor behaviours suitable for creating low turn-on voltage. The lowering of energy barrier for higher electrical conductivities has also been well established in hydrogen-bonded solids.[61]

Considering the above facts and our expedition to develop a new bio-inspired multifunctional CP with a broad range of applications,[62-64] we have synthesized a Cd^{2+} based CP $[Cd(C_8N_2O_3H_7)_2(H_2O)_2]$, **1**, with two-dimensional structure using the hydrothermal method. The present research approach was developed by employing a bio-inspired ligand, N-nicotinoyl glycinate,[65] where the amide functional group provides flexibility and binding sites to the guest analytes. The strong blue emission of compound **1** was utilized for the selective luminescence turn-on based detection of p-xylene in the aqueous medium, and the theoretical calculations also support the experimental results. The pH-dependent luminescence behaviour of compound **1** was studied and it showed the most sensitive response in the range of pH (1-8) and exceptional stability in full range of pH (1-14) with outstanding reversibility. To our knowledge, this is the first reported CP that can selectively detect p-xylene and have pH-dependent luminescence behaviour simultaneously. Schottky diodes fabricated using this CP materials showed ideal diode-like behaviour at the low voltage regime.

2.2. EXPERIMENTAL SECTION

2.2.1. Materials

The chemicals used for the synthesis of compound **1** are $Cd(CH_3CO_2)_2.2H_2O$ (Sigma-Aldrich, 98%) and N-Nicotinoyl Glycine (TCI, 98%) were used as received. The chemicals used for the sensing experiment is Benzene (Merck, 99%), Toluene (Merck, 99%), Ethyl benzene (Sigma-Aldrich, 99.8%), 1,3,5-Trihydroxybenzene dehydrate (Sigma-Aldrich, 97%), o-Xylene anhydrous (Sigma-Aldrich, 97%), m-Xylene anhydrous (Sigma-Aldrich, 99%), p-Xylene anhydrous (Sigma-Aldrich, 99%), Acetonitrile anhydrous (Sigma-Aldrich, 99.8%). The necessary chemicals for the pH sensing experiment are HCl (Merck, 99%) and NaOH (Merck, 99%). Double distilled water was used for the sensing experiment.

2.2.2. Synthesis.

$[Cd(C_8N_2O_3H_7)_2(H_2O)_2]_n$, **1** was synthesized through the hydrothermal process. $Cd(CH_3CO_2)_2.2H_2O$ (1mM, 0.2719g), N-Nicotinoyl Glycine (N-NG) (0.5 mM, 0.0919g) were dissolved in 5 ml distilled water. Then the mixture was stirred for 30 min at room temperature

using a magnetic stirrer to homogenize the reaction mixture. After 30 min the homogenized solution was potted in a 23 ml PTFE-lined stainless-steel autoclave and heated at 80°C for 24 hours. After 24 hours final product was obtained in the form of colorless block-shaped crystals. Crystals were filtered and washed with deionized water under a vacuum and dried under ambient conditions (yield 76% based on metal). Anal. Calcd. for $C_{16}H_{18}N_4O_8Cd$: C, 37.89; H, 3.6; N, 11.05. Found: C, 37.83; H, 3.57; N, 11.13%.

2.2.3. Single Crystal X-ray Diffraction.

A single crystal with suitable dimension was carefully selected under an optical microscope and mounted on tinny glass fiber carefully. The diffraction data of colorless block shaped crystal of compound **1** were collected using Bruker D8 Quest diffractometer. The instrument was equipped with Mo Kα (λ=0.71073Å) radiation source and operating voltage of X-ray generator was 50kV and 1 mA. Diffraction data were collected with ω scan width of 0.5º. Three different setting of φ (0, 90, 180º) were used to collect the total 408 frames, keeping a fixed distance of sample-to-detector at 6.03 cm and the detector position (2θ) was fixed at -25º. The initial indexing, final data sets, and cell refinements were handled by an APEX3 program, while a SAINTPLUS[66] program was utilized for the frame integration and final cell parameter calculation. The multi-scan absorption data was corrected by a SADABS program.[67] We initially solved the structure by SIR 92,[68] and the full matrix least-square method (SHELXL-2016[69]) was used further, which is present in the WinGx suit of programs (Version 1.63.04a).[70,71] With the help of Fourier maps, we successfully located all the non-hydrogen atoms and refined them anisotropically. Finally, all the hydrogen atoms were fixed at proper positions and incorporated them in the refinement process. The details of the crystal data and final refinement is given in the Table 2. CCDC: 2167734 contain the diffraction and crystallographic data for this paper. The Cambridge Crystallographic Data Center (CCDC) via www.ccdc.cam.ac.uk/data_request/cif can provide these data with free of charge.

Table 2: Summary of crystal data and refinement parameters for $[Cd(C_8N_2O_3H_7)_2(H_2O)_2]_n$, **1**.

Empirical formula	$C_8H_9Cd_{0.5}N_2O_4$
Formula weight	253.37
Crystal system	Monoclinic

Space group	*C*2/*c*
a (Å)	12.0239(9)
b (Å)	14.4579(11)
c (Å)	10.2546(8)
α (deg)	90
β (deg)	95.081(2)
γ (deg)	90
Volume (Å^3)	1775.7(2)
Z	8
T (K)	273(2)
ρcalc (mg m^{-3})	1.896
μ (mm^{-1})	1.287
θ range (deg)	3.075 to 27.212
λ (Mo Kα) (Å)	0.71073
R indices [I>2σ(I)]	R_1 = 0.0173, wR_2 = 0.0668
R indices (all data)	R_1 = 0.0195, wR_2 = 0.0785

$R_1 = \Sigma\ ||F_0|-|F_c|| / \Sigma\ |F_0|$; $wR_2 = \{\Sigma[w(F_0^2 - F_c^2)^2] / \Sigma[w(F_0^2)^2]\}^{1/2}$. $w = 1/[\sigma^2(F_0)^2 + (aP)^2 + bP]$, $P = [max.(F_0^2,0) + 2(F_c)^2]/3$, *where a = 0.0452 and b = 0.4163*

2.2.4. Powder X-ray diffraction.

Powder X-ray diffraction (PXRD) pattern of well ground sample was obtained from a Bruker D8 Advance X-ray diffractometer with Cu Kα radiation (λ= 1.5418 Å) in the 2θ range 5-50° and operated at 40 kV and 40 mA (Figure 1). Obtained XRD pattern of the sample indicates that compound **1** is new and the pattern consists of the new material with the simulated XRD pattern obtained from the structure determined using single-crystal XRD confirming that the compound is entirely pure in phase.

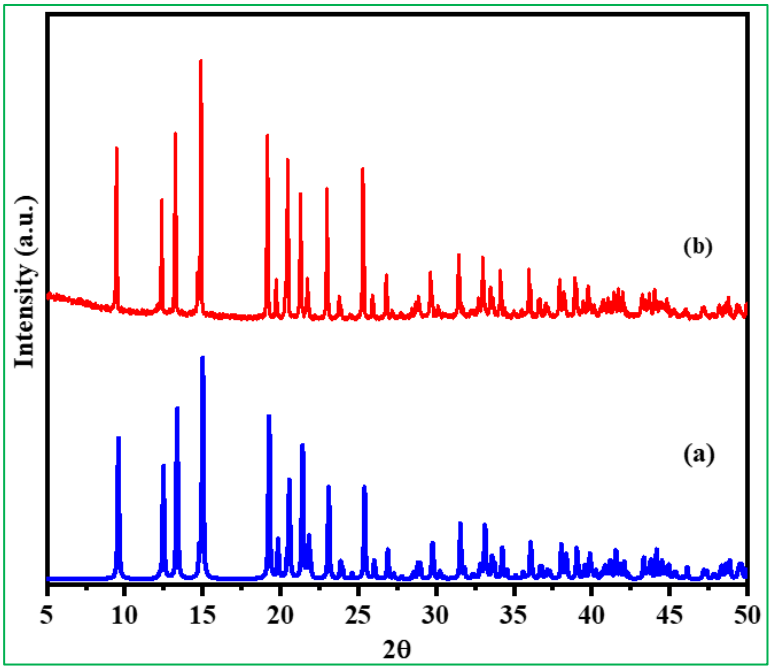

Figure 1. Powder XRD (CuKα) patterns of $[Cd(C_8N_2O_3H_7)_2(H_2O)_2]_n$, **1**: **(a)** simulated from single crystal X-ray data, **(b)** experimental.

2.2.5. FTIR measurements.

Nicolet Magna IR 750 series-II instrument (range: 400-4000 cm^{-1}) were used for recording FT-IR spectra (Figure 2). The observed IR frequencies are listed in Table 3.

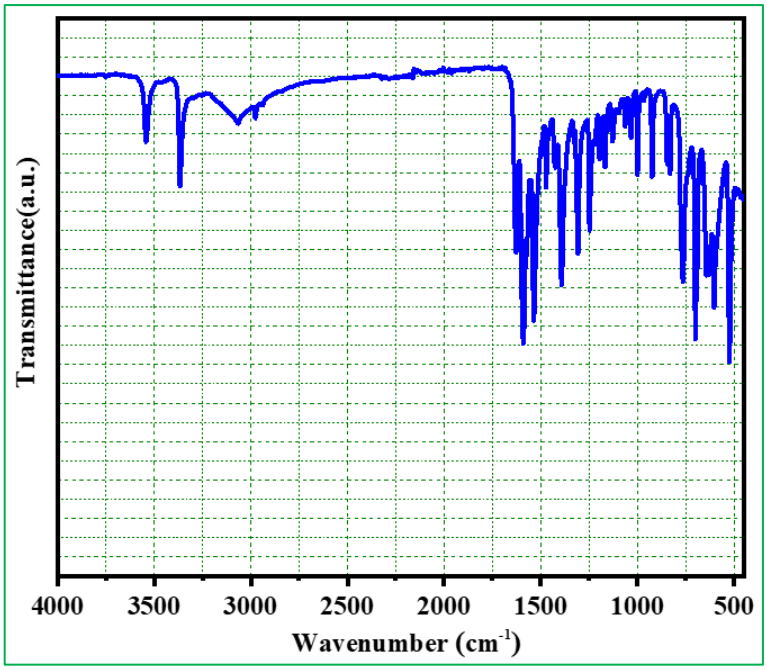

Figure 2. IR spectrum of $[Cd(C_8N_2O_3H_7)_2(H_2O)_2]_n$, **1**.

Table 3. The observed IR bands for $[Cd(C_8N_2O_3H_7)_2(H_2O)_2]_n$, **1.**

Bands	Wavenumber (cm^{-1})	Bands	Wavenumber (cm^{-1})
$\upsilon_{str}(H_2O)$	3536(s)	$\upsilon_{sy.\ str}$(carboxylate)	1313(s)
υ_{str}(amide N-H)	3360(w)	υ_{str}(C-N)	1244(s), 1204(m)
$\upsilon_{asy.str}(sp_2$ C-H)	3067(s), 2969(w)	δ(aromatic C-H)$_{in}$ plane bending	1152(s), 1063(s), 1018(w),989(m)
$\upsilon_{sy.str}(sp_2$ C-H)	2922(w), 2809(w)	δ(aromatic C-H)$_{out\ of}$ plane bending	944(m), 883(m), 800(w)
$\upsilon_{asy.\ str}$(carboxylate)	1634(s)	δ(carboxylate)$_{bending}$	725(w), 691(w)
υ_{str}(amide carboxylate)	1592(s)	δ(aromatic C=C)$_{out\ of}$ plane bending	668(s), 644(m)

2.2.6. Thermal Stability.

Thermogravimetric analysis (TGA) was carried out on a Perkin-Elmer instrument STA 6000 under a nitrogen atmosphere (flow rate = 20 ml min^{-1}) in the temperature range 30 - 800 °C (heating rate 10°C/min)(Figure 3). The first weight loss of 6.95% (calculated 7.1%) up to 182°C may be due to the removal of the coordinated water. The weight loss above 385˚C is due to the decomposition of the framework.

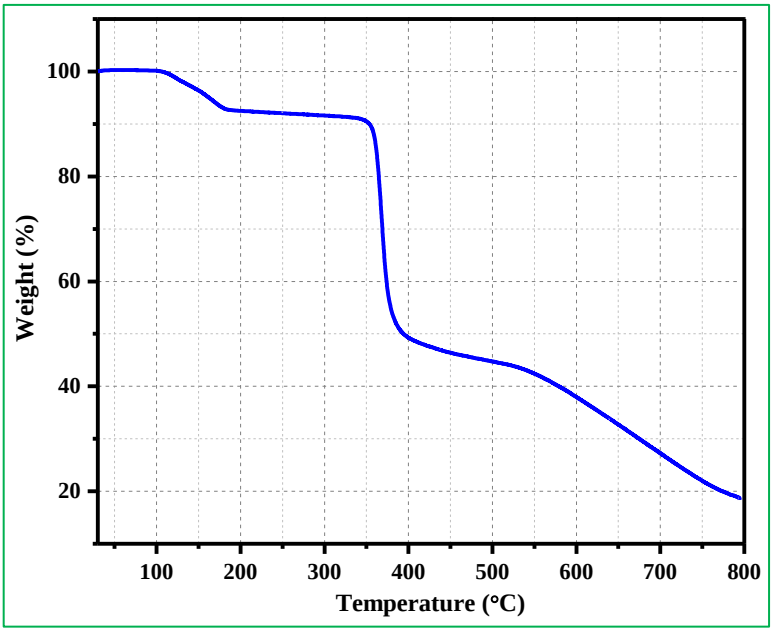

Figure 3. Thermogravimetric analysis (TGA) of $[Cd(C_8N_2O_3H_7)_2(H_2O)_2]_n$, **1**, in nitrogen atmosphere.

2.2.7. BET analysis.

Gas sorption isotherm for N_2 (77K) in the pressure range 0 to 1 bar was measured with an AutosorbiQ (Quantachrome Inc., USA). To investigate the porosity, we have studied the nitrogen gas sorption studies (BET experiment) of compound **1**. To ensure the removal of solvent molecules, powder sample of compound **1** was degassed at 180 °C for 60 min. The experimental results show the type II adsorption isotherm behaviour with a saturated uptake of 109.65 cm^3 g^{-1} and a Langmuir and BET surface area of 659.69 m^2 g^{-1}, 84.02 m^2 g^{-1} respectively (Figure 4).

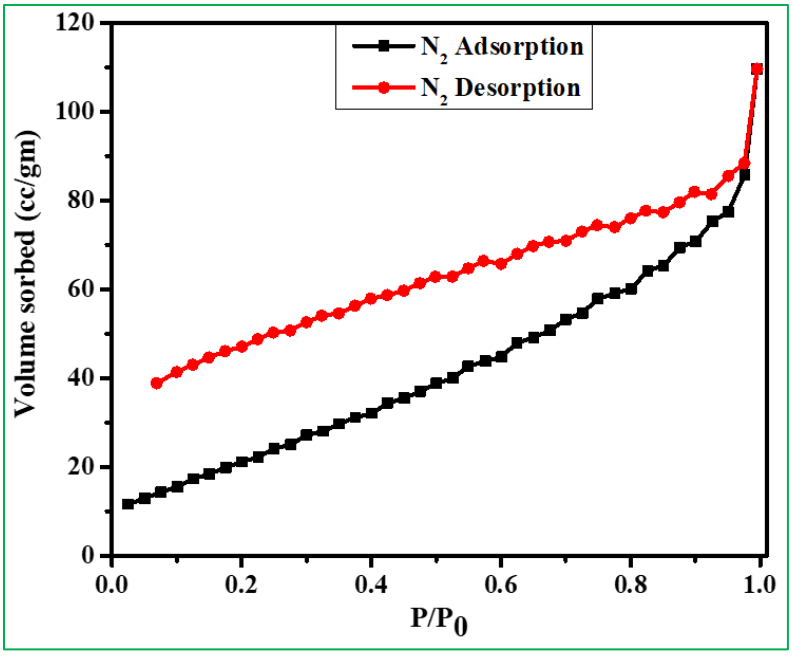

Figure 4. N_2 adsorption (at 77 K) isotherms of compound **1**. Rectangles and circles represent the adsorption and desorption, respectively.

2.2.8. Photoluminescence Measurements.

The aqueous solution of compound **1** was prepared by introducing compound **1**(3 mg) into 3 ml water. The luminescence measurements were performed by adding 100 µl of the stock solution with 2 ml double distilled water in a 2 ml quartz cuvette. Luminescence properties of compound **1** were investigated at room temperature in aqueous medium using a Horiba fluoromax- 4 luminescence spectrofluorometer upon excited at 280 nm. Both the excitation

and emission the slit width was 5 nm. UV-Vis spectra of analytes in aqueous medium were recorded using UV-1700 Pharma Spec UV-Vis spectrophotometer (Shimadzu)(Figure 5).

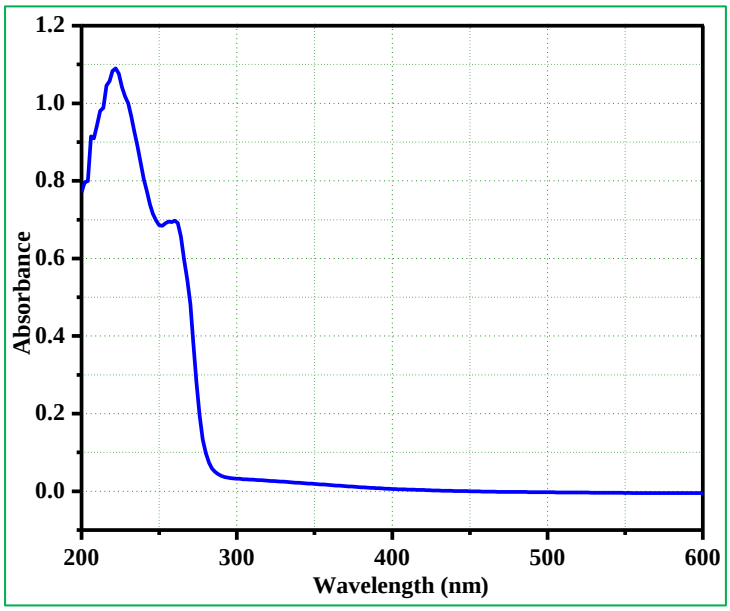

Figure 5. Absorption spectra of $[Cd(C_8N_2O_3H_7)_2(H_2O)_2]_n$, **1.** in aqueous medium.

2.2.9. Lifetime Measurements.

Time correlated single photon counting (TCSPC) measurements were carried out at room temperature in water using a HORIBA Jobin Yvon instrument in the nanosecond time domain. For TCSPC measurement, the excitation wavelength was selected at 280 nm and the emission decay curve was monitored at 420 nm. The luminescence lifetime decays were collected on a Hamamatsu MCP photomultiplier (R3809). All the decays were deconvoluted and fitted with exponential function using origin software.

2.2.10. Field Emission Scanning Electron Microscopy (FE-SEM).

To monitor the morphology changes of compound **1** before and after the p-xylene sensing experiment**,** FE-SEM experiment was carried out using a Zeiss Gemini SEM 450 field emission scanning electron microscope.

2.2.11. Device Fabrication and Measurement.

Indium tin oxide (ITO) coated glass substrates were cleaned following the sequential protocol with soap solution, rinsing with deionized water in a ultrasonicator for 15 to 20 minutes followed by ultrasonication in acetone and isopropanol for 10 minutes. Substrates were dried

under hot air flow from a blower. Finally, substrates were kept inside a UV-ozone chamber (Holmarc, HO-TH-UVT) to remove any organic contaminants from the surface and to make the surface hydrophilic. To form a stable dispersion of compound **1**, 60 mg of the solid was dissolved into 1 mL of DMSO and the mixture was sonicated for considerable time. For device fabrication, water based dispersion of PEDOT:PSS (Clevios P VP Al4083) was spin coated onto ITO as buffer layer at 2000 rpm for 60 sec and was annealed at 100 °C to remove excess moisture. The prepared dispersion of compound **1** was then spin coated onto ITO/PEDOT:PSS substrate at 600 rpm for 60 secs followed by 2000 rpm for 60sec. Substrates were immediately transferred to a hot plate for drying out the film in ambient atmosphere. This spin coating and drying processes was repeated few more times to obtain a pinhole free thick film with uniform thickness (≈ 1 μm). For Schottky contact, low work function metal such as aluminum was deposited as the top contact by slow evaporation of Al (0.2Å/s) through shadow mask under high vacuum (≈10^{-5}mbar) condition. Final device configuration was glass/ITO/PEDOT:PSS/Compound 1/Al. Current voltage was performed in air ambient using a source meter unit (Ossila) under dark condition in the voltage range +10V to -10 V.

2.3. RESULTS AND DISCUSSION

2.3.1. Structural Description.

Compound **1** crystallized in a monoclinic crystal system with C_2/c space group. The asymmetric unit of **1** consists of half crystallographically independent Cd^{2+} ion, one N-nicotinoyl glycinate (N-NG), and one coordinated water molecule (Figure 6a). The Cd^{2+} ion is eight coordinated by the six oxygen atoms and two nitrogen atoms and has a bicapped trigonal prism geometry through the four oxygen atoms from two carboxylate groups of two N-nicotinoyl glycinate ligands, two oxygen atoms from two coordinated water molecules, and two nitrogen atoms from two aromatic pyridyl rings of two N-nicotinoyl glycinate ligands (Figure 6b).

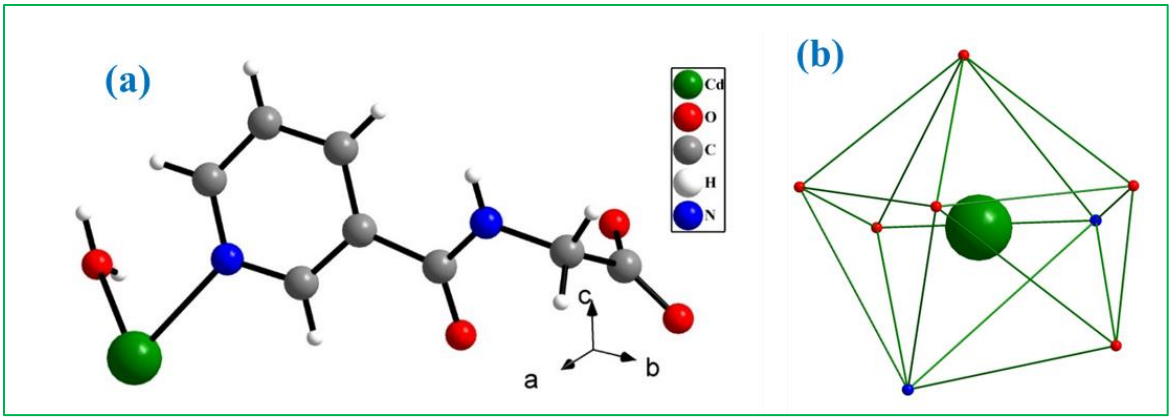

Figure 6. (a) Figure shows the asymmetric unit of **1**. **(b)** Figure shows bicapped trigonal prism geometry around Cd^{2+} ion in $[Cd(C_8N_2O_3H_7)_2(H_2O)_2]_n$, **1**.

The Cd−O bonds have an average distance of 2.47 Å, and Cd-N bonds have an average distance of 2.39 Å. The O/N-Cd-N/O bond angles rangeis in the range 51.62(5) - 151.92(7)°. The selected bond distances are listed in Table 4 and the selected bond angles are listed in Table 5.

Table 4. Selected bond distances (Å) observed in $[Cd(C_8N_2O_3H_7)_2(H_2O)_2]_n$, **1**.

Bond	Distances, Å	Bond	Distances, Å
Cd(1)-O(4)	2.3444(19)	Cd(1)-O(2)#2	2.4670(16)
Cd(1)-O(4)#1	2.3445(19)	Cd(1)-O(2)#3	2.4670(16)
Cd(1)-N(1)	2.3886(18)	Cd(1)-O(1)#3	2.587(2)
Cd(1)-N(1)#1	2.3886(18)	Cd(1)-O(1)#2	2.587(2)

Symmetry transformations used to generate equivalent atoms: #1 –x+1, y , -z+1/2 #2 -x+1/2,y-1/2,-z+1/2 #3 x+1/2, y-1/2 , z

Table 5. Selected bond angles observed in $[Cd(C_8N_2O_3H_7)_2(H_2O)_2]_n$, **1**.

Angle	Amplitude (º)	Angle	Amplitude (º)
O(4)-Cd(1)-O(4)#1	84.87(12)	O(2) #2-Cd(1)-O(2) #3	145.22(8)
O(4)-Cd(1)-N(1)	88.55(7)	O(4)-Cd(1)-O(1) #3	133.88(6)

O(4)#1-Cd(1)-N(1)	151.92(7)	O(4) #1-Cd(1)-O(1) #3	84.88(7)
O(4)-Cd(1)-N(1) #1	151.92(7)	N(1)-Cd(1)-O(1) #3	80.15(6)
O(4)#1-Cd(1)-N(1) #1	109.02(9)	N(1)#1-Cd(1)-O(1) #3	72.30(6)
O(4)-Cd(1)-O(2) #2	71.91(6)	O(2) #2-Cd(1)-O(1) #3	149.93(6)
O(4) #1-Cd(1)-O(2) #2	82.49(7)	O(2) #3-Cd(1)-O(1) #3	51.62(5)
N(1)-Cd(1)-O(2) #2	121.17(6)	O(4)-Cd(1)-O(1) #2	84.88(7)
N(1) #1-Cd(1)-O(2) #2	80.18(6)	O(4) #1-Cd(1)-O(1) #2	133.88(6)
O(4) -Cd(1)-O(2) #3	82.49(7)	N(1)-Cd(1)-O(1)#2	72.30(6)
O(4) #1 -Cd(1)-O(2) #3	71.91(6)	N(1) #1-Cd(1)-O(1)#2	80.16(6)
N(1) -Cd(1)-O(2) #3	80.18(6)	O(2) #2-Cd(1)-O(1) #2	51.62(5)
N(1) #1-Cd(1)-O(2) #3	121.17(6)	O(2) #3-Cd(1)-O(1) #2	149.93(6)
O(1)#3-Cd(1)-O(1) #2	131.71(8)		

Symmetry transformations used to generate equivalent atoms: #1 –x+1, y , -z+1/2 #2 -x+1/2,y-1/2,-z+1/2 #3 x+1/2, y-1/2 , z

The connectivity between Cd^{2+} ions and N-nicotinoyl glycinate (N-NG) ligands form a two-dimensional layer structure (Figure 7a). The layers are arranged along the *c* axis in *ABAB*…. fashion to give a three-dimensional packing arrangement (Figure 7b). The arrangement of layers in *ab* plane shows the formation of channel (pore) along the *c* axis (Figure 7c).

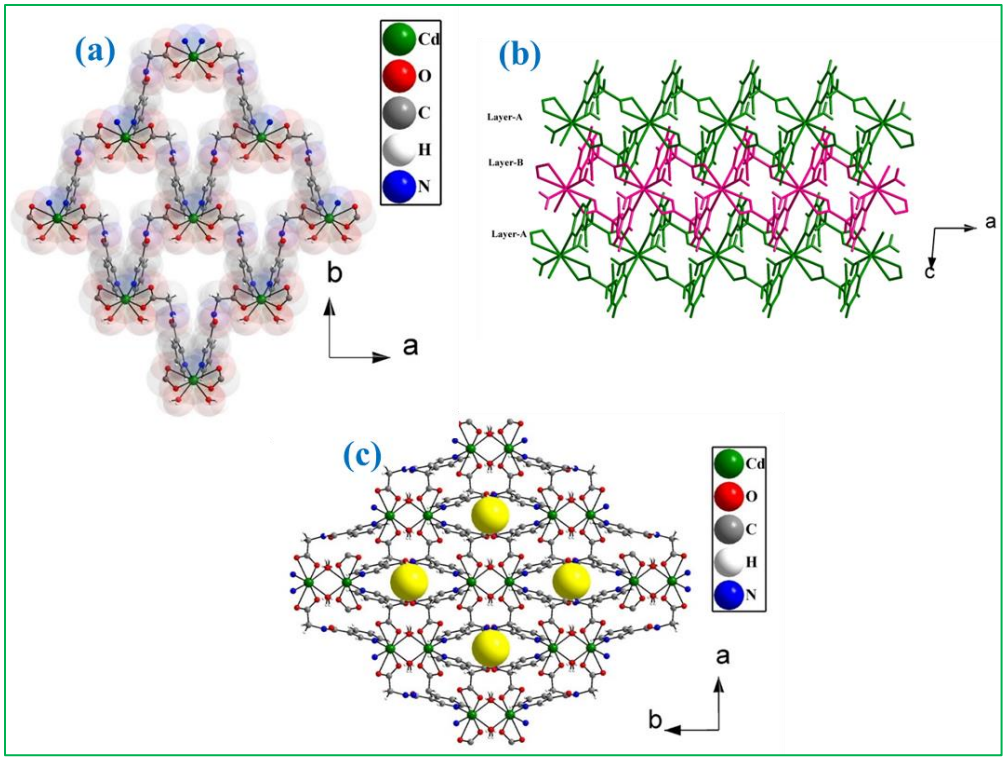

Figure 7. (a) Figure shows the connectivity between Cd^{2+} ions and N-nicotinoyl glycinate (N-NG) ligands to form layer structure in **1**. **(b)** The three-dimensional packing arrangement of layers in *ABAB*… fashion. Three layers are shown (two A layers in green and one B layer in pink). **(c)** The arrangement of layers in *ab* plane showing the formation of channel. The yellow spheres indicate position of the pore (channel).

The three-dimensional arrangement is stabilized through inter-layer π…π interactions (centroid-centroid distance of inter-layer pyridine ring ~ 3.6 Å with nearly parallel arrangement) and inter-layer N-H…O and O-H…O hydrogen bond interactions (Figure 8a & b). The details of hydrogen bond interactions (inter-and intra-layer) are shown in Table 6.

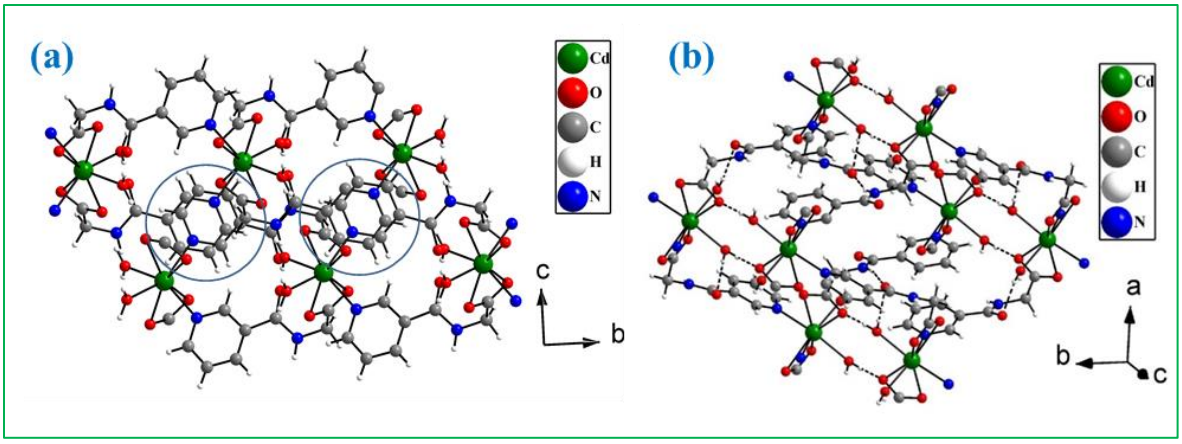

Figure 8. **(a)** Figure shows the position of pyridine rings for the possible π…π interactions between two layers in compound **1**. **(b)** Figure shows the hydrogen bond interactions in compound **1**. Dotted lines represent hydrogen bond interactions.

Table 6. Selected hydrogen-bond interaction in $[Cd(C_8N_2O_3H_7)_2(H_2O)_2]_n$, **1**.

D – H····A[a]	D – H (Å)	H····A (Å)	D····A (Å)	D – H····A (°)
N(2) --H(2A) ··O(3)#1 (Inter)	0.85	2.16	2.9810	161
O(4) --H(4B) ··O(2)#2 (Inter)	0.88	1.79	2.6649	173
O(4) --H(4A) ··O(3)#3 (Intra)	0.82	2.21	3.0253	171

[a] #1 x, -y, -1/2+z; #2 1-x, -y, 1-z; #3 1-x, y, 3/2-z

2.3.2. Luminescence-Based Detection of Xylene Isomers.

An aqueous dispersion of compound **1** exhibits strong emission at 420 nm upon excitation at 280 nm (Figure 9a). The nature of emission from the ligand indicates that the observed emission from **1** is due to the ligand-centered transitions (π* → π and π* → n) of pyridyl carboxylate ligands bonded with the metal ions. Luminescence quantum yields (QYs) of compound **1** were determined by using pyrene (QY = 0.3 in heptane) as the standard sample and it was found, 0.23 in water. To investigate the performance of **1** for detecting the trace amount of electron-rich C_8 alkyl aromatic isomers, luminescence-based titrations were performed with the cumulative addition of xylenes solution (in acetonitrile) to the aqueous dispersion of compound **1**. The change in luminescence intensity with the increasing addition of p-xylene (up to 75 μM) in compound **1** is shown in figure 9b. It indicates that the emission

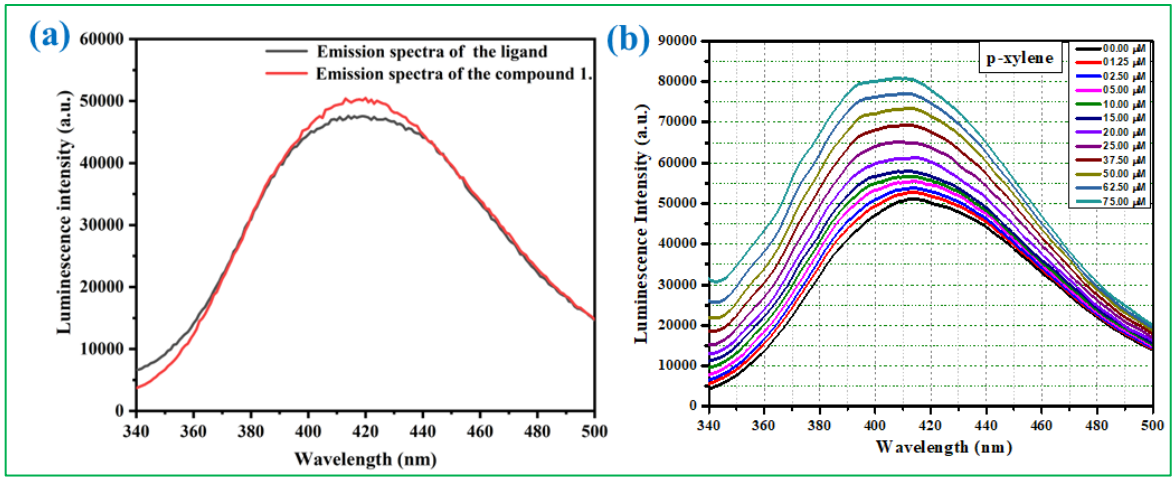

Figure 9. (a) Emission spectra (excited at 280 nm) of aqueous dispersion of $[Cd(C_8N_2O_3H_7)_2(H_2O)_2]_n$, **1** and free N-Nicotinoyl Glycine ligand. **(b)** Emission spectra of **1** dispersed in water upon incremental addition of acetonitrile solution of p-xylene. The final concentration of p-xylene in the medium is indicated in the legend.

It indicates that the emission intensity of compound **1** was significantly increased upon the addition of p-xylene. Almost 57% turn-on in luminescence intensity was observed with the addition of 75 µM p-xylene solution (Figure 10a).

The luminescence enhancement effect of p-xylene inspired us to further investigate the possibility of detecting other similar alkyl aromatic compounds in detail. For this purpose, similar luminescence-based titrations were also performed for other similar aromatic compounds like benzene, toluene, ethylbenzene, o-xylene, and m-xylene. In the case of toluene, a moderate luminescence turn-on was observed and for the rest of the similar alkyl aromatic compounds, negligible luminescence turn-on response of **1** were witnessed (Figure 10a).

We have further investigated the efficiency of **1** towards p-xylene in presence of other xylene isomers. The results represented in figure 10b depicted the negligible effect of o-xylene and m-xylene on the emission intensity of the compound **1**. However, the huge enhancement of luminescence intensity was marked in the simultaneous presence of p-xylene. The combined results conclude that **1** is an outstanding material for selective detection of p-xylene, even when other isomeric xylene isomers coexist in the solution.

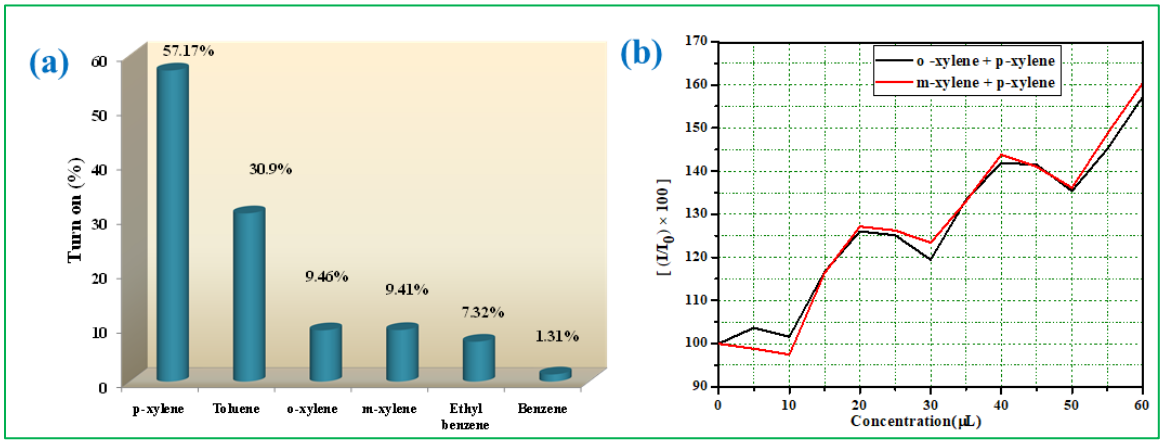

Figure 10. (a) Luminescence turn-on efficiency [$(I/I_0-1)\times100\%$ where I and I_0 denotes the emission intensity after (75 μM) and before the addition of analytes] of aqueous dispersion of **1** for different aromatic analytes. **(b)** Plot showing the selective turn-on response for p-xylene in the presence of other xylene isomers. The added volume of analytes (o-xylene + p-xylene and m-xylene + p-xylene) solution: 10 μL o-xylene/ m-xylene + 10 μL p-xylene and this pattern repeated up to 60μL. The concentration of all the used xylene isomers was 5 mM.

Inspired by the turn-on effect of p-xylene, we have also performed luminescence turn-on titration using an ultralow concentration of p-xylene to get the value of the limit of detection. The limit of detection (LOD) for p-xylene was calculated using the equation, LOD = 3σ/m, where σ = standard deviation of blank determination and m = slope of the linear curve plotted at the lower concentration for LOD measurements.[72] Following this equation the LODs are found to be 84.55 ppb (Figure 11a). Interestingly the limit of detection of p-xylene is far below than the safe limit of p-xylene (300 ppb in water). The enhancement constant was calculated using the equation $(I/I_0) = K_{EC}[M] + 1$, where K_{EC} stands for the enhancement coefficient (M^{-1}) and other terms bear their significances (vide supra).[73] K_{EC} was calculated to be 17.37×10^3, 8.08×10^3, 3.47×10^3, 3.07×10^3, and 2.15×10^3 M^{-1} for p-xylene, toluene, o-xylene, m-xylene, and ethylbenzene, respectively (Figure 11b).

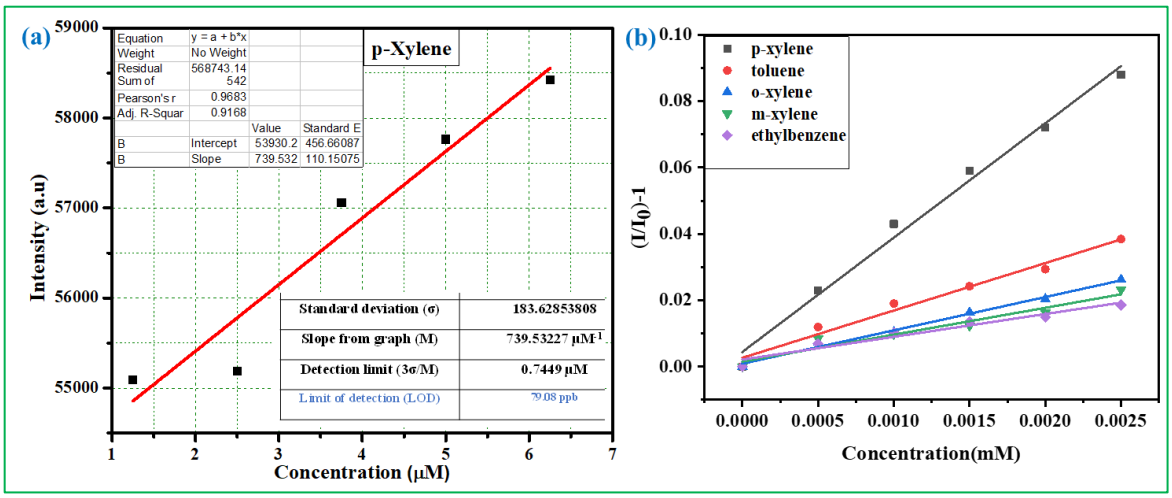

Figure 11. (a) Plot of luminescence intensity vs concentration of p-xylene and the LOD calculation. **(b)** Linear plot for the enhancement constant (EC) of p-xylene, toluene, o-xylene, m-xylene, ethylbenzene in aqueous dispersion of **1**.

To understand the details of the molecular-level interaction between compound **1** and the three xylene isomers, an excited-state lifetime of compound **1** was measured by TCSPC technique. The luminescence lifetime decay of **1** was measured at 420 nm upon the excitation at 280nm. Compound **1** has an average lifetime of 0.72ns and the nature of the decay curve is biexponential. This indicates intra-ligand emissions with multiple centers (like $\pi^* \rightarrow \pi$ and $\pi^* \rightarrow n$). The addition of p-xylene to compound **1**, resulted in a threefold increase in the average lifetime to 2.08ns (figure 12), whereas the addition of the other two isomeric analogues did not have any significant influence on excited-state lifetime (Table 4).

Table 7: Details of time-resolved experiments and calculation of average lifetime of compound **1** before and after the addition of different analytes.

Sl. No	o-Xylene	τ (ns)	m-xylene	τ (ns)	p-xylene	τ (ns)
1	0 µM	0.73	0 µM	0.72	0 µM	0.73
2	25 µM	0.82	25 µM	0.84	25 µM	1.67
3	50 µM	0.89	50 µM	0.83	50 µM	2.03
4	75 µM	0.99	75 µM	0.89	75 µM	2.08

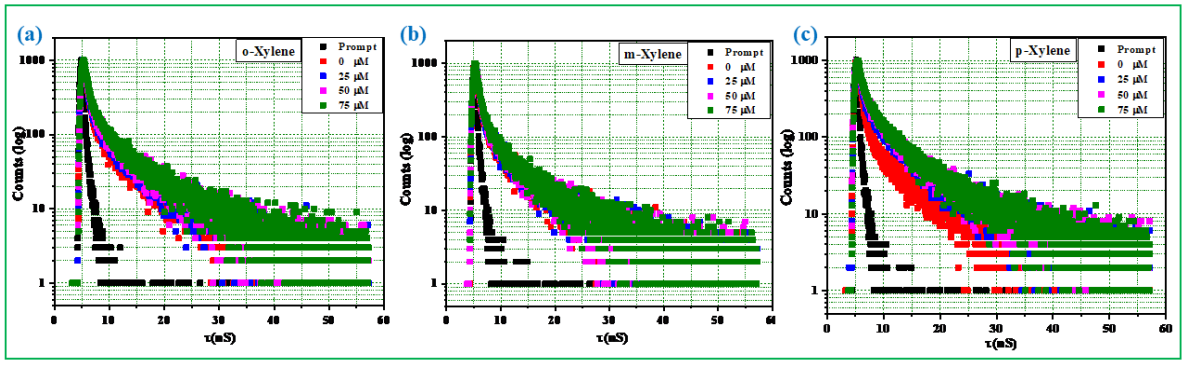

Figure 12. Time resolved luminescence decay of **1** with the gradual addition of **(a)** o-xylene **(b)** m-xylene **(c)** p-xylene solution (λ_{ex} = 280 nm and λ_{em} = 420 nm).

The above-stated experimental results indicate that the fluorescence enhancement of **1**, upon the addition of p-xylene is due to the increased rigidity of structure of compound **1** and freezing of non-radiative channels.

To rationalize the experimental data, the optical gap of the optimized conjugated ligand moiety of compound **1** and the electron-rich alkyl aromatics are calculated by density functional theory with basis set B3LYP/6-31G+(d,p) using Gaussian09.[74]All the calculations are done on the optimized structure in the gas phase. The calculated energies are provided in the table 8.

Table 8: Results of DFT calculation using Gaussian09.

Species	HOMO (ev)	LUMO (ev)	ΔE (ev)
N-nicotinoyl glycine	-7.25	-1.71	5.54
Benzene	-7.01	-0.42	6.59
Toluene	-6.68	-0.37	6.31
Ethylbenzene	-6.69	-0.37	6.32
o-Xylene	-6.50	-0.22	6.28
m-Xylene	-6.49	-0.29	6.20
p-Xylene	-6.39	-0.33	6.06

All the electron-rich aromatic compounds show a turn-on effect, probably, due to the energy transfer from the analytes to compound **1**. As can be seen from table 5, the HOMO-LUMO energy gap of all the aromatic compounds (analytes) is higher than the HOMO-LUMO energy gap of the ligand. Now, this energy transfer effect will be more pronounced when the HOMO-LUMO energy gap of the aromatic compound is closer to the corresponding energy gap of the ligand. From the calculation, it can be seen that among all the aromatic compounds, p-xylene is closer to the ligand. So based on this calculation, experimental observations showing the highest turn-on effect in the case of p-xylene is realized. The HOMO-LUMO energy gaps are in order: p-xylene<m-xylene < o-xylene < toluene < ethylbenzene < benzene. The significant luminescence turn-on effect in the case of toluene indicates that along with the energy gap, the size effects of aromatic compounds are also an important factor to rationalize the observed order. For the turn-on effect, the molecular level of interactions between the analytes and compound **1** is essential and these interactions depend on the penetration power of the analytes with the micro-pore of the compound(see figure 2b). Among these analytes, toluene and p-xylene are sterically less hindered compared to all others (except benezene). So the size factor and energy both are favouring for p-xylene resulting in the highest turn-on effect. On the other

hand, for benzene size factor is favoring but energy factor is disfavouring. In case of toluene, the size factor is favouring and the energy factor are in the intermediate state resulting moderate turn-on effect. In all other cases (o-xylene, m-xylene, ethyl benzene), both factors are not helping much to give a turn-on effect.

2.3.3. pH-Dependent Luminescence Behaviour.

To explore the pH-dependent luminescence behavior of compound **1**, luminescence measurements were performed at different pH by adding HCl/NaOH solution. The change in luminescence intensity of compound **1** with increasing pH (pH: 1-14) was shown in the figure 13a. As shown in the figure, the luminescence intensity of compound **1**, increases up to pH 8 (figure 13b) with seven times luminescence enhancement, and in the pH range, 8-12 luminescence intensity was almost unchanged. Whereas luminescence intensity slightly decreased at pH 13-14.

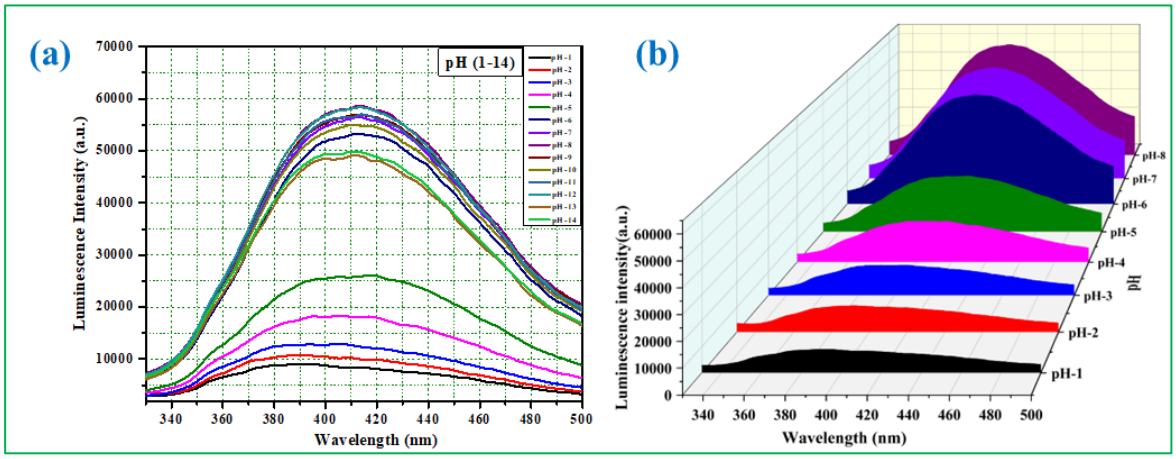

Figure 13. (a) Fig. S23: Figure shows luminescence spectra of aqueous dispersion of compound **1** from pH 1 to pH 14 upon excitation at 280 nm. **(b)** Figure shows luminescence spectra of an aqueous dispersion of compound **1** from pH 1 to pH 8 upon excitation at 280 nm.

The change in intensity of compound **1**, with pH indicates that compound **1** has a very high sensitivity to pH which can be tuned by changing the pH of the medium in the acidic region and having a wide range of pH stability. To check the reversibility in the acidic region as well as basic region, first luminescence spectra of compound **1**, were recorded at pH 6 then, with the incremental addition of acidic solution (HCl solution) pH was lowered to 1 and the corresponding luminescence spectra were also recorded. The luminescence intensity was fully recovered when the pH of the solution return to 6 with the addition of alkaline solution

(NaOH). We have also checked the reversibility of compound **1**, in the basic medium using the same procedure as above, a slight change in luminescence intensity was observed in the basic medium pH 6 to 14 and then returned to pH 6 with the addition of HCl solution luminescence intensity was almost same as the initial luminescence intensity of compound **1** at pH 6. The overall reversible behaviour is shown in figure 14a based on the intensity of emission peak at 420 nm.

To check the stability of **1** in the extreme pH range (1-14), we have immersed the powder sample in three different aqueous solutions with pH 1, 6 and 14 for 12 hrs. After that, the samples were filtered and dried in open air before checking the PXRD patterns. As can be seen from figure 14b, the PXRD patterns of all three compounds matches well with the simulated patterns determined from single-crystal X-ray studies. This study further established the stability of compound **1** in the entire pH range.

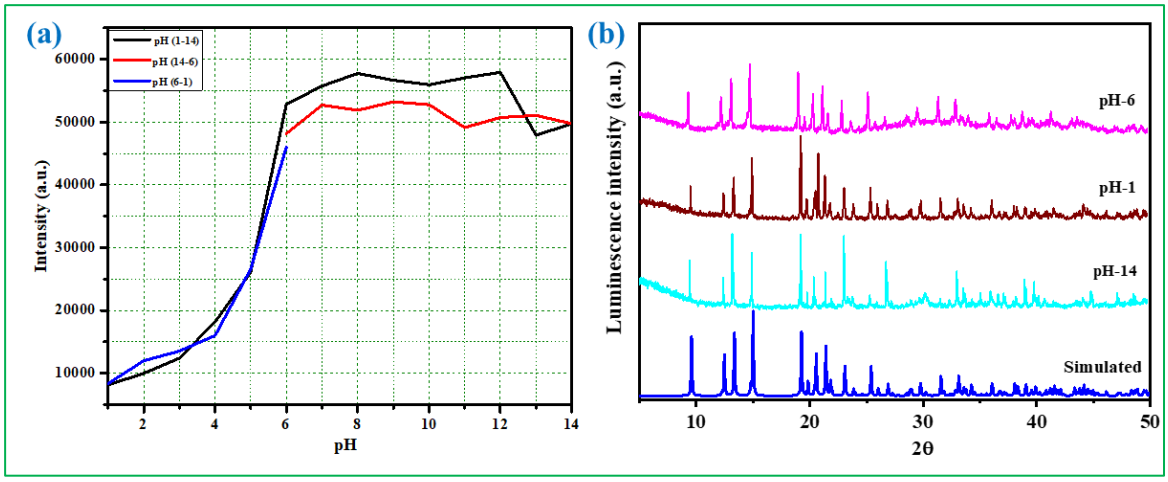

Figure 14. (a) Plot of luminescence intensity (at 420 nm) vs pH showing reversible pH response of compound **1** in the pH range of 1-14. **(b)** Powder XRD (CuKα) patterns of **1** at different pH and blue line represents the simulated pattern of compound **1.**

To get a deep understanding of the pH sensing mechanism, luminescence lifetime decay measurements were carried out at different pH values. The luminescence lifetime decay curves were measured at 420 nm upon excitation at 280nm. The average lifetime of compound **1** was found to be 0.72 ns at pH 6 and when it reaches pH 1 lifetime value increases almost four times (3.13 ns). As the pH value increases from 1 to 8 average lifetime of compound **1** gradually

decreases from 3.13ns to 0.71ns. As we move to higher pH up to pH 12 average lifetime was almost unchanged but when it reaches pH 14 slight increase in an average lifetime was observed. The average lifetime values are summarized in Table 9.

The obtained average lifetime data shows exactly the opposite correlation between luminescence enhancement and average lifetime. The increased value of lifetime with the concentration of H^+ ions indicates reduction of non-radiative pathways whereas the decrease of luminescence intensity indicate loss of excitation light intensity by the addition of HCl.

Table 9. Details of pH dependent time-resolved experiments and calculation of average lifetime of compound **1**.

Sl. No	**pH (6-1)**	a_1	a_2	τ_1	τ_2	$a_1\tau_1 + a_2\tau_2$
1	pH 6	0.0767	0.0036	0.4774	5.88	0.72 ns
2	pH 5	0.0527	0.0089	0.8642	7.83	0.75 ns
3	pH 4	0.475	0.110	0.982	8.03	2.30 ns
4	pH 3	0.0437	0.0119	1.17	8.27	2.59 ns
5.	pH 1	4.35	1.17	1.58	8.89	3.13 ns
Sl. No	**pH (1-14)**	a_1	a_2	τ_1	τ_2	$a_1\tau_1 + a_2\tau_2$
1	pH 1	4.35	1.17	1.58	8.89	3.13 ns
2	pH 2	.572	.0041	1.34	8.37	2.73 ns
3	pH 4	.1306	.0279	1.22	7.81	2.38 ns
4	pH 6	.0785	.0053	.4295	5.56	0.76 ns
5	pH 8	.0826	.0054	.403	5.34	0.71 ns
6	pH 10	.0841	.0067	.411	5.25	0.77 ns
7	pH 12	.0798	.006	.429	5.38	0.780 ns
8	pH 14	.0765	.0061	.6583	5.20	0.993 ns

2.3.4. Schottky Diode Parameters.

Metal-semiconductor junction based Schottky diodes were fabricated using compound **1** in the conventional configuration, ITO/PEDOT:PSS/Compound 1/Al. The *J-V* characteristics of the device obtained under dark condition is shown in Figure 15(a). Device *J-V* response shows

diode like behaviour as the ratio of current in the reverse bias and that in the forward bias (rectification ratio) is ≈ 2. Junction properties at the Al/compound **1** interface was assessed using standard Shockley-diode equation:

$$J = J_0\left[\exp\left(\frac{qV_D}{\eta kT}\right) - 1\right] \qquad (1)$$

where J is the forward current and J_0 is the reverse saturation current. Treating charge carrier injection under thermionic emission theory, J_0 is expressed as, $J_0 = A^*T^2\exp\left(-\frac{e\varphi_B}{kT}\right)$. Here, A^* is the effective Richardson constant whose value was considered as 120 A/cm$^2K^2$ for all the devices.[76] Moreover, φ_B is the Schottky barrier height at Al/material interface and η is the diode ideality factor. Assuming R_s to be the series resistance, and considering large bias voltages ($V_D > 3kT/q$), equation (1) can be written as

$$I = I_0\exp\left(\frac{q}{\eta kT}(V - IR_s)\right) \qquad (2)$$

where $I = J \times A$ and $I_0 = J_0 \times A$ ($A = 0.2$ cm^2 is the area of the device) and IR_s is the voltage drop across the series resistance of the device. Differentiation of equation 2 leads to,

$$\frac{dV}{d(\ln\frac{I}{I_0})} = \frac{\eta kT}{q} + IR_s \qquad (3)$$

Linear part of the $dV/d\left(\ln\frac{I}{I_0}\right)$ versus I plot [Figure 15(b)] will yield R_s as the slope and $\eta kT/q$ as y-axis intercept. To evaluate Schottky-barrier height φ_B at the Al/material interface a function $H(I)$ is defined as $H(I) = V - \frac{\eta kT}{q}\ln\left(\frac{I}{AA^*T^2}\right)$. On substituting the expression for J_0 and $H(I)$, equation 1 takes a simpler form: $H(I) = IR_s + n\varphi_B$. Using the value of idelaity factor (η) already extracted, a plot of $H(I)$ vs I will yield a straight line with y-intercept yielding the value of φ_B [Figure 15(c)]. Further R_s can be extracted and compared with the previously obtained value for consistency.[75] The parameters extracted from these graphs have been summarized in Table 10.

Table 10. Schottky diode Parameters of compound **1**.

Device Structure	Series resistance R_s (Ω)		

	From $dV/d\left(\ln\frac{I}{I_0}\right)$ Vs I	From $H(I)$ Vs I	Ideality factor (n)	Barrier height φ_B (eV)
ITO/PEDOT/Compound **1**/Al	1445.5 ± 38.3	1300.8 ± 9.7	1.9	0.772

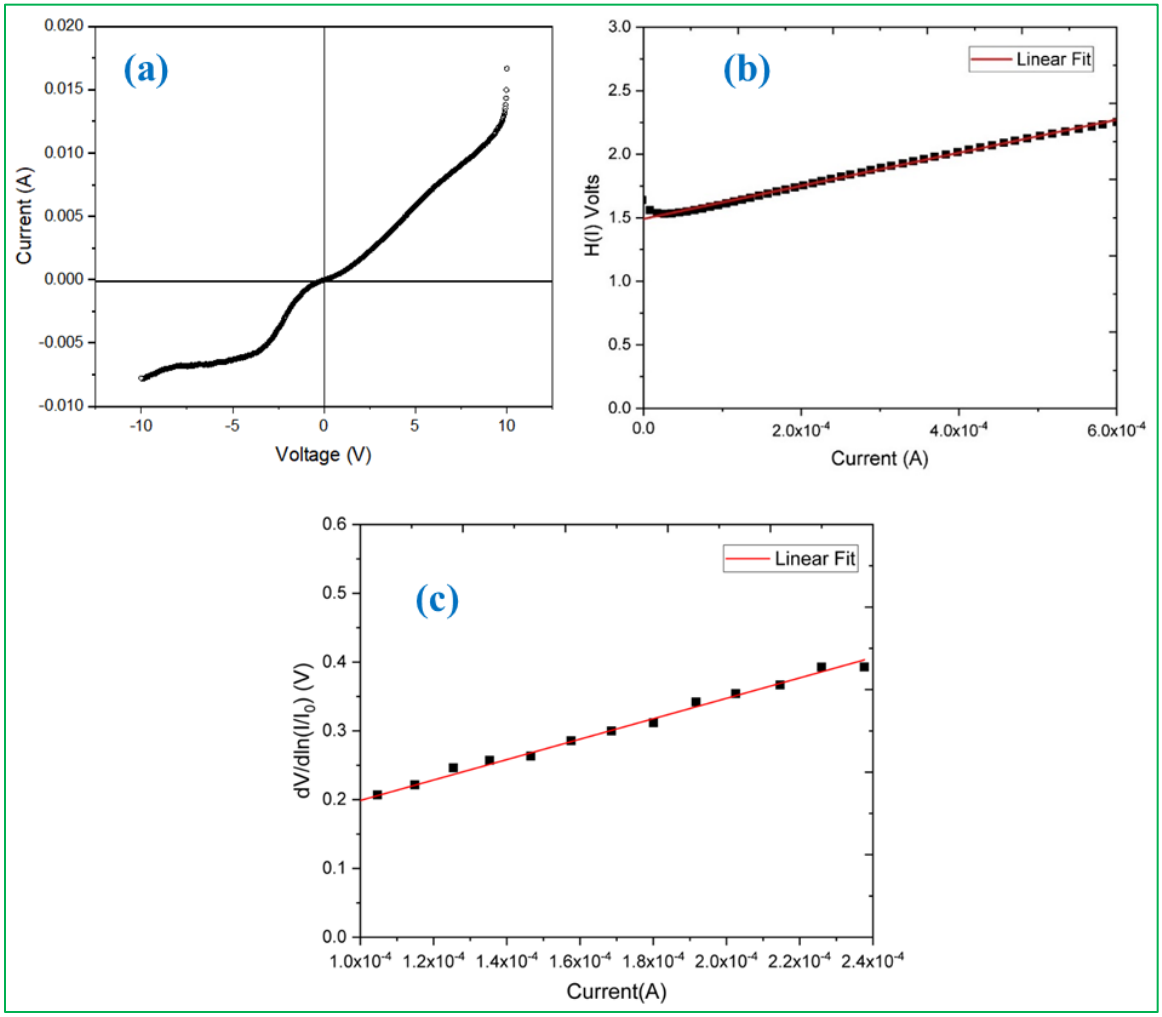

Figure 15. (a) I-V characteristics under dark condition for the device ITO/PEDOT/**1**/Al **(b)** Plot of $dV/d\left(\ln\frac{I}{I_0}\right)$ versus I in dark condition **(c)** H(I) vs. I for the device in dark condition.

Ideality factor of 1.9 was extracted [Figure 15(b)] in the low voltage range 0.2V – 0.5V where the measured current from the device was in the range of 100 –240 μA. It is to be noted that in the higher volatge range (V > 0.5 V), idelity factor incresears and becomes greater than 2. Somewhat lower series resistance (≈ 1020 Ω) and lower barrier potential ($\varphi_B \approx 0.647$ eV) was achieved in the volatge range 0.43 V – 0.85 V. Therefore, presumably, the deviation from the ideal diode characteristics can be attributed to high injection current at higher voltage range due to the lowering of Schottky barrier height induced by interfacial defect states.

2.4. CONCLUSION.

A Cd^{2+} based coordination polymer with layer structures was synthesized using a bio-inspired ligand, N-nicotinoyl glycinate. Single crystal X-ray analysis were used to determine the structure and these studies showed three-dimensional packing arrangement stabilized by inter-layer N-H···O and O-H···O hydrogen bond and π···π interactions. Photoluminescence behaviour of the compound was used for the selective detection of p-xylene over other related electron-rich C_8 aromatic isomers based on luminescence turn-on. The limit of detection (LOD) was found to be 84.55 ppb which is far lower than the safe limit of p-xylene (300 ppb in water). This compound also shows pH dependent luminescence property and stability in the entire pH range (1-14). Time-resolved studies using TCSPC were used to determine the excited state lifetime and to understand the mechanism of luminescence behaviour in presence of analytes. DFT based computational studies also strongly support the experimental luminescence behaviour. These studies indicate that compound **1** could be an effective sensor for *p*-xylene and pH in the range of 1 to 8. Schottky diodes fabricated using compound **1** showed ideal diode like behaviour at the low voltage regime.

REFERENCES

1. H.-C. Zhou, J. R. Long, O. M. Yaghi, *Chem. Rev*. 2012, **112**, 673–674.
2. C. Wang, T. Zhang, W. Lin, *Chem. Rev*. 2012, **112**, 1084–1104.
3. J. A. Mason, M. Veenstra, J. R. Long, *Chem. Sci.*, 2014, **5**, 32–51.
4. J.-R. Li, R. J. Kuppler, H.-C. Zhou, *Chem. Soc. Rev*., 2009, **38**, 1477–1504.
5. J. Lee, O. K. Farha, J. Roberts, K. A. Scheidt, S. T. Nguyen, J. T. Hupp, *Chem. Soc. Rev*., 2009, **38**, 1450–1459.
6. A. Corma, H. García, F. X. L. Xamena, *Chem. Rev*., 2010, **110**, 4606–4655.
7. P. Horcajada, C. Serre, M. V. Regí, M. Sebban, F. Taulelle, G. Férey, *Angew. Chem. Int. Ed*., 2006, **45**, 5974–5978.

8. S. S. Nagarkar, B. Joarder, A. K.Chaudhari, S. Mukherjee,; S. K. Ghosh, *Angew. Chem., Int. Ed*., 2013, **52**, 2881–2885.
9. L. E. Kreno, K. Leong, O. K. Farha, M. Allendorf, R. P. V. Duyne, J. T. Hupp, *Chem. Rev*., 2012, **112**, 1105–1125.
10. Y. Cui, Y. Yue, G. Qian, B. Chen, *Chem. Rev*., 2012, **112**, 1126–1162.
11. K. K. Tanabe, C. A. Allen, S. M. Cohen, *Angew. Chem. Intl. Ed*., 2010, **49**, 9730–9733.
12. S. Kim, K. W. Dawson, B. S. Gelfand, J. M. Taylor, G. K. H. Shimizu, *J. Am. Chem. Soc.*, 2013, **341**, 354–355.
13. T. Yamada, K. Otsubo, R. Makiura, H. Kitagawa, *Chem. Soc. Rev*., 2013, **42**, 6655–6669.
14. M. Nagarathinam, J. J.Vittal, *Angew. Chem. Int. Ed*., 2006, **45**, 4337–4341.
15. E. A. Dolgopolova, A. M. Rice, C. R. Martin, N. B. Shustova, *Chem. Soc. Rev.*, 2018, **47**, 4710-4728.
16. H. Wang, W. P. Lustig, J. Li, *Chem. Soc. Rev.*, 2018,**47**, 4729-4756.
17. A. Karmakar, P. Samanta, S. Dutta, S. K. Ghosh, *Chem. Asian J*., 2019, **14**, 4506 – 451
18. Y. Yang, P. Bai, X. Guo, *Ind. Eng. Chem. Res*., 2017, **56**, 14725−14753.
19. M. A. Moreira, A. F. P. Ferreira, J. C. Santos, J. M. Loureiro, A. E. Rodrigues, *Chem. Eng. Technol*., 2014, **37**, 1483–1492.
20. M. A. Moreira, J. C. Santos, A. F. P. Ferreira, J. M. Loureiro, F. Ragon, P. Horcajada, K. E. Shim, Y. K. Hwang, U. –H. Lee, J. S. Chang, C.Serre, A. E. Rodrigues, *Langmuir.*, 2012, **28**, 5715−5723.
21. R. Krishna, *Phys.Chem.Chem.Phys.*, 2015, **17**, 39.
22. R. Lu, W. W. Li, B. Mizaikoff, A. Katzir, G. P. Sheng, H. Q. Yu, *Nat. Protoc*., 2016, **11**, 377−386.
23. C. M. Lu, S. Q. Liu, J. Q. Xu, Y. J. Ding, G. F. Ouyang, *Anal. Chim. Acta*, 2016, **902**, 205−211.
24. P. S. Chen, Y. H. Tseng, Y. L. Chuang, J. H. Chen, *J. Chromatogr. A*, 2015, **1395**, 41−47.
25. V. Finsy, C. E. A. Kirschhock, G. Vedts, M. Maes, L. Alaerts, D. De Vos, G. V. Baron, J. F. M. Denayer, *Chem. - Eur. J*., 2009, 15, 7724−7731.
26. D. H. Desty, A. Goldup, W. T. Swanton, *Nature*, 1959, **183**, 107−108.
27. T. Xu, P. Xu, D. Zheng, H. Yu, X. Li, *Anal. Chem*., 2016, **88**, 12234−12240.
28. Q. H. Tan, Y. Q. Wang, X. Y. Guo, H. T. Liu, Z. L. Liu, *RSC Adv*., 2016, **6**, 61725–61731.
29. S. -I. Kim, S. Lee, Y. G. Chung, Y. -S. Bae, *ACS Appl. Mater. Interfaces*, 2019, **11**, 31227−31236.
30. S. Lee, D. Kim, J. Kim, O. -S. Jung, *Cryst. Growth Des*, 2020, **20**, 3601−3604.
31. W. Huang, J. Jiang, D. Wu, J. Xu, B. Xue, and A. M. Kirillov, *Inorg. Chem.* 2015, **54**, 10524−10526.
32. L. Alaerts, C. E. A. Kirschhock, M. Maes, M. A. van der Veen, V. Finsy, A. Depla, J. A. Martens, G. V. Baron, P. A. Jacobs, J. F. M. Denayer, and D. E. D. Vos, *Angew. Chem. Int. Ed.*, 2007, **46**, 4293 –4297.
33. M. d. Plessis, V. I. Nikolayenko, and L. J. Barbour, *J. Am. Chem. Soc.*, 2020, **142**, 4529−4533.
34. K. Jie, M. Liu, Y. Zhou, M. A. Little, A. Pulido, S. Y. Chong, A. Stephenson, A. R. Hughes, F. Sakakibara, T. Ogoshi, F. r. Blanc,́ G. M. Day, F. Huang, and A. I. Cooper, *J. Am. Chem. Soc.*, 2018, **140**, 6921−6930

35. F. Vermoortele, M. Maes, P. Z. Moghadam, M. J. Lennox, F. Ragon, M. Boulhout, S. Biswas, K. G. M. Laurier, I. Beurroies, R. Denoyel, M. Roeffaers, N. Stock, T. Düren, C. Serre, D. E. D. Vos, *J. Am. Chem. Soc*., 2011, **133**, 18526–18529.
36. S. Mukherjee, B. Joarder, B. Manna, A. V.Desai, A. K. Chaudhari, S. K. Ghosh, *Sci Rep.*, 2014, **4,** 5761.
37. M. I. Gonzalez, M. T. Kapelewski, E. D. Bloch, P. J. Milner, D. A. Reed, M. R. Hudson, J. A. Mason, G. Barin, C. M. Brown, J. R. Long, *J. Am. Chem. Soc*., 2018, **140**, 3412−3422.
38. B. Wang, T. P. Huynh, W. Wu, N. Hayek, T. T. Do, J. C. Cancilla, J. S. Torrecilla, M. M. Nahid, J. M. Colwell, O. M. Gazit, S. R. Puniredd, C. R. McNeill, P. Sonar, H. Haick, *Adv. Mater.*, 2016, **28**, 4012–4018.
39. T. H. Kim, C. H. Kwak, J. H. Lee, *ACS Appl. Mater. Interfaces*, 2017, **9**, 32034−32043.
40. H. S. Woo, C. H. Kwak, J. H. Chung, J. H. Lee, *ACS Appl. Mater. Interfaces*, 2014, **6**, 22553−22560.
41. P. Hoang, N. M. Khashab, *Chem. Mater*., 2017, **29**, 1994−1998.
42. L. Ma, Y. Xie, R. S. H. Khoo, H. Arman, B. Wang, W. Zhou, J. Zhang, R.-B. Lin, and B. Chen, *Chem. Eur. J*., 2022, **28**, e202104269.
43. X. Fan, B. Du, *Sensors and Actuators B*, 2012, 166–167, 753–760.
44. B. -Y. Kim, J. -W. Yoon, J. K. Kim, Y. C. Kang, J. -H. Lee, *ACS Appl. Mater. Interfaces*, 2018, **10**, 16605−16612.
45. J. Zhang, J. Wang, S. Long, S. B. Peh, J. Dong, Y. Wang, A. Karmakar, Y. D. Yuan, Y. Cheng, D. Zhao, *Inorg. Chem.*, 2018, **57**, 13631−13639.
46. S. Bej, R. Das, N. C. Murmu, P. Banerjee, *Inorg. Chem*., 2020, **59**, 4366−4376.
47. X. Zhang, T. Li, J. Wei, G. -H. Tian, Q. -L. Cao, Y. -J. Wang, W.-L. Hou, W.-F. Zhou, Z.-W. Zhang, H. Hu, Y. -Z. Zhang, D. -S. Zhang, Q. Lib and L. Geng, *Dalton Trans.***,** 2022, **51**, 4790-4797.
48. L. Santos, J. P. Neto, A. Crespo, D. Nunes, N. Costa, I. M. Fonseca, P. Barquinha, L. Pereira, J. Silva, R. Martins, E. Fortunato, *ACS Appl. Mater. Interfaces*, 2014, **6**, 12226−12234.
49. F. E. Galdino, J. P. Smith, S. I. Kwamou, D. K. Kampouris, J. Iniesta, G. C. Smith, J. A. Bonacin, C. E. Banks, *Anal. Chem.* 2015, **87**, 11666−11672.
50. M. Li, W. Yang, P. Qiu, G. Ren, C. Li, Z. Chen, Y. Wang, Q. Pan, *J. Lumin.*, 2019, **205**, 380−384.
51. K. N. Weilbaecher, T. A. Guise, L. K. McCauley, *Nat. Rev. Cancer*, 2011, **11**, 411−425.
52. P. Kassal, M. Zubak, G. Scheipl, G. J. Mohr, M. D. Steinberg, I. M. Steinberg, *Sens. Actuators. B*, 2017, **246**, 455−460.
53. T. Liu and B. Yan, *Ind. Eng. Chem. Res.*, 2020, **59**, 1764−1771.
54. L. S. Xie, G. Skorupskii, and M. Dinca, *Chem. Rev.* 2020, **120**, 8536−8580.
55. E. M. Johnson, S. Ilic, and A. J. Morris *ACS Cent. Sci*. 2021, **7**, 445−453.
56. A. Nath, K. S. Asha and S. Mandal, *Chem. Eur. J*. 2021, **27**, 11482–11538.
57. B. Pattengale, J. G. Freeze, M. J. Guberman-Pfeffer, R. Okabe, S. Ostresh, S. Chaudhuri, V. S. Batista, and C. A. Schmuttenmaer, *Chem. Sci.* 2020, ***11***, 9593.
58. S. Halder, A. Dey, A. Bhattacharjee, J. Ortega-Castro, A. Frontera, P. P. Ray, P. Roy, *Dalton Trans.* 2017, ***46***, 11239.
59. L.-A. Cao, M. -S. Yao, H. -J. Jiang, S. Kitagawa, X. -L. Ye, W. -H. Li, and G. Xu, *J. Mater. Chem. A* 2020, ***8***, 9085.

60. B. Bhattacharya, A. Layek, Md. M. Alam, D. K. Maity, S. Chakrabarti, P. P. Ray and D. Ghoshal, *Chem. Commun.*, 2014, ***50***, 7858.
61. C. C. Gravatt, P. M. Gross, *J. Chem. Phys.* 1967, ***46***, 413– 419, DOI: 10.1063/1.1840681
62. X. Wang, Y. Zhang, Z. Shi, T. Lu, Q. Wang, and B. Li, *ACS Appl. Mater. Interfaces*, 2021, ***13***, *45*, 54217–54226.
63. Q. Zhang, J. Wang, A. M. Kirillov, W. Dou, C. Xu, C. L. Yang, R. Fang, and W. Liu, *ACS Appl. Mater. Interfaces*, 2018, ***10***, *28*, 23976–23986.
64. R. Goswami, S. C. Mandal, B. Pathak, and S. Neogi, *ACS Appl. Mater. Interfaces*, 2019, ***11***, *9*, 9042−9053.
65. Y. -C. Zhang, *Crystals*, 2017, ***7***, 151.
66. *Apex3 v2017.3-0, Saint V8.38A, SAINT V8.38A*; Bruker AXS Inc.: Madison, WI, 2018.
67. L. Krause, R. Herbst-Irmer, G. M. Sheldrick, *Appl. Crystallogr.* 2015, ***48***, 3.
68. A. Altomare, G. Cascarano, C. Giacovazzo, A. Guagliardi, *J. Appl. Crystallogr.* 1993, ***26***, 343.
69. G. M. Sheldrick, *Crystal Structure Refinement with SHELXL. Acta Crystallogr., Sect. C: Struct. Chem.*, 2015, ***71***, 3.
70. Farrugia, L. J. *WinGX suite for Small-Molecule Single-Crystal Crystallography. J. Appl. Crystallogr.*, 1999, ***32***, 837.
71. A. L. Spek, *Single-Crystal Structure Validation with the Program PLATON. J. Appl. Crystallogr.* 2003, ***36***, 7.
72. Committee, A. M. *Analyst*, 1987, ***112***, 199.
73. M. Wang, L. Guo and D. Cao, *Anal. Chem.*, 2018, ***90***, 3608-3614.
74. M. J. Frisch, G. W. Trucks, H. B. Schlegel, G. E. Scuseria, M. A. Robb, J. R. Cheeseman, G. Scalmani, V. Barone, G. A. Petersson, H. Nakatsuji, X. Li, M. Caricato, A. V. Marenich, J. Bloino, B. G. Janesko, R. Gomperts, B. Mennucci, H. P. Hratchian, J. V. Ortiz, A. F. Izmaylov, J. L. Sonnenberg, D. Williams-Young, F. Ding, F. Lipparini, F. Egidi, J. Goings, B. Peng, A. Petrone, T. Henderson, D. Ranasinghe, V. G. Zakrzewski, J. Gao, N. Rega, G. Zheng, W. Liang, M. Hada, M. Ehara, K. Toyota, R. Fukuda, J. Hasegawa, M. Ishida, T. Nakajima, Y. Honda, O. Kitao, H. Nakai, T. Vreven, K. Throssell, Jr. J. A. Montgomery, J. E. Peralta, F. Ogliaro, M. J. Bearpark, J. J. Heyd, E. N. Brothers, K. N. Kudin, V. N. Staroverov, T. A. Keith, R. Kobayashi, J. Normand, K. Raghavachari, A. P. Rendell, J. C. Burant, S. S. Iyengar, J. Tomasi, M. Cossi, J. M. Millam, M. Klene, C. Adamo, R. Cammi, J. W. Ochterski, R. L. Martin, K. Morokuma, O. Farkas, J. B. Foresman, D. J. Fox, *Gaussian 16*, Wallingford, CT, 2016
75. S. M. Sze, K. K. Ng, Third Edition, John Wiley & Sons, Inc., Hoboken, New Jersey, 2007.

CHAPTER-3

Differential Supercapacitor and Schottky Diode behaviours in Two New Isostructural Coordination Polymers Based on Redox Active Metal Ions

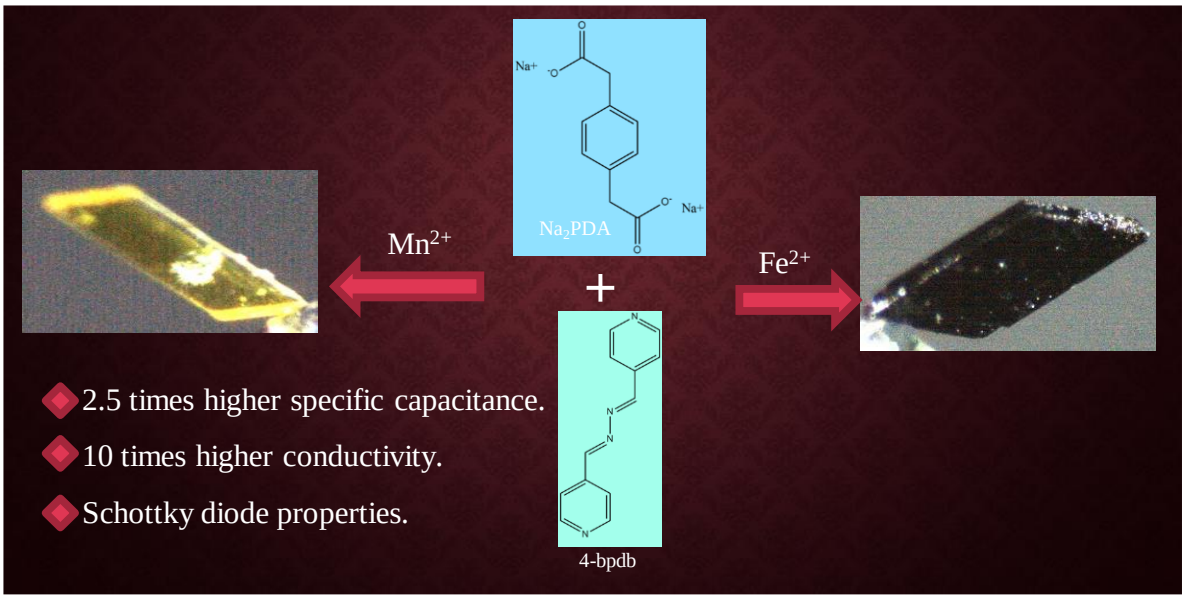

CHAPTER-3

Differential Supercapacitor and Schottky Diode behaviours in Two New Isostructural Coordination Polymers Based on Redox Active Metal Ions

3.1. INTRODUCTION

The imminent depletion of fossil fuels and escalating environmental concerns have necessitated the utilization of clean and renewable energy resources.[1-2] Conventional green energy resources such as solar, tidal, and wind energy are sporadic, and it requires highly efficient energy storage and conversion devices to further strengthen the applications.[3-7] Among the different kinds of electrochemical energy storage systems supercapacitors (SCs) are the most promising and have many distinctive advantages like fast charging/discharging, high power output, long cycle life, and excellent reversibility.[8] On the contrary, SCs are most ideal energy storage devices for hybrid vehicles and electronic devices due to their rapid energy delivery and capture.[9] It has been observed that many kinds of carbon materials such as activated carbon have been extensively used as electrode materials for energy storage devices but due to their low specific capacitance further development in supercapacitors is hindered.[10] In the contrast with carbon materials, metal sulfides have attracted more and more attention because of their high theoretical capacity and abundant redox sites but due to the lack of long-term cycling stability, disordered active sites, and low rate performance again it requires further improvement. Thus the exploration of new materials with high specific capacitance and cycling stability is of great importance.[11-12]

In this milieu, emerging as a new class of organic-inorganic hybrid materials with porous structure and well-defined pores,[13] metal−organic frameworks (MOFs) have attracted great attention with a huge expansion of new MOF families and exploiting their potential applications in different fields such as catalysis,[14-15] sensor,[16-18] gas storage and separation,[19-21] drug delivery,[22] and conductivity.[23] Due to the presence of electrolyte accommodating pores, channels, and redox active metal centers, applications of MOFs have also come to appear in the field of energy storage and conversion.[24-25] In recent times, several important research works have been done on MOF-based supercapacitors.[26-35] From the previous studies it was confirmed that the 2D layered structured MOFs are excellent electrode materials for supercapacitors but the mechanistic pathway(structure property corelation) of MOF-based

supercapacitor materials is a more or less unexplored area. In this domain, Yaghi *et al*. have studied the role of different sizes, structures, organic functionality, and metal ions on supercapacitor behaviour over a series of different nano-crystalline MOFs. Highly electron-deficient functional group (-Cl, -Br, -NO_2) shows relatively better performance over electron-rich functional group such as -NH_2 and mixed metallic MOF shows excellent performance over its monometallic precursors.[36] Feng *et al*. have investigated the molecular dynamics involved in capacitive performance and charging dynamics of conductive metal-organic framework based supercapacitors.[37]

Coordination polymers (CPs) with electrical conductivity have become a subject of considerable interest because of their diverse applications. These materials are currently being extensively investigated for their potential use in various fields, including electrocatalysis, chemiresistive sensing, and energy storage technologies.[38-41] In recent times conductive coordination polymers have appeared into the field of Schottky diodes.[42-45] In this context, Mondal *et. al*, have reported the influence of conformation and counter anion in Schottky diode device fabrication.[46,47] Furthermore, the impact of distinct functional groups and hydrogen bonding within coordination polymers, along with their photosensitive properties, on conductivity and device manufacturing has been established as a well-explored area of research.[48-52] However, the exploration of the Schottky diode perspective within the context of isostructural coordination polymers, where the sole distinction lies in the metal ion, remains uncharted territory.

In our quest to develop isostructural coordination polymers, we have successfully synthesized two new isostructural CPs namely, **1**(Mn) and **2**(Fe) by combining the flexible 1,4-phenylenediacetate and 1,4-bis(4-pyridyl)-2,3-diaza-1,3-butadiene (4-bpdb) auxiliary ligand. The isostructural nature of both compounds were confirmed with the help of single crystal X-ray diffraction (SCXRD), powder X-ray diffraction (PXRD), and fourier-transform infraRed spectroscopy (FT-IR) analysis. The supercapacitor properties of two coordination polymers were explored and both compounds showed better capacitive behaviour in H_2SO_4 electrolyte system as compared to Na_2SO_4 and KOH electrolyte systems. Among them **1**(Mn) exhibited a specific capacitance of 174.3 F/g and 78% retention of its initial capacitance after 5000 charge-discharge cycles. On the other hand, **2**(Fe) exhibited a lower capacitance of 72.3 F/g

compared to **1**(Mn) and has excellent retention of its capacitance (98%) after 5000 cycles. We have also measured the conductivity of both the compounds. **1**(Mn) showed 10 times better conductivity compared to **2**(Fe) and both the compounds showed promising results for Schottky diode fabrication. From the perspective of Schottky diodes, this study represents the first of its kind. This study exemplifies how an individual redox-active metal ion influences both the supercapacitor behavior and conductivity of isostructural coordination polymers.

3.2. EXPERIMENTAL SECTION

3.2.1. Materials

The required chemicals for the synthesis of compounds 1(Mn) and 2(Fe) are $Mn(ClO_4)_2$ (Sigma-Aldrich, 99%), $FeCl_2.4H_2O$ (Sigma-Aldrich, 98%) and 1,4-phenylenediacetic acid(TCI, 98%) pyridine-4-carbaldehyde (Sigma-Aldrich, 98%), NaOH(Merck, 98%) and hydrazine hydrate (Sigma-Aldrich, 98%) used without any further purification and the used solvents for synthesis are methanol (Merck, 98%), ethanol (Merck, 98%),and double distilled water. 1,4-bis(4-pyridyl)-2,3-diaza-1,3-butadiene (4-bpdb) were synthesized by following previously reported procedure.[53]

3.2.2. Synthesis of 1 (Mn) and 2 (Fe).

1(Mn) and **2**(Fe) were prepared at room temperature by using the layer diffusion method. An aqueous solution (30 ml) of Na_2PDA (0.75 mmol, 0.1822 gm) was prepared and mixed with a previously prepared methanol solution (30 ml) of 1,4-bis(4-pyridyl)-2,3-diaza-1,3-butadiene (4-bpdb) (0.75 mmol, 0.1607gm) while being stirred and the resulting solution was further stirred for one hour to mix well. For **1**(Mn), $Mn(ClO_4)_2$(1.5mmol, 0.3885 gm) was dissolved in 60 ml of water and stirred well to make it homogeneous. From the homogeneous metal ion solution, 2 ml is withdrawn and put in a separate capped test tube. To it, 2 mL of the above-mixed ligand solution was slowly and carefully layered and closed the caps of each tube. After 2 weeks yellow coloured parallelogram-shaped crystals suitable for single-crystal diffraction were obtained from the junction of the layers (Figure 1a). For **2**(Fe), $FeCl_2.4H_2O$ (1.5mmol, 0.3012gm) were used in place of $Mn(ClO_4)_2$ by keeping composition and procedures identical that used in **1**. The resulting product contained large quantities of parallelogram-shaped violet crystals at the junction of the layers (Figure 1b). After that, both the crystals were collected and washed with water-methanol mixture and dried in air [yield: 78% based on **1**(Mn) and 80

% based on **2**(Fe)]. Elemental analysis Calcd (%) for **1**(Mn): C 57.98, H 4.54, N 15.91. Found: C 57.72, H 4.47, N 15.98 and for **2**(Fe): C 57.91, H 4.54, N 15.89 found: C 57.84, H 4.41, N 15.99.

(a) **(b)**

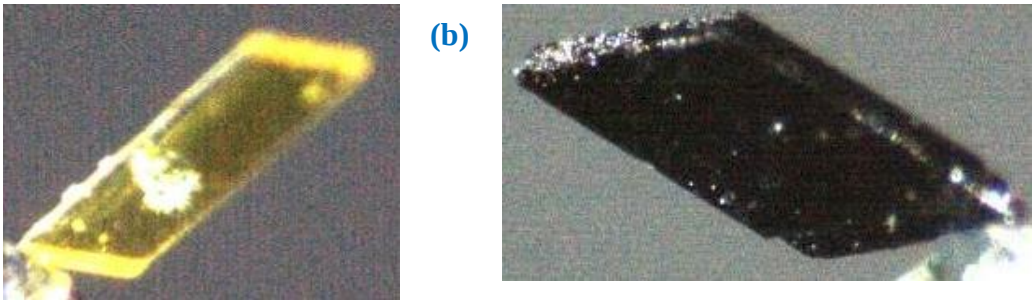

Figure 1. **(a)** Yellow coloured parallelogram shaped crystal image of **1**(Mn). **(b)** Violet coloured parallelogram shaped crystal image of **2**(Fe).

3.2.3 Single Crystal X-ray Diffraction.

Suitable single crystals were carefully selected under an optical microscope and mounted on thin glass fiber carefully. The single crystal data of both the compounds were collected using Bruker D8-Quest diffractometer. The instrument was equipped with Mo Kα (λ=0.71073Å) radiation source and operating voltage of X-ray generator was 50kV and 1mA. Diffraction data were collected with ω scan width of 0.5º. Three different setting of φ (0, 90, 180º) were used to collect the total 408 frames, keeping a fixed distance of sample-to-detector at 6.03 cm and the detector position (2θ) was fixed at -25º. The initial indexing, final data sets, and cell refinements were handled by an APEX3 program, while a SAINTPLUS[54]program was utilized for the frame integration and final cell parameter calculation. The multi-scan absorption data was corrected by a SADABS program.[55] We initially solved the structure by SIR 92,[56] and the full matrix least-square method (SHELXL-2016[57]) was used further, which is present in the WinGx suit of programs (Version 1.63.04a).[58,59] With the help of Fourier maps, we successfully located all the non-hydrogen atoms and refined them anisotropically. Finally, all the hydrogen atoms were fixed at calculated positions and included them in the refinement process using riding model associated with isotropic thermal parameters. The details of the crystal and final refinements are given in the Table 1. CCDC: 2253225-2253226 contain the crystallographic data for this paper. These data can be obtained free of charge from The Cambridge Crystallographic Data Center (CCDC) via www.ccdc.cam.ac.uk/data_request/cif.

Table 1. Crystal data and structure refinement parameters for {[Mn(PDA)(4-bpdb)(H_2O)$_2$].4-bpdb}n, **1**(Mn) and {[Fe(PDA)(4-bpdb)(H_2O)$_2$].4-bpdb}n, **2**(Fe) {PDA= 1,4-phenylenediacetate and 4-bpdb = 1,4-bis(4-pyridyl)-2,3-diaza-1,3-butadiene}.

Structural parameter	**1**(Mn)	**2**(Fe)
Empirical formula	$C_{17}H_{16}Mn_{0.5}N_4O_3$	$C_{17}H_{16}Fe_{0.5}N_4O_3$
Formula weight	351.81	352.26
Crystal system	Triclinic	Triclinic
Space group	$P1^-$	$P1^-$
a (Å)	7.9293(7)	7.9266(8)
b (Å)	8.5740(7)	8.5888(8)
c (Å)	11.9825(10)	11.8991(11)
α (deg)	81.591(2)	82.016(3)
β (deg)	88.173(2)	87.908(3)
γ (deg)	89.232(2)	89.364(3)
Volume (Å^3)	805.44(12)	801.69(13)
Z	2	2
T (K)	298	298
ρ_{calc} (mg m^{-3})	1.451	1.459
μ (mm^{-1})	0.470	0.513
θ range (deg)	2.401 to 27.074	1.729 to 27.251
λ (Mo Kα) (Å)	0.71073	0.71073
R indices [I>2σ(I)]	R_1=0.0710, wR_2=0.1101	R_1=0.0504, wR_2=0.1009
R indices (all data)	R_1=0.0870, wR_2=0.1152	R_1=0.0667, wR_2=0.1077

$R_1 = \Sigma ||F_0|-|F_c|| / \Sigma |F_0|$; $wR_2 = \{\Sigma[w(F_0^2 - F_c^2)^2] / \Sigma[w(F_0^2)^2]\}^{1/2}$. $w = 1/[\sigma^2(F_0)^2 + (aP)^2 + bP]$, $P = [max.(F_0^2,0) + 2(F_c)^2]/3$, *where* $a = 0.0002$ *and* $b = 1.3986$ *for* ***1****(Mn) and* $a = 0.0247$ *and* $b = 0.9152$ *for* ***2****(Fe).*

3.2.4 Powder X-ray Diffraction.

Powder X-ray diffraction (PXRD) patterns of well ground samples were obtained from a Bruker D8 Advance X-ray diffractometer with Cu Kα radiation (λ= 1.5418 Å) in the 2θ range 5-50° and operated at 40 kV and 40 mA (Figure 2.). Obtained PXRD patterns of the samples indicate that **1**(Mn) and **2**(Fe) are new and the patterns consist of the new materials with the simulated PXRD patterns obtained from the structures determined using SCXRD confirming that the compounds are isostructural and entirely pure in phase.

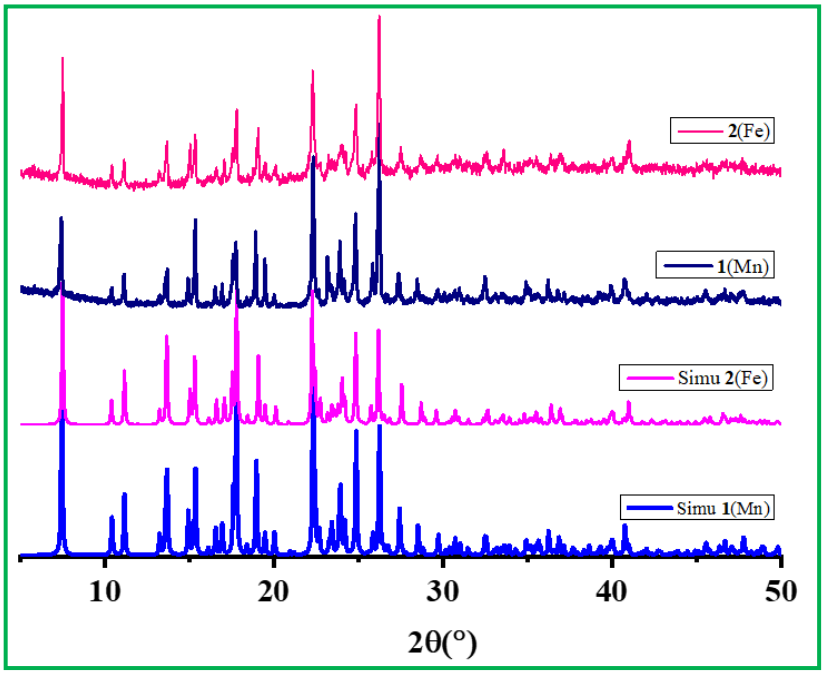

Figure 2. PXRD (CuKα) patterns of **1**(Mn) and **2**(Fe).

3.2.5 FT-IR Measurements.

FT-IR spectra were recorded on Nicolet Magna IR 750 series-II instrument, range 400-4000 cm^{-1} (Figure 3). The observed FT-IR frequencies are tabulated in Table 2. For both the compounds, observed FT-IR frequencies are completely merged and represent their isostructural nature.

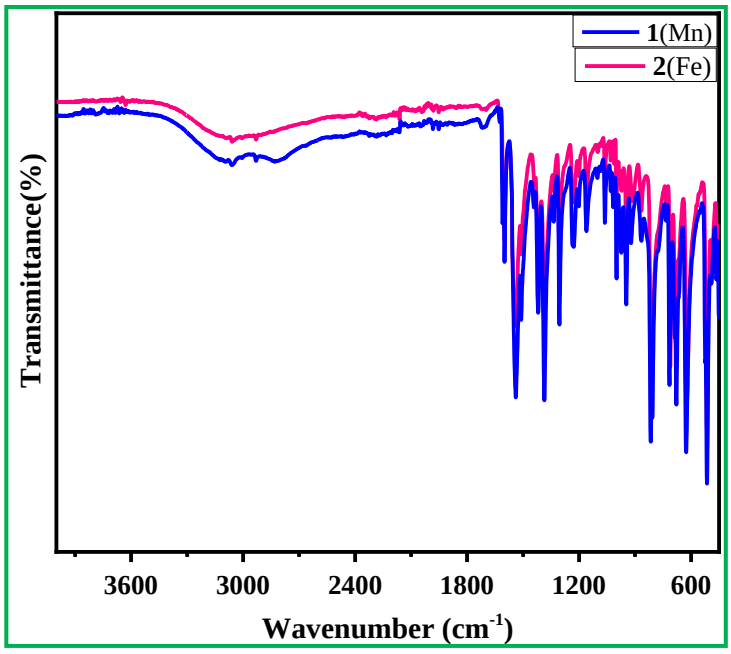

Figure 3. FT-IR spectrum of **1**(Mn) and **2**(Fe).

Table 2. The observed FT-IR bands for **1**(Mn) and **2**(Fe).

Bands	Absorption frequencies (cm^{-1})	Bands	Absorption frequencies (cm^{-1})
$\upsilon_{str}(H_2O)$	3120(w)	$\upsilon_{sy.\ str}$(carboxylate)	1302(s)
$\upsilon_{asy.str}(sp_2$ C-H)	3052(m), 2924(m)	υ_{str}(C-N)	1230(s), 1195(w)
$\upsilon_{asy.str}(sp_3$ C-H)	2820(w)	δ(aromatic C-H)$_{in}$ plane bending	1156(s), 1063(s), 1018(w),989(m)
$\upsilon_{asy.\ str}$(carboxylate)	1604(s)	δ(aromatic C-H)$_{out}$ of plane bending	944(m), 873(m), 808(w)
υ_{str}(C=N)	1540(s)	δ(carboxylate)$_{bending}$	717(s), 680(w)
υ_{str}(C=C)	1498(s), 1416(m)	δ(aromatic C=C)$_{out}$ of plane bending	617(s), 512(m)

3.2.6 Thermal Stability.

To check the thermal stability of **1**(Mn) and **2**(Fe), thermogravimetric analysis (TGA) was carried out with the help of a Perkin-Elmer instrument STA 6000 under a nitrogen atmosphere (flow rate = 20 ml min^{-1}) in the temperature range of 30 - 800 °C (heating rate 10°C/min) (Figure 4). It was observed that both compounds have almost similar thermal stability. The first weight loss of 5.19 % (calculated 5.11%) **1**(Mn) and **2**(Fe) was marked at 140°C, due to

the removal of coordinated water molecules. The subsequent weight losses of both the compounds were started at 260°C due to the decomposition of the frameworks.

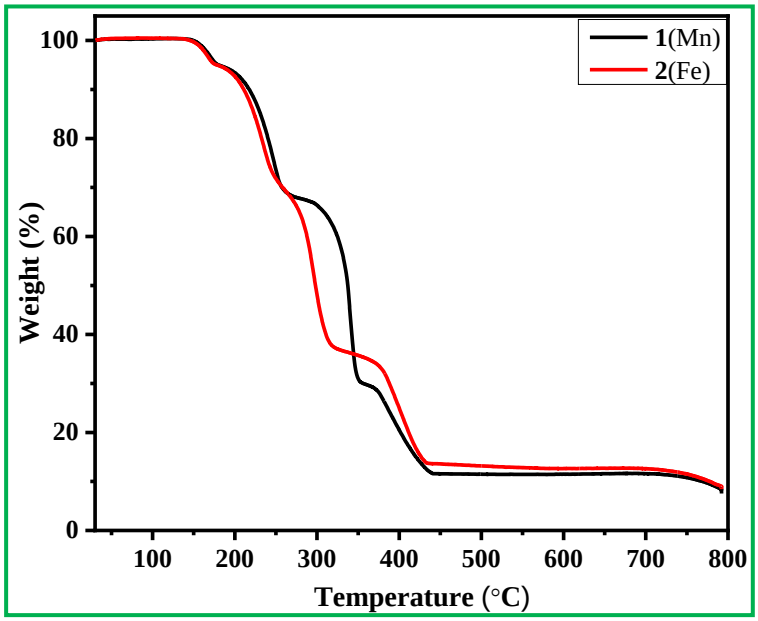

Figure 4. Thermogravimetric analysis (TGA) of **1**(Mn) and **2**(Fe) in nitrogen atmosphere.

3.2.7 SEM-EDX.

The well ground powder samples of **1**(Mn) and **2**(Fe) were analysed to evaluate the size and surface morphology by using field-emission scanning electron microscopy (FESEM, FEI INSPECT F50). It is evident that powder grains of both samples are in the micron dimension with various shapes (Figure 5).

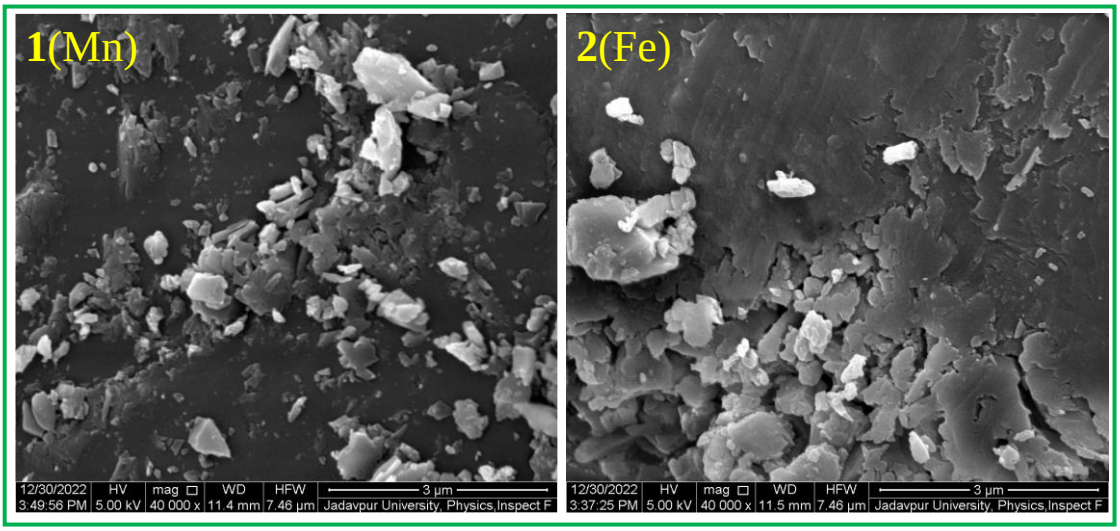

Figure 5. SEM images of **1**(Mn) and **2**(Fe).

3.2.8 BET Analysis.

Nitrogen gas sorption isotherms for **1**(Mn) and **2**(Fe) were measured at 77K and in the pressure range of 0 to 1 bar using an Autosorb iQ instrument from Quantachrome Inc., USA. Prior to the sorption experiment, both powder samples were pre-treated at 120°C for 60 minutes. The obtained adsorption isotherm behavior for both compounds exhibited a type II adsorption isotherm pattern, reaching a saturated gas uptake of 52.78 $cm^3\ g^{-1}$ for **1**(Mn) and 41.38 $cm^3\ g^{-1}$ for **2**(Fe) at a pressure of 0.99 bar and a temperature of 77K. The calculated BET (Brunauer-Emmett-Teller) surface area for **1**(Mn) is 23.30 $m^2\ g^{-1}$, while for 2(Fe), it is 19.74 $m^2\ g^{-1}$ (Figure 6). The obtained correlation coefficient (R^2) values are 0.986 for **1**(Mn) and 0.9838 for **2**(Fe), respectively. Additionally, the C values for **1**(Mn) and **2**(Fe) are 6.89 and 9.66, respectively.

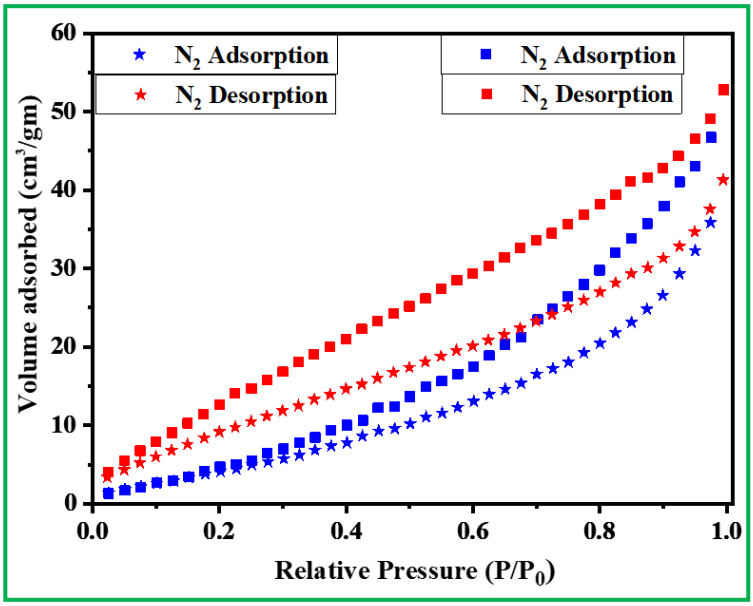

Figure 6. N_2 adsorption (at 77 K) isotherms of **1**(Mn**)** and **2**(Fe), squares represent the adsorption(blue) and desorption(red) by **1**(Mn) and stars represent the adsorption(blue) and desorption(red) by **2**(Fe), respectively.

3.2.9 UV-Vis Absorbance Measurements.

The solution of **1**(Mn) and **2**(Fe) were prepared by adding 3 mg powder sample of **1**(Mn) and **2**(Fe) in separate capped bottle with 3 ml water then sonicated it to make a dispersion. The absorbance measurements were performed using 100 µl of the stock solution and 2 ml water in separate quartz cuvette. UV-Vis spectra of **1**(Mn) and **2**(Fe) in water were investigated

(Figure 7) using UV-1900i UV-Vis spectrophotometer (Shimadzu) and both the compound shows absorption maxima at 280 nm.

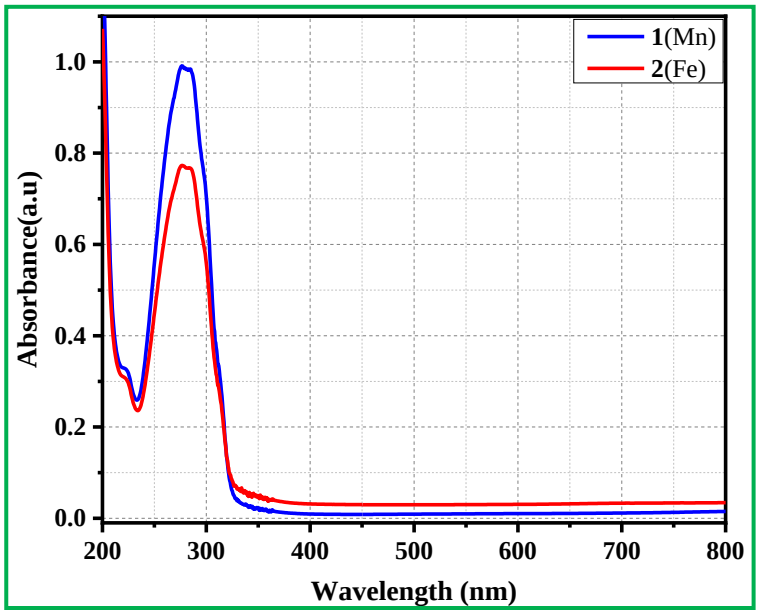

Figure 7. Absorption spectra of **1**(Mn) and **2**(Fe) in aqueous medium.

3.2.10 Electrochemical Characterizations.

The **1**(Mn) and **2**(Fe) were electrochemically characterized in 3-electrode cell assembly through cyclic Voltammetric (CV) analysis and electrochemical impedance spectroscopy (EIS). The 3-electrode cell was assembled by previously grounded active material (**1**(Mn)/**2**(Fe)) coated glassy carbon working electrode, platinum foil counter electrode and Ag/AgCl reference electrode (+0.197 V *vs*. Standard Hydrogen Electrode/SHE). The working electrodes were fabricated by the drop-casting of active material slurry onto the glassy carbon electrodes. The active material slurry was prepared in N, N-dimethylformamide (DMF) solvent by mixing 85% active material, 10% conducting carbon black and 5% polyvinylidene fluoride (PVDF) binder. The resulting slurry-coated working electrodes were dried at 60 °C for 3 h in hot air oven. The electrochemical measurements were carried out in multichannel Autolabpotentiostat & galvanostat instrument (Model: M204) at ambient temperature (25 °C).

3.2.11 Device Fabrication.

Indium tin oxide (ITO) coated glass substrates were cleaned with soap solution followed by further rinsing of the substrate with distilled water in ultrasonic bath for 15 to 20 minutes. Subsequently, ITO substrates were sonicated in acetone and isopropanol for 10 minutes each and after dried with hot-air gun. Prior to spin coating PEDOT: PSS, the ITO substrates were treated in UV-Ozone chamber (Holmarc, India) for 45 minutes. Next, low conductivity PEDOT: PSS (Clevios P VP Al4083) was spin coated on UV-ozone treated ITO substrates at 2000 rpm. The Mn and Fe compounds in proper concentration (≈ 40 mg/mL) were dispersed in DMSO solvent and ultrasonicated for long time to form a stable dispersion. The prepared solution was drop casted atop ITO/PEDOT: PSS and was subsequently annealed in ambient atmosphere on a hot plate at 80°C for few seconds to evaporate the residual solvent. The procedure of drop casting was repeated few times to get a thick film free from pinholes. To complete the device fabrication, top aluminium electrode was evaporated (at 0.2 Å/S evaporation rate) in a thermal evaporation chamber under high vacuum (≈ 10-5 mbar).

3.2.12 Device Measurement:

Current voltage characteristics measurements under dark condition were performed using a source meter unit (Ossila) in the voltage range +4V to -4 V. All the measurements were performed in ambient condition.

3.3. RESULTS and DISCUSSION

3.3.1 Structural Description.

Single-crystal X-ray diffraction revealed that the compounds, **1**(Mn) and **2**(Fe) are isostructural and crystallized in a triclinic crystal system with *P*-1 space group. For the description of structures, X-ray crystallographic data of **1**(Mn) are illustrated here. The asymmetric unit of **1**(Mn) consists of crystallographically independent half Mn(II) ion, half 1,4-phenylenediacetate (PDA), half coordinated 1,4-bis(4-pyridyl)-2,3-diaza-1,3-butadiene (4-bpdb), one coordinated water molecule and half lattice 1,4-bis(4-pyridyl)-2,3-diaza-1,3-butadiene (4-bpdb) (Figure 8a). The Mn(II) ion is six coordinated by the four oxygen atoms at equatorial position and two nitrogen atoms at axial position and has an octahedral geometry through the two oxygen atoms from two carboxylate groups of two 1,4-phenylenediacetate

(PDA) ligands, two oxygen atoms from two coordinated water molecules, and two nitrogen atoms from two aromatic pyridyl rings of two 4-bpdb ligands (Figure 8b).

The M−O bonds have an average distance of 2.18 Å and 2.14 Å respectively, for **1**(Mn) and **2**(Fe), and the M−N bonds have length of 2.29 Å for compound **1**(Mn) and 2.22 Å for compound **2**(Fe). The O/N-M-N/O bond angles are in the range of 87.49(10) - 180°. The selected bond distances are given in Table 3 and the selected bond angles are listed in Table 4.

Table 3: Selected bond distances (Å) observed in **1**(Mn) and **2**(Fe).

1(Mn)		**2** (Fe)	
Bond	**Distances, Å**	**Bond**	**Distances, Å**
Mn(1)-O(1)	2.148(2)	Fe(1)-O(1)	2.1005(18)
Mn(1)-O(1)#1	2.148(2)	Fe(1)-O(1)#1	2.1005(18)
Mn(1)-O(3)	2.215(3)	Fe(1)-O(3)#1	2.172(2)
Mn(1)-O(3)#1	2.215(3)	Fe(1)-O(3)	2.173(2)
Mn(1)-N(1)#1	2.295(3)	Fe(1)-N(1)#1	2.226(2)
Mn(1)-N(1)	2.295(3)	Fe(1)-N(1)	2.226(2)

Symmetry transformations used to generate equivalent atoms: #1 -x+1,-y+1,-z+1.

Table 4: Selected bond angles observed in **1**(Mn) and **2**(Fe).

1(Mn)		**2**(Fe)	
Angle	Amplitude	Angle	Amplitude
O(1)#1-Mn(1)-O(1)	180.0	O(1)-Fe(1)-O(1)#1	180.0
O(1)#1-Mn(1)-O(3)	92.51(10)	O(1)-Fe(1)-O(3)#1	91.31(8)
O(1)-Mn(1)-O(3)	87.49(10)	O(1)#1-Fe(1)-O(3)#1	88.69(8)
O(1)#1-Mn(1)-O(3)#1	87.49(10)	O(1)-Fe(1)-O(3)	88.69(8)
O(1)-Mn(1)-O(3)#1	92.51(10)	O(1)#1-Fe(1)-O(3)	91.31(8)

O(3)-Mn(1)-O(3)#1	180.0	O(3)#1-Fe(1)-O(3)	180.0
O(1)#1-Mn(1)-N(1)#1	87.72(9)	O(1)-Fe(1)-N(1)#1	91.67(7)
O(1)-Mn(1)-N(1)#1	92.28(9)	O(1)#1-Fe(1)-N(1)#1	88.33(7)
O(3)-Mn(1)-N(1)#1	88.48(10)	O(3)#1-Fe(1)-N(1)#1	90.32(8)
O(3)#1-Mn(1)-N(1)#1	91.52(10)	O(3)-Fe(1)-N(1)#1	89.68(8)
O(1)#1-Mn(1)-N(1)	92.28(9)	O(1)-Fe(1)-N(1)	88.33(7)
O(1)-Mn(1)-N(1)	87.73(9)	O(1)#1-Fe(1)-N(1)	91.67(7)
O(3)-Mn(1)-N(1)	91.52(10)	O(3)#1-Fe(1)-N(1)	89.68(8)
O(3)#1-Mn(1)-N(1)	88.48(10)	O(3)-Fe(1)-N(1)	90.32(8)
N(1)#1-Mn(1)-N(1)	180.0	N(1)#1-Fe(1)-N(1)	180.0

Symmetry transformations used to generate equivalent atoms: #1 -x+1,-y+1,-z+1.

The connectivity between Mn(II) ions and 1,4-phenylenediacetate (PDA) ligands forms one-dimensional zigzag chains along the *a*-axis. The chains are connected by 4-bpdh ligands to form two-dimensional layer structure (Figure 8c) based on 4-connected nodes (Mn(II)) with vertex symbol 4.4.4.4.*.* (Figure 8d).

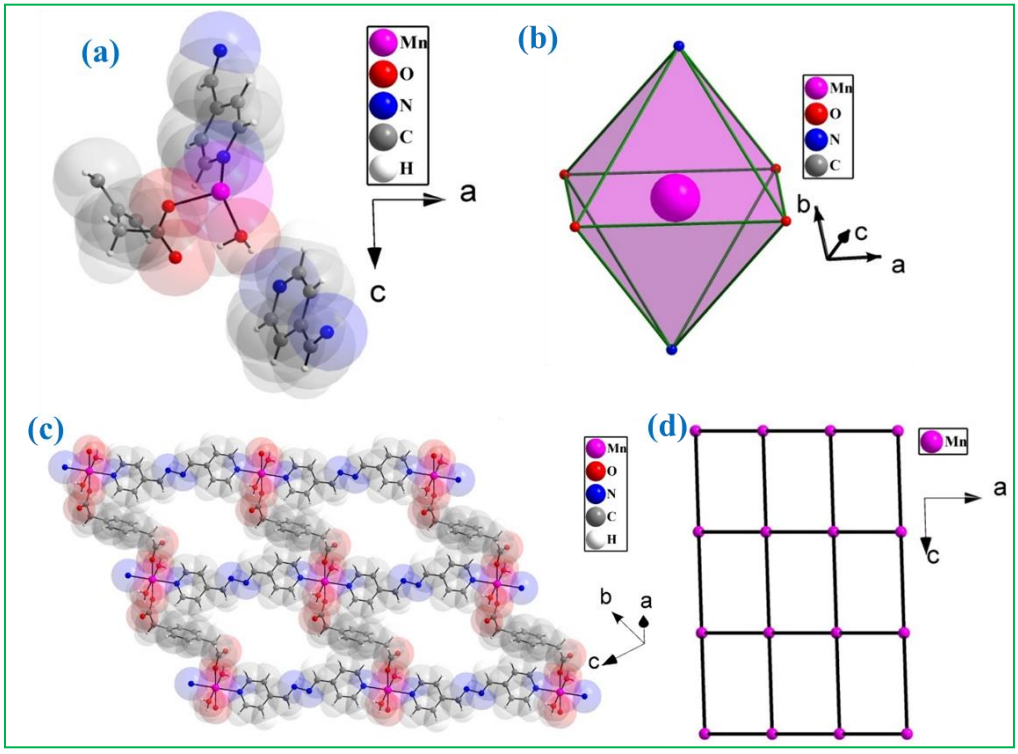

Figure 8. **(a)** Figure shows the asymmetric unit of **1**(Mn). **(b)** Octahedral coordination geometry around Mn(II) ions. **(c)** Metal connected network topology based on 4-connected nodes. **(d)** Figure shows two-dimensional layer structure formed through the connectivity of Mn(II) ions with two ligands (PDA and 4-bpdb) in **1**(Mn).

The layers are organized in AAA…. fashion along the b axis resulting in the formation of three-dimensional supramolecular structure (Figure 9). The non-bonded 4-bpdb molecules occupy voids created by the three-dimensional packing arrangement.

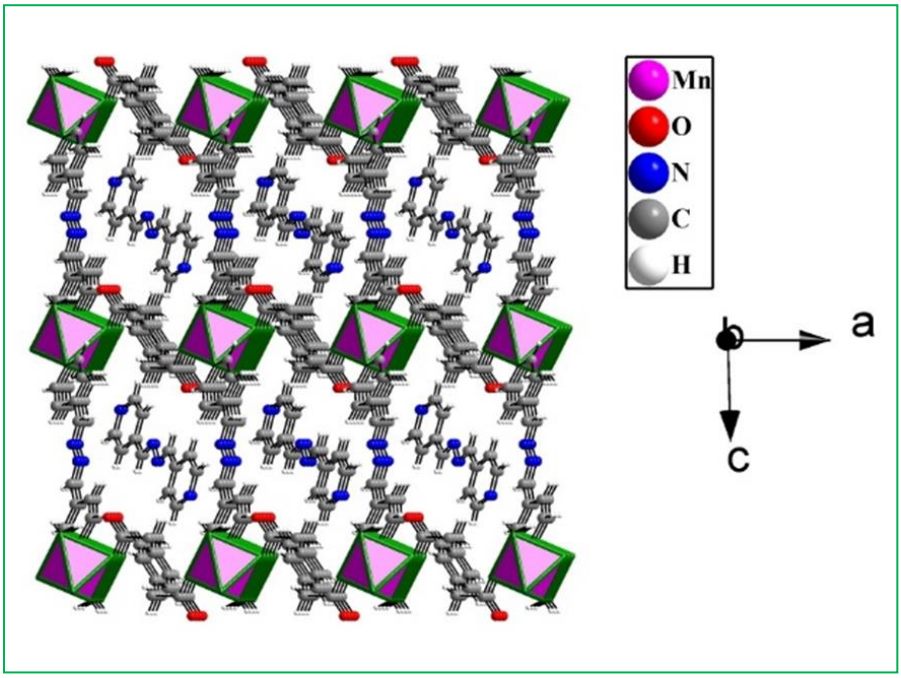

Figure 9. Figure shows the three-dimensional packing arrangement of two-dimensional layers along with non-bonded 4-bpdb molecules occupying the void spaces created by the arrangement in **1**(Mn).

The two-dimensional layer is also stabilized through intra-layer O – H···O hydrogen bond interactions between hydrogen atoms of the coordinated water molecules [H(3A)] and the unbound oxygen atoms [O(2)] of carboxylate group of 1,4-PDA. On the other hand, free 4-bpdb molecules take important part to connect layers to form three-dimensional supramolecular arrangement through O – H···N hydrogen bond interactions. Here the hydrogen atoms of the coordinated water molecules [H(3B)] and the pyridine nitrogen atoms

[N(3)] of the free 4-bpdb molecules form the hydrogen bonds. The overall hydrogen bond interactions are presented in figure 10a. The details of hydrogen bond interactions are shown in Table 5. The three-dimensional arrangement is also stabilized through π…π interactions between the pyridine rings of bonded 4-bpdb and free 4-bpdb molecules (centroid-centroid distance of pyridines rings ~ 3.7 Å and inter-planar angle ~ 15°) (Figure 10b).

Table 5. Selected hydrogen-bond interaction in **1**(Mn) and **2**(Fe).

D – H···A[a]	D – H (Å)	H···A (Å)	D···A (Å)	D – H···A (°)
O(3) – H(3A)···O(2)	0.88(5) (**1**) 0.82(2) (**2**)	1.78(5) (**1**) 1.83(4) (**2**)	2.648(4) (**1**) 2.639(3) (**2**)	168(5) (**1**) 167(4) (**2**)
O(3) – (3B)···N(3)#1	0.79(4) (**1**) 0.78(4) (**2**)	2.07(4)(**1**) 2.08(4) (**2**)	2.861(4) (**1**) 2.861(3) (**2**)	176(3) (**1**) 176(4) (**2**)

[a] #1 1-x,1-y,1-z

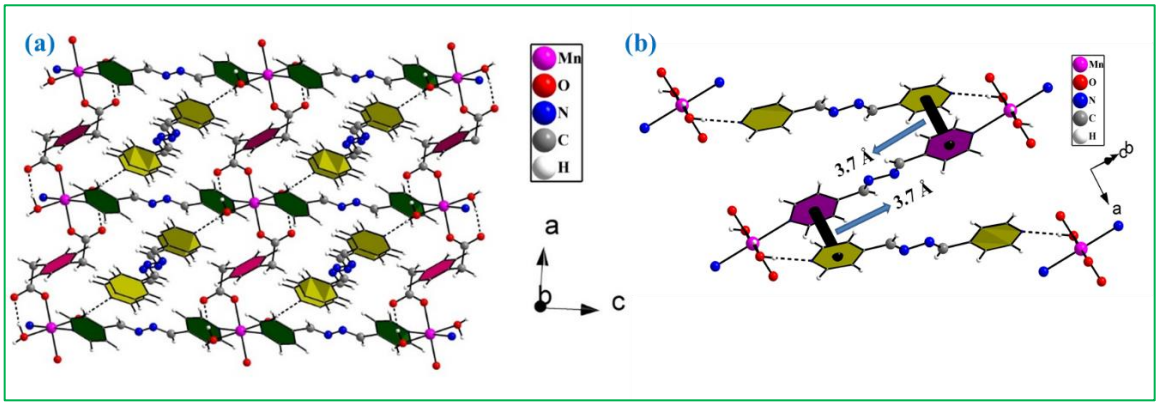

Figure 10. (a) Figure shows the O – H···O and O – H···N hydrogen bond interactions to form three-dimensional supramolecular structure in **1**(Mn). The dotted lines indicate the hydrogen bonds. **(b)** Figure shows π···π interactions between two pyridine rings of bonded 4-bpdb and free 4-bpdb molecules.

3.3.2 Studies on Supercapacitive Characteristics.

Due to the presence of active redox centres, namely **1**(Mn**)** and **2**(Fe**)**, and the two-dimensional networks for facile electrolyte diffusions in the coordination polymers structures, the **1**(Mn) and **2**(Fe) could be envisaged for advanced supercapacitive applications.[60-63] The BET surface area values for **1**(Mn) and **2**(Fe), *i.e.*, 23.30 $m^2 g^{-1}$, and 19.74 $m^2 g^{-1}$ respectively, significantly

contribute to the electrical double layer capacitances, while the surface redox (pseudocapacitive) properties from Mn(II) and Fe(II) centres improve the overall charge storage capacitance. The supercapacitive characteristics of **1**(Mn) and **2**(Fe) in different electrolyte mediums were investigated through CV analysis at 5 mV/s, and the relevant profiles were demonstrated in figure 11a & 11b. Herein, we have selected three types of aqueous solutions based on their pH ranges, namely acidic (1 M H_2SO_4), neutral (1 M Na_2SO_4) and alkaline (1 M KOH) electrolytes. It is evidenced that the **1**(Mn) and **2**(Fe) are showing the best supercapacitive performances in 1 M H_2SO_4 electrolyte medium compared to 1 M Na_2SO_4 and 1 M KOH systems. In 1 M H_2SO_4 medium, both compound showed quasi-rectangular CV profiles with distinct pseudocapacitive responses. The **1**(Mn) and **2**(Fe) exhibited anodic/cathodic humps at 0.46/0.35 V and 0.48/0.37 V, respectively, due to the presence of Mn(II)/Mn(III) and Fe(II)/Fe(III) active redox couples; while

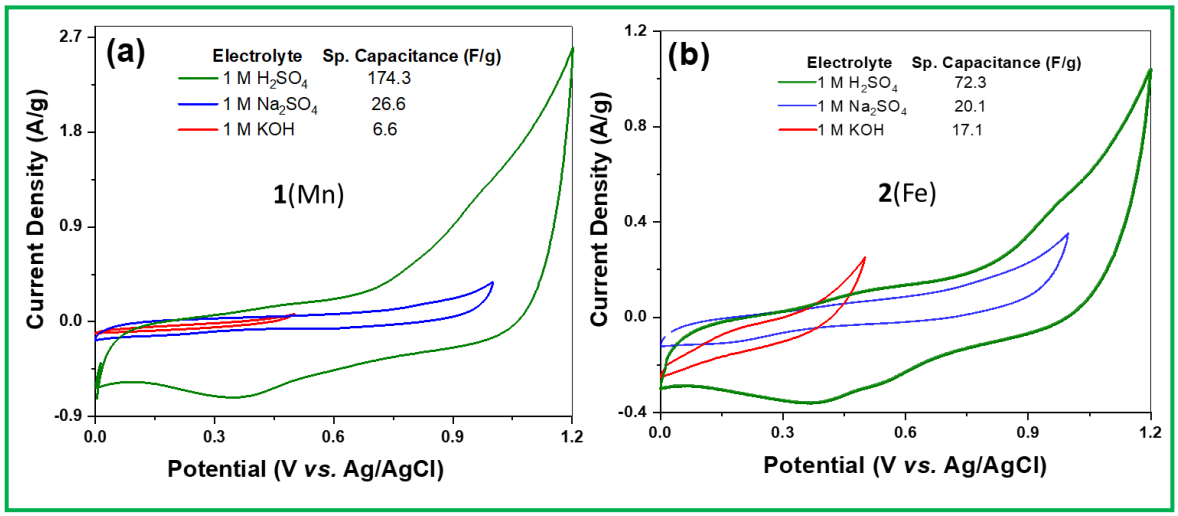

Figure 11. Comparative CV profiles of **(a)** **1**(Mn) and **(b)** **2**(Fe) at 5 mV/s scan rate under 1 M H_2SO_4, 1 M Na_2SO_4 and 1 M KOH electrolyte mediums.

similar surface redox humps are not evidenced in 1 M Na_2SO_4 and 1 M KOH electrolyte systems. In later cases, quasi-rectangular CV profiles appear without pseudo capacitance contributions, and hence, lower specific capacitances are achieved. The **1**(Mn) demonstrated 174.3 (within 0-1.2V), 26.6 (within 0-1.0 V) and 6.6 (within 0-0.5 V) F/g specific capacitances in 1 M H_2SO_4, 1 M Na_2SO_4 and 1 M KOH electrolytes, respectively, while, **2**(Fe) showed respective specific capacitances of 72.3 (within 0-1.2V), 20.1 (within 0-1.0 V) and 17.1 (within

0-0.5 V) F/g. The increased specific capacitances in **1**(Mn) compared to **2**(Fe) are attributed due to the higher BET surface area than that of **2**(Fe). During the anodic scan, the higher potential for oxygen evolution reaction (OER) were obtained in 1 M H_2SO_4 (~1.2 V) than that of 1 M Na_2SO_4 (~1 V) and 1 M KOH (~0.5 V), in both CP samples. Therefore, higher operational potential is another benefit in 1 M H_2SO_4 medium compared to 1 M Na_2SO_4 and 1 M KOH mediums. Henceforth, 1 M H_2SO_4 medium was selected for detailed electrochemical studies of **1**(Mn) and **2**(Fe).

Figure 12a and 12b depicts the CV profiles of **1**(Mn) and **2**(Fe), respectively, at different scan rates, ranging from 5 to 50 mV/s. The charge storage mechanisms of **1**(Mn) and **2**(Fe) could be elucidated from the variable scan rate CV profiles by using the following power law.[64]

$$i = a\,\upsilon^{b} \quad \text{(A)}$$

Whereas i and υ are current response at a particular potential and scan rate, respectively, while a and b are characteristic constants. The b = 0.5 suggests diffusion-controlled faradaic mechanism as per the Randles-Sevcik equation, while b = 1 indicates surface-controlled capacitive/pseudocapacitive mechanism. Herein, we have plotted the current response *vs*. scan rate, and found a linear relationship (*i.e*., b = 1) in both **1**(Mn) and **2**(Fe), which are shown in figure 12c and 12d. It signifies that the operating charge storage mechanisms for both CPs are surface-controlled capacitive and pseudocapacitive in nature. The surface redox humps are not much shifted towards higher overpotential regions at higher anodic/cathodic scans, which implies minimal mass-transfer resistances are operated. The facile electrolyte infiltrations into the CP-network structures are minimizing the mass-transfer overpotentials for faster kinetics.[60,62] However, the specific capacitances (F/g) are calculated from the CV profiles by using Eq. B,[60] and figure 13a demonstrates the capacitance of **1**(Mn) and **2**(Fe) at different scan rates, whereas, **1**(Mn) exhibits higher values than that of **2**(Fe).

$$\textit{Specific Capacitance} = \frac{Area\ Under\ the\ CV\ Profile}{Scan\ Rate \times Voltage\ Window \times Electrode\ Mass} \quad \text{(B)}$$

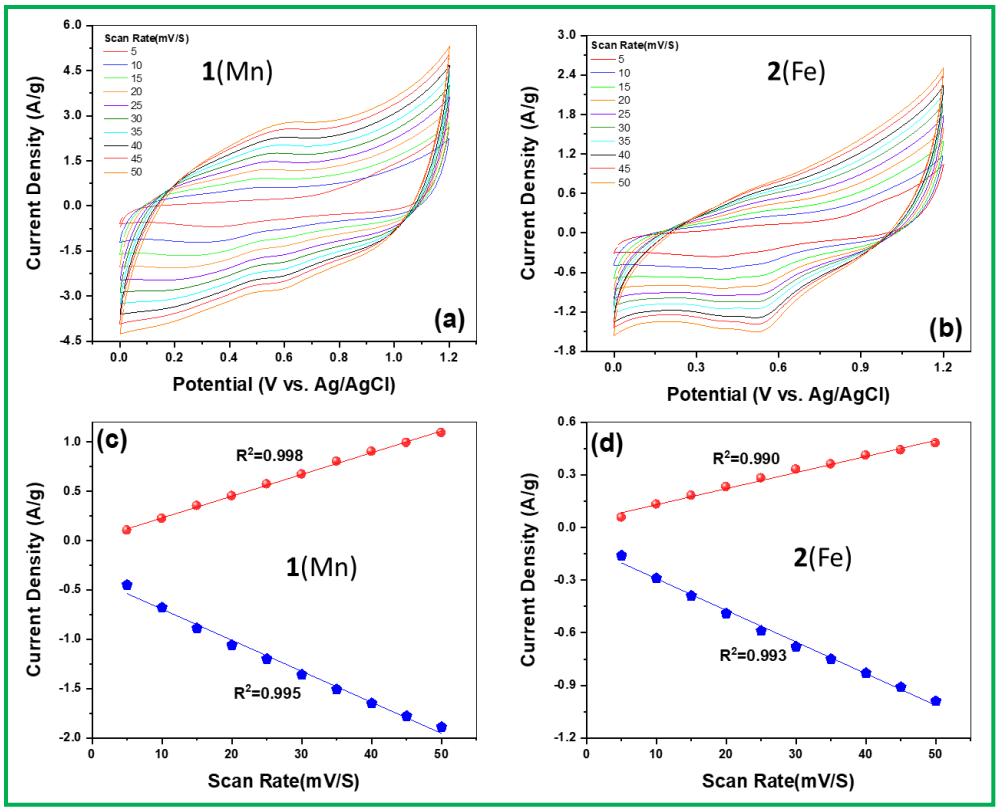

Figure 12. CV profiles at variable scan rates in 1 M H_2SO_4: **(a)** **1**(Mn) and **(b)** **2**(Fe), current response *vs*. scan rate profiles: **(c)** **1**(Mn) and **(d)** **2**(Fe).

The cycling stabilities of both CPs were elucidated by repetitive CV scans at 25 mV/s rate, and the data are represented in figure 13b. It has appeared that the **1**(Mn) and **2**(Fe) demonstrates 78 and 98 % capacitance retentions over 5000 cycles.

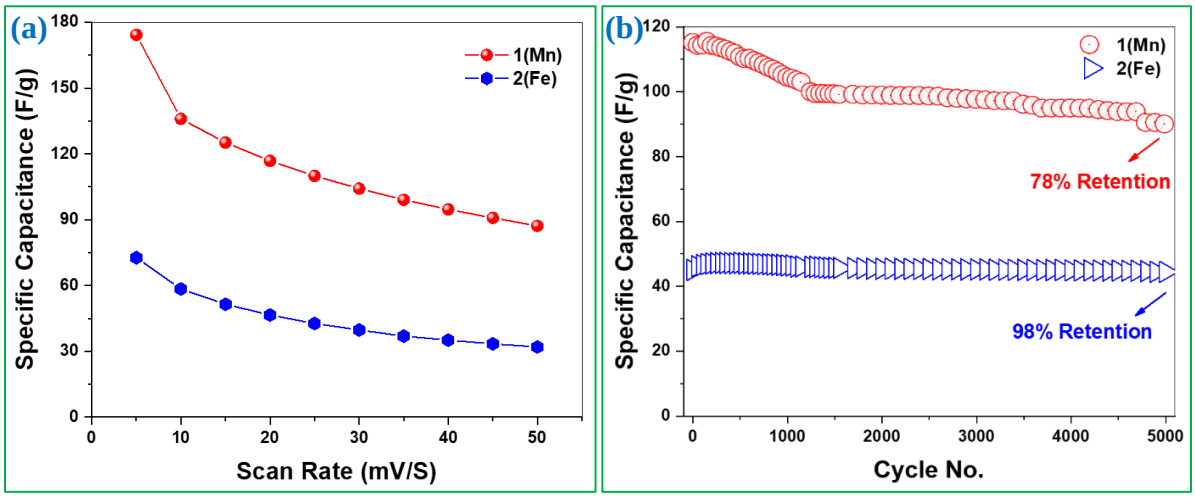

Figure 13. (a) Specific capacitance of **1**(Mn) and **2**(Fe) under variable scan rates in 1 M H_2SO_4. **(b)** Cycle life data of **1**(Mn**)** and **2**(Fe**)** at 25 mV/s scan rate in 1 M H_2SO_4.

Due to the disproportion of Mn(III) state, Mn-dissolution from electrode to electrolyte solution is unavoidable, and the same is responsible for lower capacitance retention.[65] On the other hand, such disproportionation of Fe(III) state is not common, and hence, excellent reversibility is achieved.

The EIS analysis has been carried out before and after cycling for both **1**(Mn) and **2**(Fe), and the Nyquist plots are presented in figure 14a & b, respectively. The solution resistance (R_S) and charge transfer resistance (R_{CT}) data are calculated from Nyquist plots by equivalent circuit fitting method and summarized in Table 6, whereas, inset of figure 14a depicts the construction of equivalent circuit. However, the R_S values remain almost unaltered before and after cycling for both CPs. On the other side, the R_{CT} value remains close for **2**(Fe), but increases for **1**(Mn) upon 5000 cycling. This trend is well synchronized with the cycling data, whereas **2**(Fe) shows better reversibility than **1**(Mn). The increased R_{CT} is the result of structural disintegration of **1**(Mn) over prolonged cycling. So, **1**(Mn) demonstrates high specific capacitance but lower reversibility, while **2**(Fe) is characterized by inferior specific capacitance but excellent cyclability.

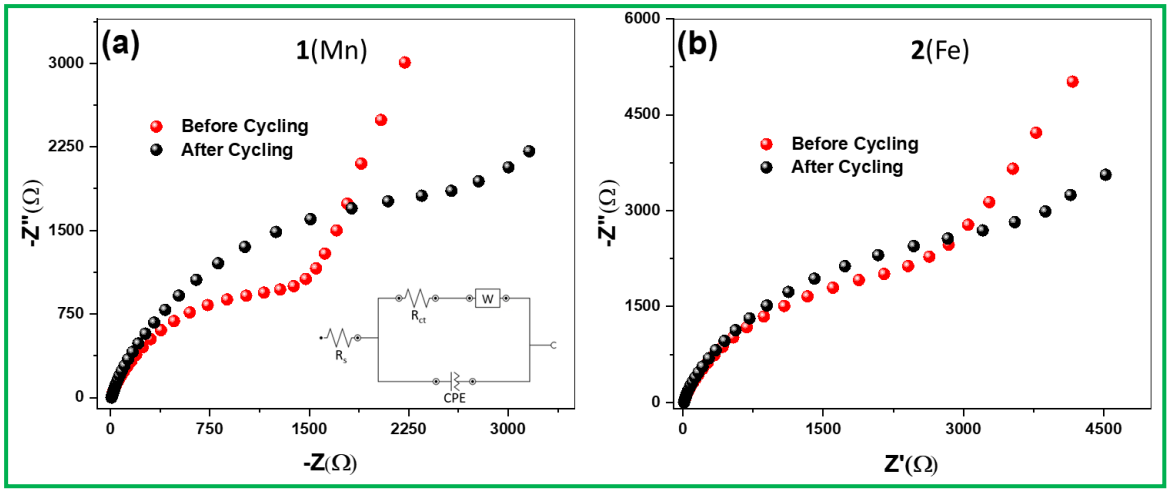

Figure 14. Nyquist plots of **(a)** **1**(Mn) and **(b)** **2**(Fe) at before and after cycling experiments. Inset of (a) depicts the components of equivalent circuit: R_S: solution resistance, R_{CT}: charge transfer resistance, CPE: constant phase element and W: Warburg component.

Table 6. EIS data of **1**(Mn) and **2**(Fe)at before and after cycling.

Compound	Solution Resistance (R_S)/Ohm		Charge Transfer Resistance (R_{CT})/Ohm	
	Before Cycling	After Cycling	Before Cycling	After Cycling
1(Mn)	8.60	8.64	2100	3640
2(Fe)	12.47	12.58	4000	4200

3.3.2 Schottky Diode Characteristics.

To gain insight of the electrical conductivity properties, Schottky junction diodes were fabricated with the configuration ITO/PEDOT/Mn/Al and ITO/PEDOT/Fe/Al. *J-V* characteristics of these devices were measured under dark condition (Figure 15a) and were analysed using well known Shockley-diode equation:

$$J = J_0 \left[\exp\left(\frac{qV_D}{\eta kT}\right) - 1\right] \qquad (1)$$

where J is the current under forward bias, q is charge of the electron, V_D is the voltage across the diode and η is the diode ideality factor which is a measure of the departure from ideal diode characteristics. If the carrier injection is described by thermionic emission, then J_0 can be approximated as, as $J_0 = A^* T^2 \exp\left(-\frac{e\varphi_B}{kT}\right)$. In this expression, A^* is the effective Richardson constant and its value was considered as $120\ A/cm^2K^2$ for all the devices[66] and φ_B is the Schottky barrier height. For large forward bias ($V_D > 3kT/q$, or $V_D > 77$ mV at room temperature) Equation1 can be expressed as

$$I = I_0 \exp\left(\frac{q}{\eta kT}(V - IR_s)\right) \qquad (2)$$

where $I = J \times A$ and $I_0 = J_0 \times A$ ($A = 0.2$ cm^2 is the area of the device) and IR_s is the voltage drop

across the series resistance R_s of the device. Differentiation of Equation 2 leads to

$$\frac{dV}{d(\ln\frac{I}{I_0})} = \frac{\eta kT}{q} + IR_s \qquad (3)$$

Slope of the linear part of the $dV/d\left(\ln\frac{I}{I_0}\right)$ versus I plot (Figure 15b) yields R_s whereas the y-axis intercept yields $\eta kT/q$. We further define a function, $H(I) = V - \frac{\eta kT}{q}\ln\left(\frac{I}{AA^*T^2}\right)$ and substitute it in Equation 1 to obtain a much simpler form; $H(I) = IR_s + \eta\varphi_B$. Using the value of η already extracted, a plot of $H(I)$ vs I (Figure 16) will result in a straight line and φ_B can be extracted from its y-intercept. Further, R_s can also be extracted and compared with that obtained from Equation 3, for consistency. The parameters extracted from these graphs have been tabulated in Table 7.

The ideality factor of 1.93 and 2.71 and the barrier height of 0.97 eV and 1.09 eV was obtained for Mn and Fe devices respectively. Low voltage range (0.0-0.6 V for Mn and 0.0-1.2 V for Fe) and current range (0 to 0.7µA for Mn and 0 to 0.8µA for Fe) was chosen for linear fit and extraction of parameters. Dark *J-V* characteristics (Figure 15a) shows that the current for Mn devices is 10 times higher compared to Fe devices at all the voltages. However, Fe devices exhibit a better rectification in the reverse bias. Series resistance values extracted from Figure 15b, shows a lower series resistance for Mn devices.

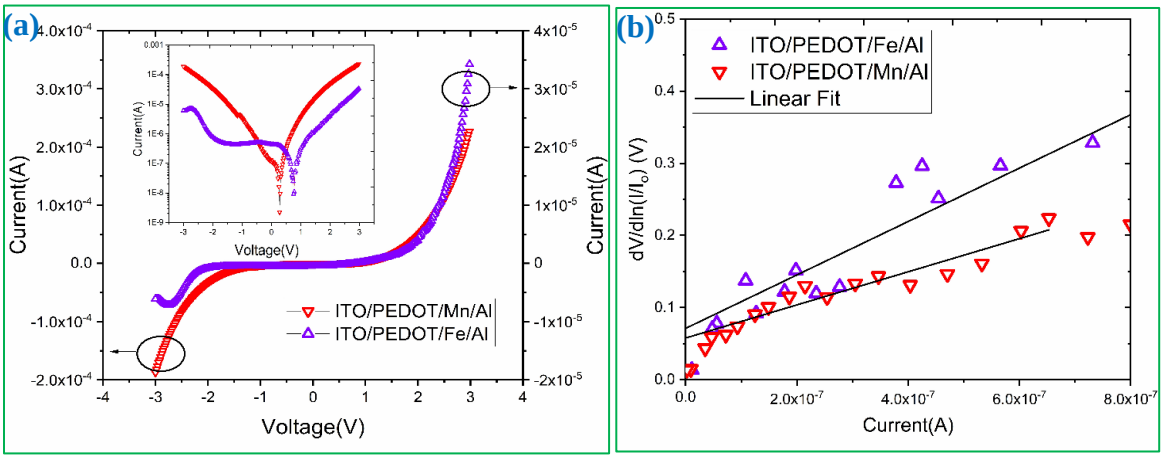

Figure 15. (a) *J-V* characteristics under dark conditions for Schottky junction diodes with Mn and Fe compound as active material. Corresponding plot in log-scale is shown in the inset, **(b)** $dV/d\left(\ln\frac{I}{I_0}\right)$ versus current (I) plot for both the devices with the linear fit (solid black lines) over a selected range of data,

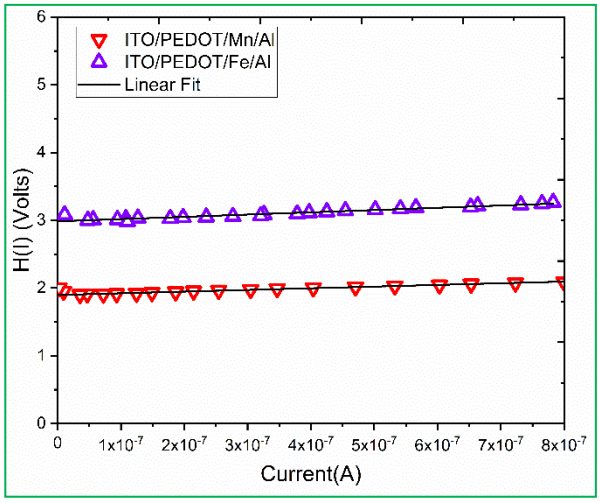

Figure 16. $H(I)$ versus I plot for both the devices with the linear fit (solid black lines).

Table 7. Summary of device parameters of Mn and Fe compound-based Schottky-diode devices.

Device Structure	Series resistance R_s(MΩ)		Ideality factor (η)	Barrier height φ_B (eV)
	From $dV/d\left(\ln\frac{I}{I_0}\right)$ vs I	From$H(I)$ vs I		
ITO/PEDOT/Mn/Al	0.22 ± 0.02	0.24 ± 0.004	1.93	0.97
ITO/PEDOT/Fe/Al	0.37 ± 0.04	0.33 ± 0.01	2.71	1.09

Schottky barrier height also reduces. However, the ideality factor increases significantly and becomes >2. This deviation from ideal thermionic emission type characteristics ($\eta \approx 1$ to 2) is quite common in most of the disordered materials and can be attributed to carrier mobility, existence of surface sates and recombination at the surface characterized by reduced surface recombination velocity.[67]

3.4. CONCLUSION

In conclusion, we successfully synthesized two isostructural 2D coordination polymers utilizing redox-active metal ions, Fe(II) and Mn(II), along with 1,4-phenylenediacetate (PDA) and 1,4-bis(4-pyridyl)-2,3-diaza-1,3-butadiene (4-bpdb) ligands. Single-crystal X-ray analysis revealed the structures, showcasing a three-dimensional supramolecular arrangement achieved through *AAA*... layer stacking. The vacant spaces created by this arrangement were occupied by non-bonded 4-bpdb molecules, stabilized via N-H···O hydrogen bonding and π···π interactions. Supercapacitor studies on compounds **1**(Mn) and **2**(Fe) exhibited favorable capacitive behavior within an H_2SO_4 electrolyte system, revealing specific capacitance values of 174.3 F/g and 72.3 F/g, respectively. The observed higher specific capacitance in **1**(Mn) correlated well with its larger BET surface area compared to **2**(Fe). Remarkably, **1**(Mn) demonstrated 78% capacitance retention after 5000 cycles, while **2**(Fe) displayed outstanding cycling stability with 98% retention. These retention differences were attributed to the disproportionation nature of the Mn(III) state. Conductivity measurements highlighted the distinct conductive properties of the compounds, with **1**(Mn) exhibiting approximately 10 times higher conductivity than **2**(Fe). Furthermore, the promising outcomes in Schottky diode fabrication for both compounds indicated their potential for diverse electronic applications. In summary, our findings underscore the significant influence of individual metal ions within the isostructural coordination polymers on their differential supercapacitor and conductive properties, providing valuable insights for future functional material design.

REFERENCES

1. M. Liu, M. F. Gao, X. F. Ren, F. N. Meng, Y. N. Yang, L. G. Gao, Q. Y. Yang, T. L. Ma, *J. Mater. Chem. A*, 2020, **8**, 3541–3562.
2. X. Zou, Y. Zhang, *Chem. Soc. Rev.*, 2015, **44**, 5148 – 5180.
3. J. Zhao, H. Li, C. Li, Q. Zhang, J. Sun, X. Wang, J. Guo, L. Xie, J. Xie, B. He, Z. Zhou, C. Lu, W. Lu, G. Zhu, Y. Yao, *Nano Energy*, 2018, **45**, 420 – 431.
4. D. W. Feng, T. Lei, M. R. Lukatskaya, J. Park, Z. H. Huang, M. Lee, L. Shaw, S. C. Chen, A. A. Kulkarni, A. Yakovenko, J. P. Xiao, K. Fredrickson, J. B. Tok, X. D. Zou, Y. Cui, Z. A. Bao, *Nat. Energy*, 2018, **3**, 30–36.
5. Z. Jin, A. J. Bard, *Proc. Natl. Acad. Sci. USA*, 2020, **117**, 12651 – 12656.
6. P. Li, Z. Jin, Y. Qian, Z. Fang, D. Xiao, G. Yu, *ACS Energy Lett.*, 2019, **4**, 1793 – 1802.
7. L. Tang, X. G. Meng, D. H. Deng, X. H. Bao, *Adv. Mater.*, 2019, **31**, 1901996.
8. Y. Wang, Y. Song, Y. Xia, *Chem. Soc. Rev.*, 2016, **45**, 5925−5950.

9. Y. Xiao, W. Wei, M. Zhang, S. Jiao, Y. Shi and S. Ding, *ACS Appl. Energy Mater.*, 2019, **2**, 2169−2177.
10. T. Kou, B. Yao, T. Liu, Y. Li, *J. Mater. Chem. A*, 2017, **5**, 17151−17173.
11. Y. Yang, M.-L. Li, J.-N. Lin, M.-Y. Zou, S.-T. Gu, X.-J. Hong, L.-P. Si, Y.-P. Cai, *Inorg. Chem.*, 2020, **59**, 2406−2412.
12. A. Borenstein, O. Hanna, R. Attias, S. Luaski, T. Brousse and D. Aurbach, *J. Mater. Chem. A*, 2017, **5**, 12653-12672.
13. D. Zheng, H. Wen, X. Sun, X. Guan, J. Zhang, W. Tian, H. Feng, H. Wang, Y. Yao, *Chem. -Eur. J.*, 2020, **26**, 17149 – 17155.
14. A. Bavykina, N. Kolobov, I. S. Khan, J. A. Bau, A. Ramirez, *Chem. Rev.*, 2020, **120**, 8468−8535.
15. J. Y. Lee, O. K. Farha, J. Roberts, K. A. Scheidt, S. B. T. Nguyen, J. T. Hupp, *Chem. Soc. Rev.*, 2009,**38**, 1450-1459.
16. J. F. Oloruyomi, S. T. Geh, R. A. Caruso, C. M. Doherty, *Mater. Horiz.*, 2021,**8**, 2387-2419.
17. Y. Takashima, V. M. Martinez, S. Furukawa, M. Kondo, S. Shimomura, H. Uehara, M. Nakahama, K. Sugimoto, S. Kitagawa, *Nat. Commun.*, 2011, **2**, 168.
18. Y. Guo, X. Feng, T. Han, S. Wang, Z. Lin, Y. Dong, B. Wang, *J. Am. Chem. Soc.*, 2014, **136**, 15485-15488.
19. J.-R. Li, R. J. Kuppler, H.-C. Zhou, *Chem. Soc. Rev.*, 2009, **38**, 1477-1504.
20. R. Banerjee, H. Furukawa, D. Britt, C. Knobler, M. O'Keeffe, O. M. Yaghi, *J. Am. Chem. Soc.*,2009, **131**, **11**, 3875-3887.
21. M. Eddaoudi, J. Kim, N. Rosi, D. Vodak, J. Wachter, M. O'Keeffe, O. M. Yaghi, *Science*, 2002, **295**, 469-472.
22. E. Linnane, S. Haddad, F. Melle, Z. Mei and D. Fairen-Jimenez, *Chem. Soc. Rev.* 2022, **51**, 6065-6086.
23. L. S. Xie, G. Skorupskii and M. Dincă, *Chem. Rev.*,2020, **120**, 16, 8536−8580.
24. X. Liu, C. Shi, C. Zhai, M. Cheng, Q. Liu and G. Wang, *ACS Appl. Mater. Interfaces*, 2016, **8**, **7**, 4585–4591.
25. X. Zhao, K. Tao and L. Han, *Nanoscale*. 2022, **14**, 2155-2166.
26. D. Tian, C. Wang, X. Lu, *Adv. Energy Sustainability Res.*,2021, **2**, 2100024.
27. Y. Wang, Y. Liu, H. Wang, W. Liu, Y. Li, J. Zhang, H. Hou, J. Yang, *ACS Appl. Energy Mater.*, 2019, **2**, 2063−2071.
28. D. Sheberla, J. C. Bachman, J. S. Elias, C.-J. Sun, Y. Shao-Horn, M. Dinca, *Nature Mater*, 2017, **16**, 220–224.
29. L. Wang, X. Feng, L. Ren, Q. Piao, J. Zhong, Y. Wang, H. Li, Y. Chen, B. Wang, *J. Am. Chem. Soc.*,2015, **137**, 4920−4923.
30. Y. Yan, P. Gu, S. Zheng, M. Zheng, H. Pang, H. Xue, *J. Mater. Chem. A*, 2016, **4**, 19078-19085.

31. S. Sanati, R. Abazari, A. Morsali, A. M. Kirillov, P. C. Junk, J. Wang, *Inorg. Chem.*, 2019, **58**, 16100−16111.
32. W, Li, X. Zhao, Q. Bi, Q. Ma, L. Han and K. Tao, *Dalton Trans*., 2021, **50**, 11701-11710.
33. X. Zhang, N. Qu, S. Yang, D. Lei, A. Liu and Q. Zhou, *Mater. Chem. Front.*, 2021, **5**, 482-491.
34. J. Yang, Z. Ma, W. Gao and M. Wei, *Chem. Eur. J*., 2017, **23**, 631 – 636.
35. X. Liu, C. Shi, C. Zhai, M. Cheng, Q. Liu, G. Wang, *ACS Appl. Mater. Interfaces*, 2016, **8**, 4585−4591.
36. K. M. Choi, H. M. Jeong, J. H. Park, Y.-B. Zhang, J. K. Kang, O. M. Yaghi, *ACS Nano*, 2014, **8**, 7451-7457.
37. S. Bi, H. Banda, M. Chen, L. Niu, M. Chen, T. Wu, J. Wang, R. Wang, J. Feng, T. Chen, M. Dincă, A. A. Kornyshev, G. Feng, *Nature Materials*, 2020, **19**, 552–558.
38. S. L. Xie, G. Skorupskii, and M. Dinca, *Chem. Rev*. 2020, **120**, 8536−8580.
39. M. E. Johnson, S. Ilic, and J. A. Morris, *ACS Cent. Sci*. 2021, **7**, 445−453.
40. A. Nath, K. S. Asha, and S. Mandal, *Chem. Eur. J*. 2021, **27**, 11482–11538.
41. L. B. Zasada, L. Guio, A. A. Kamin, D. Dhakal, M. Monahan, G. T. Seidler, C. K. Luscombe, and D. J. Xiao, *J. Am. Chem. Soc.* 2022, **144**, 4515−4521
42. B. Bhattacharya, A. Layek, Md. M. Alam, D. K. Maity, S. Chakrabarti, P. P. Ray and D. Ghoshal, *Chem. Commun.*, 2014, **50**, 7858.
43. S. Halder, A. Dey, A. Bhattacharjee, J. Ortega-Castro, A. Frontera, P. P. Ray and P. Roy, *Dalton Trans.*, 2017, **46**, 11239.
44. L. -A. Cao, M. -S. Yao, H. -J. Jiang, S. Kitagawa, X. -L. Ye, W. -H. Lia, and G. A. Xu, *J. Mater. Chem. A*, 2020, **8**, 9085.
45. C. Das, V. D. Patel, D. Gupta, and P. Mahata., *Cryst. Growth Des.*, 2022, **22**, 12, 7050–7061.
46. A. De, O. Basu, T. Basu, and R. Mondal, *Cryst. Growth Des.*, 2021, **21**, 1461−1472.
47. K. S. Das, B. Pal, S. Saha, S. Akhtar, A. De, P. P. Ray and R. Mondal, *Dalton Trans*., 2020, **49**, 17005.
48. P. Manna, A. K. Chandra, V. D. Patel, D. Gupta, and P. Mahata, *Cryst. Growth Des.*, 2022, **22**, 4559−4569.
49. S. Saha, K. S. Das, P. Pal, S. Hazra, A. Ghosh, S. Bala, A. Ghosh, A. K. Das, and R. Mondal, *Inorg. Chem.*, 2023, **62**, 3485−3497.
50. A. Hossain, A. Dey, S. K. Seth, P. P. Ray, P. Ballester, R. G. Pritchard, J. Ortega-Castro, A. Frontera, and S. Mukhopadhyay, *ACS Omega*, 2018, **3**, 9160−9171.
51. M. Shit, A. K. Karan, D. Sahoo, N. B. Manik, B. Dutta and C. Sinha, *New J. Chem*., 2023, **47**, 5922.
52. P. Ghorai, A. Dey, P. Brandão, J. Ortega-Castro, A. Bauza, A. Frontera, P. P. Ray and A. Saha, *Dalton Trans.*, 2017, **46**, 13531.
53. A. R. Kennedy, K. G. Brown, D. Graham, J. B. Kirkhouse, M. Kittner, C. Major, C. J. McHugh, P. Murdoch, W. E. Smith, *New J. Chem.*, 2005, **29**, 826–832.

54. *Apex3 v2017.3-0, Saint V8.38A, SAINT V8.38A*; Bruker AXS Inc.: Madison, WI, 2018.
55. L. Krause, R. Herbst-Irmer, G. M. Sheldrick, *Appl. Crystallogr.* 2015, **48**, 3.
56. A. Altomare, G. Cascarano, C. Giacovazzo, A. Guagliardi, *Completion and Refinement of Crystal Structures with SIR92. J. Appl. Crystallogr.* 1993, **26**, 343.
57. G. M. Sheldrick, *Crystal Structure Refinement with SHELXL. ActaCrystallogr., Sect. C: Struct. Chem.*,2015, **71**, 3.
58. L. J. Farrugia, *WinGX suite for Small-Molecule Single-Crystal Crystallography. J. Appl. Crystallogr.*,1999, **32**, 837.
59. A. L. Spek, *Single-Crystal Structure Validation with the Program PLATON. J. Appl. Crystallogr.,* 2003, **36**, 7.
60. B. E. Conway, Electrochemical supercapacitors: Scientific fundamentals and technological applications, Kluwer Academic/Plenum Publishers, New York, **1999**
61. P. Naskar, D. Kundu, A. Maiti, P. Chakraborty, B. Biswas, A. Banerjee, *ChemElectroChem,* 2021, **8**, 1393-1429.
62. P. Naskar, P. Chakraborty, D. Kundu, A. Maiti, B. Biswas, A. Banerjee, *ChemistrySelect*, 2021, **6**, 1127-1161.
63. P. Naskar, A. Maiti, P. Chakraborty, D. Kundu, B. Biswas, A. Banerjee, *J. Mater. Chem. A,* 2021, **9**, 1970-2017.
64. T. Brezesinski, J. Wang, J. Polleux, B. Dunn, S. H. Tolbert, *J. Am. Chem. Soc*. 2009, **131**, 1802-1809.
65. A. Banerjee, Y. Shilina, B. Ziv, J. M. Ziegelbaure, S. Luski, D. Aurbach, I. C. Halalay, *J. Am. Chem.Soc.*,2017,**139**, 1738-1741.
66. S. M. Sze, K. K. Ng, *Physics of Semiconductor Devices*, 3rd ed.; John Wiley & Sons, Inc: Hoboken, New Jersey, 2007.
67. T. Kirchartz, F. Deledalle, P. S. Tuladhar, J. R. Durrant, and J. Nelson, On the differences between dark and light ideality factor in polymer: fullerene solar cells. *J. Phys. Chem. Lett.* 2013, **4**, 2371.

CHAPTER-4

Isolation of a Cd-based Coordination Polymer Containing Mixed Ligands: Time and Temperature Dependent Synthesis, Sulfonamide Antibiotics Detection and Schottky Diode Fabrication

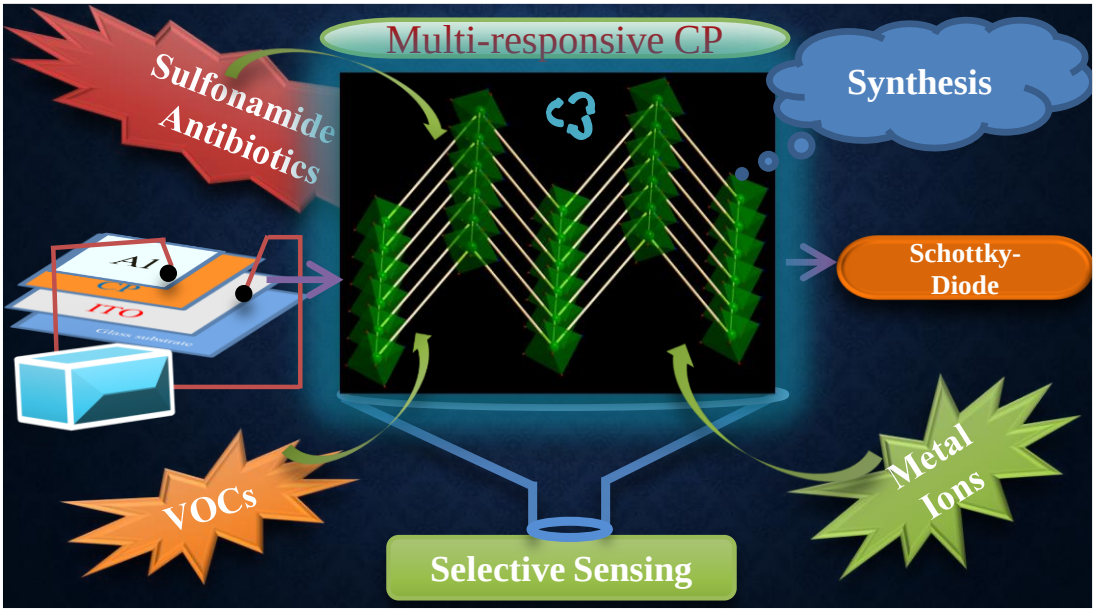

CHAPTER-4

Isolation of a Cd-based Coordination Polymer Containing Mixed Ligands: Time and Temperature Dependent Synthesis, Sulfonamide Antibiotics Detection and Schottky Diode Fabrication

4.1. INTRODUCTION

From the discovery of the first antibiotic penicillin in 1928 till the present-day antibiotics have played a crucial role in human medicine and the farming industry due to their potential application to prevent the growth and reproduction of several pathogens and their modified products have already been recognized and considered an important class of pollutants.[1-4] Till now, more than 160000 antibiotics have been developed and popularly used in many fields. Sulfonamide antibiotics are widely used as antimicrobial agents in aquaculture, animal husbandry and are successfully applied to treat human infectious diseases caused by bacteria and certain other microorganisms.[5] However, misuse of antibiotics can lead to the developing and promoting the spread of antibiotic-resistant genes (ARGs) and antibiotic-resistant bacteria (ARB), which have serious impact on human health and the ecosystem in the long term.[6-10] Therefore, keeping track of antibiotics in water has great importance to secure the environment and human health.[11] At present, there are some established analytical techniques[12-18] to detect the antibiotics in water such as liquid chromatography with UV detection (LC-UV), capillary electrophoresis (CE), liquid chromatography-tandem mass spectrometry (LC-MS), and Raman spectroscopy (RS). Most of these techniques are complicated, time-consuming, laborious, and expensive. Therefore, it is in demand to develop an easily accessible low-cost new facile method for detecting the antibiotics in water.

Since the last two decades, coordination polymers (CPs) have been emerged as important class of materials due to their large surface area, structural flexibility, high stability, and potential application in various fields including separation, magnetism, conductivity, gas storage, catalysis, recognition and sensing.[19-27] Fluorescent CPs are regarded as one of the most promising chemosensors because of their high sensitivity, short response time, simple and low-cost operation process.[28] So far, CP-based chemosensors have significant contributions in the field of environmental pollutants detection[29-33] such as heavy metals,[34,35] explosives,[36-37] and organic pollutants[38] but sensing of antibiotics in water by CPs is still in the developing stage.

Only a few fluorescent CP-based antibiotic sensors have been reported so far.[39-60] To the best of our knowledge there is only one CP has been reported so far which used in the fluorescent sensing of sulfonamide antibiotics.[60] Hence, this sustained us to further develop CP-based novel sensing materials for efficiently detecting sulfonamide antibiotics in water.

Electrically conductive coordination polymers (CPs) have garnered significant attention due to their wide range of applications. They are actively explored as active materials in electrocatalysis, chemiresistive sensing, and energy storage technologies.[61-62] Overcoming the challenges associated with creating conductive CPs, especially those suitable for manufacturing electronic devices, presents both obstacles and promising opportunities in this rapidly evolving field.[63-64]

In line with this objective, our research expedition aimed to develop a novel coordination polymer with exceptional stability. Through the utilization of a solvothermal method, we have successfully synthesized a cadmium-based luminescent coordination polymer [Cd(L)(NA)(H_2O)] (L = Iminol form of N-nicotinoyl glycinate, NA = Nicotinate), **1**. The duration and temperature of the synthesis of compound **1** by solvothermal methods were established through the detailed time and temperature dependent studies (temperature: 80 to 140 °C; duration: one to five days). Formation of three different phases during the investigation is noteworthy. Among these, the compound **1** contain two linkers- iminol form of N-nicotinoyl glycinate (L) and nicotinate (NA) generated from the N-nicotinoyl glycine. The connectivity among the Cd^{2+} ions and the two generated linker formed a corrugated layer structure. The layers are stabilized through hydrogen bond interactions using the coordinated water molecules to give rise a three-dimensional supramolecular structure. Compound **1** displayed excellent ligand centered luminescent behaviours owing to d^{10} outer electron configuration of Cd(II). The highly water stable nature and luminescence quenching behaviour has been utilized for the detection of sulfonamide antibiotics in aqueous medium with limit of detection value as low as 226 ppb. Furthermore, the compound **1** was used for the fabrication of Schottky diode device and it showed promising values with respect to barrier height of 0.86 eV and ideality factor of 1.24.

4.2. EXPERIMENTAL SECTION

4.2.1. Materials

The required chemicals for the synthesis of compound **1** were $Cd(CH_3CO_2)_2$. $2H_2O$ (Sigma-Aldrich, 98%) and N-nicotinoyl glycine (TCI, 98%) and these chemicals were used as received. The chemicals used for the sensing experiment were benzene (Merck, 99%), toluene (Merck, 99%), chlorobenzene(Merck, ≥99%), 2-aminophenol (Sigma-Aldrich, 99%), sulfathiazole (Sigma-Aldrich, ≥98%), sulfachloropyridazine (Sigma-Aldrich, 98%), sulfamethazine (Sigma-Aldrich, ≥99%), sulfadiazine (Sigma-Aldrich, ≥99%), sulfaquinoxaline sodium salt (Sigma-Aldrich, ≥ 92%), sulfameter (Sigma-Aldrich, 97%), aluminium(III) nitrate nonahydrate (Merck, 95%), chromium(III) nitrate nonahydrate (Sigma-Aldrich, 99%), manganese(II) chloride tetrahydrate (Merck, 99%), iron(II) chloride (Sigma-Aldrich, ≥99%), copper(II) chloride dihydrate (Merck, 99%), cadmium(II) chloride monohydrate (Merck, 98%), lead (II) nitrate (Merck, 99%), mercury(II) chloride (Sigma-Aldrich, ≥99%), NaOH (Merck, 99%), HCl (Merck, 99%), acetonitrile anhydrous (Sigma-Aldrich, 99.8%). The water used was double distilled.

4.2.2. Synthesis of Single Crystals

The compound **1** was synthesized by employing the hydrothermal method. $Cd(CH_3CO_2)_2$. $2H_2O$ (1mM, 0.2719g), N-nicotinoyl glycine (N-NG) (0.5 mM, 0.0919g) were dissolved in 5 ml distilled water. Then the mixture was homogenized for 30 min at room temperature. After 30 min the homogenized solution was sealed in a 23 ml PTFE-lined stainless-steel autoclave and heated at 140°C for 72 hours. After 72 hours final product was obtained in the form of colorless block-shaped crystals. Crystals were filtered and washed with deionized water under a vacuum and dried under ambient conditions (yield 75% based on metal). Anal. calcd. for $C_{14}H_{13}N_3O_6$ Calc: C, 38.91%; H, 3.01% ; N, 9.72%. Found: C, 38.85%; H, 2.95%; N, 9.77%.

4.2.3. Single crystal X-ray diffraction

A single crystal with a suitable dimension was carefully selected under an optical microscope and mounted on a tiny glass fibre carefully. The diffraction data of the colorless block-shaped crystal of compound **1** were collected using a Bruker D8 Quest diffractometer. The instrument was equipped with a Mo Kα (λ = 0.71073Å) radiation source, and the operating voltage of the X-ray generator was 50 kV at 1 mA. The diffraction data were collected with a ω scan width of 0.5°. Three different settings of φ (0, 90, 180°) were used to collect the total 408 frames,

keeping a fixed sample-to-detector distance of 6.03 cm, and the detector position (2θ) was fixed at −25°. The initial indexing, final data sets, and cell refinements were handled by an APEX3 program, while a SAINTPLUS[65] program was utilized for the frame integration and final cell parameter calculation. The multiscan absorption data were corrected by a SADABS program.[66] We initially solved the structure by SIR 92,[67] and the full matrix least-squares method (SHELXL-2016[68]) was used further, which is present in the WinGx suite of programs (Version 1.63.04a).[69,70] With the help of Fourier maps, we successfully located all of the non-hydrogen atoms and refined them anisotropically. Finally, all of the hydrogen atoms were fixed at proper positions and incorporated into the refinement process. The details of the crystal data and final refinement are given in Table 1. CCDC: 2292270 contains the diffraction and crystallographic data for this paper. The Cambridge Crystallographic Data Center (CCDC) via www.ccdc.cam.ac.uk/data_request/cif can provide these data free of charge.

Table 1. Crystal data and structure refinement parameters for [Cd(L)(NA)(H_2O)], **1**.

Empirical formula	$C_{14}H_{13}CdN_3O_6$
Formula weight	431.67
Crystal system	Monoclinic
Space group	$P2_1/n$
a (Å)	8.019(4)
b (Å)	14.114(4)
c (Å)	13.386(5)
α (deg)	90
β (deg)	95.748(16)
γ (deg)	90
Volume (Å^3)	1507.4(10)
Z	4
T (K)	298(2)
ρcalc (g cm^{-3})	1.902
μ (mm^{-1})	1.487
θ range (deg)	2.102 to 27.091
λ (Mo Kα) (Å)	0.71073

R indices [I>2σ(I)]	R_1 = 0.0280, wR_2 = 0.0864
R indices (all data)	R_1 = 0.0307, wR_2 = 0.0988

$R_1 = \Sigma ||F_0|-|F_c|| / \Sigma |F_0|$; $wR_2 = \{\Sigma[w(F_0^2 - F_c^2)^2] / \Sigma[w(F_0^2)^2]\}^{1/2}$. $w = 1/[\sigma^2(F_0)^2 + (aP)^2 + bP]$, $P = [max.(F_0^2,0) + 2(F_c)^2]/3$, where a = 0.0385 and b = 2.2098

4.2.4. Powder X-ray diffraction.

Powder X-ray diffraction (PXRD) pattern of well ground sample was obtained from a Bruker D8 Advance X-ray diffractometer with Cu Kα radiation (λ= 1.5418 Å) in the 2θ range 5-50° and operated at 40 kV and 40 mA (Figure 1). The obtained X-ray diffraction (XRD) pattern of the sample suggests the presence of a new compound, referred to as compound **1**. The observed XRD pattern corresponds precisely to the simulated XRD pattern generated from the structure determined using single-crystal XRD. This agreement between the experimental and simulated patterns confirms that the compound **1** is entirely pure.

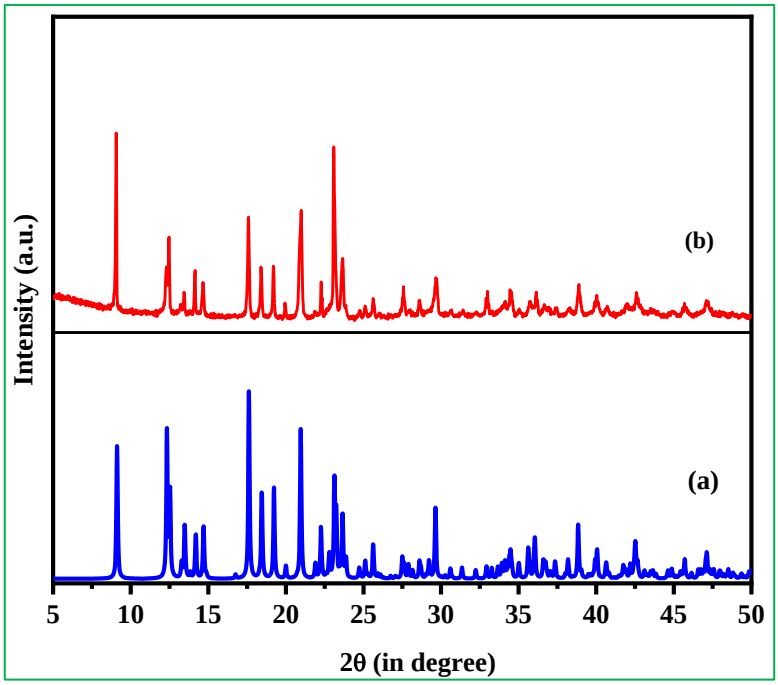

Figure 1. Powder XRD (CuKα) patterns of [Cd(L)(NA)(H_2O)], **1**: (a) simulated from single crystal X-ray data, (b) experimental.

4.2.5. FTIR measurements.

The Fourier-transform infrared (FT-IR) spectra were acquired using a Nicolet Magna IR 750 series-II instrument, covering a spectral range of 400-4000 cm^{-1} (Figure 2). The identified IR frequencies are documented in Table 2.

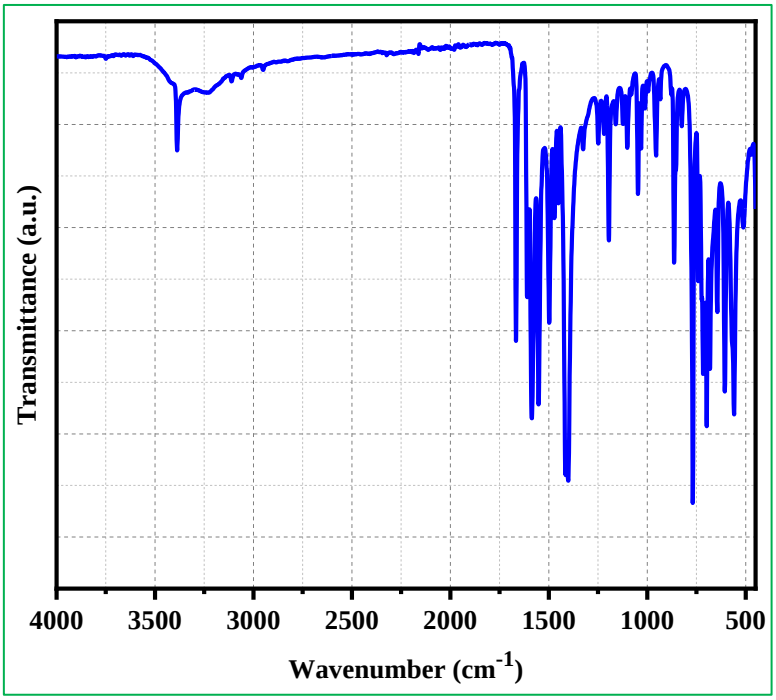

Figure 2. IR spectrum of [Cd(L) (NA)(H_2O)], **1**.

Table 2. The observed IR bands for [Cd(L)(NA)(H_2O)], **1.**

Bands	**Wavenumber (cm^{-1})**	**Bands**	**Wavenumber (cm^{-1})**
υ_{str}(O-H)	3386(s)	$\upsilon_{sy.\ str}$(carboxylate)	1413(s)
υ_{str}(H_2O)	3231(w)	υ_{str}(O-H bending)	1198(s)
$\upsilon_{asy.str}$(sp_2 C-H)	3103(w)	δ(aromatic C-H)$_{in\ plane\ bending}$	1152(s), 1063(s), 1018(w), 989(m)
$\upsilon_{asy.str}$(sp_3 C-H)	3062(w)	δ(aromatic C-H)$_{out\ of\ plane\ bending}$	944(m), 883(m), 800(w)
$\upsilon_{sy.str}$(sp_2 C-H)	2939(w)	υ_{str} (C=C)	1543(s)
$\upsilon_{asy.\ str}$(carboxylate)	1667(s)	δ(carboxylate)$_{bending}$	725(w), 691(w)
υ_{str} (C=N)	1590(s)	δ(aromatic C=C)$_{out\ of\ plane\ bending}$	668(s), 644(m)

4.2.6. Thermal Stability.

Thermogravimetric analysis (TGA) was performed using a Perkin-Elmer instrument, specifically the STA 6000 model. The analysis was conducted under a nitrogen atmosphere with a flow rate of 20 ml/min. The temperature range for the analysis was set from 30 to 800 °C, with a heating rate of 10 °C/min (Figure 3). The thermogravimetric analysis (TGA) results indicate that the compound remains stable up to a temperature of 315 ˚C. The initial weight loss (4.24%) observed in the temperature range 200 -255 °C corresponds to the loss of coordinated water molecules (calculated: 4.16%). The compound started to decompose at ~ 300 °C and the removal of the organic part has been completed at 620 °C. The total observed weight loss corresponds to 70% and it matches well with formation of CdO (calculated: 70.26%).

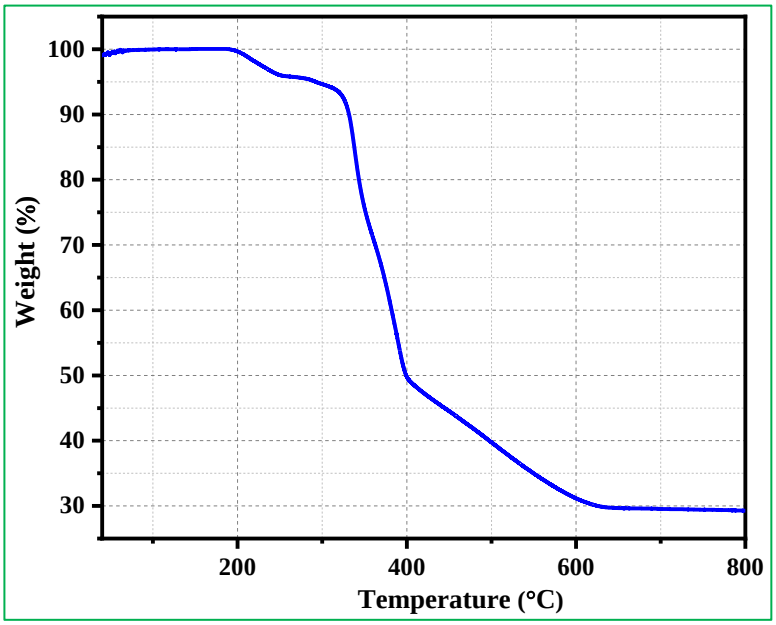

Figure 3. Thermogravimetric analysis (TGA) of [Cd(L)(NA)(H_2O)], **1,** in nitrogen atmosphere.

4.2.7. Photoluminescence Measurements.

The solution of compound **1** was prepared by introducing powder sample of compound **1** (3 mg) into 3 ml water. The photoluminescence measurements were performed using 100 µl of the stock solution in a 3 ml quartz cuvette diluted with 2 ml water. Photoluminescence properties of compound **1** were investigated at room temperature in water using a Horiba

fluoromax- 4 luminescence spectrofluorometer upon excited at 260 nm. The slit width was 5 nm for both excitation and emission. UV-Vis spectra of compound **1** (Figure 4) and analytes in water were recorded using UV-1900i UV-Vis spectrophotometer (Shimadzu).

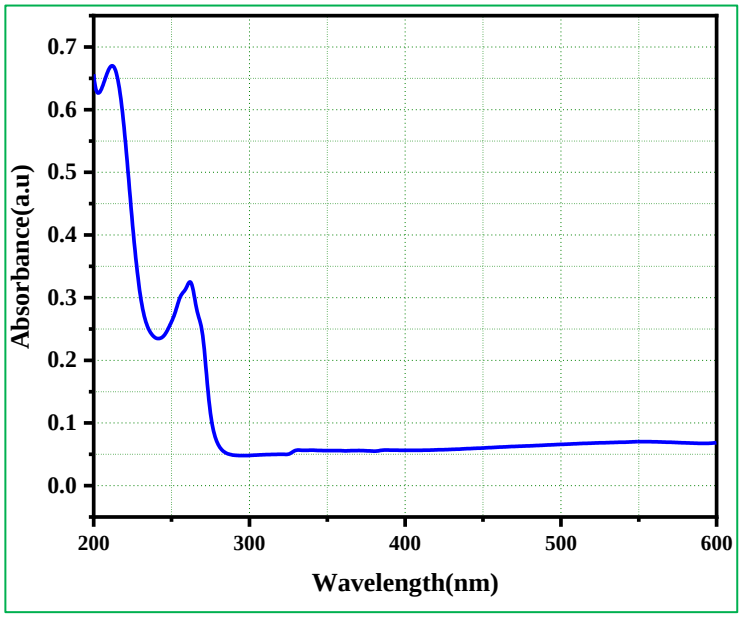

Figure 4. Absorption spectra of [Cd(L)(NA)(H_2O)], **1,** in aqueous medium**.**

4.2.8. Preparation of Antibiotic Stock Solutions.

In all cases 5 mM aqueous solution of sulfonamide antibiotics was prepared. As a standard procedure involving sulfachloropyridazine (SCP), a quantity of 7.19 mg of SCP was introduced to a 5 mL solution of NaOH (0.001 mol·L^{-1}). The mixture was then dissolved using magnetic stirring, resulting in a solution that served as a stock solution with a pH approximately equal to 8.0. Please note that antibiotics should be handled and disposed of with utmost caution.

4.2.9. Lifetime measurements.

Time correlated single photon counting (TCSPC) experiments were conducted at room temperature in water medium, employing a HORIBA Jobin Yvon instrument operating in the nanosecond time domain. In these TCSPC measurements, an excitation wavelength of 280 nm was utilized while the emission decay curve was monitored at 420 nm. Luminescence lifetime data were acquired using a Hamamatsu MCP photomultiplier (R3809). Subsequently, all

obtained decay curves were subjected to deconvolution and fitted with exponential functions using Origin software.

4.2.10. Electrochemical Characterizations.

The electrochemical characterization of compound **1** was conducted using a 3-electrode cell assembly with cyclic voltammetric (CV) analysis. The assembly consisted of a glassy carbon working electrode coated with previously grounded compound **1** as the active material, a platinum foil counter electrode, and an Ag/AgCl reference electrode. The glassy carbon working electrodes were prepared by drop-casting a slurry of the active material onto them. The slurry was made by homogeneously dispersing 2mg of compound **1** in 1ml of water, followed by 30 minutes of ultrasonication without the use of any binder. Subsequently, the slurry-coated working electrodes were dried at 60 °C for 3 hours in a hot air oven. We employed a blank glassy carbon electrode to assess the redox potentials of antibiotics. Measurements were conducted in a 1M Na_2SO_4 electrolyte medium by introducing antibiotic solutions. Electrochemical measurements were performed using a CHI600A electrochemical workstation (USA) at ambient temperature (25 °C).

4.2.11. Device Fabrication and Measurement.

Indium tin oxide (ITO) coated glass substrates were cleaned with soap solution followed by further cleaning of the substrate with distilled water in ultrasonicator for 15 to 20 minutes. ITO substrates were sonicated in acetone and isopropanol for 10 minutes each and after drying the substrate were treated in UV-Ozone chamber (Holmarc, India) for 45 minutes before coating the samples. The materials in proper concentration were dispersed in DMSO medium and ultrasonicated well to form a stable dispersed solution. For the fabrication of the device the prepared solution was drop casted on ITO substrate and further annealed at 150 ^{o}C in ambient air condition for 20 minutes on hot plate to dry up the solvent. The procedure of coating was repeated for few times so that we can get a good desired uniform thickness of film. The thickness of the drop casted film on ITO substrate was analysed using Bruker GT-Contour non-contact type optical profilometer and the film thickness was observed to be ~26µm (see ESI, Fig. S5). Device fabrication ITO/Compound **1**/Al was completed by slow evaporation of Al (0.2Å/s) through shadow mask under high vacuum ($\approx 10^{-5}$ mbar). Current voltage was

performed in air ambient using a source meter unit (Ossila) under dark condition in the voltage range +6V to -6 V.

4.3. RESULTS AND DISCUSSION

4.3.1. Structural Description

Compound **1** crystallized in a monoclinic crystal system with a $P2_1/n$ space group. The asymmetric unit of **1** consists of one crystallographically independent Cd^{2+} ion, one L ligand, one nicotinate and one coordinated water molecule (Figure 5a). The Cd^{2+} ion exhibits a distorted octahedral geometry though the coordination of three carboxylate oxygen atoms, two pyridyl nitrogen atoms and one coordinated water molecule (Figure 5b).

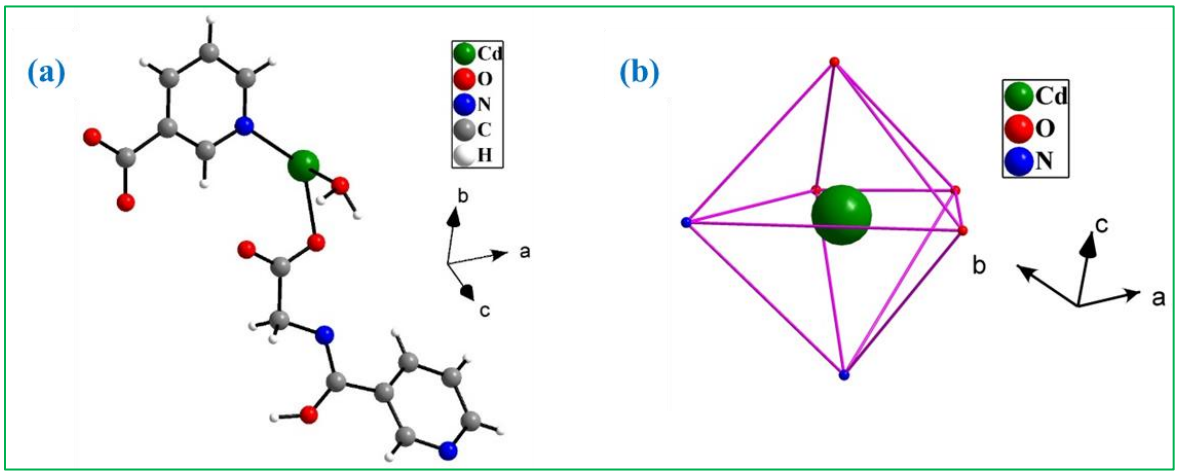

Figure 5. (a) Figure shows the asymmetric unit of [Cd(L)(NA)(H_2O)], **1**. **(b)** Distorted octahedral geometry around Cd^{2+} ions in **1**.

The L ligand connects the Cd^{2+} ions through carboxylate group (monodentate) and the nitrogen atom of the pyridine ring (Figure 6a). Whereas the nicotinate connects the Cd^{2+} ions through carboxylate group (bidentate) and the nitrogen atom of the pyridine ring (Figure 6b).

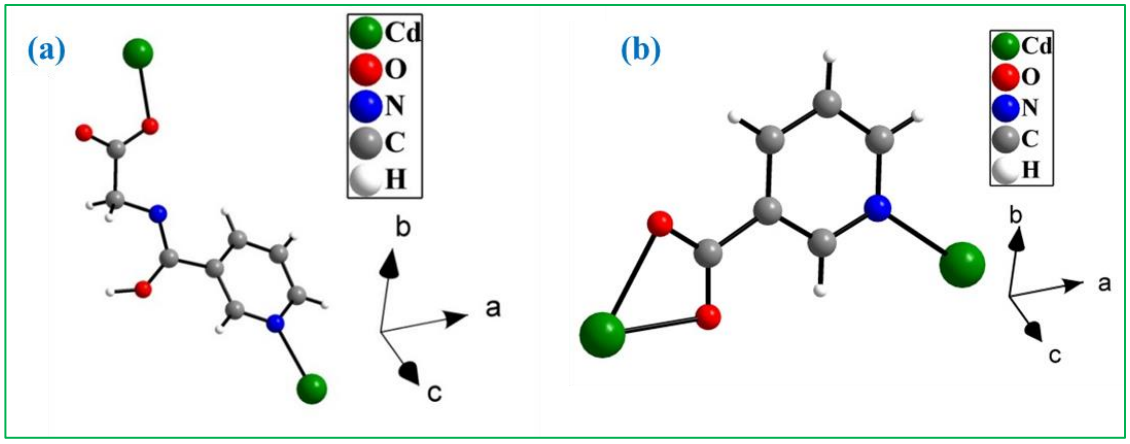

Figure 6. **(a)** Figure shows the coordination mode of L ligand in [Cd(L)(NA)(H_2O)], **1**. **(b)** Coordination mode of nicotinate.

The Cd−O bonds have an average distance of 2.35 Å and Cd-N bonds have an average distance of 2.34 Å. The O/N-Cd-N/O bond angles range 54.35(10) – 170.00(13)°. The selected bond distances are listed in Table 3 and the selected bond angles are listed in Table 4.

Table 3: Selected bond distances (Å) observed in [Cd(L)(NA)(H_2O)], **1**.

Bond	Distances, Å	Bond	Distances, Å
Cd(1)-O(1)	2.257(3)	Cd(1)-O(5)#1	2.361(3)
Cd(1)-O(6)	2.355(3)	Cd(1)-O(4)#1	2.449(3)
Cd(1)-N(2)	2.312(3)	Cd(1)-N(3)#2	2.376(4)

Symmetry transformations used to generate equivalent atoms: #1 x+1,y,z #2 x-1/2,-y+1/2,z-1/2

Table 4: Selected bond angles observed in [Cd(L)(NA)(H_2O)], **1**.

Angle	Amplitude (º)	Angle	Amplitude (º)
O(1)-Cd(1)-N(2)	135.56(11)	O(1)-Cd(1)-O(6)	88.29(12)
N(2)-Cd(1)-O(6)	88.32(11)	O(1)-Cd(1)-O(5)#1	82.11(10)
N(2)-Cd(1)-O(5)#1	142.31(10)	O(6)-Cd(1)-O(5)#1	94.06(12)
O(1)-Cd(1)-N(3)#2	86.99(13)	N(2)-Cd(1)-N(3)#2	88.89(12)
O(6)-Cd(1)-N(3)#2	170.00(13)	O(5)#1-Cd(1)-N(3)#2	94.01(13)
O(1)-Cd(1)-O(4)#1	136.37(11)	N(2)-Cd(1)-O(4)#1	87.99(11)
O(6)-Cd(1)-O(4)#1	96.55(12)	O(5)#1-Cd(1)-O(4)#1	54.35(10)
N(3)#2-Cd(1)-O(4)#1	92.94(13)		

Symmetry transformations used to generate equivalent atoms:#1 x+1, y , z #2 x-1/2, -y+1/2, z-1/2

The connectivity among Cd^{2+} ions, L ligands and nicotinate (NA) ligands formed two-dimensional structure (Figure 7a). The up and down connectivity of L ligands in alternate chains within the layer structure gave rise corrugated nature of the two-dimensional structure. The two-dimensional structure can be reduced to a corrugated grid type topology based on the Cd-Cd connectivity (Figure 7b).

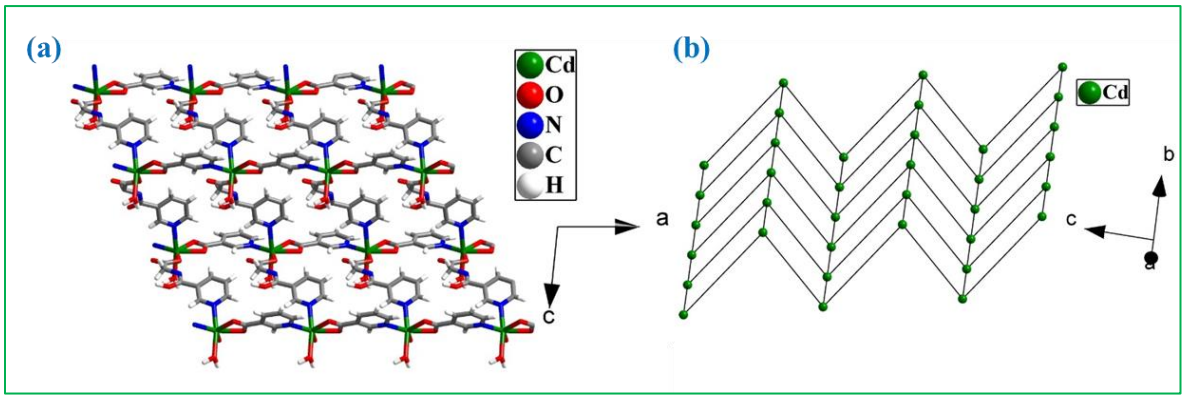

Figure 7. (a) Two-dimensional structure through the connectivity of Cd^{2+} ions with two ligands in **1**. **(b)** The Cd-Cd connectivity showing the corrugated nature of the layer.

The layers are organized in *ABABAB*…. fashion resulting in the formation of three-dimensional supramolecular structure (Figure 8a). The presence of hydrogen bond interactions played crucial role in connecting two-dimensional layers and facilitated the formation of three-dimensional supramolecular arrangement. In this arrangement, O – H···O hydrogen bonds were formed between the hydrogen atoms [H(6A)] of coordinated water molecules and the oxygen atoms [O(5)] of the carboxylate groups of nicotinate (NA). Another hydrogen bond interaction occurred between the hydrogen atom [H(6B)] of the coordinated water molecules and the oxygen atom [O(2)] of the carboxylate group of L ligands. Figure 8b illustrates the overall hydrogen bond interactions to form the three-dimensional supramolecular structure. All the details about the hydrogen bond interactions are summarized in Table 5.

Table 5: Summary of hydrogen-bond interaction observed in [Cd(L)(NA)(H_2O)], **1**.

D – H· ··A[a]	D – H (Å)	H· ··A (Å)	D· ··A (Å)	D – H· ··A (°)
O(6) – H(6A)· ··O5$^{\#1}$	0.95	1.97	2.8976(14)	167
O(6)–H(6B)· ··O(2)$^{\#2}$	0.95	1.87	2.8209(14)	175

[a] #1 = 1-x,1-y,1-z; #2 = 2-x,1-y,1-z

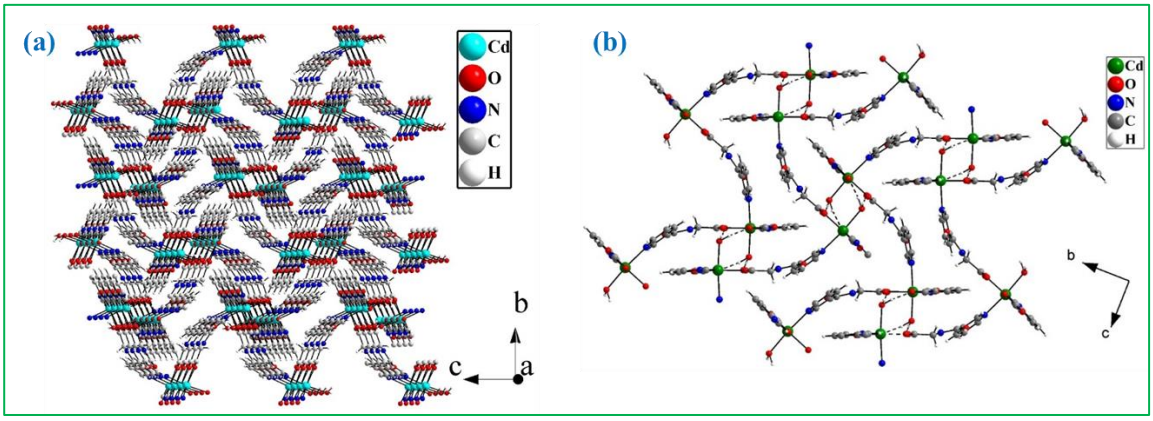

Figure 8. (a) Figure shows the three-dimensional packing arrangement of two-dimensional layers in **1**. **(b)** Figure shows the O – H···O hydrogen bond interactions to form three-dimensional supramolecular structure in **1**. The dotted lines indicate the hydrogen bonds.

4.3.2. Temperature and time dependence on the Synthesis.

Our synthesis procedure involved the *in-situ* synthesis of ligands from N-nicotinoyl glycine through hydrothermal method. The crystal structure of compound **1** revealed the presence of two linkers: iminol form of N-nicotinoyl glycine and nicotinic acid originated from N-nicotinoyl glycine. This intriguing aspect has motivated us to investigate further for the understanding of role of temperature and time in the hydrothermal method. Twenty different reactions were carried out from the reaction mixture of same composition. Four different temperature (80, 100, 120 and 140 °C) and five different reaction duration (1, 2, 3, 4 and 5 days) were set to identify the generated products. These variations led to the formation of different phases, including mixtures and pure phases, which were identified as phases I, II, and III (III = compound **1**) (Figure 9). Through a thorough analysis of the powder X-ray diffraction (XRD) patterns of the reaction products, all the products were identified through the comparison of their simulated XRD patterns. Out of these three products, two products (I and II)[71,72] was reported previously. In all the three phases, the ratio of metal ions and organic ligand are 1:2. The basic structures of all the three phases are shown in Figure 9. In phase I, $[Cd(C_8N_2O_3H_7)_2(H_2O)_2]$, the Cd^{2+} ions are eight coordinated and each Cd^{2+} ions are bonded with two water molecules. The connectivity between the Cd^{2+} ions and N-nicotinoyl glycinate formed two-dimensional layer structure. In phase II, $[Cd(C_8N_2O_3H_7)_2(H_2O)]\cdot 3H_2O$, the Cd^{2+} ions are seven coordinated and each Cd^{2+} ions are bonded with one water molecule. The connectivity between the Cd^{2+} ions and N-nicotinoyl glycinate formed one-dimensional structure. The presence of extra-framework water molecules stabilized the one-dimensional structure. In phase III (= compound **1**), $[Cd(C_8N_2O_3H_7)(C_6NO_2H_4)(H_2O)]$, the Cd^{2+} ions are six coordinated and each Cd^{2+} ions are bonded with one water molecule. The connectivity among Cd^{2+} ions, Iminol form of N-nicotinoyl glycinate, and nicotinate formed two-dimensional structure. Here both the ligands generated *in-situ* from the N-nicotinoyl glycine.

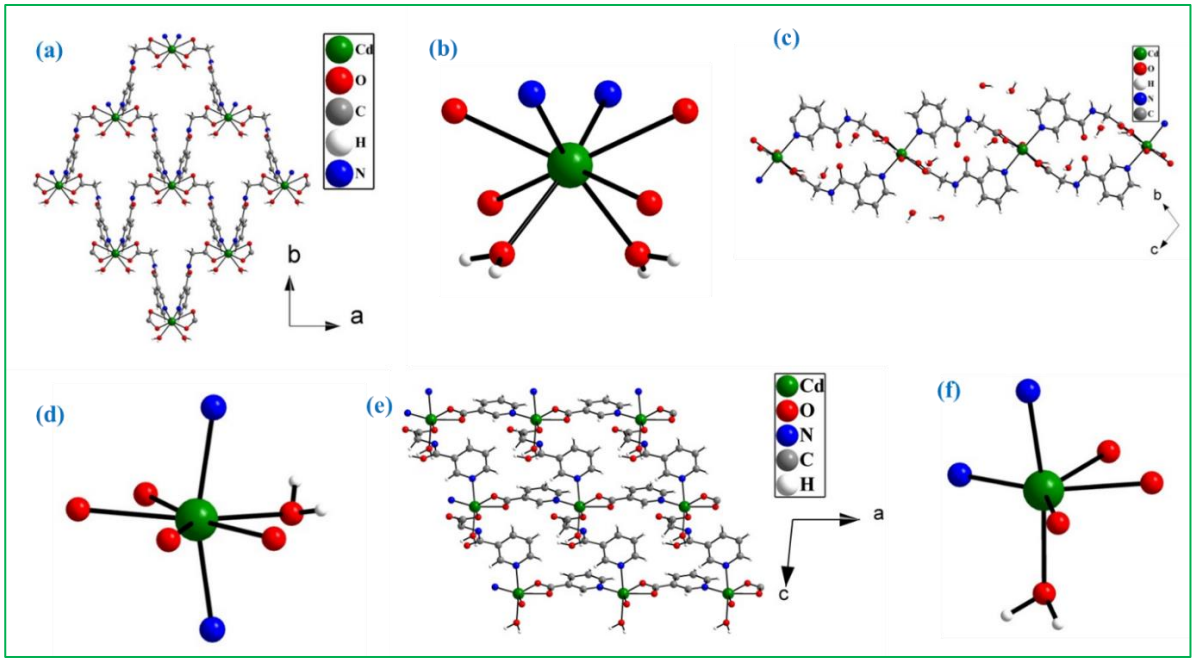

Figure 9. (a) Figure shows the two-dimensional structure of phase I, **(b)** eight coordination around Cd^{2+} ion in phase I. Note presence of two coordinated water molecules, **(c)** figure shows the one-dimensional structure of phase II, **(d)** seven coordination around Cd^{2+} ion in phase II. Note the presence of one coordinated water molecule, **(e)** figure shows the two-dimensional structure of phase II, **(f)** six coordination around Cd^{2+} ion in phase III. Note the presence of one coordinated water molecule.

At 80°C, phase I was formed in pure phase during all time durations. However, at 100°C with increasing duration, a mixture of phases II and III was observed. At 120°C, we observed the formation of two phases, I and III with phase I present as a pure phase at low reaction time and as a mixture with phase III at higher reaction time. When the reaction was conducted at 140°C for 2-5 days, phase III was obtained in a pure phase (Figure 10A, 10B, 10C, and 10D). The results are represented as two-dimensional temperature vs time plot in Figure 11.

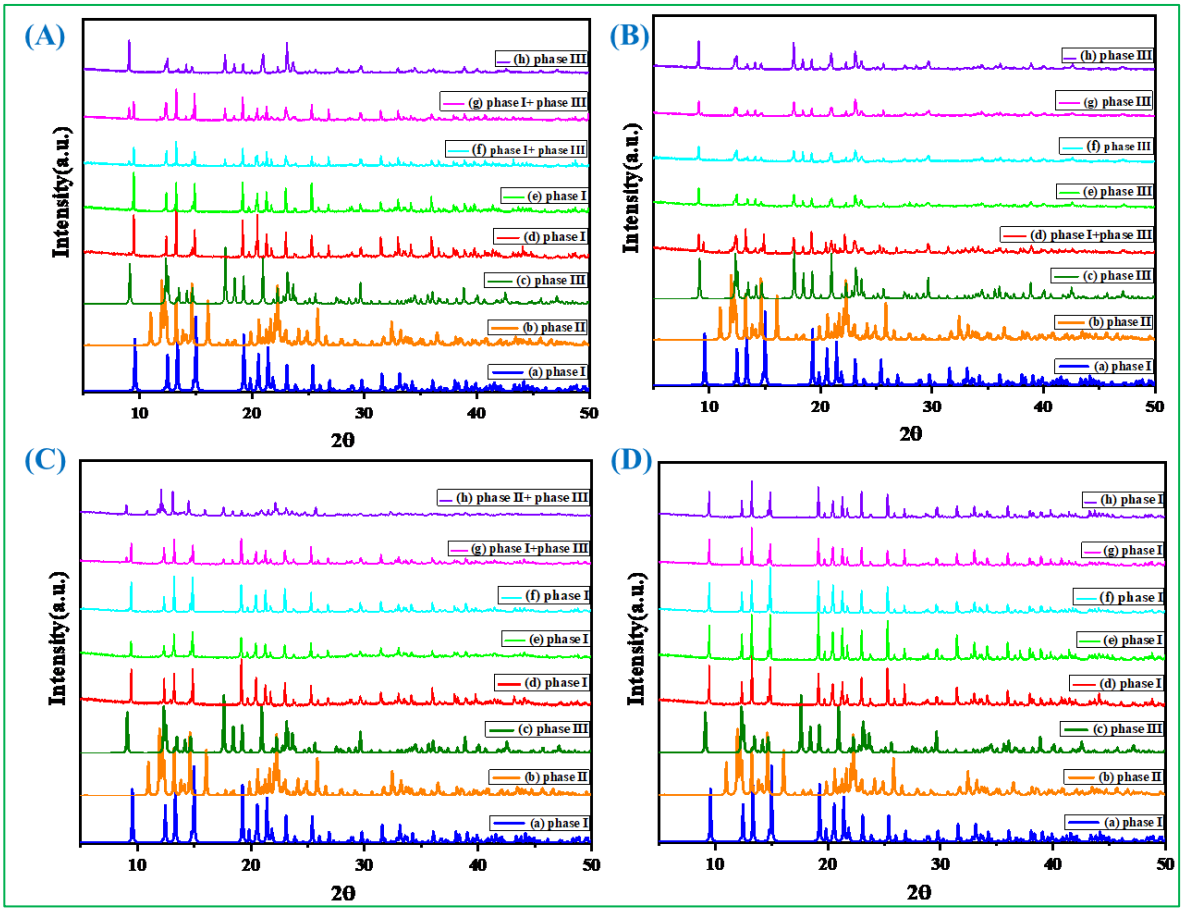

Figure 10. Powder XRD (CuKα) patterns of **(A)** 80°C, **(B)** 100°C **(C)** 120°C **(D)**140°C products at different duration: (a) simulated data of phase I, (b) simulated data of phase II (c) simulated data of phase III (d) one day (e) two days (f) three days (g) four days (h) five days.

An important observation from these studies was that the phases formed at lower temperatures had higher hydration levels. As the temperature increased, the compounds underwent dehydration, and the total water content decreased with longer reaction times. Additionally, the high temperature phase (III) contains the nicotinate ligand generated through the thermal decomposition of N-nicotinoyl glycine. These results open up new avenues for further exploration and understanding of the reaction mechanism with respect to thermodynamically and kinetically controlled product.

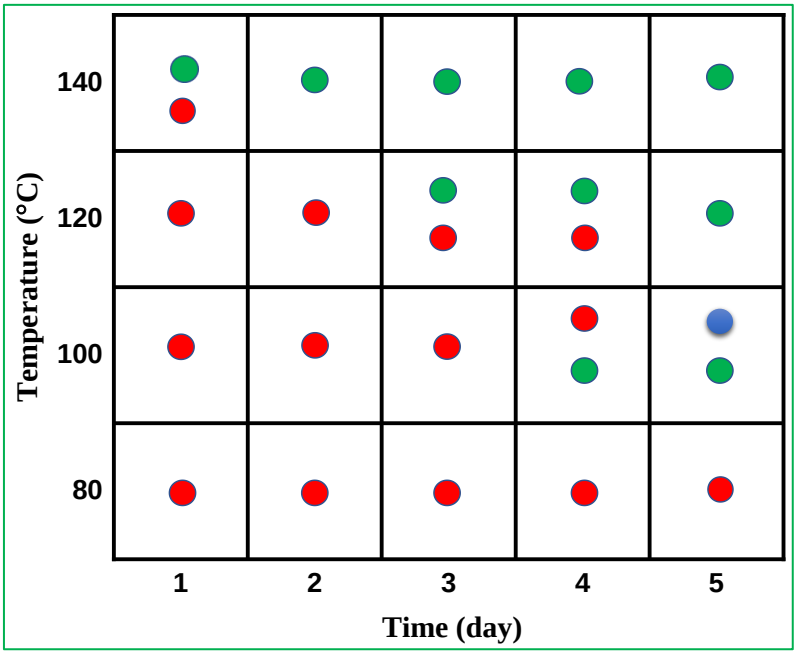

Figure 11. Temperature vs time plot of the formation of the three phases (I-III). The various phases were identified by comparing the powder XRD patterns with the simulated patterns generated from the single-crystal structure. Color code: I, red; II, blue; III, green.

4.3.3. Detection of antibiotics.

Fluorescence measurement was carried out for the aqueous dispersion of compound **1**. In aqueous medium compound **1** exhibited strong blue emission centered at 420 nm by the excitation at 260 nm. This emission can be assigned as ligand centered based on the similarity between the emission spectra of compound **1** and free ligands (Figure 12a). Emission quantum yield (QY) of compound **1** were determined by using pyrene (QY = 0.3 in heptane) as the standard sample and it was found 0.24 in water. The pH tolerance and water stability of the compound **1** was demonstrated by PXRD measurements of the compound **1** immersed in acid and base solutions (Figure 12b). After the acid and base treatment, the structure of compound **1** remained intact. The satisfactory match between simulated and experimentally obtained PXRD pattern confirmed the excellent water and pH stability of compound **1**.

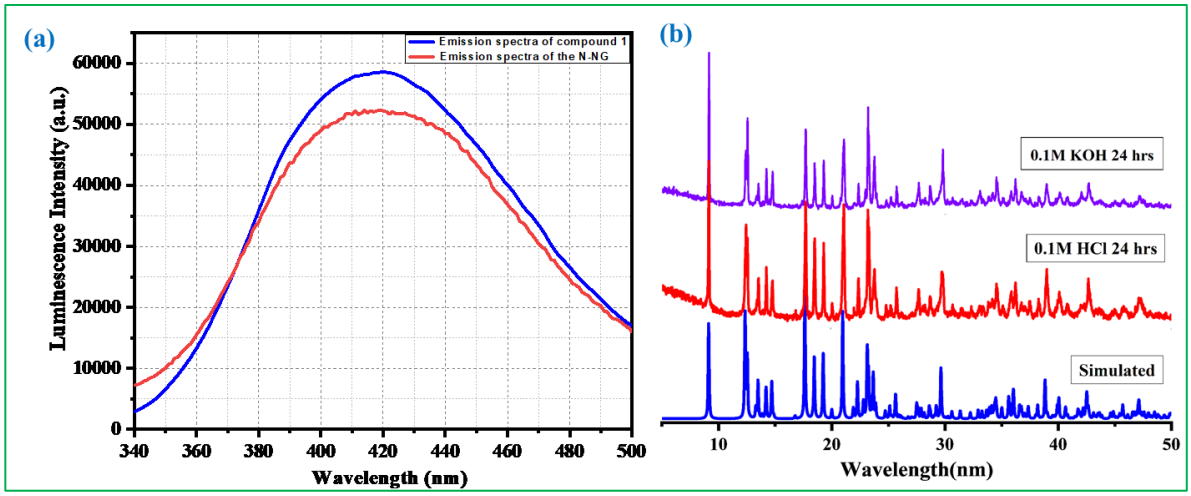

Figure 12. (a) Emission spectra of [Cd(L)(NA)(H_2O)], **1** upon excitation at 260 nm. **(b)** Powder XRD (CuKα) patterns of [Cd(L)(NA)(H_2O)], **1** after acid base treatments.

Owing to high water stability and excellent fluorescent nature of compound **1**, fluorescence-based sensing performance of compound **1** for monitoring the antibiotics in water was investigated. The sensing experiment were performed with six different sulfonamide antibiotics - sulfadiazine (SDZ), sulfamethazine (SMZ), sulfachloropyridazine (SCP), sulfameter (SM), sulfaquinoxaline (SQX), and sulfathiazole (STZ). In all the six cases significant luminescence quenching of compound **1** were observed. After preliminary screening, we have further repeated the sensing experiment to confirm the quenching phenomena and graphed the results (Figure 13a-13f).

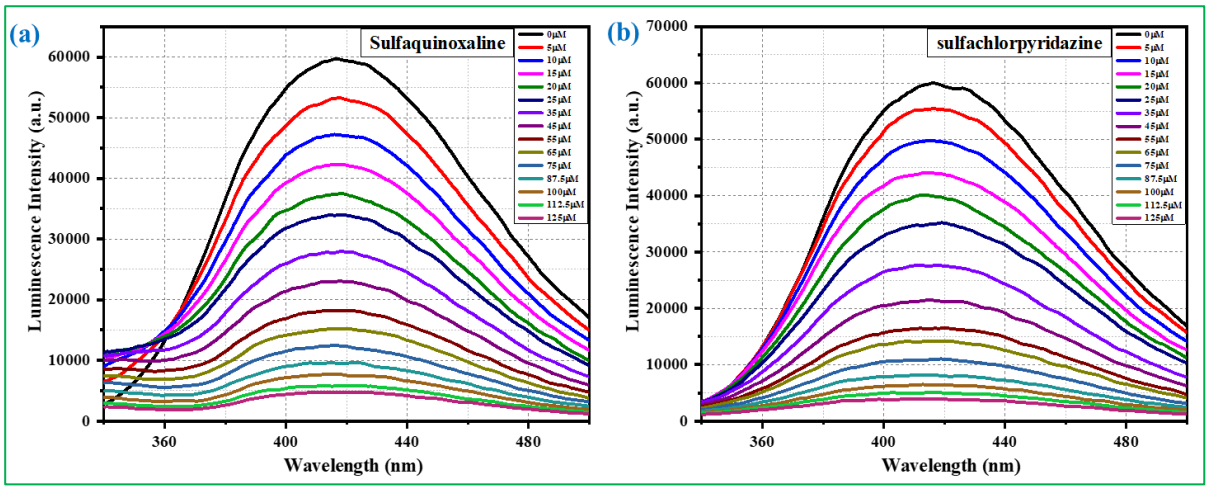

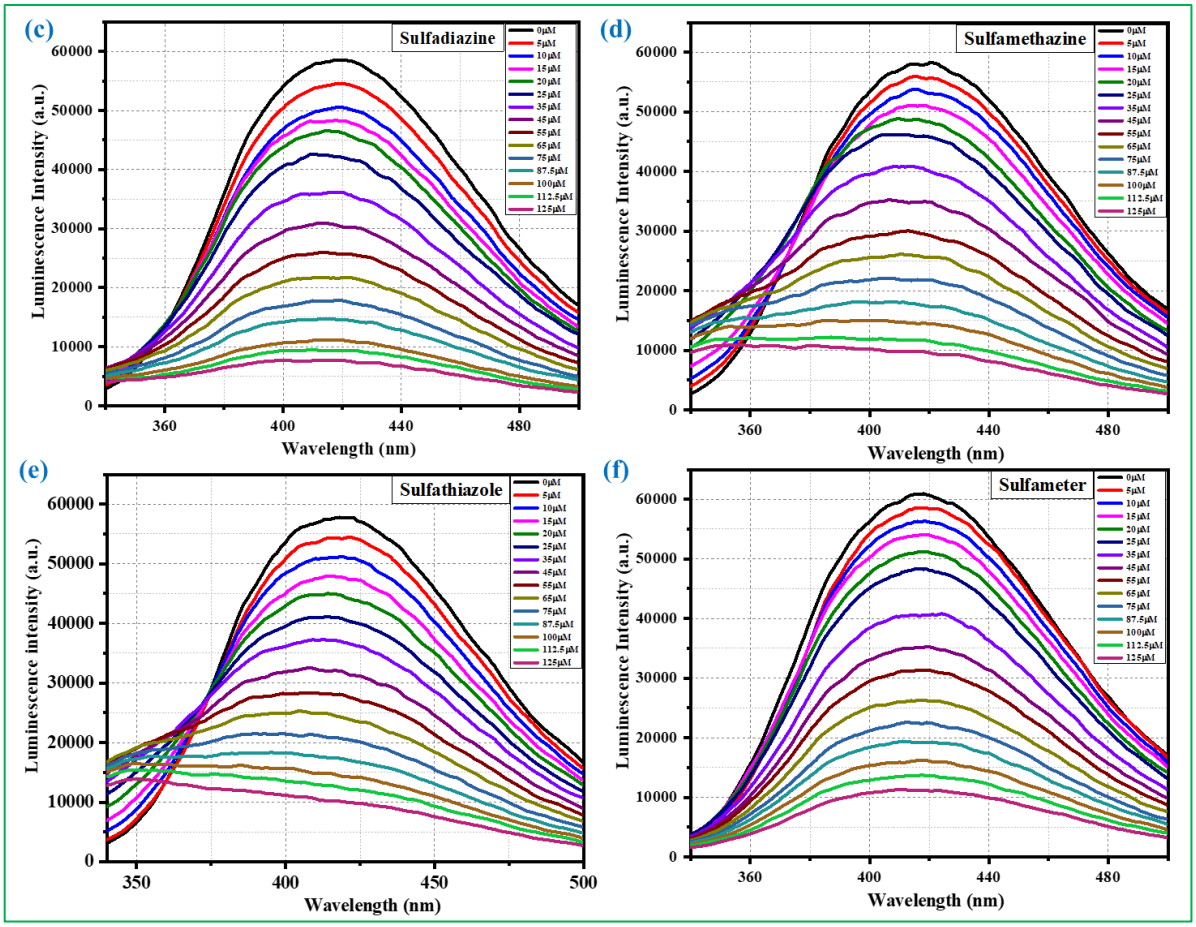

Figure 13. Emission spectra of **1** dispersed in water upon incremental addition of **(a)** sulfaquinoxaline **(b)** sulfachloropyridazine **(c)** sulfadiazine **(d)** sulfamethazine **(e)** sulfathiazole **(f)** sulfathiazole (λ_{ex} = 260 nm). The final concentration of sulfaquinoxaline in the medium is indicated in the legend.

The antibiotics exhibited the following order of luminescence quenching for compound **1**: SQX> SCP > SDZ > SMZ > STZ > SM (see figure 14a). Sensing ability of compound **1** towards metal ions and electron-rich volatile organic compounds (VOCs) were investigated. When compound **1** exposed to transition metals such as Al^{3+}, Cr^{3+}, Mn^{2+}, Fe^{2+}, Cu^{2+}, Cd^{2+}, Pb^{2+}, and Hg^{2+}, there was no significant change observed in the intensity of luminescence. Similarly, in the presence of VOCs such as benzene, toluene, chlorobenzene and 2-amino phenol, the luminescence intensity of compound **1** remained unchanged (representative plot shown in Figure 14b).

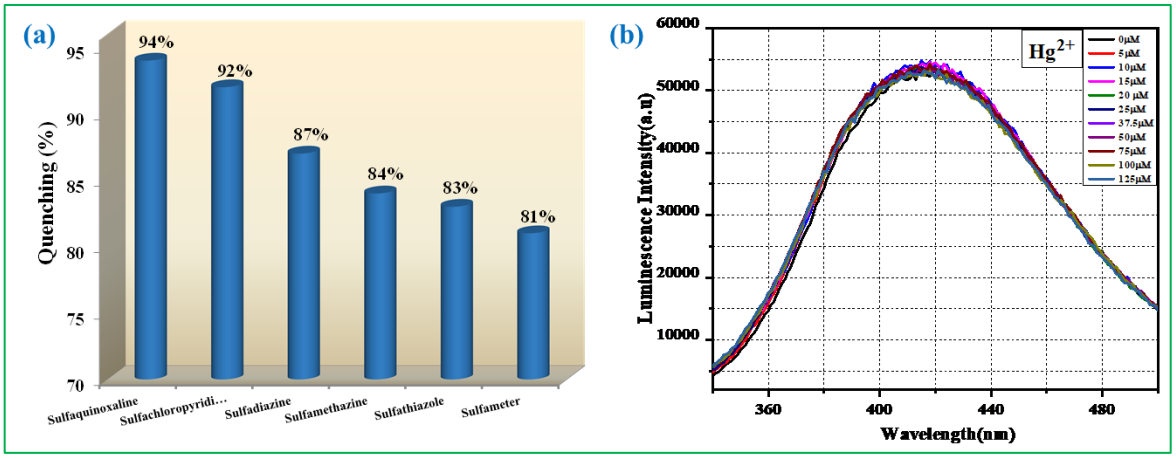

Figure 14. (a) Fluorescence quenching efficiency of aqueous dispersion of **1** for different sulfonamide antibiotics. **(b)** Emission spectra of **1** in aqueous dispersion upon incremental addition of aqueous solution of Hg^{2+} (λ_{ex} = 260 nm). Final concentration of Hg^{2+} in the medium is indicated in the legend.

These studies indicate compound **1** is highly selective for sulfonamide antibiotics (Figure 15a). Furthermore, the structural integrity and phase purity of the recovered compound **1** were confirmed by analyzing the PXRD patterns (Figure 15b). These patterns demonstrated that the compound remained unchanged in its structure and maintained its original phase composition.

To determine the limit of detection (LOD) for the antibiotics, we conducted luminescence turn-off titration experiments using ultralow concentrations of the antibiotics. The LOD was calculated using the equation LOD = 3σ/m, where σ represents the standard deviation of blank determination and m represents the slope of the linear curve plotted at the lower concentration for LOD measurements.[73]

The LOD values of compound **1** towards SQX, SCP, SDZ, STZ, SMZ and SM are calculated to be 226 ppb, 361.5 ppb, 345 ppb, 416 ppb, 576.64 ppb and 726 ppb respectively. Remarkably, the calculated LODs were found to be significantly below the reported limits of detection of well-known spectroscopic and analytical methods. Additionally, we performed linear fitting of the plots using the Stern-Volmer (S-V) equation to determine the quenching constant (Ksv) (Figure 16a)

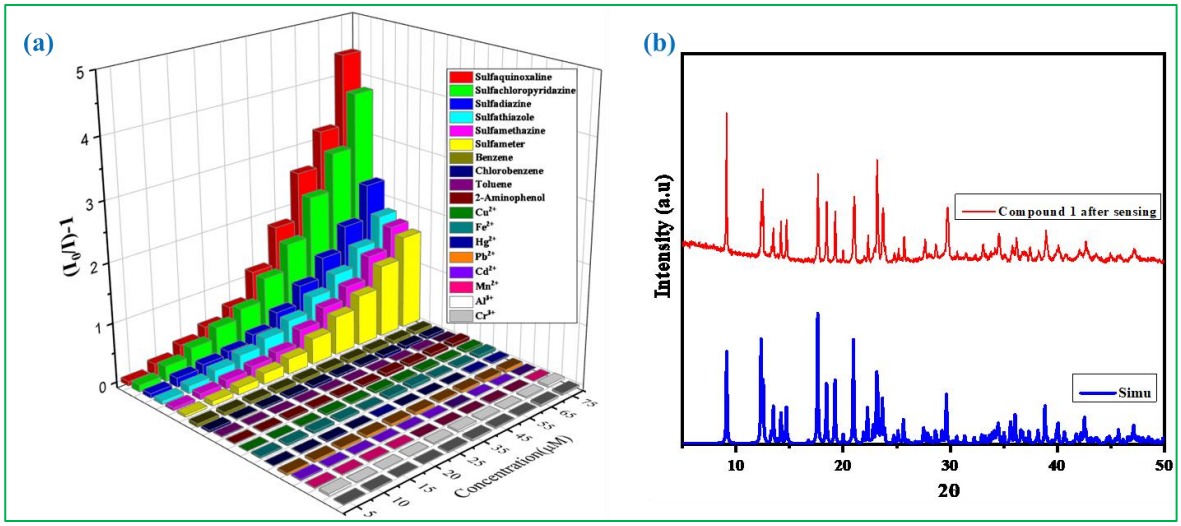

Figure 15. (a) Three-dimensional (I_0/I-1) vs concentration plot for all types of analytes (I_0 and I are the luminescence intensities before and after addition of the analyte, respectively). **(b)** Powder XRD (CuKα) patterns of [Cd(L)(NA)(H_2O)], **1** after sensing experiments.

(I_0/I) = K_{SV}[A] + 1, where K_{SV} is the quenching constant (M^{-1}), [A] is the molar concentration of the analyte, and I_0 and I are the luminescence intensities before and after addition of the analyte, respectively.[74] The calculated Ksv values were as follows: 3.03× 10^4 M^{-1} for sulfaquinoxaline, 2.78 × 10^4 M^{-1} for sulfachloropyridazine, 1.66 × 10^4 M^{-1} for sulfathiazole, 1.48 × 10^4 M^{-1} for sulfadiazine, 1.06 × 10^4 M^{-1} for sulfamethazine, and 1.0 × 10^4 M^{-1} for sulfameter.

The tolerance towards metal ions and VOCs is an important factor in evaluating the reliability of chemical sensors in waste water treatment. Therefore, we studied the fluorescent detection of sulfaquinoxaline antibiotics, a representative of sulfonamide antibiotics, using compound **1**. We examined its performance in the presence of different volatile organic compounds and the interference of various metal ions (Figure 16b).

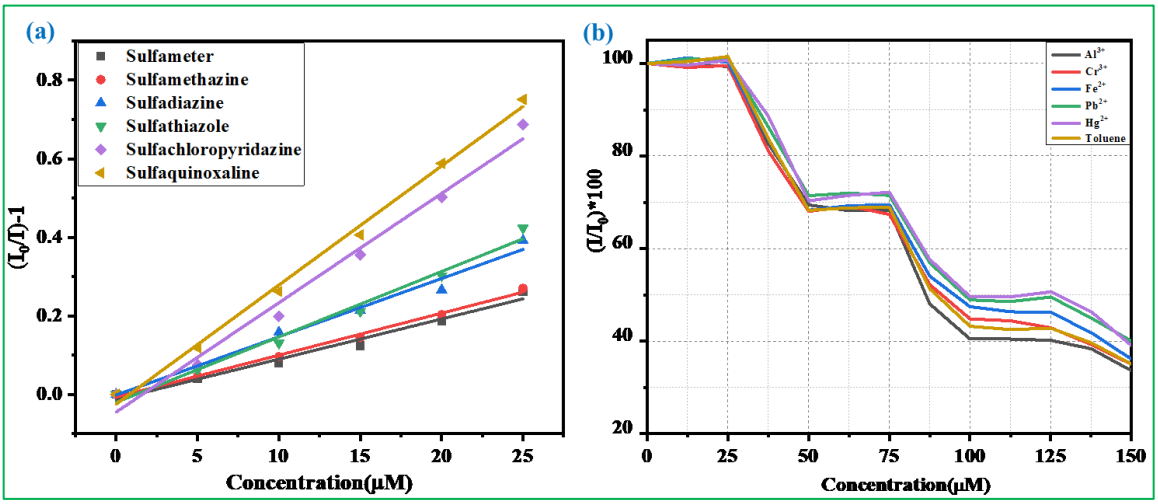

Figure 16. (a) Linear plot of the Stern-Volmer constant (Ksv) for sulfaquinoxaline, sulfachloropyridazine, sulfathiazole, sulfadiazine, sulfamethazine, and sulfameter in aqueous dispersion of **1**. **(b)** Plot showing the selective luminescence quenching response for sulfaquinoxaline in the presence of metal ions and VOCs. The added volume of analytes (SQX + Al^{3+}, SQX + Cr^{3+}, SQX + Fe^{2+}, SQX + Pb^{2+}, SQX + Hg^{2+} and SQX + toluene) solution: 25 μM metal ions/VOCs + 25 μM SQX and this pattern repeated up to 150 μM.

It was found that the quenching efficiency of compound **1** in the presence of the most common metal ions Al^{3+}, Cr^{3+}, Fe^{2+} including heavy metal ions, Pb^{2+}, Hg^{2+} remained nearly unchanged. Similarly, the quenching efficiency of compound **1** also remained unchanged in the presence of toluene (Figure 16b). These results indicate that compound **1** shows promising potential as a fluorescence sensor for detecting trace amounts of sulfonamide antibiotics in water, even in the presence of well-known metal-based quenchers.

To find out the exact quenching mechanism we have carried out the excited state lifetime measurements of the compound **1** in presence of sulfaquinoxaline antibiotics. From the lifetime experiment results it was found that the excited state life time of the compound **1** was decreased with increasing concentration of sulfonamide antibiotics and this result also merged well with the fluorescence quenching trend. In case of sulfaquinoxaline (SQX) we have observed the highest decrease in excited state life time (figure 17a) and in case of sulfameter (SM), sulfamethazine (SMZ) excited state luminescence lifetime of the compound **1** were almost halved. In case of sulfadiazine (SDZ), sulfachloropyridazine (SCP), and sulfathiazole

(STZ) a little decrease in luminescence lifetime was observed (Table 6). From the above discussed excited state lifetime measurement results it was confirmed that photo-induced electron transfer is the most plausible quenching mechanism for SQX, SMZ, and SM and have less contribution towards SCP, STZ, and SDZ. However, it is evident that an alternative or additional quenching mechanism may be at play. To explore this further, we conducted UV-Vis experiments for compound 1 and all sulfonamide antibiotics. Figure 17b illustrates the UV-Vis data for the selected antibiotics and compound **1**, highlighting their respective absorption spectra. Notably, a remarkable overlap is observed solely between the excitation band of compound **1** and the absorption band of sulfonamide antibiotics. Intriguingly, among these antibiotics, only sulfaquinoxaline exhibits a spectral overlap between its absorption spectrum and the emission spectrum of compound **1**. Building upon prior findings, it can be inferred that the most plausible quenching mechanism for SCP, STZ, and SDZ, involves an energy competition between the sulfonamide antibiotics and compound **1** in an aqueous environment like in previous reports.[2,4,40-49] Additionally, in the case of SQX, SMZ, and SM, energy competition could potentially contribute as an additional factor.

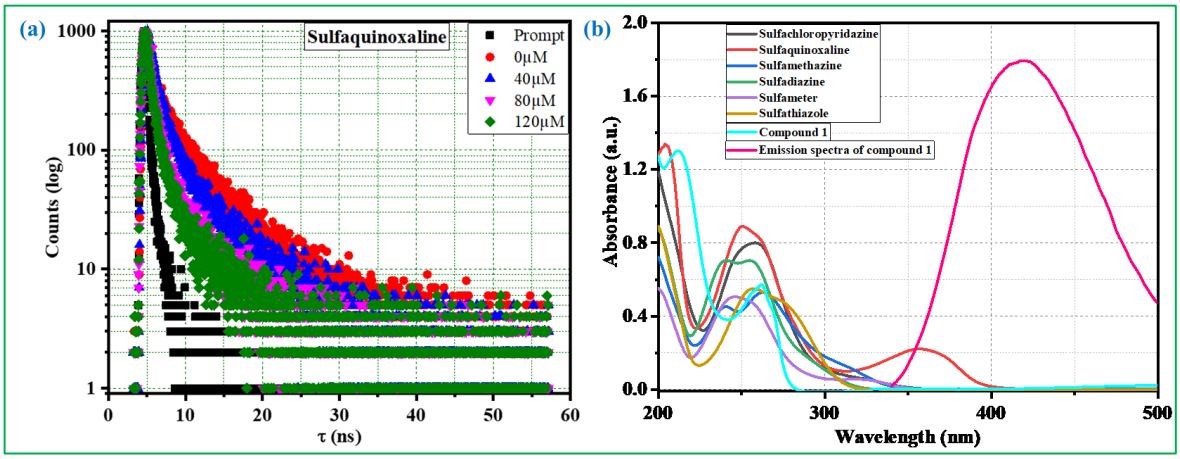

Figure 17. **(a)** Time resolved luminescence decay of **1** with the gradual addition of sulfaquinoxaline solution (λ_{ex} = 280 nm and λ_{em} = 420 nm). **(b)** Plot shows the merged absorption spectra of all the antibiotics and compound **1** with the emission spectra of compound **1**.

Table 6. Details of time-resolved experiments and calculation of average lifetime of compound **1** before and after the addition of different sulfonamide antibiotics.

SI no.	Sulfameter	τ (ns)	Sulfachloropyridazine	τ (ns)	Sulfadiazine	τ (ns)
1	0µM	3.17	0µM	3.17	0µM	3.03
2	40µM	2.80	40µM	3.04	40µM	2.70
3	80µM	2.25	80µM	2.87	80µM	2.32
4	120µM	1.75	120µM	2.82	120µM	2.39
SI no.	**Sulfaquinoxaline**	**τ (ns)**	**Sulfamethazine**	**τ (ns)**	**Sulfathiazole**	**τ (ns)**
1	0µM	2.94	0µM	3.02	0µM	3.16
2	40µM	2.47	40µM	1.95	40µM	2.70
3	80µM	1.36	80µM	1.70	80µM	2.48
4	120µM	0.84	120µM	1.54		

To acquire specific evidence regarding photo-induced electron transfer phenomena, it is crucial to gain a comprehensive understanding and estimate the redox potentials in both the ground state and excited state of compound **1**. For this purpose, we have carried out the cyclic voltammetry experiment of compound **1** and all antibiotics separately in 1M Na_2SO_4 medium to confirm the redox behaviour of compound **1** involved in PET process. The CV profile of compound **1** shows the presence of oxidative peaks positioned at 0.351V and 0.86V and the CV profile is irreversible in nature (Figure 18a) and from the CV profiles of all the antibiotics we have obtained the ground state reduction potentials (Figure 18b) and the reduction potential values are tabulated in table 7.

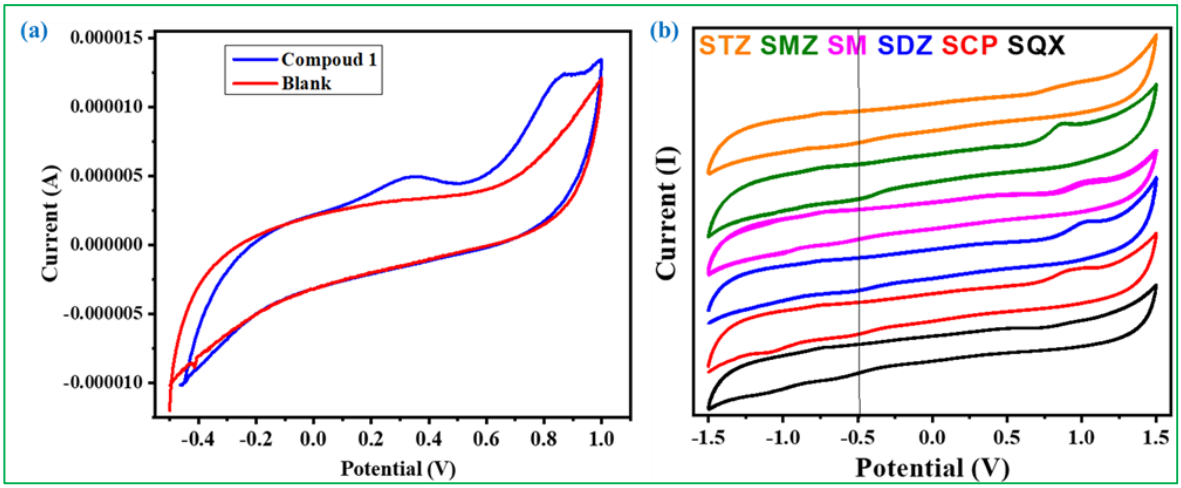

Figure 18. (a) CV curves of **1** measured at a scan rate of 20mV/Sec in 1M Na_2SO_4 solution. **(b)** CV curves of all six antibiotics measured at a scan rate of 50mV/Sec in 1M Na_2SO_4 solution.

Table 7. Reduction potentials of sulfonamide antibiotics obtained from CV analysis.

Sulfaquinoxaline (SQX)		Sulfameter (SM)	Sulfamethazine (SMZ)	Sulfadiazine (SDZ)	Sulfachloropyridazine (SCP)	Sulfathiazole (STZ)
E^{red}	-0.622	-0.568	-0.559	-0.703	-0.519	-0.593

The excited-state oxidation potential $*E^{ox}$ of compound **1** is calculated -2.58 V, by employing both the emission energy (3.44 eV) and the standard ground-state redox potentials (0.86V), as outlined in Equation 1.[75]

$$*E^{ox} = E^{ox} - E_{0,0} \quad \text{.....(1)}$$

A higher negative value of $*E^{ox}$ indicates that compound **1** possesses a greater ability to act as a potent photoreductant. In the case of sulfonamide antibiotics interacting with compound **1**, a less negative E^{red} value for the acceptor signifies favorable photo induced electron transfer at excited state of compound **1** to the antibiotics.[76]

4.3.4. Schottky Diode Properties.

Material electrical conductivity values can be assessed by analysing the dark *J-V* characteristics of the Schottky-barrier diode fabricated in the metal-semiconductor heterojunction configuration in the sandwich geometry where, Compound 1 in sandwiched between ITO bottom electrode and Al top electrode (ITO/ Compound **1**/Al). The dark *J-V* characteristics was analysed (Figure 19a) and studied using well known Shockley-diode equation:

$$J = J_0\left[\exp\left(\frac{qV_D}{\eta kT}\right) - 1\right] \qquad (2)$$

where J is the forward current, J_0 is the reverse saturation current and it can be approximated as $J_0 = A^*T^2\exp\left(-\frac{e\varphi_B}{kT}\right)$. Here, A^* is the effective Richardson constant and its value was considered as 120 A/cm$^2K^2$ (for all the devices), φ_B is the Schottky barrier height, η is the diode ideality factor, q is the electronic charge and V_D is the voltage across the diode.[77] Under large forward bias, Equation 2 can be expressed as

$$I = I_0\exp\left(\frac{q}{\eta kT}(V - IR_s)\right) \qquad (3)$$

where $I = J \times A$ and $I_0 = J_0 \times A$ ($A = 0.2$ cm^2 is the area of the device) and IR_s is the voltage drop across the series resistance R_S of the device. Differentiation of Equation 3 leads to

$$\frac{dV}{d(\ln\frac{I}{I_0})} = \frac{\eta kT}{q} + IR_s \qquad (4)$$

Linear part of the $dV/d\left(\ln\frac{I}{I_0}\right)$ versus I plot (Figure 19b) will yield R_s as its slope and $\eta kT/q$ as y-axis intercept. One can further define a function, $H(I) = V - \frac{\eta kT}{q}\ln\left(\frac{I}{AA^*T^2}\right)$ and substitute in Equation 2 to obtain a simple linear equation of the form, $H(I) = IR_s + \eta\varphi_B$. Using the value of idelaity factor (η) already extracted (from Equation 4), a plot of $H(I)$ vs I (Figure 19c) will yield a straight line. While value of φ_B can be extracted from the y-intercept, the slope will yield the value of R_s which can be compared with the previously calculated value (from Equation 4) for consistency. The parameters extracted from these graphs have been

summarized in Table 8. To extract the parameters (summarized in Table-8), low voltage-range portion (0.3 – 1.3 V) of the $J-V$ characteristics was used. At this range of voltage, the measured current from the device was in the range of 0.001-2.59 μA. The extracted series resistance, at this range, is found to be few hundreds of kΩ. Although, at higher voltage ranges ($V > 1.3$ V), the series resistance decreases to few hundreds of ohms, it should be noted that the ideality factor (η) increases significantly and exceeds two. Injection current in the high forward bias regime also increases significantly. Deviation from ideal thermionic emission

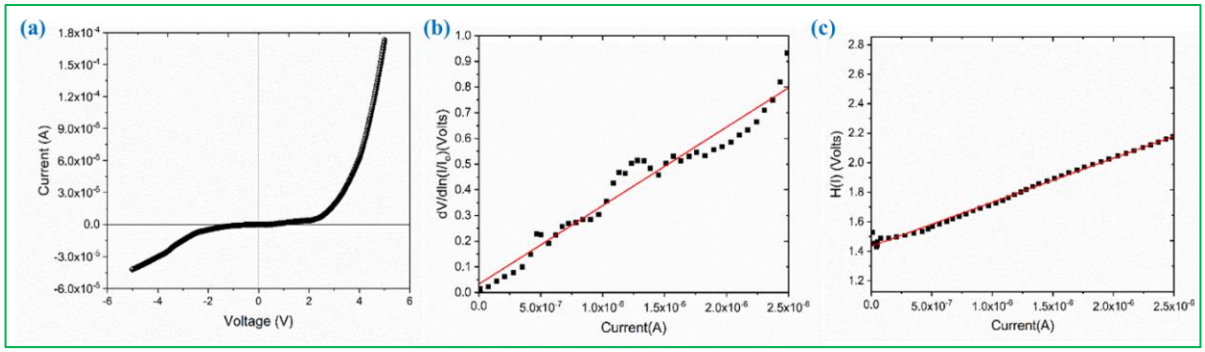

Figure 19. (a) J-V characteristics under dark condition for the device ITO/Compound **1** /Al **(b)** Plot of $dV/d\left(\ln\frac{I}{I_0}\right)$ *versus Current(A) in dark.* **(c)** H(I) vs. *Current(A) for the device in dark condition.*

type $J-V$ characteristics (where $\eta = 1$ to 2) is quite common in most of the disordered solids. In our case, a high injection current at the higher voltage ranges can be attributed to interfacial defect assisted barrier-lowering and subsequent high rate of charge carrier injection from Al electrode.

Table 8. Schottky diode Parameters of compound **1**.

Device Structure	Series resistance R_s (MΩ)		Ideality factor (η)	Barrier height φ_B (eV)
	From $dV/d\left(\ln\frac{I}{I_0}\right)$ vs I	From $H(I)$ vs I		
ITO/Compound **1**/Al	0.31 ± 0.012	0.30 ± 0.003	1.24	0.86

4.4 CONCLUSION.

In conclusion, a new cadmium-based two-dimensional fluorescent coordination polymer was synthesized. The synthesized compound contains two *in-situ* generated ligands from N-nicotinoyl glycine. The role of time and reaction temperature during the synthesis has been examined and it revealed the formation of three-different phases from same reaction mixture. The structure of the newly synthesized compound was determined by single crystal X-ray diffraction and it shows corrugated layer structure with hydrogen bond interactions leading to three dimensional supramolecular *ABABAB*…type packing arrangement. The blue emissive behaviour of this compound was used for the detections of various sulfonamide antibiotics in the presence of common water pollutants such as transition and heavy metal ions and volatile organic compounds (VOCs). The luminescence quenching response of the compound to sulfonamide antibiotics was significant, ranging from 81% to 94%, and the detection sensitivity reached ppb levels (226-726 ppb). The compound showed promising response for the fabrication of Schottky diode devices with barrier height 0.86 eV along with excellent ideality factor of 1.24. The bi-functional materials properties shown by the synthesized compound with respect to excellent sensing ability of sulfonamide antibiotics and Schottky diode behaviour made this compound interesting in the family of coordination polymer. This work opened up a new avenue for the design and synthesis of new coordination polymers for their optical and electronic properties within a single compound.

REFERENCES

1. M. Tabrizchi and V. Ilbeigi, *J. Hazard. Mater*., 2010, **176**, 692–696.
2. B. Wang, X.-L. Lv, D. Feng, L.-H. Xie, J. Zhang, M. Li, Y. Xie, J.-R. Li, H.-C. Zhou, *J. Am. Chem. Soc*., 2016, **138**, 6204− 6216.
3. Y. Xie, X. Zhu, Y. Sun, H. Wang, H. Qian, W. Yao, *Eur. Food Res. Technol.*, 2012, **235**, 555−561.
4. S.-L. Hou, J. Dong, X.-L. Jiang, Z.-H. Jiao, C.-M. Wang, B. Zhao, *Anal. Chem.*, 2018, **90**, 1516−1519.
5. G. -G. M Jesús, D. -C. M. Silvia, B., Damià, *TrAC Trends in Analytical Chemistry*, 2008, **27**, 1008-1022.
6. B. Halling-Sørensen, S. Nors-Nielsen, P. F. Lanzky, F. Ingerslev, H. C. Holten-Lützhøft, S. E. Jørgensen, *Chemosphere*, 1998, **36**, 357−393.
7. M. Imran, K. R. Das, M. M. Naik, *Chemosphere*, 2019, **215**, 846−857.

8. Y. Zhu, K. Liu, J. Zhang, X. Liu, L. Yang, R. Wei, S. Wang, D. Zhang, S. Xie, F. Tao, *Environ. Pollut.*, 2020, **256**, 113311.
9. F. Yin, H. Dong, W. Zhang, Z. Zhu, B. Shang, *Bioresour. Technol.*, 2018, **250**, 247−255.
10. X. Peng, F. Hu, T. Zhang, F. Qiu, H. Dai, *Bioresour. Technol.* 2018, **249**, 924−934.
11. J. L. Martinez, *Pollut*., 2009, **157**, 2893–2902.
12. F. Fernandez, F. Sanchez-Baeza and M. P. Marco, *Biosens. Bioelectron.*, 2012, **34**, 151–158.
13. E. Benito-Pena, J. L. Urraca and M. C. Moreno-Bondi, *J. Pharm. Biomed. Anal*., 2009, **49**, 289–294.
14. P. Jakubec, V. Urbanova, Z. Medrikova and R. Zboril, *Chem. – Eur. J*., 2016, **22**, 14279–14284.
15. F. Zhang, H. Yao, Y. Zhao, X. Li, G. Zhang and Y. Yang, *Talanta*, 2017, **174**, 660–666.
16. Q. Zhang, M. Lei, H. Yan, J. Wang and Y. Shi, *Inorg. Chem.*, 2017, **56**, 7610–7614.
17. J. Moros and J. J. Laserna, *Anal. Chem.*, 2011, **83**, 6275–6285.
18. D. Moreno-Gonzalez, F. J. Lara, N. Jurgovska, L. GamizGracia and A. M. Garcia-Campana, *Anal. Chim. Acta*, 2015, **891**, 321–328.
19. C. Blasco, A. Di Corcia and Y. Pico, *Food Chem.*, 2009, **116**, 1005–1012.
20. H.-C. J. Zhou and S. Kitagawa, *Chem. Soc. Rev*., 2014, **43**, 5415–5418.
21. T. R. Cook, Y.-R. Zheng and P. J. Stang, *Chem. Rev.*, 2013, **113**, 734–777.
22. Y. Liu, H. Dong, F. Hu and Y. S. Zhao, *Sci. Bull*., 2017, **62**, 3–4.
23. M.-M. Xu, X.-J. Kong, T. He, X.-Q. Wu, L.-H. Xie and J.-R. Li, *Inorg. Chem*., 2018, **57**, 14260–14268.
24. L.-H. Xie, X.-M. Liu, T. He and J.-R. Li, *Chem*, 2018, **4**, 1911–1927.
25. X. Zhao, Y. Wang, D.-S. Li, X. Bu and P. Feng, *Adv. Mater*., 2018, **30**, 1705189.
26. Y. Wang, L. Wang, W. Huang, T. Zhang, X. Hu, J. A. Perman and S. Ma, *J. Mater. Chem. A*, 2017, **5**, 8385–8393.
27. R.-X. Yao, H.-H. Fu, B. Yu and X.-M. Zhang, *Inorg. Chem. Front*., 2018, *5*, 153– 159.
28. Z. H. Fard, Y. Kalinovskyy, D. M. Spasyuk, B. A. Blight and G. K. H. Shimizu, *Chem. Commun*., 2016, 52, 12865–12868.
29. Jian-Xin Wang, Jun Yin, Osama Shekhah, Osman M. Bakr, Mohamed Eddaoudi, and Omar F. Mohammed, *ACS Appl. Mater. Interfaces*, 2022, 14, 8, 9970–9986.
30. Y. Cui, Y. Yue, G. Qian, and B. Chen, *Chem. Rev*., 2012, **112**, 1126–1162.
31. Z. Hu, B. J. Deibert and J. Li, *Chem. Soc. Rev*., 2014, **43**, 5815–5840.
32. B. Yan, *Acc. Chem. Res*., 2017, **50**, 2789–2798.
33. W. P. Lustig, S. Mukherjee, N. D. Rudd, A. V. Desai, J. Li and S. K. Ghosh, *Chem. Soc. Rev*., 2017, **46**, 3242–3285.
34. H. Wang, W. P. Lustig and J. Li, *Chem. Soc. Rev.*, 2018, **47**, 4729–4756.
35. M. Formica, V. Fusi, L. Giorgi, M. Micheloni, *Coordination Chemistry Reviews*, 2012, **256**, 170-192.
36. L. A. Malik, A. Bashir, A. Qureashi, A. H. Pandith, *Environ. Che. Lett.* 2019, **17**, 1495– 1521.
37. S. S. Nagarkar, B. Joarder, A.K. Chaudhari, S. Mukherjee, and S.K. Ghosh, *Angew. Chem. Int. Ed*., 2013, **52**, 2881-2885.
38. D. K. Singha, S. Bhattacharya, P. Majee, S. K. Mondal, M. Kumar and P. Mahata, *J. Mater. Chem. A*, 2014, **2**, 20908-20915.

39. E. M. Dias and C. Petit, *J. Mater. Chem. A*, 2015, **3**, 22484-22506.
40. Q. Zhang, M. Lei, H. Yan, J. Wang, Y. Shi, *Inorg. Chem.* 2017, **56**, 7610− 7614.
41. Z. -S. Qin, W.-W. Dong, J. Zhao, Y.-P. Wu, Q. Zhang, D.- S. Li, *Inorg. Chem. Front.* 2018, **5**, 120−126.
42. H. Pan, S. Wang, X. Dao, Y. Ni, *Inorg. Chem.* 2018, **57**, 1417−1425.
43. M.-L. Han, G.-X. Wen, W.-W. Dong, Z.-H. Zhou, Y.-P. Wu, J. Zhao, D.-S. Li, L.-F. Ma, X. Bu, *J. Mater. Chem. C* 2017, **5**, 8469−8474.
44. H. He, Q. -Q. Zhu, F. Sun, and G. Zhu, *Cryst. Growth Des.* 2018, **18**, 5573−5581.
45. F. Zhang, H. Yao, T. Chu, G. Zhang, Y. Wang, Y. Yang, *Chem. - Eur. J.* 2017, **23**, 10293−10300.
46. H. He, Q.-Q. Zhu, C.-P. Li, M. Du, *Cryst. Growth Des.*, 2019, ***19***, 694−703.
47. J. Li, T.-J. Chen, S. Han, L.-F. Song, *J. Solid State Chem.*, 2019, **277**, 107−114.
48. B. -X. Dong, Y. -M. Pan, W. -L. Liu, and Y. -L. Teng, *Cryst. Growth Des.*, 2018, **18**, 1, 431–440.
49. D. Zhao, X.-H. Liu, Y. Zhao, P. Wang, Y. Liu, M. Azam, S. L. Al Resayes, Y. Lu, W.-Y. Sun, *J. Mater. Chem. A*,2017, **5**, 15797−15807.
50. Y. Zhou, Q. Yang, D. Zhang, N. Gan, Q. Li, J. Cuan, *Sensors and Actuators B*, 2018, **262**, 137–143.
51. J. Xiao, M. Liu, F. Tian, and Z. Liu, *Inorg. Chem.* 2021, **60**, 5282−5289.
52. X. -D. Zhu, K. Zhang, Y. Wang, W.-W. Long, R.-J. Sa, T.-F. Liu, and J. Lu, *Inorg. Chem.* 2018, **57**, 1060−1065.
53. W.-B. Zhong, R.-X. Li, J. Lv, T. He, M.-M. Xu, B. Wang, L.-H. Xie, and J.-R. Li, *Inorg. Chem. Front.*, 2020, **7**, 1161.
54. Q. Liu, D. Ning, W.-J. Li, X.-M. Du, Q. Wang, Y. Li and W.-J. Ruan, *Analyst*, 2019, **144**, 1916.
55. D. Tian, X.-J. Liu, R. Feng, J.-L. Xu, J. Xu, R.-Y. Chen, L. Huang, and X.-H. Bu, *ACS Appl. Mater. Interfaces 2018*, **10**, 5618−5625.
56. Z. Hu, W. P. Lustig, J. Zhang, C. Zheng, H. Wang, S. J. Teat, Q. Gong, N. D. Rudd, and J. Li, *J. Am. Chem. Soc.*, 2015, **137**, 16209−16215.
57. K. Wang, Y. Duan, J. Chen, H. Wang and H. Liu, *Dalton Trans.*, 2022, **51**, 685.
58. P. Li, M.-Y. Guo, L.-L. Gao, X.-M. Yin, S.-L. Yang, R. Bu and E.-Q. Gao, *Dalton Trans.*, 2020, **49**, 7488.
59. Q.-Q. Zhu, Q.-S. Zhou, H.-W. Zhang, W.-W. Zhang, D.-Q. Lu, M.-T. Guo, Y. Yuan, F. Sun, and H. He, *Inorg. Chem.* 2020, **59**, 2, 1323–1331.
60. N. Xu, Q. Zhang, B. Hou, Q. Cheng, and G. Zhang, *Inorg. Chem.* 2018, **57**, 13330−13340.
61. J. -x. Ma, T. Ma, R. Qian, L. Zhou, Q. Guo, J.-H. Yang, and Q. Yang, *Inorg. Chem.* 2021, **60**, 7937−7951.
62. X. -D. Zhu, K. Zhang, Y. Wang,; W.-W. Long, R.-J. Sa, T.-F. Liu, J. Lü, *Inorg. Chem.* 2018, **57**, 1060−1065.
63. S. L. Xie, G. Skorupskii, and M. Dinca, *Chem. Rev.* 2020, **120**, 8536−8580.
64. S. Halder, A. Dey, A. Bhattacharjee, J. Ortega-Castro, A. Frontera, P. P. Ray and P. Roy, *Dalton Trans.*, 2017, **46**, 11239.
65. B. Bhattacharya, A. Layek, Md. M. Alam, D. K. Maity, S. Chakrabarti, P. P. Ray and D. Ghoshal, *Chem. Commun.*, 2014, **50**, 7858.

66. L. -A. Cao, M. -S. Yao, H. -J. Jiang, S. Kitagawa, X. -L. Ye, W. -H. Lia, and G. A. Xu, *J. Mater. Chem. A*, 2020, **8**, 9085.
67. *Apex3 v2017.3-0, Saint V8.38A, SAINT V8.38A*; Bruker AXS Inc.: Madison, WI, 2018.
68. L. Krause, R. Herbst-Irmer, G. M. Sheldrick, *Appl. Crystallogr.* 2015, **48**, 3.
69. A. Altomare, G. Cascarano, C. Giacovazzo, A. Guagliardi, Completion and Refinement of Crystal Structures with SIR92. *J. Appl. Crystallogr*. 1993, **26**, 343.
70. G. M. Sheldrick, Crystal Structure Refinement with SHELXL. *Acta Crystallogr., Sect. C: Struct. Chem*., 2015, **71**, 3.
71. L. J. Farrugia, WinGX suite for Small-Molecule Single-Crystal Crystallography. *J. Appl. Crystallogr*., 1999, **32**, 837.
72. A. L. Spek, Single-Crystal Structure Validation with the Program PLATON. *J. Appl. Crystallogr*. 2003, **36**, 7.
73. C. Das, V. D. Patel, D. Gupta, and P. Mahata., *Cryst. Growth Des.*, 2022, 22, 12, 7050–7061.
74. X. -S. Tai, X. Wang and P. -F. Li, *Crystals*, 2017, **7**, 33.
75. A. M. Committee, *Analyst*, 1987, **112**, No. 199.
76. R. Goswami, S. C. Mandal, B. Pathak and S. Neogi, *ACS Appl. Mater. Interfaces*, 2019, **11**, 9, 9042–9053.
77. S. M. Sze, K. K. Ng, *Physics of Semiconductor Devices*, 3rd ed.; John Wiley & Sons, Inc: Hoboken, New Jersey, 2007.

CHAPTER-5

Cd-Based Crystalline Network Material: Catalytic Properties and Post Synthetic Metal-Ion Metathesis with Enhanced Stability and Gas Sorption Behaviour

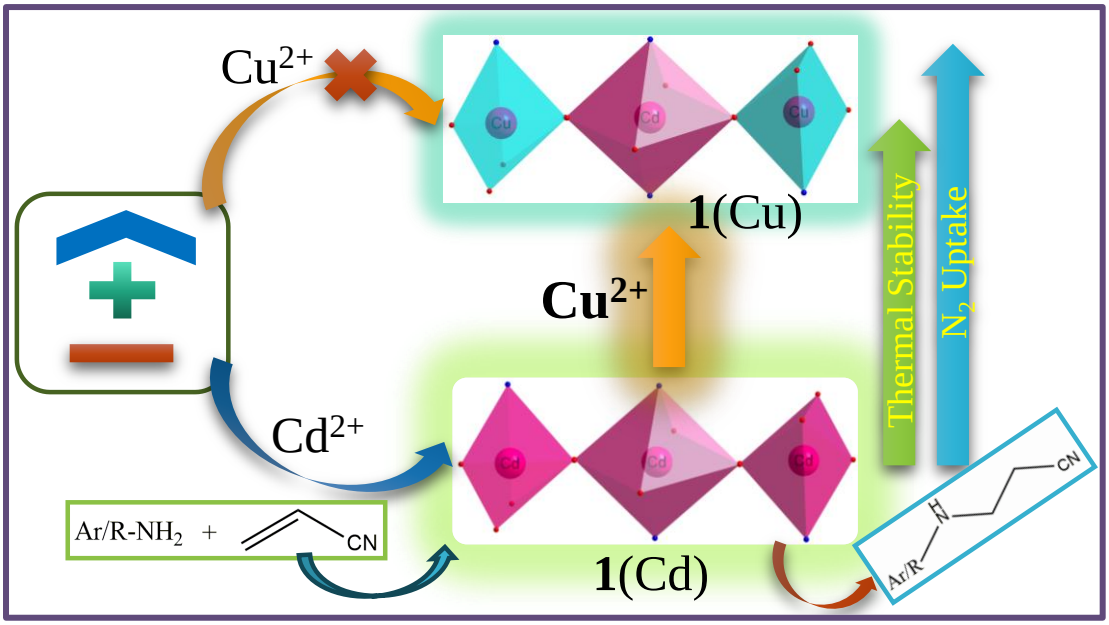

CHAPTER-5

Cd-Based Crystalline Network Material: Catalytic Properties and Post Synthetic Metal-Ion Metathesis with Enhanced Stability and Gas Sorption Behaviour

5.1. INTRODUCTION

The progress of synthetic approaches to β-amino nitrile compounds containing aromatic amines has significant importance due to its diverse synthetic applications to various natural products, drug molecules, and functional materials.[1-5] Therefore, significant effort has been dedicated to the formation of numerous C-N bonds.[6-10] Among the all-developed synthesis procedure, the aza-Michael reaction is one of the simplest and most effective methods with a high step and atom economic character.[11-16] Due to the very low nucleophilicity of aromatic aza-heteroarenes and aryl amines, aza-Michael reaction is mostly limited to the aliphatic amines.[17-18] To overcome this issue, strongly acidic or basic reaction medium and high temperature are needed to perform the aza-Michael addition reaction of aromatic amines.[19-20] This harsh condition further hampers the functionality of acid-base sensitive functional substrates and produces undesirable side products.[21-25] Alternatively, various Lewis acid metal catalysts have been intensively developed and they can perform aza-Michael addition reaction under mild conditions.[26-38] Despite the progress in metal-catalyzed aza-Michael additions, the use of expensive metals, air- and moisture-sensitive metal catalysts, and their homogeneous nature are still shortcomings for practical utility.[18]

The synthesis and design of crystalline network materials (CNMs) had a very rapid and wide-ranging growth over the past two decades and display diverging applications in many fields such as gas adsorption, separation, catalysis, drug delivery, sensors, etc.[39-45] Due to the interplay of many factors, controlling the CNMs structure is always difficult and that's why the properties of the material for a certain function are not always fulfilled.[46] To overcome the issue of structural unpredictability, the post-synthetic modification (PSM) of the synthesized CNMs seems to provide an appropriate solution for it.[49-55] The exchange of components of CNMs in suitable medium through post-synthetic modification and creation of novel scaffolds with improved properties have also been observed in some cases.[56-58] Therefore, swapping the cation and/or ligand is the most effective and alternative route to design new CNMs which are unachievable through the de novo synthesis.[59-65] This post-synthetic modification introduced new physical and chemical properties in CNMs without changing their structural integrity.[66-72]

In our quest to develop a hydrophobic CNM,[73] we have reported here the strategic construction of $[Cd_3(L)_2(LH)_2(bpe)_2]$, **1**, surmising the astute combination of carboxylic acid 4,4'-(hexafluroisopropylidine)bis(benzoic acid) and 1,2-di(4-pyridyl) ethylene as auxiliary ligand. Herein, we attempted to perform a metal exchange reaction between compound **1** and Cu^{2+} ions using the Irving-Williams approach,[74] resulting in the formation of the corresponding **1**(Cu) compounds. The metal exchange process was monitored through EDX analysis, and visual observation. The parent CNM and its daughter is isostructural. The results indicate that **1**(Cu) exhibits better thermal stability, improved gas uptake properties and red shifted emission with enhanced excited state lifetime compared to its parent CNM. Furthermore, the study highlights the success of using **1**(Cd) as a catalyst for the aza-Michael addition of α, β-unsaturated olefins to nucleophilic aromatic/aliphatic amines under ambient conditions as heterogeneous and acid-base free approach.

5.2. EXPERIMENTAL SECTION

5.2.1. Materials

The chemicals required for the synthesis of compound **1**(Cd), $Cd(ClO_4)_2.2H_2O$ (Sigma-Aldrich, 98%), 1,2-di(4-pyridyl) ethylene (TCI, 98%), 4,4'-(hexafluroisopropylidine)bis(benzoic acid) (Sigma-Aldrich, 98%) and CH_3OH (Merck, 99%) were used as received. The chemicals used for the metal ion metathesis experiments were $CuCl_2.2H_2O$ (98.5%, Merck), $Cu(CH_3COO)_2.H_2O$ (98%, Merck), $Cu(NO_3)_2.3H_2O$ (99%, Merck), $Cu(SO_4)_2.5H_2O$ (98%, Merck), DMF (99%, Merck). The chemicals used for the cyanoethylation reaction were aniline (≥99%, Merck), p-toluidine (99.6%, Merck), p-anisidine (99%, Merck), morpholine (≥99%, Merck), benzylamine (99%, Merck), methyl propargyl amine (95%, Merck), and acrylonitrile (99%, Merck) and used as received without further purification. The water used was double distilled.

5.2.2. Synthesis of 1(Cd).

1(Cd) was synthesized at room temperature *via* layer diffusion method. For this, a methanolic solution (30 mL) of 4,4'-(hexafluroisopropylidine)bis(benzoic acid) (0.375 mmol, 0.15 g) was mixed with separately prepared methanolic solution (30 mL) of 1,2-di(4-pyridyl) ethylene (bpe) (0.375 mmol, 0.07 g), and the mixture was stirred for 5 min to make a homogeneous solution. On the other hand, an aqueous solution of Cd^{2+} ions was prepared by dissolving $Cd(ClO_4)_2.2H_2O$ (0.75 mmol, 0.2382 g) in 60 mL of water in a beaker and in another beaker 30 ml of methanol was mixed with 30 mL of water (1:1) and stirred for one hours to make a homogeneous buffer solution. Two

ml of the aqueous solution of Cd^{2+} ions was taken in a test tube and 2 mL of the buffer solution was layered over it. After that 2mL of the ligand solution was slowly and carefully layered above this buffer solution. After two weeks, colourless block-shaped crystals (Figure 1a) suitable for single crystal diffraction were collected from the test tube and washed with a water-methanol mixture and dried in air. The final product, containing large quantities of colorless block-shaped crystals, was filtered, washed with deionized water under vacuum, and dried at ambient conditions (yield: 72% based on metal). Elemental analysis Calcd (%) for **1**(Cd): C 48.79, H 2.29, N 2.47. Found: C 48.71, H 2.26, N 2.56.

5.2.3. Procedure for ion exchange of 1(Cu).

In the metal ion exchange experiment, 20 mg of **1**(Cd) crystals was immersed in a 15 mL DMF solution containing 12 mg of $CuCl_2$ (5 mM) in a 20 mL glass vial. A color change began within 30 minutes, and after 7 days, the crystals turned completely green (Figure 1b) indicating saturation of the Cd^{2+} to Cu^{2+} metal ion metathesis. The solution was then removed, and the ion-exchanged crystals of **1**(Cu) were washed multiple times with DMF to eliminate excess metal salts. For bulk preparation, a high concentration $CuCl_2$ solution (20 g/L) in 10 mL of DMF was utilized, and metal exchanged compound **1**(Cu) was obtained within 24 hours.

(a)  **(b)** 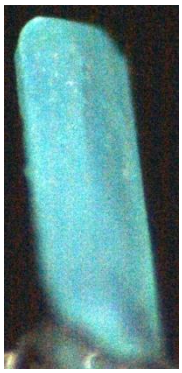

Figure 1. (a) Colourless block shaped crystal image of **1**(Cd). **(b)** Green coloured block shaped crystal image of **1**(Cu).

5.2.4. Single Crystal X-ray Diffraction.

Suitable single crystals of **1**(Cd) were carefully selected under an optical microscope and mounted on thin glass fiber carefully. The single crystal data of both the compounds were collected using Bruker D8-Quest diffractometer. The instrument was equipped with Mo Kα (λ=0.71073Å)

radiation source and operating voltage of X-ray generator was 50kV and 1mA. Diffraction data were collected with ω scan width of 0.5º. Three different setting of φ (0, 90, 180º) were used to collect the total 408 frames, keeping a fixed distance of sample-to-detector at 6.03 cm and the detector position (2θ) was fixed at -25º. The initial indexing, final data sets, and cell refinements were handled by an APEX3 program, while a SAINTPLUS[75]program was utilized for the frame integration and final cell parameter calculation. The multi-scan absorption data was corrected by a SADABS program.[76] We initially solved the structure by SIR 92,[77] and the full matrix least-square method (SHELXL-2016[78]) was used further, which is present in the WinGx suit of programs (Version 1.63.04a). [79,80]) With the help of Fourier maps, we successfully located all the non-hydrogen atoms and refined them anisotropically. Finally, all the hydrogen atoms were fixed at calculated positions and included them in the refinement process using riding model associated with isotropic thermal parameters. The details of the crystal and final refinements are given in the Table 1. CCDC: 2331787 contain the crystallographic data for this paper. These data can be obtained free of charge from The Cambridge Crystallographic Data Center (CCDC) via www.ccdc.cam.ac.uk/data_request/cif.

Table 1. Crystal data and structure refinement parameters for $[Cd_3(L)_2(LH)_2(bpe)_2]$, **1**, {L= 4,4'-(hexafluroisopropylidine)bis(benzoate)} and 1,2-di(4-pyridyl) ethylene (bpe).

empirical formula	$C_{46}H_{27}Cd_{1.5}F_{12}N_2O_8$
formula weight	1132.29
crystal system	monoclinic
space group	$P2_1/c$
a (Å)	13.1915(12)
b (Å)	25.052(2)
c (Å)	14.8240(13)
β (deg)	113.853(2)
volume ($Å^3$)	4480.5(7)
Z	4
T (K)	298

ρ_{calc} (g cm^{-3})	1.679
μ (mm^{-1})	0.824
θ range (deg)	1.873 to 27.249
λ (Mo Kα) (Å)	0.71073
R indices [I>2σ(I)]	R_1=0.0337, wR_2 = 0.0921
R indices (all data)	R_1= 0.0459, wR_2 = 0.1154

$R_1 = \Sigma\ ||F_0|-|F_c|| / \Sigma\ |F_0|$; $wR_2 = \{\Sigma[w(F_0^2 - F_c^2)^2] / \Sigma[w(F_0^2)^2]\}^{1/2}$. $w = 1/[\sigma^2(F_0)^2 + (aP)^2 + bP]$, $P = [max.(F_0^2,0) + 2(F_c)^2]/3$, *where a = 0.0612 and b = 1.674*

5.2.5. Powder X-ray Diffraction.

The Powder X-ray diffraction (PXRD) pattern for a finely ground sample was acquired using a Bruker D8 Advance X-ray diffractometer utilizing Cu Kα radiation with a wavelength (λ) of 1.5418 Å. The experiment spanned the 2θ range of 5-50° and was conducted at 40 kV and 40 mA (Figure 2a). Analysis of the obtained X-ray diffraction (XRD) pattern reveals the existence of a new compound, denoted as **1**(Cd). Remarkably, the observed XRD pattern aligns precisely with the simulated XRD pattern generated from the structure determined through single-crystal XRD. This concordance between the experimental and simulated patterns serves as unequivocal confirmation that **1**(Cd) is entirely pure.

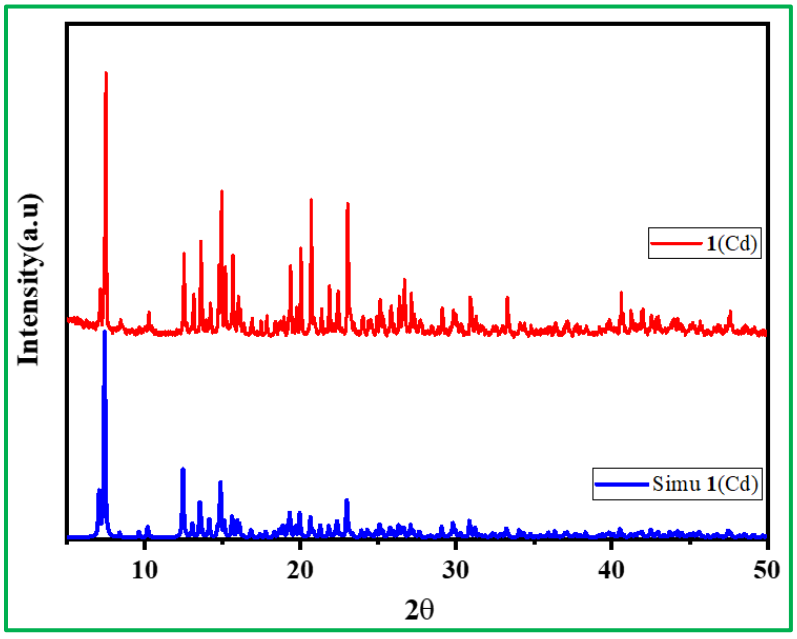

Figure 2. Powder XRD (CuKα) patterns of $[Cd_3(L)_2(LH)_2(bpe)_2]$, **1**.

5.2.6. FTIR Measurements.

The Fourier Transform Infrared (FT-IR) spectrum was meticulously captured using the Nicolet Magna IR 750 series-II instrument covering a comprehensive range from 400 to 4000 cm^{-1} (Figure 3). The discerned infrared frequencies have been precisely documented in Table 2.

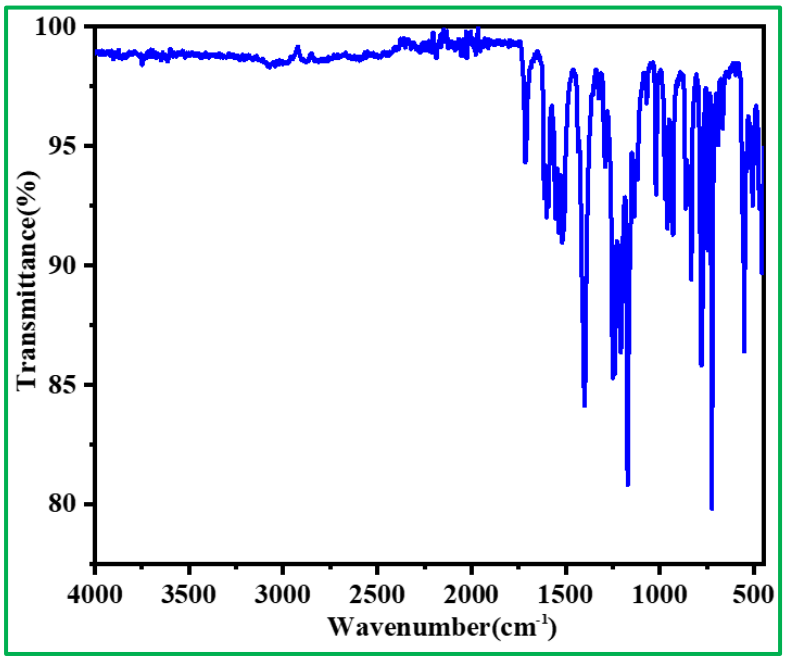

Figure 3. IR spectrum of **1**.

Table 2. The observed IR bands for $[Cd_3(L)_2(LH)_2(bpe)_2]$, **1**.

Bands	**Wavenumber (cm^{-1})**	**Bands**	**Wavenumber (cm^{-1})**
υ_{str}(free carboxylic acid)	1717(s)	δ(aromatic C-H)$_{in\ plane\ bending}$	1165(s), 1020(s), 961(m)
$\upsilon_{asy.\ str}$ (carboxylate)	1626(s), 1518(s)	δ(aromatic C-H)$_{out\ of\ plane\ bending}$	934(m), 834(m),
υ_{str}(C=C)	1400(s)	δ(carboxylate)$_{bending}$	789(s), 721(s)
υ_{str}(C-F)	1251(s)	δ(aromatic C=C)$_{out\ of\ plane\ bending}$	558(s), 500(m)
$\upsilon_{sy.\ str}$(carboxylate)	1205(s)		

5.2.7. Thermal Stability.

Thermogravimetric analysis (TGA) of **1**(Cd) was carried out on a Perkin-Elmer instrument STA 6000 under a nitrogen atmosphere (flow rate = 20 ml min^{-1}) in the temperature range 30 - 800°C (heating rate 10°C/min) (Figure 4). This compound is stable up to 306 ºC. The compound started to decompose at ~ 306 °C and the removal of the organic part has been completed at 446 °C. The total observed weight loss corresponds to 82% and it matches well with the formation of CdO (calculated: 82.99%).

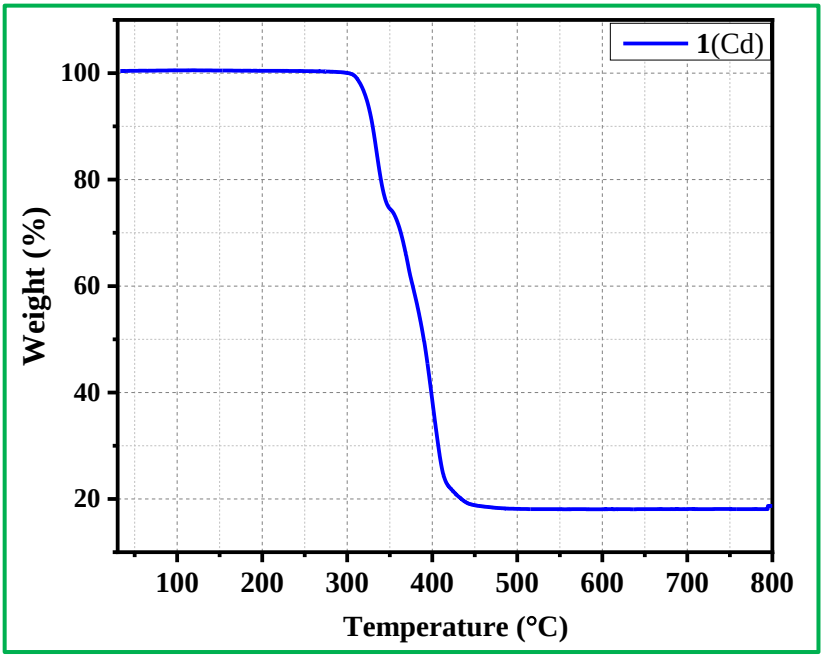

Figure 4. Thermogravimetric analysis (TGA) of **1**(Cd) in nitrogen atmosphere.

5.2.8. BET Analysis.

To explore the porosity of **1**(Cd) and **1**(Cu), an investigation into nitrogen gas sorption was conducted through the BET experiment. The powder samples underwent a pre-treatment at 120°C for 120 minutes, ensuring the removal of any adsorbed water molecules. The gas sorption isotherm for nitrogen (77K) was precisely measured within the pressure range of 0 to 1 bar utilizing an Autosorb iQ instrument from Quantachrome Inc., USA. This meticulous approach aims to provide a comprehensive understanding of the compound's porosity characteristics before and after the metathesis.

5.2.9. Photoluminescence Measurements.

For the examination of photoluminescence properties at room temperature in DMF a Horiba FluoroMax-4 spectrofluorometer was employed. Solutions of **1**(Cd) and **1**(Cu) were intricately prepared by introducing 3 mg of each compound separately into 3 mL of DMF solvent. For photoluminescence measurements, 100 µL of the resulting stock solution was placed in a 2 mL quartz cuvette along with 2 mL of DMF. The excitation and emission processes were executed with precise and consistent slit widths of 5 nm. UV-Vis spectra of the compounds in DMF were precisely recorded using a Shimadzu UV-1900 Pharma Spec UV-Vis spectrophotometer (Figure 5).

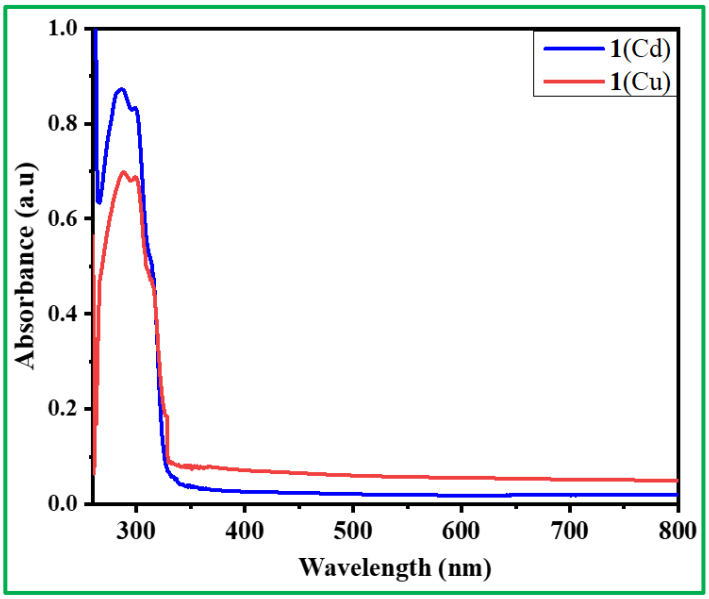

Figure 5. Absorption spectra of **1**(Cd) and **1**(Cu) in DMF medium.

5.2.10. Lifetime Measurements.

Time-correlated single photon counting (TCSPC) measurements were conducted at room temperature in DMF employing a state-of-the-art HORIBA Jobin Yvon instrument specialized for nanosecond time domain analyses. Luminescence lifetime decays were precisely collected utilizing a high-performance Hamamatsu MCP photomultiplier (R3809). Each decay was subjected to meticulous deconvolution and fitted with exponential functions using the sophisticated Origin software. In the TCSPC measurements, the excitation wavelength was precisely set at 300 nm and the subsequent emission decay curve was monitored at 378 nm (for **1**(Cd)) and 392nm (for **1**(Cu)).

5.2.11. Field Emission Scanning Electron Microscopy (FE-SEM).

To monitor the morphology changes of **1**(Cd) before and after the metal ion metathesis, FE-SEM experiment were carried out using a Zeiss Gemini SEM 450 field emission scanning electron microscope.

5.2.12. General Procedures of Aza-Michael Addition.

^{1}H-NMR spectra were measured on Bruker DPX400 MHz, and Bruker DPX300 MHz spectrometers at 25°C in $CDCl_3$ solvent. To a methanol solution (1 ml) of aromatic/aliphatic amines (1.07 mmol) and acrylonitrile (285mg, 5.37mmol), the solid catalyst **1**(Cd) (5 mg) was added and stirred for 8/24 hours at room temperature. After that the reaction mixture was passed through a syringe filter (2.4 microns) to remove the catalyst and methanol was removed. The experiments mentioned here were carried out in an open pot at room temperature.

5.3. RESULT AND DISCUSSION

5.3.1. Structural Description.

Compound **1** crystallized in a monoclinic crystal system with a $P2_1/c$ space group. The asymmetric unit of **1**(Cd) consists of crystallographically independent one and half Cd^{2+} ion, one 4,4'-(hexafluroisopropylidine)bis(benzoate) (L), one mono protonated 4,4'-(hexafluroiso propylidine)bis(benzoate) (LH) and one 1,2-di(4-pyridyl) ethylene (bpe) (Figure 6a). The $Cd(1)^{2+}$ ion in CNM has a octahedral coordination geometry and is surrounded by four oxygen atoms from four carboxylate groups of ligands (L and LH) and two nitrogen atom from an aromatic pyridyl ring of the bpe ligands (Figure 6b). The $Cd(2)^{2+}$ ion, on the other hand, has a distorted trigonal bipyramidal coordination geometry and is coordinated by four oxygen atoms from three carboxylate groups of ligands (L and LH) and one nitrogen atom of aromatic pyridyl ring of bpe ligand (Figure 6c). The coordination modes of the carboxylate groups of the ligands (L and LH) are shown in Figure 6d & e.

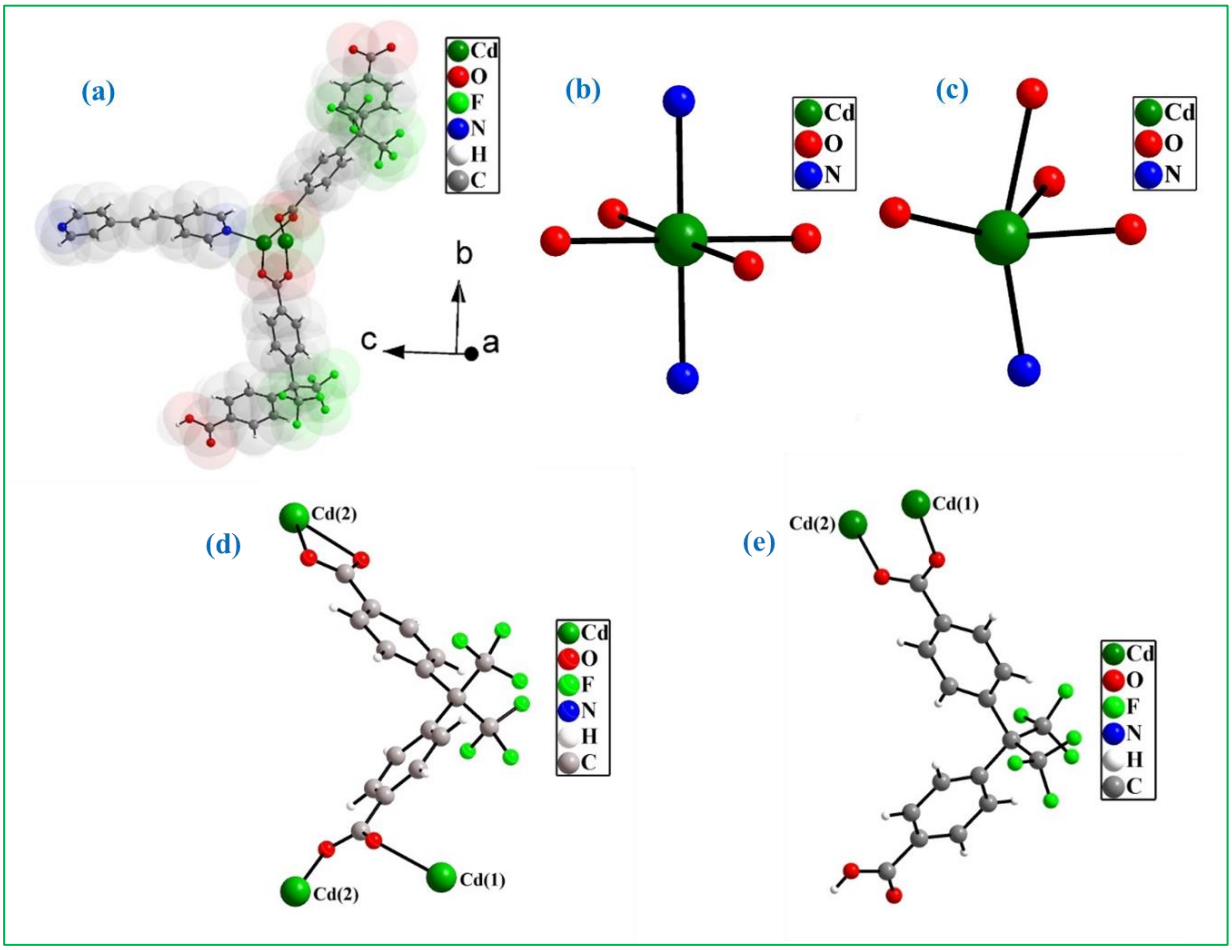

Figure 6. (a) Figure shows the asymmetric unit of $[Cd_3(L)_2(LH)_2(bpe)_2]$, **1**. **(b)** octahedral geometry around $Cd(1)^{2+}$ and **(c)** distorted trigonal bipyramidal geometry around $Cd(2)^{2+}$. **(d)** Figure shows coordination modes of ligand L and **(e)** ligand LH in $[Cd_3(L)_2(LH)_2(bpe)_2]$, **1**. Note the presence of free carboxylic acid group in ligand LH.

One of the carboxylic acid group of the ligand LH remains free in nature. The Cd-O bonds have an average distance of 2.323 Å and the Cd-N bonds have average distances of 2.296 Å. The O/N-Cd-N/O bond angles is in the range of 54.39(6)- 180°. The selected bond distances are listed in Table 3 and the selected bond angles are listed in Table 4.

Table 3. Selected bond distances (Å) observed in $[Cd_3(L)_2(LH)_2(bpe)_2]$, **1**.

Bond	**Distances, Å**	**Bond**	**Distances, Å**
Cd(1)-O(6) #1	2.2439(16)	Cd(2)-O(2)	2.1792(16)
Cd(1)-O(6)	2.2440(16)	Cd(2)-O(5)	2.2459(17)
Cd(1)-N(2)#2	2.3157(19)	Cd(2)-N(1)	2.2607(18)
Cd(1)-N(2)#3	2.3157(19)	Cd(2)-O(4)#4	2.3836(17)
Cd(1)-O(1)	2.4453(17)	Cd(2)-O(3)#4	2.4013(16)
Cd(1)-O(1) #1	2.4453(17)		

Symmetry transformations used to generate equivalent atoms: #1 -x+2,-y+1,-z+1 #2 -x+2,-y+1,-z+2 #3 x,y,z-1 #4 -x+1,y-1/2,-z+1/2

Table 4. Selected bond angles observed in $[Cd_3(L)_2(LH)_2(bpe)_2]$, **1**.

Angle	**Amplitude (º)**	**Angle**	**Amplitude (º)**
O(6)#1-Cd(1)-O(6)	180	N(2)#3-Cd(1)-O(1) #1	94.57(7)
O(6)#1-Cd(1)-N(2)#2	85.81(7)	O(1)-Cd(1)-O(1) #1	180.0
O(6)-Cd(1)-N(2)#2	94.19(7)	O(2)-Cd(2)-O(5)	119.42(7)
O(6)#1-Cd(1)-N(2)#3	94.18(7)	O(2)-Cd(2)-N(1)	117.96(7)
O(6)-Cd(1)-N(2)#3	85.81(7)	O(5)-Cd(2)-N(1)	91.67(7)
N(2)#2-Cd(1)-N(2)#3	180.0	O(2)-Cd(2)-O(4)#4	133.48(7)
O(6)#1-Cd(1)-O(1)	88.74(6)	O(5)-Cd(2)-O(4)#4	91.36(7)
O(6)-Cd(1)-O(1)	91.26(6)	N(1)-Cd(2)-O(4)#4	92.78(6)
N(2)#2-Cd(1)-O(1)	94.57(7)	O(2)-Cd(2)-O(3)#4	94.85(6)
N(2)#3-Cd(1)-O(1)	85.43(7)	O(5)-Cd(2)-O(3)#4	80.12(6)
O(6)#1-Cd(1)-O(1) #1	91.26(6)	N(1)-Cd(2)-O(3)#4	145.49(6)
O(6)-Cd(1)-O(1) #1	88.74(6)	O(4)#4-Cd(2)-O(3)#4	54.38(6)
N(2)#2-Cd(1)-O(1) #1	85.43(7)	N(2)#3-Cd(1)-O(1) #1	94.57(7)

Symmetry transformations used to generate equivalent atoms: #1 -x+2,-y+1,-z+1, #2 -x+2,-y+1,-z+2, #3 x,y,z-1, #4 -x+1,y-1/2,-z+1/2.

Three Cd^{2+} ions are connected by the carboxylate groups of the ligands (L and LH) to form a trimeric unit (Figure 7a). Each trimeric unit connects four other trimeric units to form a two-dimensional structure through the ligands L (Figure 7b).

The two-dimensional structures further connected by the bpe ligands to form three-dimensional structure (Figure 7c). Three dimensional structures are interpenetrated in nature and are stabilized by O – H···O hydrogen bond interactions. Here the O – H bonds of the free carboxylic acid groups of LH ligands act as hydrogen bond donors and oxygen atoms of carboxylate groups of the L ligands act as hydrogen bond accepter [O(7) – H(7a)···O(3)] where the distance between H(6c) and O(3) is 1.80 Å and between O(7) and O(3) is 2.60 Å and the O(7) – H(7a)···O(3) angle is 165° (Figure 7d).

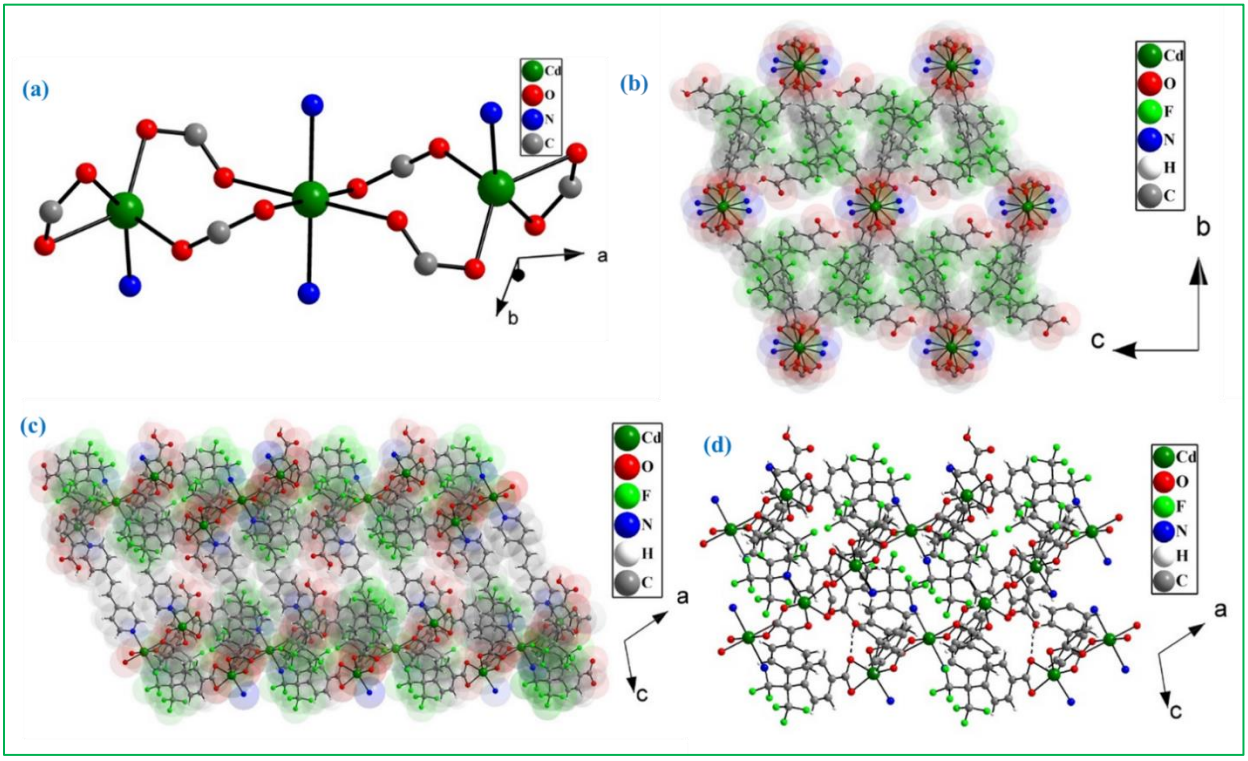

Figure 7. (a) Figure shows the carboxylate connected trimeric unit formed by one Cd(1) and two Cd(2) in $[Cd_3(L)_2(LH)_2(bpe)_2]$, **1**. **(b)** The two dimensional structure formed by the connectivity between trimeric units and 4,4'-(hexafluroisopropylidine)bis(benzoate) (L) ligands. **(c)** Figure shows three-dimensional structure through connectivity of the two-dimensional structure by the

bpe ligands in **1**. **(d)** Figure shows the presence of O – H···O hydrogen bond interactions to form interpenetrated three dimensional structure in **1**.

5.3.2. Conversion of 1(Cd) to 1(Cu).

Earlier research has demonstrated that the utilization of the metal metathesis method can improve both the characteristics and structural stability of CNMs.[55-56] Despite our efforts to produce frameworks with the same structure as **1**(Cd) by employing de novo synthesis procedures with other first-row transition elements, particularly copper, have unfortunately been unsuccessful. Consequently, we opted for a post-synthetic modification strategy for the **1**(Cd) and utilized the conventional soaking technique to perform metal-ion exchange using various copper metal salts, $Cu(NO_3)_2$, $Cu(SO_4)_2$, $Cu(CH_3COO)_2$ and $CuCl_2$ in DMF solvent. However, we observed a visible change of the colorless single crystals to green single crystals in the $CuCl_2$/DMF solution at room temperature (Figure 8a) and repeated the metal metathesis four times to confirm the exchange. This whole metathesis process was monitored by EDX analysis and visual observation of colour change (Figure 8b).

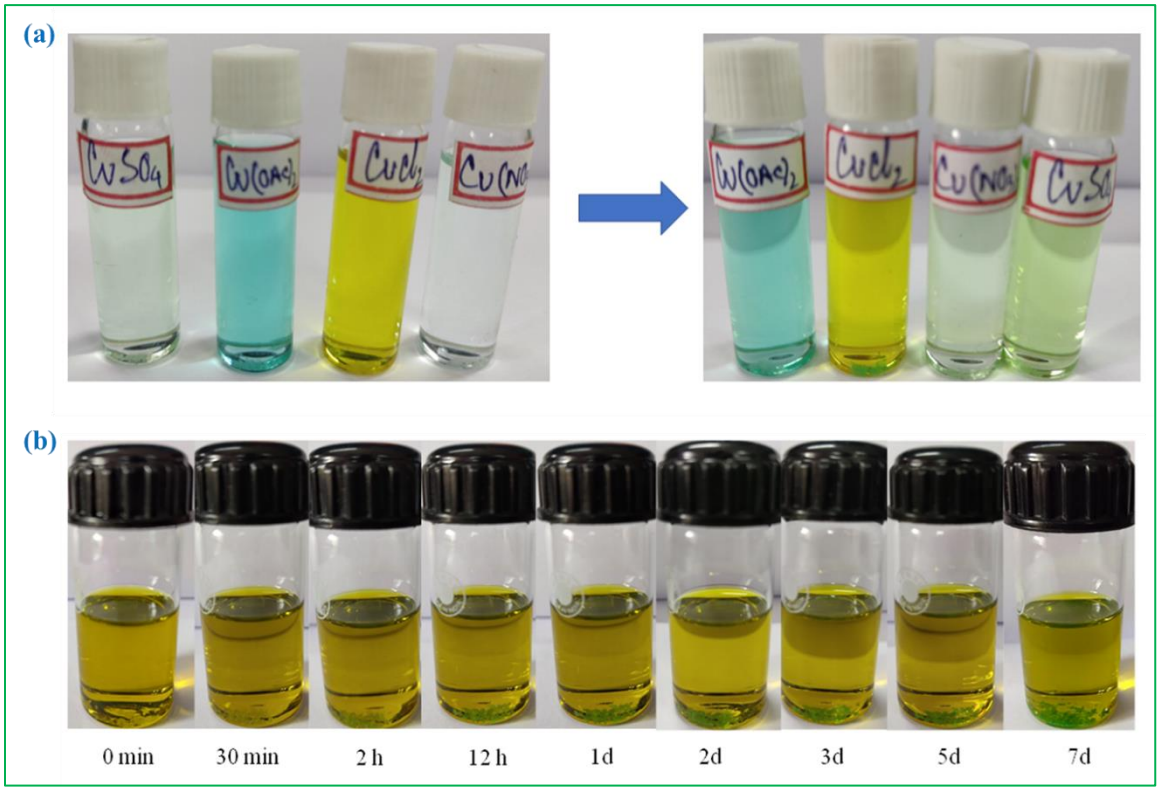

Figure 8. (a) Photographs of copper salt solution in DMF with crystal of **1**(Cd) before metathesis and after metathesis Note the change of color of **1**(Cd) only in the case of $CuCl_2$ solution. **(b)**

Photographs of **1**(Cd) taken during the exchange of Cd^{2+} with Cu^{2+} by immersion in DMF solution of $CuCl_2$ (5mM) for different duration.

The EDX analysis revealed 45% metal metathesis was completed after 3 days (Figure 9a) and it increased to 72% after 7 days (Figure 9b). The EDX elemental mapping on a single particle displays a uniform distribution of C, N, O, F, Cu and Cd with no observable indications of elemental clustering (Figure 9c). The even distribution of Cu within the particles affirms that the metal exchange occurs in a SC-SC manner. SEM images of **1**(Cd) and **1**(Cu) also validates the SC-SC transformation (Figure 10a &b).

(a)

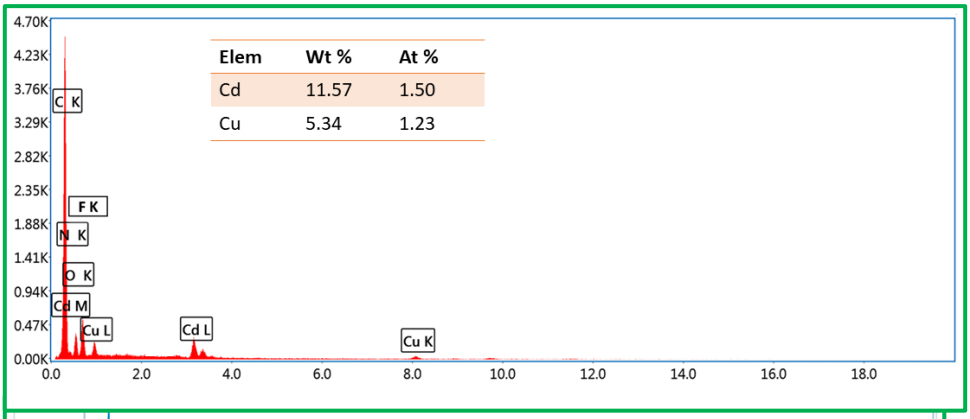

(b)

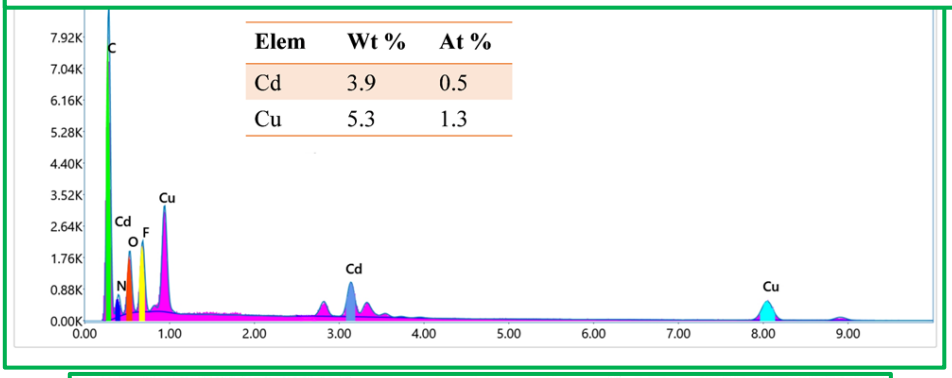

(c)

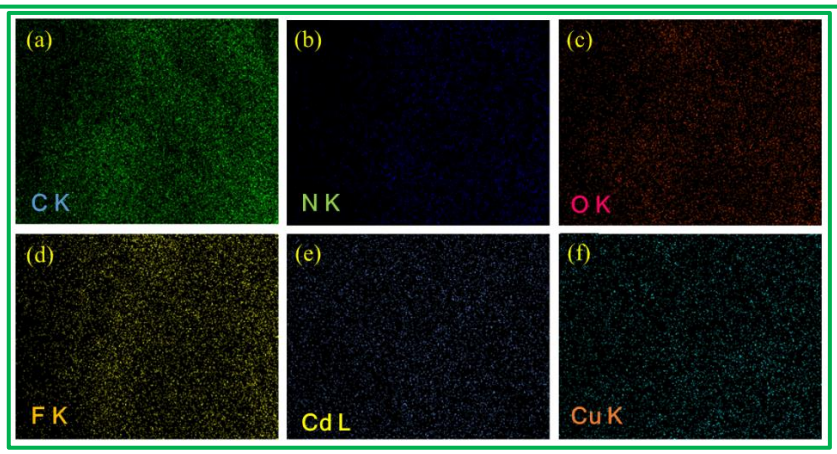

Figure 9. (a) Representative EDX plot of **1**(Cu) after 3 days. **(b)** Representative EDX plot of **1**(Cu). Note the presence of Cd and Cu. **(c)** Elemental mapping images of **1**(Cu) for (a) C-K and (b) N-K, (c) O-K (d) F-K (e) Cd-L and (f) Cu-K.

Various attempts were made to determine the single crystal structure of **1**(Cd) after metathesis but owing to the cracks on crystals it was unsuccessful. The PXRD pattern of the obtained **1**(Cu) is indistinguishable from that of the parent compound, **1**(Cd) (Figure 10c). The IR spectra's resemblance further validates the presence of similar organic groups in **1**(Cd) and **1**(Cu) (Figure 10d). Based on these findings, it can be inferred that **1**(Cu) possess a framework structure similar to its parent compound **1**(Cd). To further explore the reversibility of metal ion exchange, we immersed **1**(Cu) in a high-concentration solution of $Cd(NO_3)_2$/DMF (20g/L) for a period of one month but no notable change in colour was observed. This suggests that the metathesis process is essentially irreversible.

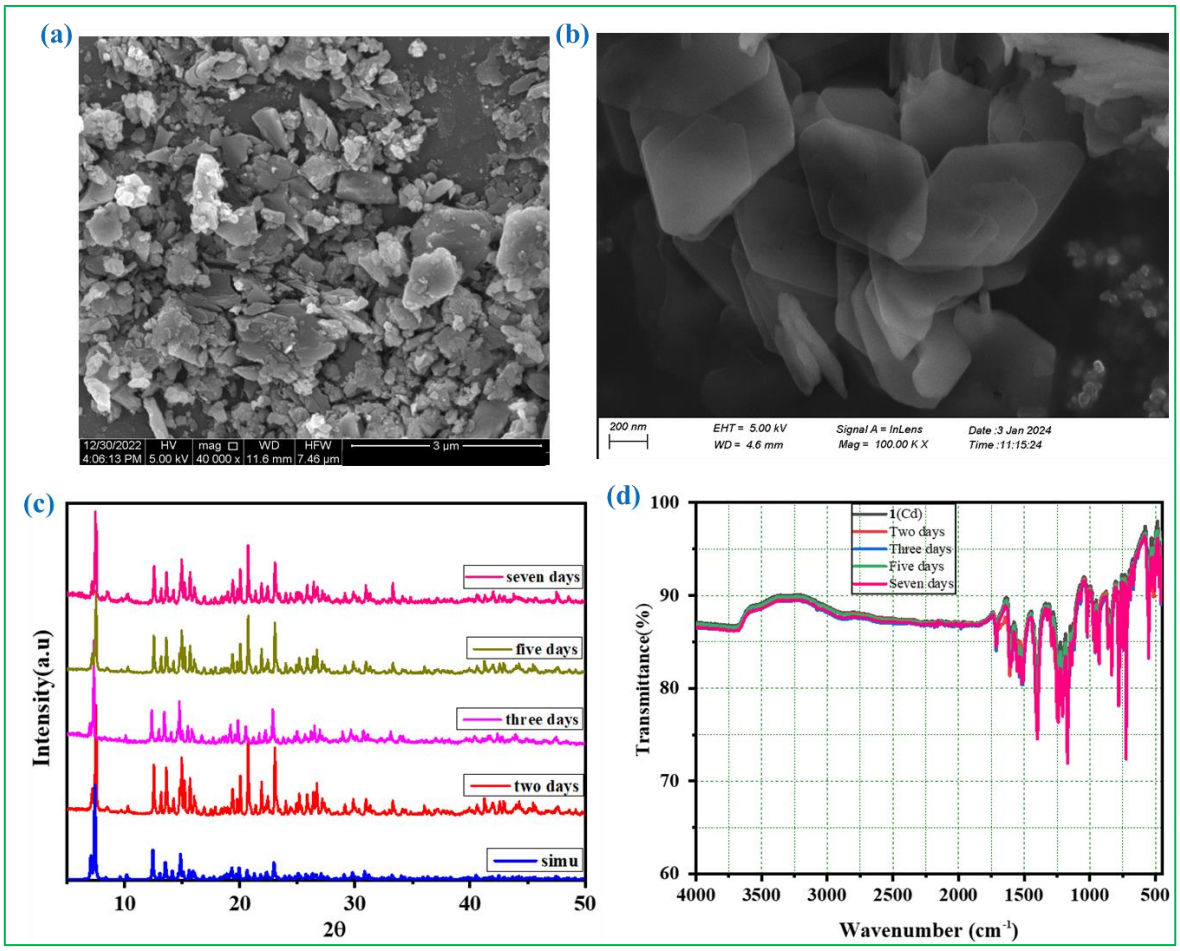

Figure 10. (a) SEM images of **1**(Cd) before metathesis. **(b)** SEM images of **1**(Cu) (after metathesis). **(c)** PXRD patterns of **1**(Cd) simulated from single crystal XRD and the samples produced in various time during the metathesis process. **(d)** FTIR spectra of **1**(Cd) and the samples produced in various time during the metathesis process.

It is also important to correlate between the crystal structure of **1**(Cd) and the reason n behind the selective and partial exchange of Cd^{2+} ions by the Cu^{2+} ions in **1**(Cd). The single crystal structure analysis of **1**(Cd) reveals the presence of two cadmium centers in the three-dimensional structure. One of them exhibits five-coordinated configuration while the other one adopts a six-coordinated configuration and the ratio between them is 2:1. Generally Cd^{2+} ions being 4d series elements prefer higher coordination numbers such as 6 and 7. On the other hand, Cu^{2+} ions favour coordination number of five over Cd^{2+}. This disparity in coordination preferences promotes metal ions exchange in **1**(Cd). Furthermore, the inherent stability of Cu^{2+} ions with coordination number five made the metathesis process irreversible in nature. It is also important to note that out of the two Cd^{2+} ions in **1**(Cd), one is in unsaturation state with respect to coordination number and this nature encouraged us to investigate the **1**(Cd) as Lewis's acid catalyst.

5.3.3. Thermal Stability.

After confirming the compound stability of **1**(Cu) by PXRD, we have carried out the TGA analysis at nitrogen atmosphere to further check the thermal stability of **1**(Cu). TGA analysis revealed that compound **1**(Cu) is stable up to 380ºC and it underwent decomposition beyond this temperature. Whereas the parent compound **1**(Cd) is stable up to 306ºC. This study indicates higher thermal stability after the metathesis reaction (Figure 11a). The strength of the metal-ligand bonds plays a crucial role for the thermal the stability of CNMs. Cu^{2+} ions tends to form strong coordination bonds with oxygen containing organic ligands contributing to the stability of the framework. On the other hand, Cd^{2+} ions form weaker bonds due to its larger size and loss of crystal field stabilization energy due to its d^{10} electronic configuration leading to a less stable structure. This suggests that post synthetic modification (PSM) can be used to make CNMs with improved stabilities.

5.3.4. N_2 Sorption Properties.

In evaluating the pore structure of complexes before and after the metal-ion metathesis process N_2 sorption experiment was conducted. The N_2 uptake capacity of **1**(Cd) was found to be poor with the value of 13 cm^3g^{-1} (at P/P_0 =1) and BET surface area of 12.5 m^2g^{-1}. Despite these disappointing results, literature report suggested that metathesis could enhance stability and sorption properties.[68,69] Motivated by this, N_2 sorption studies were performed on **1**(Cu) under similar experimental conditions. The results revealed a notable improvement with N_2 uptake capacity reaching 130 cm^3g^{-1} (at P/P_0 = 1) and exhibited a typical type II adsorption isotherm (Figure 11b). The calculated BET surface area for **1**(Cu) was found to be 114 m^2g^{-1}. The tenfold increase in the value of surface area compared to the parent compound **1**(Cd) indicates that metal ion metathesis substantially elevates the porosity of the materials.

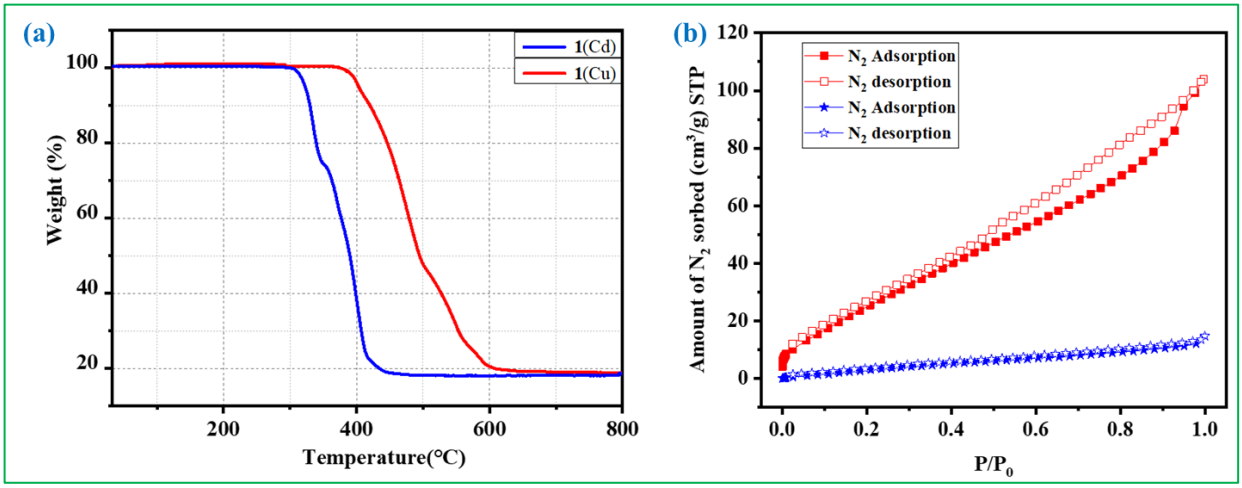

Figure 11. (a) Thermogravimetric analysis (TGA) of **1**(Cd) and **1** (Cu) in nitrogen atmosphere. **(b)** Figure shows the N_2 sorption isotherms of **1**(Cd**) (**blue**)** and **1**(Cu) (red) at 77 K (filled symbols represent sorption and empty symbols represent desorption).

Pore size distribution analysis derived from N_2 sorption data at 77 K using the non-local density functional theory (NL-DFT) method suggested pore widths of 15.35 Å for **1**(Cd) and 14.69 Å for **1**(Cu) (Figure 12 a&b). These values indicate the microporous nature in both the cases compounds and the pore width remained unchanged after metathesis. However, a significant reduction in defective pore sites and increased uniformity in pore width were observed through NL-DFT for **1**(Cu) resulting in a tenfold increase in N_2 uptake. The reduction in defective pore sites and the

improved homogeneity in pore width following metathesis reaction emerge as pivotal factors contributing to the notable enhancement in the material's sorption properties.

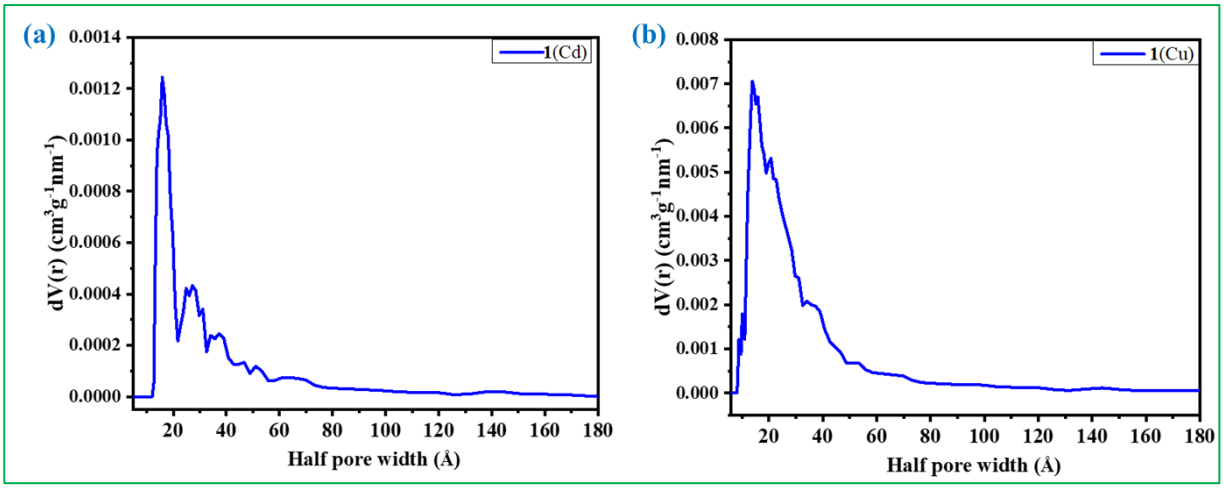

Figure 12. NL-DFT pore size distribution curve for **(a)** **1**(Cd) and **(b)** **1**(Cu) obtained from the N_2 sorption isotherm at 77K and 1 atm.

5.3.5. Photoluminescence and Lifetime Properties.

Due to their potential for emission behaviour and versatile applications in chemical sensors, photochemistry, and electroluminescent displays, there is considerable interest in CNMs of organic ligands.[71] Thus, the photoluminescence properties of **1**(Cd) and **1**(Cu) were explored in DMF. **1**(Cd) shows strong blue ligand-based emission centered at 378 nm and **1**(Cu) shows ligand-based emission centered at 392 nm upon excitation at 300nm (Figure 13a). Compared with **1**(Cd), **1**(Cu) shows 14 nm red shifted emission with decreased intensity.

To get the deeper understanding of photoluminescence properties we have also carried out the TCSPC experiment for both the compounds (Figure 13b). From the TCSPC experiment the obtained excited state lifetime of **1**(Cd) and **1**(Cu) was 1.96 ns and 2.46 ns respectively. From the excited state lifetime calculation, it was observed that **1**(Cu) exhibits higher excited state lifetime compared to its parent CNM which indicates that **1**(Cu) have higher excited state stability. This suggests that metathesis of Cd^{2+} by Cu^{2+} can be utilized to prepare a modified CNM with higher wavelength emission and higher lifetime of excited state of ligand-based emission.

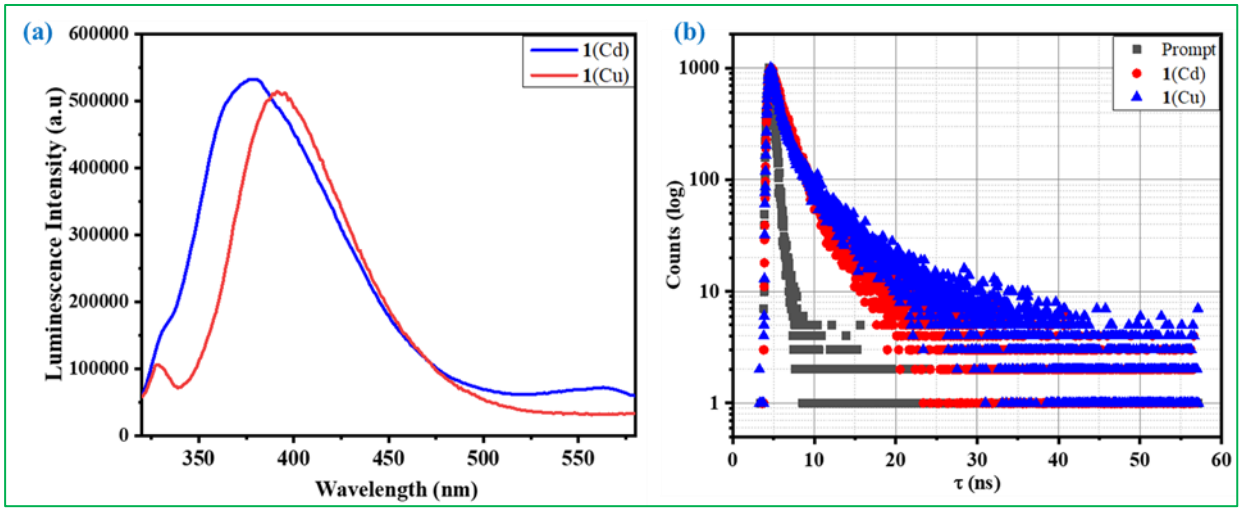

Figure 13. **(a)** Emission spectra of **1**(Cd) (blue) and **1**(Cu) (red) in DMF medium upon excitation at 300nm. **(b)** Figure shows time resolved luminescence decay of **1**(Cd) and **1**(Cu) (λ_{ex} = 300 nm and λ_{em} = 378 and 392 nm respectively for **1**(Cd) and **1**(Cu)).

5.3.6. Aza-Michael reaction by 1(Cd).

To see the catalytic activity of the **1**(Cd) by considering the Lewis acidity, we have selected the cyanoethylation of amine with acrylonitrile. Direct cyanoethylation of amines is an attractive method for installing nitriles in a molecule and synthesizing intermediates for many pharmaceuticals.[81] Initially, we optimized the reaction of cyanoethylation of aniline in various solvents such as DMF, CH_3CN, DCM, acetone, and methanol and the study revealed that the protic, polar solvent methanol gave the best result in terms of yield. After those different amines, as shown in Table 5, were reacted with acrylonitrile using the optimized condition. The crude mixture was subjected to the ^{1}H-NMR analysis to get the conversion percentage (see Figure14(a-f). The progress of the Aza-Michael reactions was monitored by TLC and yield/percentage of conversion was measured from the ^{1}H-NMR of the crude reaction mixture after removing the solid catalyst by filtration and the solvent under reduced pressure. It appeared that the reaction was susceptible to the electronic properties of the attached group to the amine. Aromatic amines such as aniline gave poor result (15% yield), toluidine gave moderate results (55% yield). The electron donation group containing aromatic amines such as 4-methoxy aniline (3) gave a quantitative yield of mono cyanoethylation product (3a). These results suggested that the **1**(Cd) could weakly activate the Michael acceptor acrylonitrile. Under the optimized condition, the aliphatic amines reacted relatively faster. Hence morpholine, benzylamine, and methyl propargyl amine give

quantitative conversion within 8 hrs. Aliphatic primary amine, however, predominantly gave the di-cyanoethylation product (5b), as shown in entry 5. The solid catalyst **1**(Cd) was reusable after recovery, and the catalytic activity almost remained unaltered for up to five cycles. Thus, the **1**(Cd) acted as a reusable solid phase catalyst for cyanoethylation reaction.

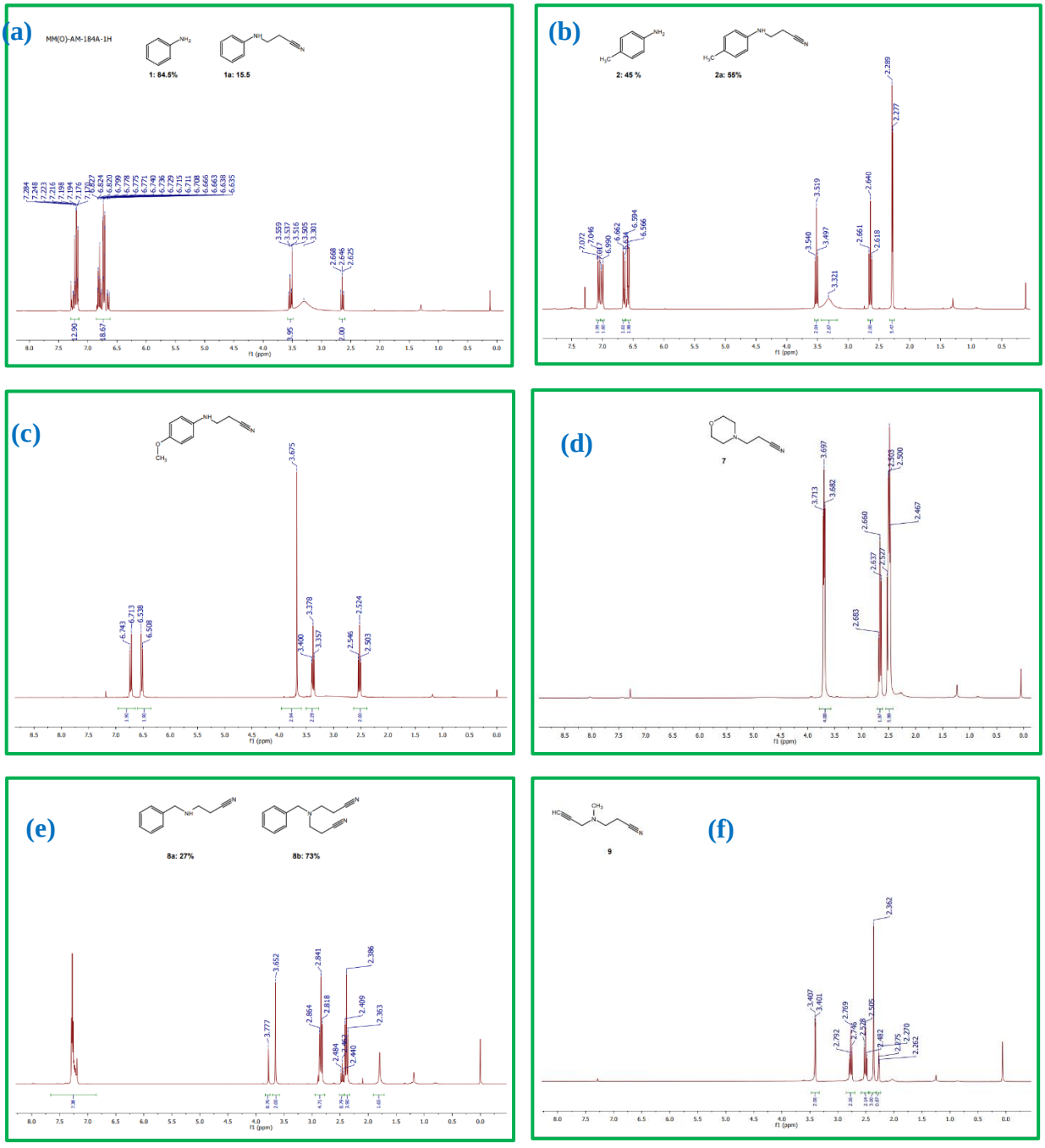

Figure 14. ^{1}H-NMR spectra of crude reation mixture of **(a)** entry 1 **(b)** entry 2 **(c)** entry 3 **(d)** entry 4 **(e)** entry 5 **(f)** entry 6.

Table 5: Cyanoethylation of amines**.**

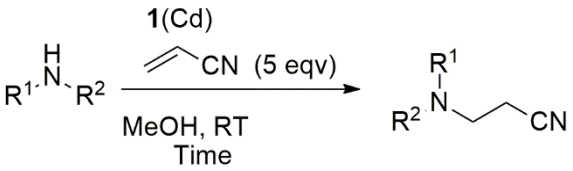

Entry	Substrate	Observed Product(s)	Conversion (Time hrs)
1	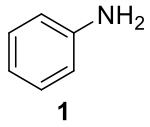 **1**	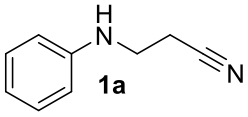 **1a**	15.5 (24)
2	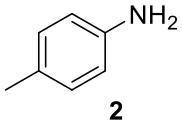 **2**	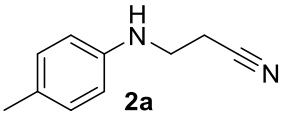 **2a**	55% (24)
3	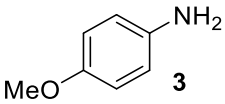 **3**	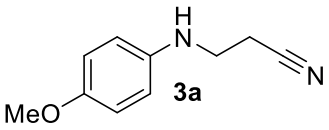 **3a**	> 99% (8)
4	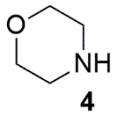 **4**	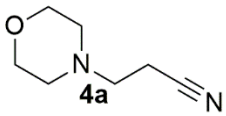 **4a** (Quantitative)	> 99% (8)
5	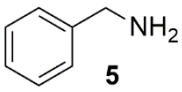 **5**	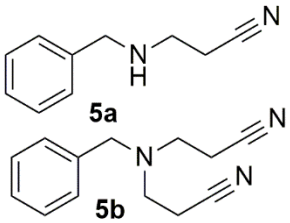 **5a** **5b**	>99% (8) **5a**: 27% **5b**: 73%
6	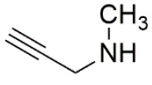 **6**	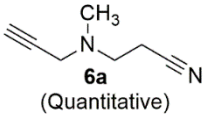 **6a** (Quantitative)	>99% (8)

The present work demonstrates that the Cd metal centre, probably penta coordinated Cd^{2+} ions, within the CNM structure could weakly activate acrylonitrile. A proposed reaction mechanism for the aza-Michael addition reaction of amine to electron-deficient alkene over heterogeneous **1**(Cd) catalyst is shown in figure 15. The mechanism involves the initial coordination of nitrile nitrogen of Michael acceptor to unsaturated Cd(II) open metal sites (five coordinated) to rise the electrophilicity of the β-carbon (I). This intermediate species reacts with the amine to generate a new carbon–nitrogen bond (II), and simultaneously form (III) by intermolecular proton transfer. In the final step, the corresponding product was formed and releasing the **1**(Cd).

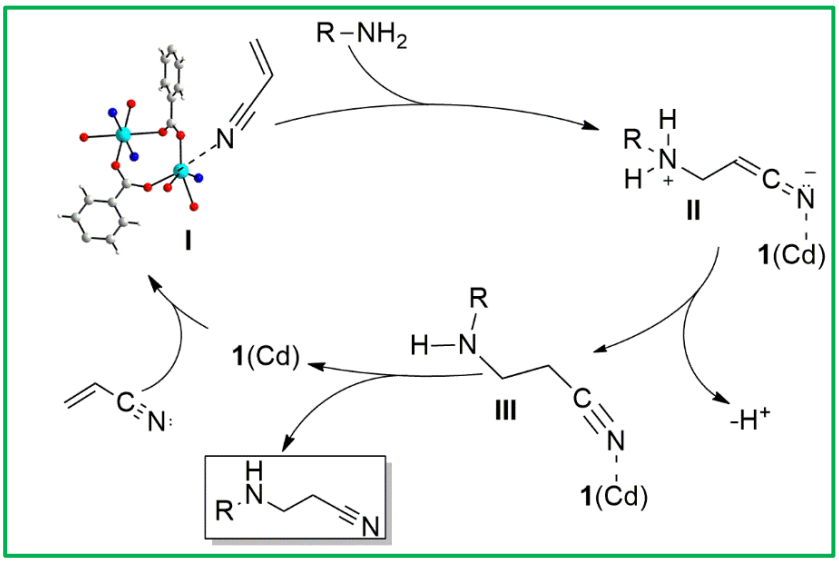

Figure 15. Figure shows the scheme of the proposed reaction mechanism for the aza-Michael addition of aromatic/aliphatic amines with acrylonitrile activated by **1**(Cd).

5.4. CONCLUSION

In conclusion, the synthesis and design of Crystalline Network Materials (CNMs) offer versatile applications across various fields, yet controlling their structure remains challenging. Post-synthetic modification (PSM) emerges as a viable strategy to overcome structural unpredictability and enhance properties. In this study, the successful construction of $[Cd_3(L)_2(LH)_2(bpe)_2]$, **1**, and its transformation into **1**(Cu) through metal exchange exemplifies the potential of PSM in tailoring CNMs. The resulting **1**(Cu) exhibited improved thermal stability, emission characteristics and gas uptake compared to its precursor. Moreover, **1**(Cd) demonstrated efficacy as a catalyst for aza-

Michael addition reactions under mild conditions, highlighting its utility in green and sustainable synthesis methodologies. Overall, this work contributes to the advancement of controlled CNM design and explores the practical utility of metal-catalyzed reactions in diverse synthetic applications.

REFERENCES

1. C.-C. Sun, K. Xu, C.-C. Zeng, *ACS Sustainable Chem. Eng.*, 2019, **7**, 2255−2261.
2. Z. Amara, J. Caron, D. Joseph, *Nat. Prod. Rep*, 2013, ***30***, 1211-1225.
3. F. Gnad, O. Reise, *Chem. Rev.*, 2003, **103**, 1603.
4. A. Michael, J. Prakt. Chem. 1887, **35**(1), 349−356.
5. G. Cardillo, C. Tomasini, *Chem. Soc. Rev.*, 1996, **25**, 117.
6. S. Herold, D. Bafaluy, K. Muñiz, *Green Chem.*, 2018, **20** (14), 3191−3196.
7. K. A. Margrey, J. B. McManus, S. Bonazzi, F. Zecri, D. A. Nicewicz, *J. Am. Chem. Soc.*, 2017, ***139*** (32), 11288−11299.
8. L. Niu, H. Yi, S. Wang, T. Liu, J. Liu, A. -W. Lei, *Nat. Commun.*, 2017, **8**, 14226−14232.
9. J. Bariwal, E. V. Eycken, *Chem. Soc. Rev.*, 2013, **42** (24), 9283−9303.
10. Q. Zhuo, J. Yang, X. Zhou, T. Shima, Y. Luo, Z. Hou, *J. Am. Chem. Soc*. 2023, **145**, 22803−22813.
11. B. Çelik, D. Kandemir, S. Luleburgaz,; E. Çakmakçi, U. S. Gunay, V. Kumbaraci, H. Durmaz, *ACS Sustainable Chem. Eng.* 2023, **11**, 831−841.
12. M. Sanchez-Rosell,́ J. L. Aceñ, A. Simón-Fuentes, C. del-Pozo, *Chem. Soc. Rev.*, 2014, ***43***, 7430.
13. D. Enders, C. Wang, J. X. Liebich, *Chem. Eur. J.* 2009, ***15***, 11058.
14. X. Gao, C. Shan, Z. Chen, Y. Liu, X. Zhao, A. Zhang, P. Yu, H. Galons, Y. Lan, K. Lu, *Org. Biomol. Chem.* 2018, **16**, 6096−6105.
15. E. M. Hinds, J. P. Wolfe, *J. Org. Chem.* 2018, **83**, 10668−10676.
16. A. Lauber, B. Zelenay, J. Cvengros, *Chem. Commun.* 2014, **50**, 1195−1197.
17. M. Sanchez-Rosell, J. L. Acen. A. Simon-Fuentes, C. del-Pozo,́ *Chem. Soc. Rev.* 2014, **43**, 7430−7453.
18. S. Kim, S. Kang, G. Kim, Y. Lee, *J. Org. Chem.* 2016, **81**, 4048−4057.
19. J. Peyrton, L. Avérous, *ACS Sustainable Chem. Eng.* 2021, **9**, 4872−4884.
20. H. Sunaba, K. Kamata, N. Mizuno, *ChemCatChem*, 2014, **6**, 2333.
21. S.-J. Lee, J.-G. Ahn, C.-W. Cho, *Tetrahedron: Asymmetry*, 2014, **25**, 1383−1388.
22. X.-J. Tang, Z.-L. Yan, W.-L. Chen, Y.-R. Gao, S. Mao, Y.-L. Zhang, Y.-Q. Wang, *Tetrahedron Lett.* 2013, **54**, 2669.
23. X.-J. Han, *Tetrahedron Lett*. 2007, **48** (16), 2845−2849.
24. S. D. Bull, S. G. Davies, S. Delgado-Ballester, G. Fenton, P. M. Kelly, A. D. Smith, *Synlett*, 2000, **9**, 1257−1260.
25. J. Wang, P.-F. Li, S. H. Chan, A. S. C. Chan, F. Y. Kwong, *Tetrahedron Lett*. 2012, **53** (23), 2887−2889.
26. L.-X. Li, Z.-L. Liu, Q.-L. Ling, X. D. Xing, *J. Mol. Catal. A*: Chem. 2012, **353**, 178−184.
27. M. L. Kantam, M. Roy, S. Roy, B. Sreedhar, R. L. De, *Catal. Commun*. 2008, **9** (13), 2226− 2230.

28. M. L. Lakshmi Kantam, B. Neelima, C. V. Reddy, R. Chakravarti, *Ind. Eng. Chem. Res.* 2007, **46** (25), 8614−8619.
29. M. Dewan, A. De, S. Mozumdar, *Inorg. Chem. Commun*. 2015, **53**, 92−96.
30. F. Rajabi, S. Razavi, R. Luque, *Green Chem.* 2010, **12** (5), 786−789.
31. L. Fadini, A. Togni, *Chem. Commun*. 2003, No. **1**, 30−31.
32. X. Lefevre, G. Durieux, S. Lesturgez, D. Zargarian, *J. Mol. Catal. A*: *Chem*. 2011, **335** (1−2), 1−7.
33. L. Dai, Y. Zhang, Q. Dou, X. Wang, Y. Chen, *Tetrahedron*, 2013, **69** (6), 1712−1716.
34. X. Ai, X. Wang, J.-M. Liu, Z.-M. Ge, T.-M. Cheng, R.-T. Li, *Tetrahedron*, 2010, **66** (29), 5373− 5377.
35. D. Stevanovic, A. Pejovic, I. Damljanovic´, M. Vukic´ evic´,´ G. A. Bogdanovic, R. D. Vukic´ evic,´ *Tetrahedron Lett*. 2012, **53** (46), 6257−6260.
36. K. Damera, K. L. Reddy, G. V. M. Sharma, *Lett. Org. Chem*. 2009, **6** (2), 151−155.
37. M. J. Bhanushali, N. S. Nandurkar, S. R. Jagtap, B. M. Bhanage, *Catal. Commun*. 2008, **9** (6), 1189−1195.
38. H. A. Hamzah, T. S. Crickmore, D. Rixson, A. D. Burrows, *Dalton Trans*., 2018, **47**, 14491–14496.
39. C. Jiang, X.Wang, Y. Ouyang, K. Lu, W. Jiang, H. Xu, X. Wei, Z. Wang, F. Dai, D. Sun, *Nanoscale Adv.*, 2022, **4**, 2077-2089.
40. V. Pascanu, G. G. Miera, A. K. Inge, B. Martín-Matute, *J. Am. Chem. Soc*. 2019, **141**, 18, 7223–7234.
41. C. Li, H. Zhang, M. Liu, F. -F. Lang, J. Pang, X. -H. Bu, *Ind. Chem. Mater*., 2023, **1**, 9-38.
42. E. Linnane, S. Haddad, F. Melle, Z. Mei, and D. Fairen-Jimenez, *Chem. Soc. Rev*., 2022, **51**, 6065-6086.
43. T. K. Pal, *Mater. Chem. Front*., 2023,**7**, 405-441.
44. S. Ghosh, A. Rana, and S. Biswas, https://doi.org/10.1021/acs.chemmater.3c02459
45. W. P. Lustig, S. Mukherjee, N. D. Rudd, A. V. Desai, J. Li, S. K. Ghosh, *Chem. Soc. Rev*., 2017, **46**, 3242.
46. S. Mandal, S. Natarajan, P. Mani, and A. Pankajakshan, *Adv. Funct. Mater*. 2021, **31**, 2006291.
47. K. S. Asha, R. Bhattacharjee, S. Mandal, *Angew. Chem. Int. Ed*. 2016, **55**, 11528 –11532.
48. G. Dutta, A. K. Jana, S. Natarajan, *Chem. Eur. J*. 2017, **23**, 8932 – 8940.
49. G. Mukherjee, and K. Biradha, *Chem. Commun*., 2012, **48**, 4293–4295.
50. C. K. Brozek, M. Dinca, *Chem. Soc. Rev*., 2014, **43**, 5456 -5467.
51. A. M. Shultz, A. A. Sarjeant, O. K. Farha, J. T. Hupp, S. T. Nguyen, *J. Am. Chem. Soc*. 2011, **133**, 13252–13255.
52. T. -F. Liu, L. Zou, D. Feng, Y. -P. Chen, S. Fordham, X. Wang, Y. Liu, H. -C. Zhou, *J. Am. Chem. Soc*. 2014, **136**, 7813−7816.
53. S. Das, H. Kim, and K. Kim, *J. Am. Chem. Soc*. 2009, **131**, 3814–3815.
54. M. Lalonde, W. Bury, O. Karagiaridi, Z. Brown, J. T. Hupp, O. K. Farha, *J. Mater. Chem. A*, 2013, **1**, 5453–5468.
55. X. Song, T. K. Kim, H. Kim, D. Kim, S. Jeong, H. R. Moon, M. S. Lah, *Chem. Mater*. 2012, **24**, 3065−3073.
56. Y. Kim, S. Das, S. Bhattacharya, S. Hong, M. G. Kim, M. Yoon, S. Natarajan, and K. Kim, *Chem. Eur. J*. 2012, **18**, 16642 – 16648.

57. J.-H. Wang, Y. Zhang, M. Li, S. Yan, D. Li, and X. -M. Zhang, *Angew. Chem. Int. Ed*. 2017, **56**, 6478 –6482.
58. T. He, X. -J. Kong, J. Zhou, C. Zhao, K. Wang, X. -Q. Wu, X. -L. Lv, G. -R. Si, J. -R. Li, Z. R. Nie, *J. Am. Chem. Soc*. 2021, **143**, 9901−9911.
59. C. K. Brozek, L. Bellarosa, T. Soejima, T. V. Clark, N. Lopez, M. Dinca. *Chem. Eur. J.* 2014, **20**, 6871 – 6874.
60. F. A. Son, A. Atilgan, K. B. Idrees, T. Islamoglu, O. K. Farha, *Inorg. Chem. Front.*, 2020, **7**, 984–990.
61. M. Kim, J. F. Cahill, H. Fei, A. K. Prather, S. M. Cohen, *J. Am. Chem. Soc.* 2012, **134**, 18082−18088.
62. H. Nasi, M. C. d. Gregorio, Q. Wen, L. J. W. Shimon, I. Kaplan-Ashiri, T. Bendikov, G. Leitus, M. Kazes, D. Oron, M. Lahav, M. E. v. d. Boom, *Angew. Chem*. 2022, **134**, e202205238.
63. D. Yu, Qi. Shao, Q. Song, J. Cui, Y. Zhang, B. Wu, L. Ge, Y. Wang, Y. Zhang, Y. Qin, R. Vajtai, P. M. Ajayan, H. Wang, T. Xu, Y. Wu, *Nat Commun*, 2020, **11**, 927.
64. R. E. Sikma, N. Katyal, S. -K. Lee, J. W. Fryer, C. G. Romero, S. K. Emslie, E. L. Taylor, V. M. Lynch, J. -S. Chang, G. Henkelman, S. M. Humphrey, *J. Am. Chem. Soc.* 2021, **143**, 13710−13720.
65. J. Park, D. Feng, H. -C. Zhou, *J. Am. Chem. Soc*. 2015, **137**, 11801−11809.
66. T. Kundu, S. C. Sahoo, S. Saha, and R. Banerjee, *Chem. Commun*., 2013, **49**, 5262.
67. X. Liu, C. Hao, J. Li, Y. Wang, Y. Hou, X. Li, L. Zhao, H. Zhu, and W. Guo, *Inorg. Chem. Front*., 2018, **5**, 2898.
68. S. Liu, B. Liu, S. Yao, and Y. Liu, *Inorg. Chem. Front*., 2020, **7**, 1591–1597.
69. F. Zhang, Y. Zhang, X. Wang, J. Li, and J. Yang, *Inorg. Chem. Front.*, 2022, **9**, 5434–5443.
70. M. Dincaˇ, J. R. Long, *J. Am. Chem. Soc.* 2007, **129**, 11172-11176.
71. P. -P. Cui, X. -D. Zhang, P. Wang, Y. Zhao, M. Azam, S. I. Al-Resayes, W. -Y. Sun, *Inorg. Chem*. 2017, **56**, 14157−14163.
72. J. Yang, X. Wang, F. Dai, L.Zhang, R. Wang, D. Sun, *Inorg. Chem*. 2014, **53**, 10649−10653.
73. A. Hazra, S. Bonakala, S. A. Adalikwu, S. Balasubramanian, and T. K. Maji, *Inorg. Chem*. 2021, **60**, 3823−3833.
74. H. Irving, R. J. P. Williams, *J. Chem. Soc*. 1953, 3192−3210.
75. *Apex3 v2017.3-0*, *Saint V8.38A*, *SAINT V8.38A*; Bruker AXS Inc.: Madison, WI, 2018.
76. L. Krause, R. Herbst-Irmer, G. M. Sheldrick, *Appl. Crystallogr.* 2015, **48**, 3.
77. A. Altomare, G. Cascarano, C. Giacovazzo, A. Guagliardi, *J. Appl. Crystallogr.* 1993, **26**, 343.
78. G. M. Sheldrick, *ActaCrystallogr., Sect. C: Struct. Chem.*,2015, **71**, 3.
79. L. J. Farrugia, *J. Appl. Crystallogr.*,1999, **32**, 837.
80. A. L. Spek, *J. Appl. Crystallogr.* 2003, **36**, 7.
81. R. C. Cookson, and F. G. Mann, *Journal of the Chemical Society (Resumed).* 1949, **67**.

CHAPTER-6

Unlocking Enhanced Hydrogen Evolution with Bimetal-Organic Framework: A Synergistic Approach

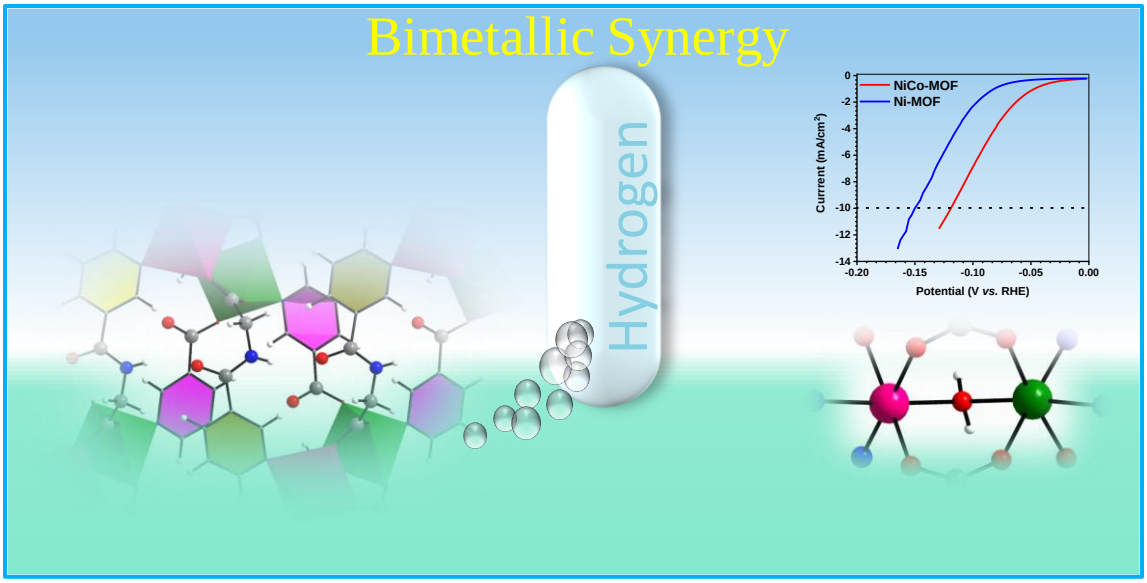

CHAPTER-6

Unlocking Enhanced Hydrogen Evolution with Bimetal-Organic Framework: A Synergistic Approach

6.1. INTRODUCTION

In the contemporary quest for a sustainable society, the focus lies on developing energy sources that are both environmentally friendly and economically viable.[1] Hydrogen, often heralded as a promising energy carrier for the future, possesses renewable attributes, widespread availability, high energy density, various production methods, and emits no pollutants.[2] However, conventional techniques like steam reforming rely on fossil fuels, contradicting the goal of reducing dependence on non-renewable energy sources and emitting greenhouse gases.[3, 4]

Electrochemical water-splitting emerges as a leading method among renewable alternatives for hydrogen production, using water as the primary raw material and minimizing environmental impact.[5] Nevertheless, this process involves two slow kinetic half-reactions: the oxygen evolution reaction and the hydrogen evolution reaction. To accelerate the process, a catalyst is necessary to break the strong bond between oxygen and hydrogen within water molecules.[6] While noble metals like iridium, ruthenium, and platinum commonly serve as catalysts,[7, 8] their high cost, limited availability, and questionable durability pose significant constraints on widespread practical application.[9] Therefore, creating catalysts from abundant materials that are both highly active and cost-effective is a key focus for advancing efficient water electrolysis systems.[10]

Addressing this challenge is crucial, and metal-organic frameworks (MOFs) present a groundbreaking solution.[11, 12] Formed by the fusion of metallic centers with organic connectors, MOFs possess unique properties such as high porosity, flexible structure, large surface area, and crystalline nature.[13, 14] These attributes make them suitable for various applications, including catalysis, alongside CO_2 capture, sensors, wastewater treatment, and biomedical uses.[15] Moreover, the precisely distributed metal sites and well-defined atomic structures within MOFs provide ideal platforms for investigating active sites' properties and understanding electrocatalytic activity origins.[16]

While pristine MOFs often exhibit inadequate electrical conductivity, modified derivatives demonstrate notable stability and serve as highly efficient catalysts for hydrogen evolution reactions.[17] These modifications encompass a variety of materials, metal oxides/hydroxides,[18, 19] carbides,[20] chalcogenides,[21, 22] phosphides,[23] nitrides,[24] and their hybrids, alongside carbon composites[25].[26] Despite challenges such as multiple synthesis steps and energy-consuming procedures, recent years have seen a remarkable increase in utilizing MOFs' versatile chemistry to develop highly effective electrocatalysts.[27, 28]

A notable trend in this domain involves the development of bimetallic MOFs specifically for enhancing Oxygen Evolution Reaction(OER) is well documented,[29-31] But the development of bimetallic MOF specifically aimed at enhancing the Hydrogen Evolution Reaction (HER) activity is remain a uncharted territory.[32] Notably, Geng et al. reported the superior HER performance of a bimetallic Cu-Co-CAT compared to monometallic counterparts, attributing it to efficient electronic coupling between Cu and Co centers. This coupling reduces the water adsorption energy ($\Delta E\ H_2O$) of Co sites, accelerating the Volmer step in the HER process. The "synergistic effect" observed in bimetallic systems directly reflects the influence of "proximity" and remains a significant advancement in electrocatalysis, particularly in the HER.[33]

Keeping this in mind, our study presents a bimetallic MOF (NiCo-MOF) comprised of Ni(II) and Co(II) metal centers, nicotinate (NA), N-nicotinoyl glycinate (N-NG) ligands, and a μ_2-H_2O molecule. The structure was determined by synthesizing isostructural homometallic Ni-based MOF (Ni-MOF). This bimetallic NiCo-MOF demonstrates remarkable performance with very low (39mV/dec) Tafel slope value and low overpotential (120mV) at 10mA/cm^2 in the electrocatalysis of the hydrogen evolution reaction (HER) under acidic conditions, outperforming its single-metal counterparts based on nickel. Moreover, it surpasses previously reported Tafel slopes and overpotential values for most existing pristine MOFs. Our results highlight the crucial role of synergistic interactions between active metal centers in bimetallic systems, presenting a promising pathway for the systematic design of highly efficient electrocatalysts based on pristine MOFs.

6.2. EXPERIMENTAL SECTION

6.2.1. Materials.

The chemicals required for the synthesis of compound Ni-MOF and NiCo-MOF, $Ni(CH_3CO_2)_2.4H_2O$ (Loba-Chemie, 98%), N- Nicotinoyl Glycine (TCI, >98%), and $Co(CH_3CO_2)_2.4H_2O$ (Sigma-Aldrich, ≥98%) were used as received. The chemicals used for the electrochemical measurements were DMF (99%, Merck), and PVDF (Merck) used as received without further purification. The water used was double distilled.

6.2.2. Synthesis of Ni-MOF.

The Ni-MOF was synthesized using the hydrothermal method. A solution was prepared by dissolving 0.5 mM (0.1269g) of $Ni(CH_3CO_2)_2.4H_2O$ and 0.5 mM (0.0919g) of N-nicotinoyl glycine (N-NG) in 5 ml of distilled water. The mixture was homogenized for 30 minutes at room temperature. Following homogenization, the solution was sealed in a 23 ml PTFE-lined stainless-steel autoclave and heated at 140°C for 72 hours. The resulting product appeared as light green-coloured block-shaped crystals. The crystals were filtered, washed with deionized water under vacuum, and dried under ambient conditions, yielding 75% based on the metal. The calculated elemental analysis for $C_{26}H_{21}N_5O_{10}$ was as follows: C, 45.82%; H, 3.08%; N, 10.28%. The found values after analysis were C, 45.78%; H, 3.02%; N, 10.36%.

6.2.3. Synthesis of NiCo-MOF.

The synthesis method similar to that employed for Ni-MOF was utilized, with a modification in the metal precursors. Equal amounts of $Co(CH_3CO_2)_2.\ 4H_2O$ and $Ni(CH_3CO_2)_2.\ 4H_2O$ were dissolved in a 1:1 ratio (.25mM each, totaling 0.0635g for $Co(CH_3CO_2)_2$ and 0.0634g for $Ni(CH_3CO_2)_2$ in 5 ml of distilled water. The final product consisted of purple-colored crystals. After this period, the crystals were filtered, washed with deionized water under vacuum, and then dried under ambient conditions.

6.2.4. Single Crystal X-ray Diffraction.

Suitable single crystals were carefully selected under an optical microscope and mounted on thin glass fiber carefully. The single crystal data of both the compounds were collected using Bruker D8-Quest diffractometer. The instrument was equipped with Mo Kα (λ=0.71073Å) radiation source and operating voltage of X-ray generator was 50kV and 1mA. Diffraction data

were collected with ω scan width of 0.5º. Three different setting of φ (0, 90, 180º) were used to collect the total 408 frames, keeping a fixed distance of sample-to-detector at 6.03 cm and the detector position (2θ) was fixed at -25º. The initial indexing, final data sets, and cell refinements were handled by an APEX3 program, while a SAINTPLUS[75]program was utilized for the frame integration and final cell parameter calculation. The multi-scan absorption data was corrected by a SADABS program.[34] We initially solved the structure by SIR 92,[35] and the full matrix least-square method (SHELXL-2016[36]) was used further, which is present in the WinGx suit of programs (Version 1.63.04a).[37, 38]) With the help of Fourier maps, we successfully located all the non-hydrogen atoms and refined them anisotropically. Finally, all the hydrogen atoms were fixed at calculated positions and included them in the refinement process using riding model associated with isotropic thermal parameters. The details of the crystal and final refinements are given in the Table 1. CCDC: 2368873 contain the crystallographic data for this paper. These data can be obtained free of charge from The Cambridge Crystallographic Data Center (CCDC) via www.ccdc.cam.ac.uk/data_request/cif.

Table 1: Crystal data and structure refinement parameters for $[Ni_2(NNG)(NA)_3(\mu_2\text{-}H_2O)]$, Ni-MOF.

Empirical formula	$C_{26}H_{21}N_5Ni_2O_{10}$
Formula weight	680.90
Crystal system	Orthorhombic
Space group	*P b c a*
a (Å)	10.0638(8)
b (Å)	20.4928(17)
c (Å)	29.083(2)
α (deg)	90
β (deg)	90
γ (deg)	90
Volume ($Å^3$)	5997.9(8)
Z	8
T (K)	298(2)

ρcalc (g cm^{-3})	1.508
μ (mm^{-1})	1.317
θ range (deg)	1.988 to 27.118
λ (Mo Kα) (Å)	0.71073
R indices [I>2σ(I)]	R_1 = 0.0670, wR_2 = 0.0856
R indices (all data)	R_1 = 0.1130, wR_2 = 0.0986

$R_1 = \Sigma ||F_0|-|F_c|| / \Sigma |F_0|$; $wR_2 = \{\Sigma[w(F_0^2 - F_c^2)^2] / \Sigma[w(F_0^2)^2]\}^{1/2}$. $w = 1/[\sigma^2(F_0)^2 + (aP)^2 + bP]$, $P = [max.(F_0^2,0) + 2(F_c)^2]/3$, where a = 0.0051 and b = 13.5345

6.2.5. Powder X-ray Diffraction.

The Powder X-ray diffraction (PXRD) pattern of a finely ground sample was recorded using a Bruker D8 Advance X-ray diffractometer, employing Cu Kα radiation with a wavelength (λ) of 1.5418 Å. The experiment covered the 2θ range of 5-50° and was carried out at 40 kV and 40 mA (Figure 1). Examination of the acquired X-ray diffraction (XRD) pattern indicates the presence of a novel compound designated as Ni-MOF. Notably, the observed XRD pattern closely matches the simulated XRD pattern derived from the structure determined via single-crystal XRD. This agreement between the experimental and simulated patterns serves as unequivocal confirmation that Ni-MOF is entirely pure.

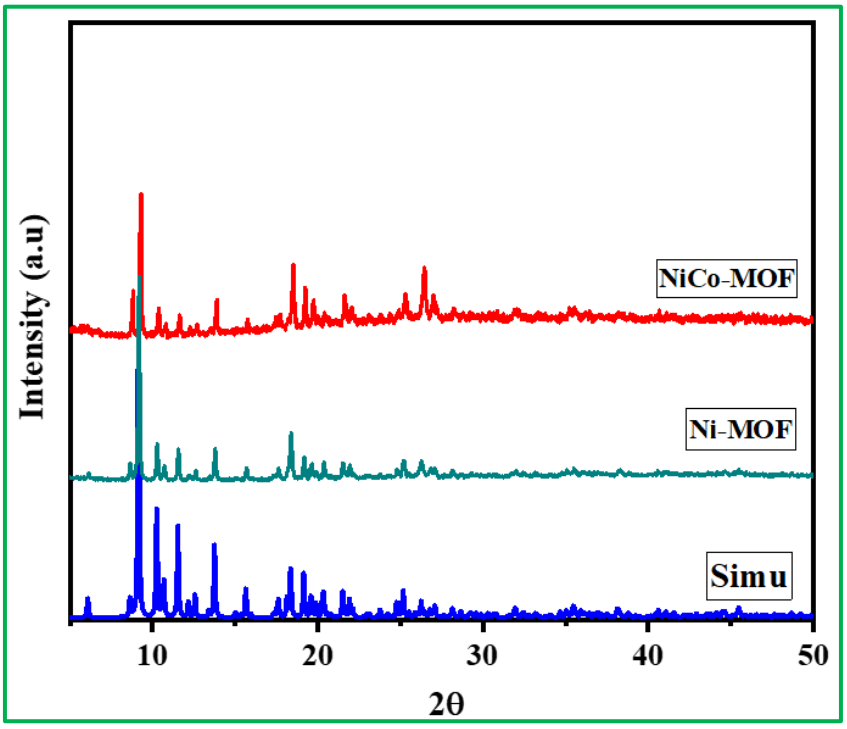

Figure 1. Powder XRD (CuKα) patterns of $[Ni_2(NNG)(NA)_3(\mu_2\text{-}H_2O)]$, Ni-MOF and NiCo-MOF.

6.2.6. FT-IR measurements.

The Fourier Transform Infrared (FT-IR) spectra were carefully obtained with the Nicolet Magna IR 750 series-II instrument, spanning a broad range from 400 to 4000 cm^{-1} (Figure 2). The identified infrared frequencies have been thoroughly recorded in Table 2.

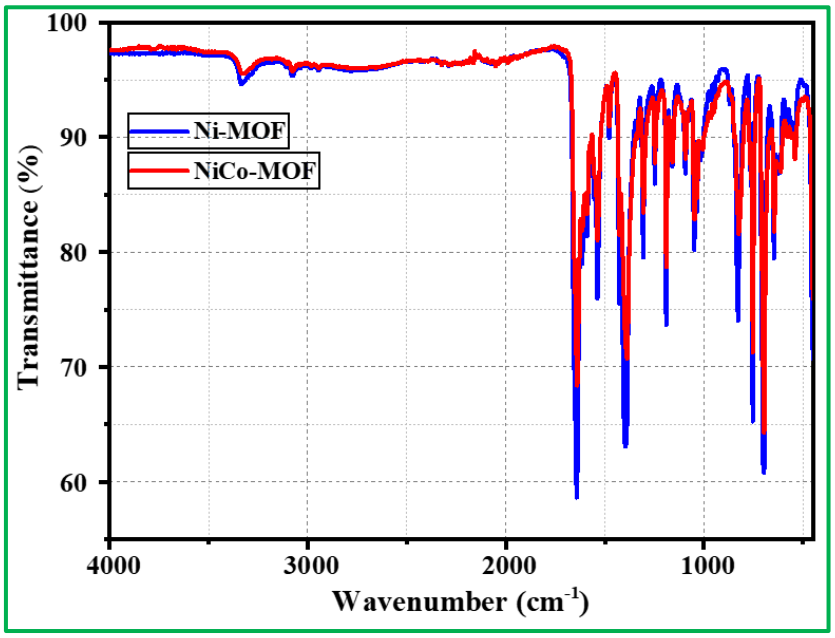

Figure 2. IR spectrum of $[Ni_2(NNG)(NA)_3(\mu_2\text{-}H_2O)]$, Ni-MOF and NiCo-MOF.

Table 2. The observed IR bands for $[Ni_2(NNG)(NA)_3(\mu_2\text{-}H_2O)]$, Ni-MOF.

Bands	Wavenumber (cm^{-1})	Bands	Wavenumber (cm^{-1})
υ_{str}(O-H stretching of μ_2-H_2O)	3323(s)	υ_{str}(C-N)	1247(s)
υ_{str}(amide N-H)	3079(w)	δ(aromatic C-H)$_{in\ plane\ bending}$	1185(s), 1094(s), 1052(w)
$\upsilon_{asy.\ str}$(carboxylate)	1644(s)	δ(aromatic C-H)$_{out\ of\ plane\ bending}$	823(m), 759(w)
υ_{str}(amide carboxylate)	1532(s)	δ(carboxylate)$_{bending}$	697(w)

υ_{str}(C=C)	1400(s)	δ(aromatic C=C)$_{out\ of\ plane\ bending}$	635(s)
$\upsilon_{sy.\ str}$(carboxylate)	1305(s)		

6.2.7. Thermal Stability.

Thermogravimetric analysis (TGA) was carried out on a Perkin-Elmer instrument STA 6000 under a nitrogen atmosphere (flow rate = 20 ml min^{-1}) in the temperature range 30 - 800°C (heating rate 10°C/min) (Figure 3). Ni-MOF and NiCo-MOF both are stable up to 345 ºC and 323 ºC respectively. Both the compounds are started to decompose at ~ 346 °C and ~ 324 °C. The removal of the organic parts has been completed at 515 °C for Ni -MOF, and at 500 °C for NiCo-MOF respectively. The total observed weight loss corresponds to 78% and 80% respectively. This weight loss matches nearly with the formation of Ni_2O_3 in Ni MOF (calculated: 76%) and Ni_2O_3 and Co_2O_3 were formed in NiCo-MOF (calculated: 76%).

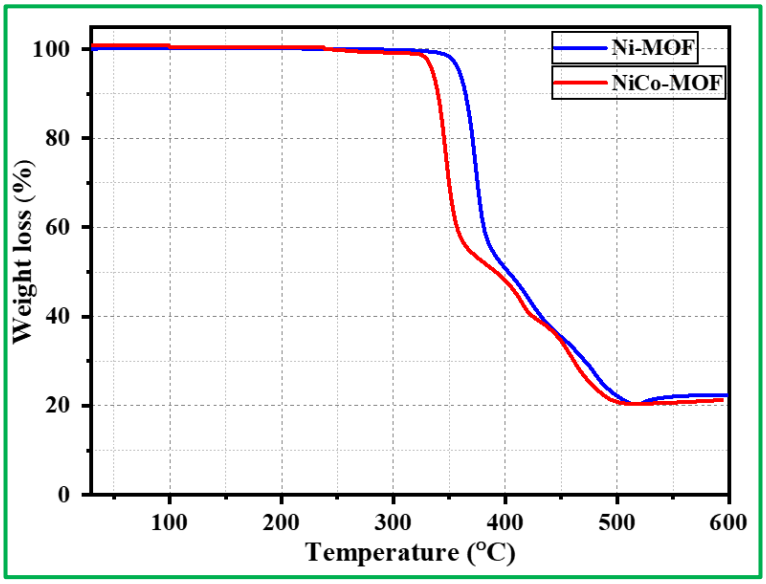

Figure 3. Thermogravimetric analysis (TGA) of Ni-MOF and NiCo-MOF in nitrogen atmosphere.

6.2.8. Field Emission Scanning Electron Microscopy (FE-SEM).

To monitor the morphology of Ni-MOF and NiCo-MOF FE-SEM experiment were carried out using a Zeiss Gemini SEM 450 field emission scanning electron microscope. The SEM images of Ni(II) and Co(II) mixed metal based NiCo-MOF have been investigated to compare its

morphology with that of the parent Ni-MOF. The images of Ni-MOF and NiCo-MOF show the same block shaped particles without any amorphous phases (Figure 4a&b). The SEM images also display homogeneous nano crystallites without the existence of any other morphology. The metal ions percentage in mixed metal MOF was also quantified by SEM–EDX analysis. The distribution of metal ions was assessed by elemental manning analysis. The elemental mapping using SEM-EDS analysis showed the presence of all the desired elements with the homogeneous distribution of it (Figure 4c) and it showed the Ni and Co ratio in NiCo-MOF is ~60:40 (Figure 4d). The integration of metal ions into the NiCo- MOF was also recognized through ICP-MS analysis. ICP-MS analysis indicates that the Ni and Co ratio in NiCo-MOF is 50:50 based on metal atom percentage.

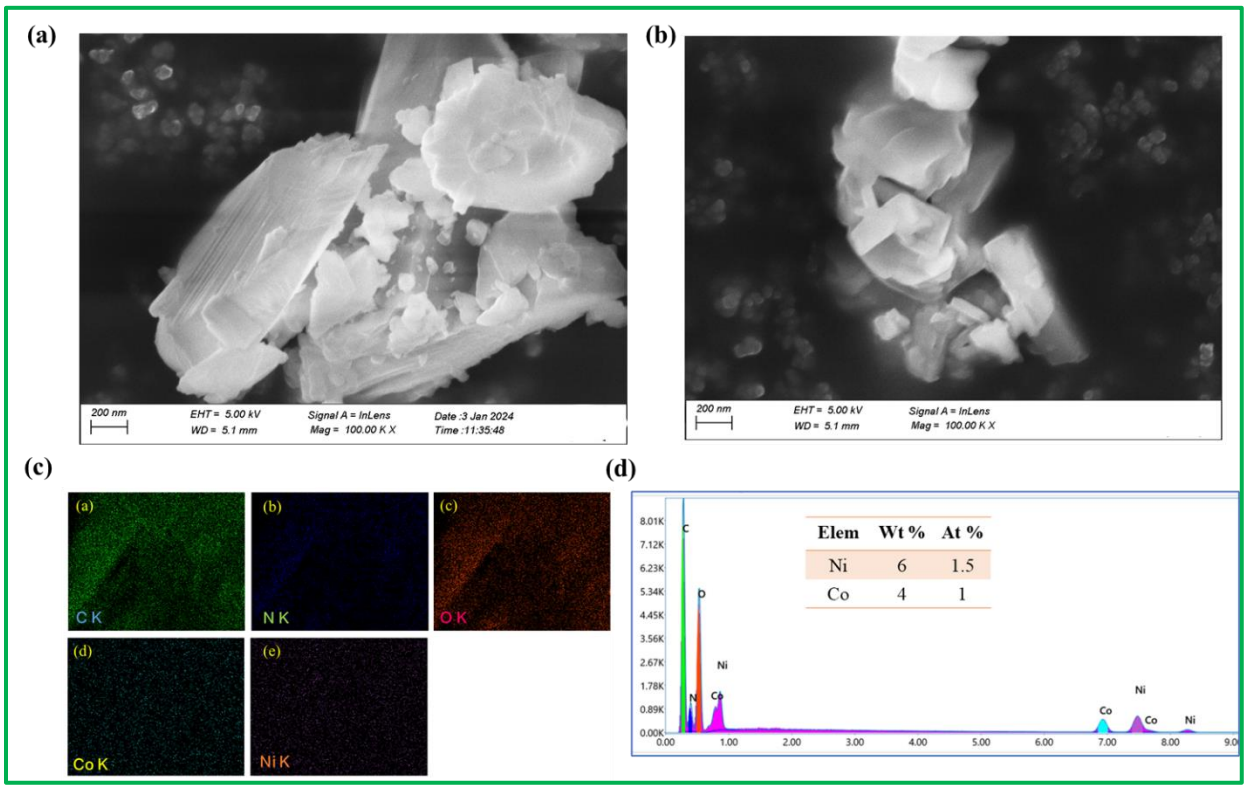

Figure 4. **(a)** SEM image of Ni-MOF **(b)** SEM image of NiCo-MOF **(c)** Representative EDX plot of NiCo-MOF. Note the presence of Ni and Co. **(d)** Elemental mapping images of NiCo-MOF for (a) C-K and (b) N-K, (c) O-K (d) Co-K and (e) Ni-K.

6.2.9. BET analysis.

The obtained adsorption isotherm behavior for both compounds exhibited a type II adsorption isotherm pattern, reaching a saturated gas uptake of 43.47 cm^3g^{-1} for Ni-MOF (Figure 5a) and 51.80 cm^3g^{-1} for NiCo-MOF (Figure 5b) at a pressure of 0.99 bar and a temperature of 77 K. The calculated BET (Brunauer–Emmett–Teller) surface area for Ni-MOF is 44.66 m^2g^{-1}, while for NiCo-MOF, it is 66.03 m^2g^{-1}. This high surface area of NiCo-MOF compared to monometallic Ni-MOF could be due to the synergistic effect between Ni and Co.

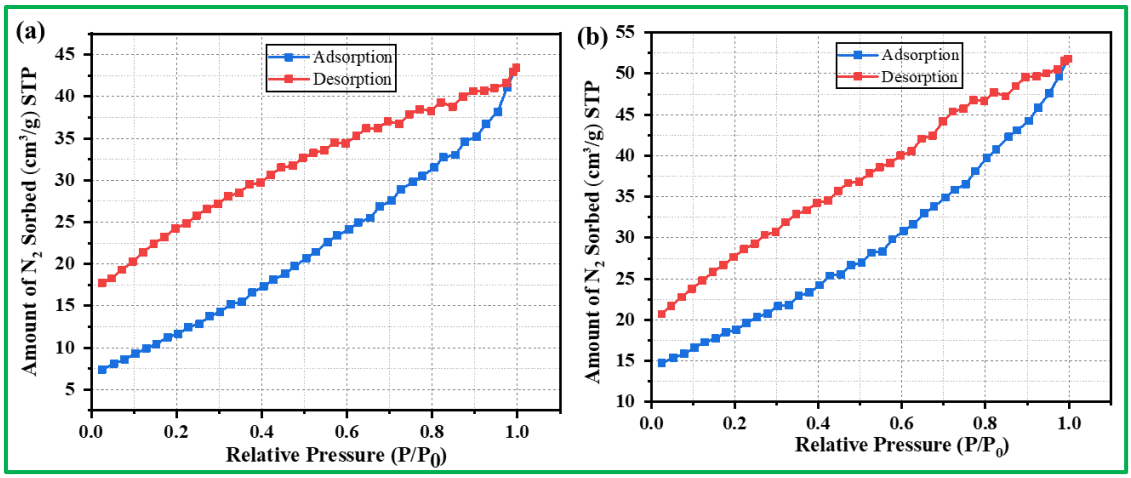

Figure 5. **(a)** N_2 adsorption (at 77 K) isotherms of Ni-MOF, **(b)** N_2 adsorption (at 77 K) isotherms of NiCo-MOF, blue represents the adsorption and red represents desorption.

6.2.10. Electrochemical Characterizations.

The electrocatalytic activities of Ni-MOF and NiCo-MOF towards HER were evaluated through Cyclic Voltammetry (CV), Linear Sweep Voltammetry (LSV), Electrochemical Impedance Spectroscopy (EIS) and chronoamperometry in 3-electrode electrochemical cell configurations. The 3-electrode electrochemical cells were assembled by catalyst (Ni-MOF and NiCo-MOF) coated glassy carbon working electrodes, Pt foil counter electrodes and Ag/AgCl reference electrodes (+0.197 V *vs*. Standard Hydrogen Electrode/SHE) in 0.5 M H_2SO_4 (aq.) electrolyte medium. The electrolyte solution became N_2-saturated by bubbling N_2 gas for 30 min duration. The glassy carbon electrodes (geometric area: 0.2 cm^2) were mechanically polished with a 0.05 μm alumina powder, and followed by washed with ethanol and deionized water for obtaining clean surfaces. The working electrodes were prepared by the

drop-casting of catalyst slurries onto the glassy carbon electrodes. The homogeneous catalyst slurries were prepared in N, N-dimethylformamide (DMF) solvent by mixing 90 % catalyst and 10 % polyvinylidene fluoride (PVDF) binder under the sonication for 30 min. The prepared catalyst-coated working electrodes were dried at 60 ºC for 3 h in hot air oven. The ~ 20 µg (100 µg/cm^2) of catalyst loadings were obtained in above mentioned working electrodes. The electrochemical measurements were acquired in multichannel Autolab potentiostat & galvanostat (Model: M204) at ambient temperature (25 ºC), and the resulting data were presented after iR-compensation. The following equation was applied for the iR-corrections.[39]

$E_{corrected}$ (*vs*. Ag/AgCl) = $E_{experimental}$ (*vs*. Ag/AgCl) - iR_s ……..……. (1)

Whereas, the $E_{corrected}$, $E_{experimental}$, i and R_s are iR-corrected potential, experimental potential, current response and solution resistance obtained from the EIS studies, respectively. However, the iR-corrected potential (E) values were reported with respect to Reversible Hydrogen Electrode (RHE) by using the following pH-dependent relationships.[40]

E (*vs*. RHE) = E (*vs*. SHE) + 0.059×pH ……..……. (2)

E (*vs*. RHE) = E (*vs*. Ag/AgCl) + 0.197 + 0.059×pH…… (3)

6.2.11. Computational Method.

All electronic structure calculations have been conducted using the Vienna Ab-initio Simulation Package (VASP) with the projector augmented wave (PAW) method. The generalized gradient approximation method, employing the Perdew-Burke-Ernzerhof (PBE) functional for the exchange-correlation term, has been utilized. In these calculations, a plane wave basis set with a cutoff energy of 550 eV was utilized. The energy and force convergence criteria have set as 10^{-5} eV and 0.02 eV/Å. A (2 × 2 × 1) mesh has been used for Brillouin zone sampling. The hydrogen adsorption energy is calculated using the following equation:

$$\Delta G_{H*} = \Delta E + \Delta E_{ZPE} - T\Delta S$$

Where ΔE, ΔE_{ZPE} and ΔS are the difference in DFT calculated energy, zero-point energy and entropy between the adsorbed H atom and the gaseous phase H_2.

6.3. RESULTS AND DISCUSSION

6.3.1. Structural Description.

Single crystal X-ray analysis reveals that Ni-MOF crystallizes in an orthorhombic system with a *Pbca* space group. The asymmetric unit contains two Ni2+ ions (Ni1 and Ni2), three nicotinates (NA1, NA2, NA3), one N-nicotinoyl glycinate (N-NG), and one water molecule (μ_2-H2O) (Figure 6a). Both Ni2+ ions exhibit octahedral coordination with four oxygen atoms and two nitrogen atoms (Fig. 6b&c). The oxygen atoms come from two NA carboxylate groups, one N-NG carboxylate group, and the bridged water molecule. Ni1 has nitrogen atoms from two NA aromatic pyridyl rings, while Ni2 has one nitrogen from the N-NG aromatic pyridyl ring and one from an NA ligand. The nickel centers are connected by the bidentate bridging oxygen atom of the water molecule and formed a dimer (Figure 6d). The carboxylate groups of NA1 and NA2 have monodentate connectivity (Figure 6e), while NA3 and N-NG have bidentate connectivity (Figure 6f&g).

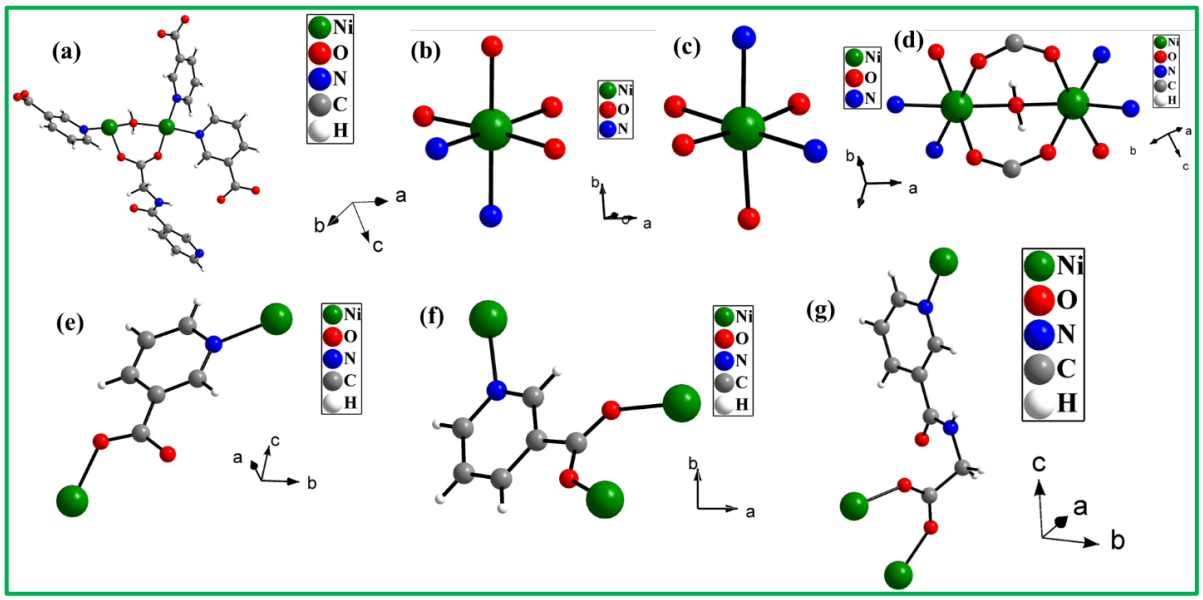

Figure 6. (a) Figure shows the asymmetric unit of [Ni_2(NNG)(NA)$_3$(μ_2-H_2O)], Ni-MOF. **(b)** octahedral geometry around Ni^{2+} ions **(c)** Octahedral geometry around Ni(2)$^{2+}$ ions. **(d)** Dimeric unit connected by bridged water molecule **(e)** Monodentate connectivity of NA1 and NA2. **(f)** Bidentate connectivity of NA3. **(g)** Bidentate connectivity of N-NG in Ni-MOF.

The Ni-O bonds have an average distance of 2.057 Å, Ni-N bonds have average distance of 2.108 Å. The O/N-Ni-N/O bond angles range is in the range 84.22 (13)- 177.67(13)°. The selected bond distances are listed in Table 3 and the selected bond angles are listed in Table 4.

Table 3: Selected bond distances (Å) observed in $[Ni_2(NNG)(NA)_3(\mu_2\text{-}H_2O)]$, Ni-MOF.

Bond	Distances, Å	Bond	Distances, Å
Ni(1)-O(8)#1	2.021(3)	Ni(2)-O(6)	2.005(3)
Ni(1)-O(2)#2	2.030(3)	Ni(2)-O(3)#3	2.036(3)
Ni(1)-O(7)	2.078(3)	Ni(2)-N(3)	2.097(3)
Ni(1)-N(1)	2.082(3)	Ni(2)-O(9)#1	2.101(3)
Ni(1)-O(10)	2.084(3)	Ni(2)-O(10)	2.107(3)
Ni(1)-N(2)	2.123(4)	Ni(2)-N(5)#2	2.132(3)

Symmetry transformations used to generate equivalent atoms: #1 x+1/2, -y+1/2, -z+1 #2 x-1/2, y, -z+3/2 #3 -x, -y, -z+1

Table 4: Selected bond angles observed in $[Ni_2(NNG)(NA)_3(\mu_2\text{-}H_2O)]$, Ni-MOF.

Angle	Amplitude (º)	Angle	Amplitude (º)
O(8)#1-Ni(1)-O(2)#2	174.46(12)	O(6)-Ni(2)-O(3)#3	173.97(13)
O(8)#1-Ni(1)-O(7)	93.96(12)	O(6)-Ni(2)-N(3)	89.72(13)
O(2)#2-Ni(1)-O(7)	88.67(12)	O(3)#3-Ni(2)-N(3)	85.84(13)
O(8)#1-Ni(1)-N(1)	90.97(12)	O(6)-Ni(2)-O(9)#1	91.49(12)
O(2)#2-Ni(1)-N(1)	84.32(12)	O(3)#3-Ni(2)-O(9)#1	84.22(13)
O(7)-Ni(1)-N(1)	86.57(13)	N(3)-Ni(2)-O(9)#1	87.09(13)
O(8)#1-Ni(1)-O(10)	94.09(12)	O(6)-Ni(2)-O(10)	94.90(12)
O(2)#2-Ni(1)-O(10)	90.79(12)	O(3)#3-Ni(2)-O(10)	89.63(13)
O(7)-Ni(1)-O(10)	89.90(13)	N(3)-Ni(2)-O(10)	175.24(13)
N(1)-Ni(1)-O(10)	174.03(13)	O(9)#1-Ni(2)-O(10)	93.92(12)

O(8)#1-Ni(1)-N(2)	87.53(12)	O(6)-Ni(2)-N(5)#2	91.26(13)
O(2)#2-Ni(1)-N(2)	89.69(13)	O(3)#3-Ni(2)-N(5)#2	93.08(13)
O(7)-Ni(1)-N(2)	177.67(13)	N(3)-Ni(2)-N(5)#2	93.49(14)
N(1)-Ni(1)-N(2)	91.62(14)	O(9)#1-Ni(2)-N(5)#2	177.20(14)
O(10)-Ni(1)-N(2)	91.77(14)	O(10)-Ni(2)-N(5)#2	85.28(13)

Symmetry transformations used to generate equivalent atoms: #1 x+1/2,-y+1/2,-z+1 #2 x-1/2,y,-z+3/2 #3 -x,-y,-z+1

Ni1 centers form a one-dimensional chain along the a-axis through NA1 ligands, while Ni2 centers form a similar chain via N-NG ligands. These chains connect via the bridged water molecule and formed 1D structure (Fig. 7a), which further connects through NA2 and NA3 to form a three-dimensional architecture (Fig. 7b).

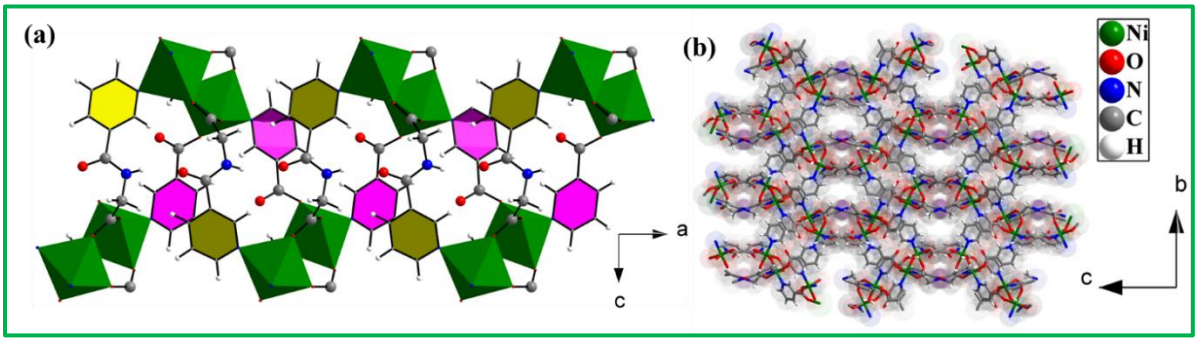

Figure 7. (a) 1D structure connected by NA(pink) and N-NG(yellow) in Ni-MOF. **(b)** Three-dimensional structure of Ni-MOF.

6.3.2. Electrocatalytic Hydrogen Evolution Reaction.

The multi-step electrochemical processes in HER could be anticipated in the following three different reaction mechanisms under acidic electrolyte mediums.[41]

Volmer Reaction: $H_3O^+ + e^- + Cat \rightarrow (Cat\text{-}H)_{ads} + H_2O$ …….…… (4)

Heyrovsky Reaction: $H_3O^+ + e^- + (Cat\text{-}H)_{ads} \rightarrow H_2 + H_2O + Cat$ ..... (5)

Tafel Reaction: $(Cat\text{-}H)_{ads} + (Cat\text{-}H)_{ads} \rightarrow H_2 + Cat$ ……..…….……(6)

The mechanistic pathways of HER could be explained either Volmer-Heyrovsky or Volmer-Tafel sequences. In the Volmer route (Eq. 4), a hydrated proton combines with an electron,

and adsorbed onto the catalyst surface [$(Cat\text{-}H)_{ads}$]. The hydrogen generation is occurred in Heyrovsky step (Eq. 5), when another hydrated proton combines simultaneously with an electron and previously H-adsorbed catalyst surface. The two $(Cat\text{-}H)_{ads}$ species combine and produce hydrogen, in Tafel route (Eq. 6). However, the determination of Tafel slope from Tafel equation (Eq. 7) is the most convenient method to elucidate the mechanistic pathways of the HER. The relationship between overpotential (η in V) and current density (j in A cm^{-2}) is depicted in the following Tafel equation

$$\eta = a + b \times \log(j) \quad \text{..... (7)}$$

whereas 'a' is the intercept related to the exchange current density (j_0), which indicates the intrinsic electron transfer rate, and 'b' is the Tafel slope that signifies the rate of the electrode process. Basically, the Tafel slope (in V/decade) is the estimation of overpotential for ten-fold increment of current density (j). Therefore, lower the Tafel slopes demonstrate faster electrode kinetics. In case of HER, the characteristics Tafel slopes are 120, 40 and 30 mV/dec for Volmer, Heyrovsky and Tafel reactions, respectively.[41]

The catalytic activity for HER of an electrode is primarily depends on electrochemical surface area (ECSA) of catalyst materials and the roughness factor (RF) of electrodes.[42] The ECSA and RF are calculated as per the following Eqs.

$$\text{ECSA} = \frac{\textit{Double layer capacitance of the electrode with catalyst loading } (Cdl)}{\textit{Double layer capacitance of the blank electrode without catalyst loading } (Cs)} \quad \text{..... (8)}$$

$$\text{RF} = \frac{\text{ECSA}}{\text{Geometric surface area of electrode}} \quad \text{.....(9)}$$

The double layer capacitances of the electrodes are estimated from the variable scan rate (υ) CV experiments within the voltage limit of the non-Faradaic electrochemical responses. Herein, the CV profiles under multiple scan rates (υ: 10-100 mV/s; Δυ = 10 mV/s) are shown in Figure 8 (a and c) within 0-0.2 V *vs*. Ag/AgCl for Ni-MOF and NiCo-MOF, respectively. The Figure 8 (b and d) demonstrate linear profiles of Δj/2 *vs*. υ ($\Delta j = j_{anodic} - j_{cathodic}$), and the resulting slopes are the measure of the respective double layer capacitance (C_{dl}) of the Ni-MOF and NiCo-MOF electrodes. The double layer capacitance (C_s) of the blank electrode is also estimated by using the similar relationships, while the cyclic voltammograms and Δj/2 *vs*. υ

profiles are presented in Figure 8. Based on the estimated values of C_{dl} and C_S, the ECSA and RF for Ni-MOF and NiCo-MOF are calculated and shown in Table 5.

Table 5: Comparison of catalytic activity of Ni-MOF and NiCo-MOF towards HER.

Catalyst	ECSA (cm^2)	RF	η (mV) @10 mA/cm^2	Tafel Slope (mV/dec)
Ni-MOF	5.5	27.5	150	52
NiCo-MOF	16	80.0	120	39

The higher values of ECSA and RF for NiCo-MOF indicate better electrocatalytic activity than that of Ni-MOF. The surface atoms of the catalysts are actually participating in the electrochemical processes. Therefore, the higher ECSA and RF specify enhanced electrode-electrolyte interfaces, and consequently facile ion transportation is achieved. Hence, superior catalytic activity is obtained for the electrodes with higher ECSA and RF.

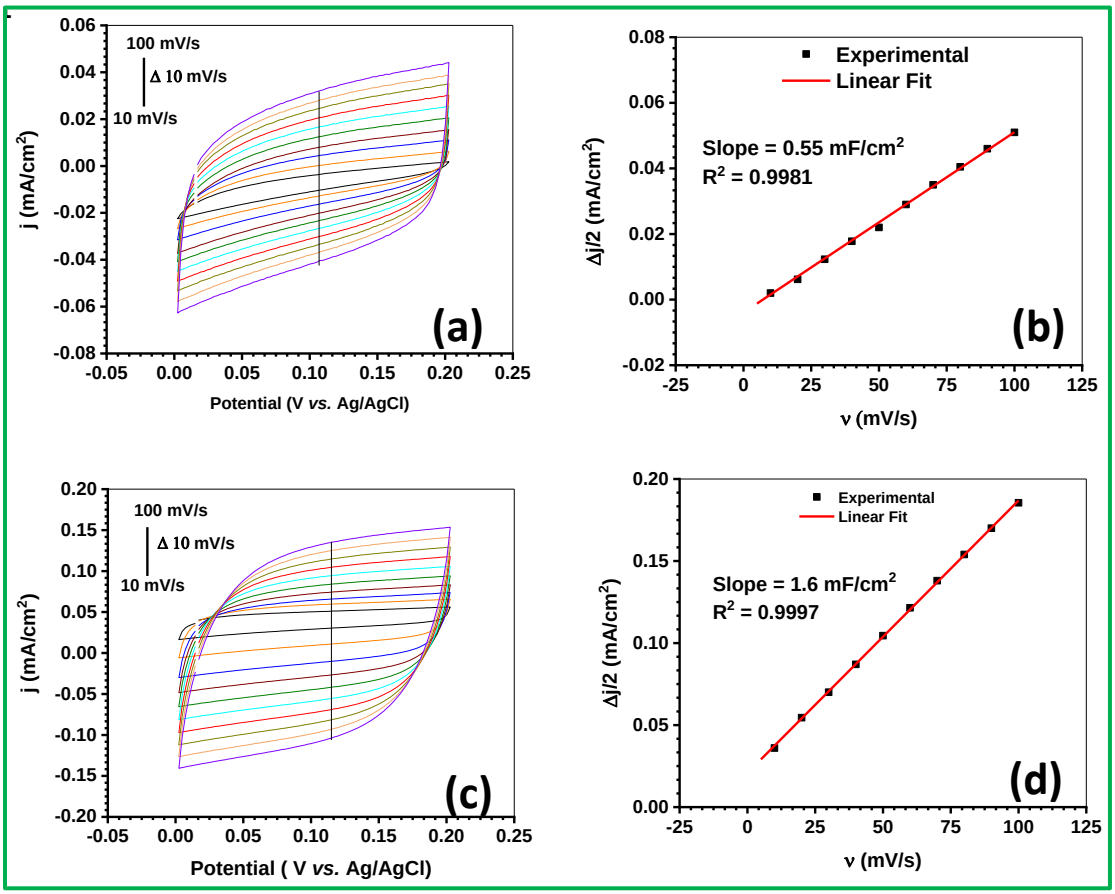

Figure 8: CV profiles at variable scan rate (υ) within the voltage range of non-Faradaic current response: **(a)** Ni-MOF & **(c)** NiCo-MOF; and Estimation of double layer capacitance from the linear fitting of Δj/2 *vs*. υ profiles: **(b)** Ni-MOF & **(d)** NiCo-MOF.

The HER activities of the Ni-MOF and NiCo-MOF in 0.5 M H_2SO_4 electrolyte (pH = ~0.3) are evaluated by the LSV experiments at 10 mV/s scan rate, and the voltammograms are depicted in Figure 9a. The η value is calculated based on the following Eq., whereas thermodynamic potential of HER is incorporated as zero.

η (V) = [E (*vs*. Ag/AgCl) + 0.197 + (0.059×pH) – 0] …… (10)

The η values at any current densities are considerably lower in NiCo-MOF compare to Ni-MOF, which indicates the better electrocatalytic activity in former. However, the overpotentials at 10 mA/cm^2 current density for both MOFs are shown in Table 5.

These results are nicely corroborating with the trends of ECSA and RF. To elucidate the mechanistic pathways, the Tafel slopes are also calculated, and the Tafel plots are shown in Figure 9b. The Ni-MOF and NiCo-MOF demonstrate respective 39 and 52 mV/dec Tafel slope, which clearly demonstrates the Volmer-Heyrovsky HER mechanism. Furthermore, the smaller Tafel slope in NiCo-MOF indicates the faster electrode kinetics than that of Ni-MOF; which means former is the better catalyst than later. To estimate the per-site activity of the electrocatalysts, Turn Over Frequency (TOF in second^{-1}) calculations are carried out by using the following Eq.[43]

$$\text{TOF } (s^{-1}) = \frac{j \times A}{2 \times F \times n} \quad \ldots\ldots (11)$$

Whereas, j is the experimental current density at fixed overpotential, A is the geometric surface area of the catalyst layer, the number 2 indicates requirement of 2 electrons to obtain 1 mole of hydrogen, F is Faraday's constant (96485.3 C/mol) and n is the mole of catalyst present on the electrode surface. However, the n is calculated from the mass and molecular weight of the catalyst. It is mention worthy that the TOF signifies the number of catalytic cycles (*i.e*., generated reaction products) on a single site per unit time, and hence, the higher values of TOF show greater catalytic activity. Figure 9c demonstrates the TOF values of Ni-MOF and NiCo-MOF under wide ranges of overpotentials, and the later depicts consistently higher values than

that of former. It also evidences the better catalytic activity in bimetallic NiCo-MOF. The EIS studies are also performed to elucidate the interfacial charge transfer kinetics of the catalyst layer at electrode-electrolyte interfaces. The Nyquist plots for both catalysts are shown in Figure 9d at open circuit condition, while the equivalent circuit is presented in the inset of the Figure. The solution resistances (R_s) are almost equal (11 Ω) for both catalysts, but lower charge transfer resistance (R_{ct}) is observed in NiCo-MOF (460 Ω) than that of Ni-MOF (530 Ω). The lower R_{ct} implies facile charge transfer at the catalyst surface, which is further synchronizing with the superior catalytic activity of NiCo-MOF. However, the better electrocatalytic activity in bimetallic NiCo-MOF could be explained by $3d^7$-$3d^8$ synergic effect, which will be elaborated later.[29, 33]

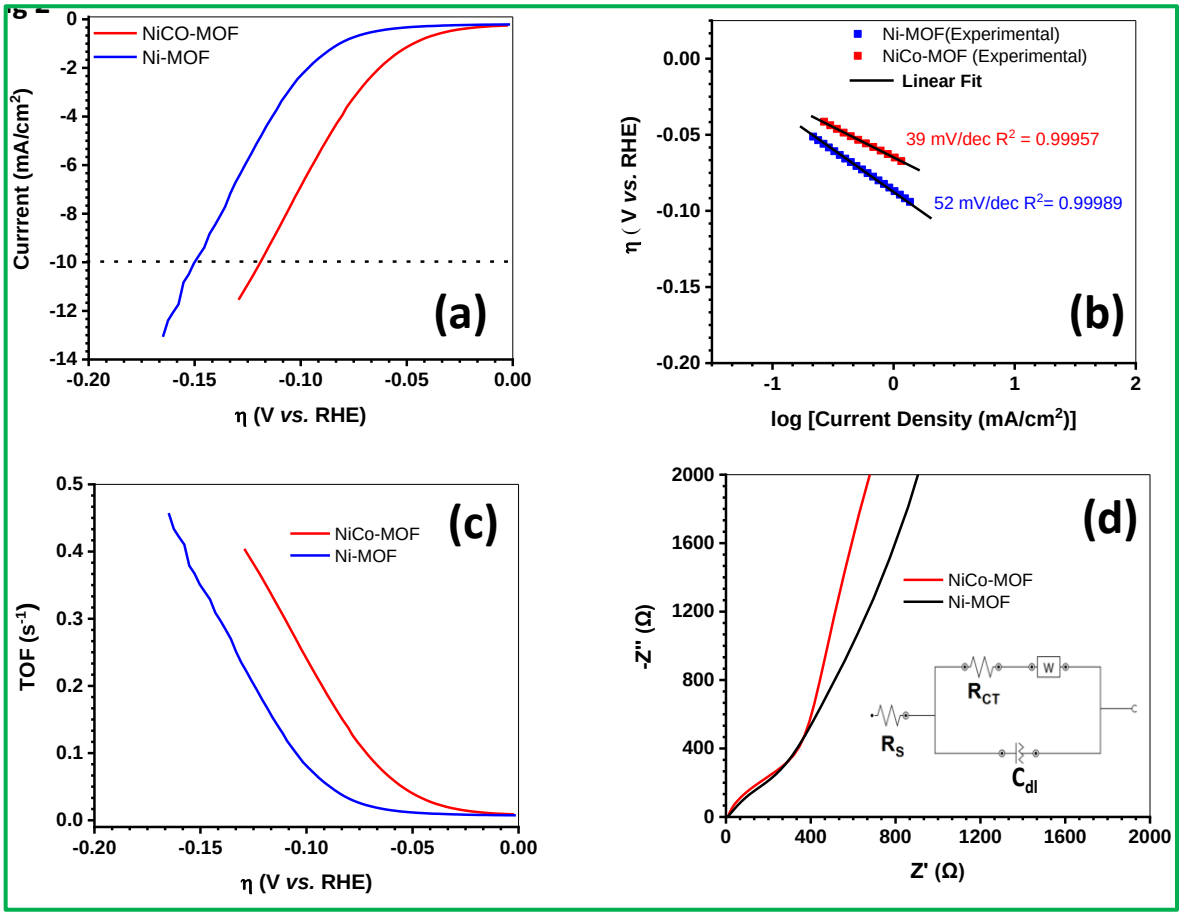

Figure 9: Catalytic activity towards HER for Ni-MOF and NiCo-MOF: **(a)** LSV profiles at 10 mV/s scan rate, **(b)** Tafel plots with Tafel slopes, **(c)** potential dependent TOF profiles, and **(d)** Nyquist plots at open circuit voltage.

The durability of the catalysts is evaluated by two different modules through (i) 1000 cycles of CV scan at 100 mV/s scan rate within 0-0.2 V *vs.* Ag/AgCl, and (ii) 20 h chronoamperometry at -0.4 V (vs. Ag/AgCl). The LSV studies are performed on pristine and CV cycled catalyst electrodes, so that the stability of the catalysts could be easily comprehended from the comparative performance data. Figure 10 (a and b) show comparative LSV profiles before and after the 1000 CV scans for Ni-MOF and NiCo-MOF electrodes, while respective 52 and 33 mV increments of overpotential (@ 10 mA/cm^2) are noted after durability experiment. The minimal increases of overpotential in bimetallic NiCo-MOF indicate superior durability than that of monometallic Ni-MOF.

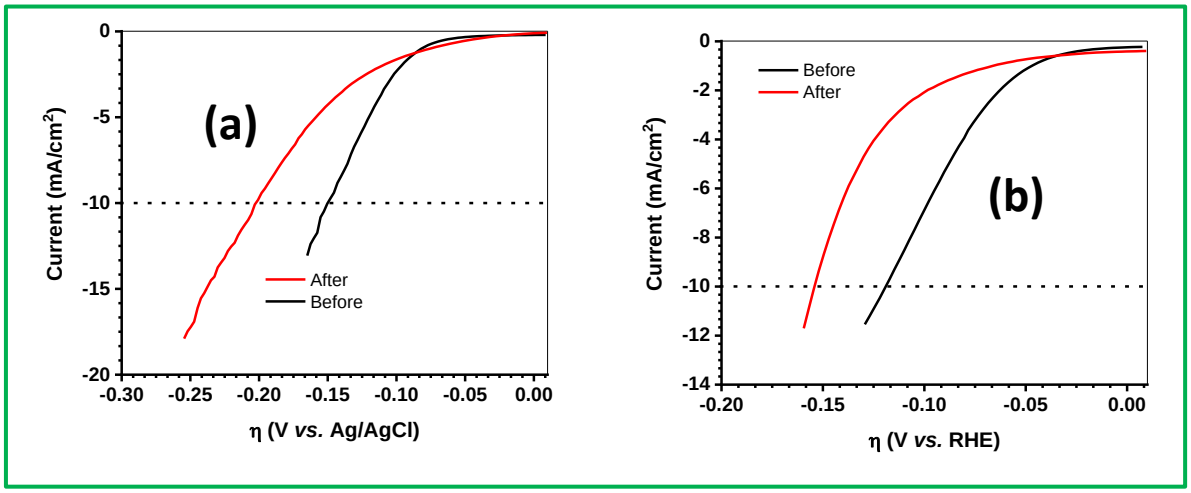

Figure 10: Durability study through CV cycling: Comparative LSV profiles for **(a)** Ni-MOF & **(b)** NiCo-MOF.

Figure 11a describes chronoamperometric profiles of both catalysts at -0.4 V for 20 h. The more stable current response is noted in NiCo-MOF (21 % decay) compare to Ni-MOF (52 % decay). Figure 11b&c describe the respective LSV profiles of catalyst electrodes, before and after the amperometric durability study.

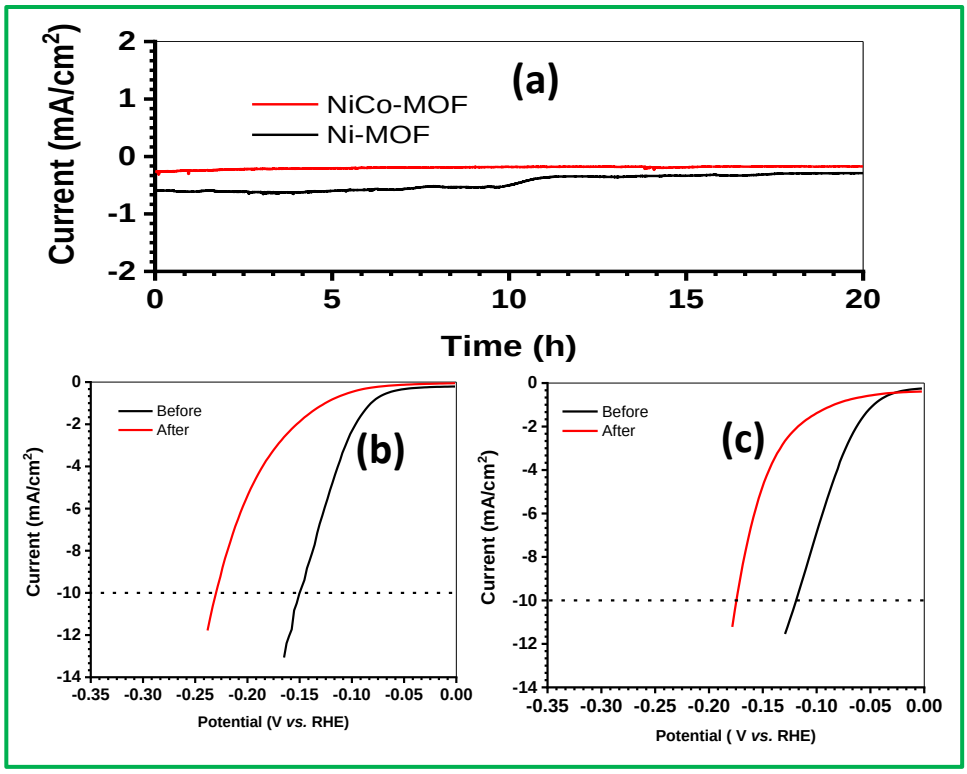

Figure 11: (a) Chronoamperometric profiles for Ni-MOF and NiCo-MOF; Comparative LSV profiles before and after durability test for **(b)** Ni-MOF & **(c)** NiCo-MOF.

Here also similar trend is followed like CV cycling based durability test. The NiCo-MOF depicts 54 mV increase in overpotential at 10 mA/cm^2 current density, while 80 mV increment is noted in Ni-MOF under similar experimental conditions. However, the both modules of durability tests synchronize well, and indicate superior stability in bimetallic NiCo-MOF than that of Ni-MOF.

6.3.3. Theoretical Calculations.

Density functional theory (DFT) was employed to calculate the Gibbs free energy for hydrogen adsorption (ΔG_{H*}) on Ni-MOF and NiCo-MOF. This calculation was used to predict the hydrogen evolution capabilities of these catalysts. The adsorption ability for hydrogen atoms on a catalyst surface (ΔG_{H*}) is a crucial indicator of catalytic activity in HER catalysts. While ΔG_{H*} alone does not provide a comprehensive understanding of HER activity, it serves as a preliminary predictor of performance. Generally, a $|\Delta G_{H*}|$ value nearer to 0 eV suggests higher activity for hydrogen evolution. HER is a two-electron transfer process and the reaction mechanism in acidic medium is as follows:

Volmer: $\text{substrate}(*) + \text{H}^+ + \text{e}^- \rightarrow \text{H}^*$

Heyrovsky: $\text{H}^* + \text{H}^+ + \text{e}^- \rightarrow \text{H}_2 + \text{substrate}\ (*)$

Tafel: $\text{H}^* + \text{H}^* \rightarrow \text{H}_2 + 2\ \text{substrate}\ (*)$

The initial stage involves the adsorption of hydrogen ions onto the electrode surface (Volmer step). Following this, there are two possible pathways: either the two hydrogen atoms adsorbed on the surface recombine (Tafel step), or a hydrated proton directly bonds with the adsorbed hydrogen atom, accompanied by electron transfer from the electrode surface (Heyrovsky step). In our study, $|\Delta G_{H*}|$ on Ni site and Co site on NiCo-MOF is 0.04 eV and 0.17 eV respectively, which are significantly lower than the 0.32 eV observed in Ni-MOF (figure 12).

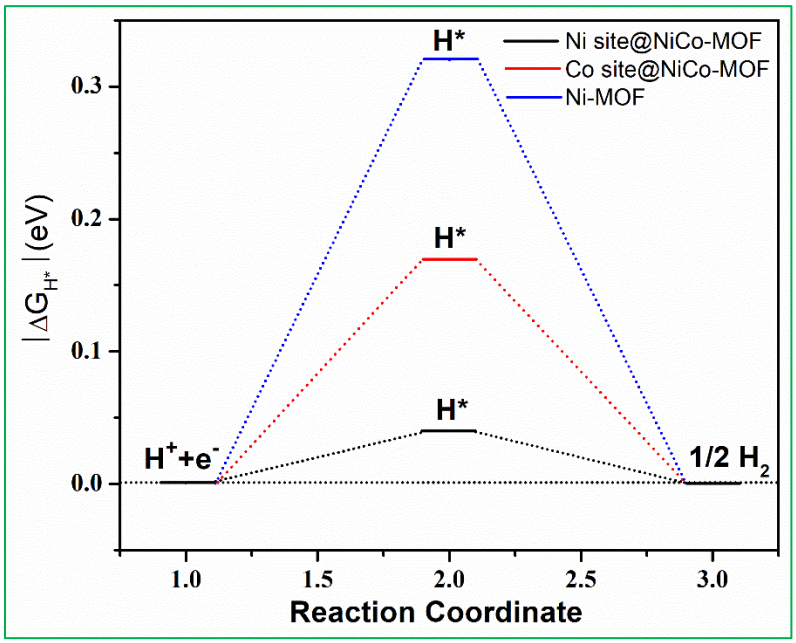

Figure 12: Free energy diagram of different catalytic metal sites for HER.

Therefore, the introduction of Co dopant enhances the desorption rate of hydrogen molecule in the subsequent step. Notably, the density of states (DOS) of NiCo-MOF is larger than that of Ni-MOF at the Fermi level (figure 13), indicating enhanced electron mobility in the NiCo-MOF heterostructure for rapid electron transport during electrocatalytic process.

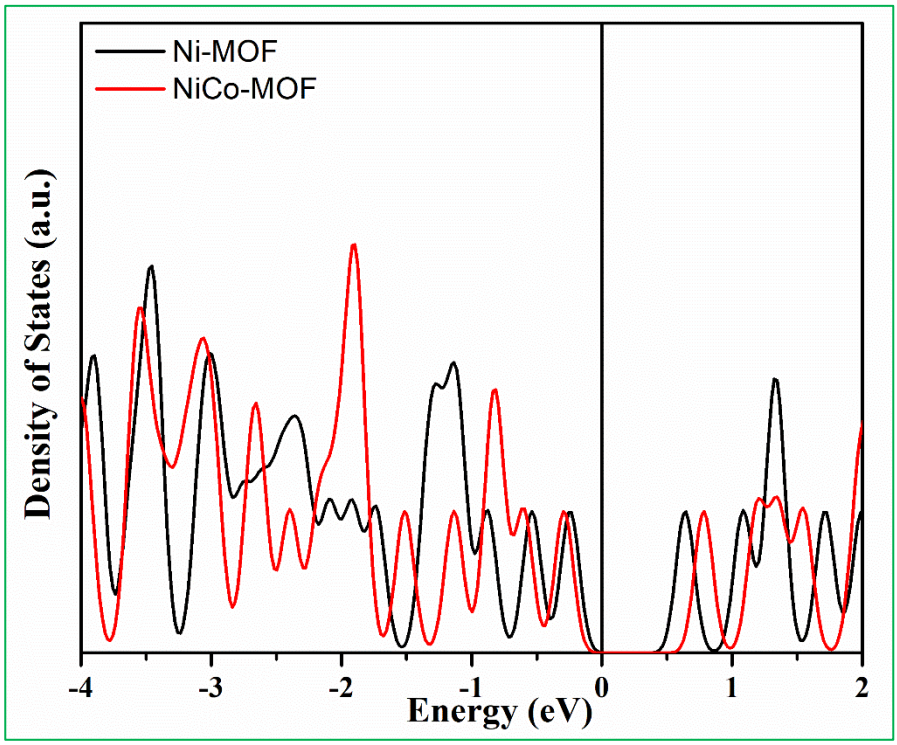

Figure 13: Density of states of Ni-MOF and NiCo-MOF at fermi level.

6.4. CONCLUSIONS

In conclusion, the urgent need for sustainable energy solutions has driven significant research efforts towards hydrogen production methods that are both environmentally friendly and economically viable. In particular, bimetallic MOFs have garnered attention for their enhanced HER activity, showcasing the significance of synergistic interactions between active metal centers. Our study contributes to this trend by presenting a bimetallic NiCo-MOF with exceptional performance in HER electrocatalysis, surpassing single-metal counterparts and previously reported MOF catalysts. These findings underscore the potential of bimetallic MOFs and effective coupling between metal centres as a promising pathway for the systematic design of highly efficient electrocatalysts, marking a significant advancement in sustainable energy research. Further exploration of MOF-based catalysts and their synergistic effects holds great promise for the development of practical solutions towards a sustainable hydrogen economy.

REFERENCES

1. S. Chu and A. Majumdar, *Nature*, 2012, **488**, 294-303.
2. Z. Abdin, A. Zafaranloo, A. Rafiee, W. Mérida, W. Lipiński and K. R. Khalilpour, *Renewable and Sustainable Energy Reviews*, 2020, **120**, 109620.
3. A. Q. Al-Shetwi, *Science of The Total Environment*, 2022, **822**, 153645.
4. M. Z. Jacobson, *Energy & Environmental Science*, 2009, **2**, 148-173.
5. P. Xiao, W. Chen and X. Wang, *Advanced Energy Materials*, 2015, **5**, 1500985.
6. G. Zhao, K. Rui, S. X. Dou and W. Sun, *Advanced Functional Materials*, 2018, **28**, 1803291.
7. H. Yin, S. Zhao, K. Zhao, A. Muqsit, H. Tang, L. Chang, H. Zhao, Y. Gao and Z. Tang, *Nature Communications*, 2015, **6**, 6430.
8. M.-Q. Wang, C. Ye, H. Liu, M. Xu and S.-J. Bao, *Angewandte Chemie International Edition*, 2018, **57**, 1963-1967.
9. H. B. Wu, B. Y. Xia, L. Yu, X.-Y. Yu and X. W. Lou, *Nature Communications*, 2015, **6**, 6512.
10. H. Zhang, J. Su, K. Zhao and L. Chen, *ChemElectroChem*, 2020, **7**, 1805-1824.
11. B. Zhu, R. Zou and Q. Xu, *Advanced Energy Materials*, 2018, **8**, 1801193.
12. J.-B. Tan and G.-R. Li, *Journal of Materials Chemistry A*, 2020, **8**, 14326-14355.
13. O. M. Yaghi, G. Li and H. Li, *Nature*, 1995, **378**, 703-706.
14. O. M. Yaghi and H. Li, *Journal of the American Chemical Society*, 1995, **117**, 10401-10402.
15. D. Li, A. Yadav, H. Zhou, K. Roy, P. Thanasekaran and C. Lee, *Global Challenges*, 2024, **8**, 2300244.
16. H. Furukawa, K. E. Cordova, M. O'Keeffe and O. M. Yaghi, *Science*, 2013, **341**, 1230444.
17. M. El Hanafi, A. BaQais, M. Saadi and H. Ait Ahsaine, *Energy & Fuels*, 2023, **37**, 10869-10885.
18. Y. Zhu, Q. Lin, Y. Zhong, H. A. Tahini, Z. Shao and H. Wang, *Energy & Environmental Science*, 2020, **13**, 3361-3392.
19. J. Song, J.-L. Chen, Z. Xu and R. Y.-Y. Lin, *Chemical Communications*, 2022, **58**, 10655-10658.
20. Q. Gong, Y. Wang, Q. Hu, J. Zhou, R. Feng, P. N. Duchesne, P. Zhang, F. Chen, N. Han, Y. Li, C. Jin, Y. Li and S.-T. Lee, *Nature Communications*, 2016, **7**, 13216.
21. J. McAllister, N. A. G. Bandeira, J. C. McGlynn, A. Y. Ganin, Y.-F. Song, C. Bo and H. N. Miras, *Nature Communications*, 2019, **10**, 370.
22. C. Lamiel, I. Hussain, H. Rabiee, O. R. Ogunsakin and K. Zhang, *Coordination Chemistry Reviews*, 2023, **480**, 215030.
23. Y. Lu, Y. Deng, S. Lu, Y. Liu, J. Lang, X. Cao and H. Gu, *Nanoscale*, 2019, **11**, 21259-21265.
24. X. Feng, H. Wang, X. Bo and L. Guo, *ACS Applied Materials & Interfaces*, 2019, **11**, 8018-8024.
25. Z. Pan, N. Pan, L. Chen, J. He and M. Zhang, *International Journal of Hydrogen Energy*, 2019, **44**, 30075-30083.
26. H.-F. Wang, L. Chen, H. Pang, S. Kaskel and Q. Xu, *Chemical Society Reviews*, 2020, **49**, 1414-1448.
27. N. Zaman, T. Noor and N. Iqbal, *RSC Advances*, 2021, **11**, 21904-21925.

28. C. Li, H. Zhang, M. Liu, F.-F. Lang, J. Pang and X.-H. Bu, *Industrial Chemistry & Materials*, 2023, **1**, 9-38.
29. U. Bhoi, S. Ray, S. Bhand, P. Ninawe, D. Roy, S. Rana, K. Tarafder and N. Ballav, *ACS Energy Letters*, 2023, **8**, 4465-4473.
30. X.-L. Wang, L.-Z. Dong, M. Qiao, Y.-J. Tang, J. Liu, Y. Li, S.-L. Li, J.-X. Su and Y.-Q. Lan, *Angewandte Chemie International Edition*, 2018, **57**, 9660-9664.
31. M. Liu, L. Kong, X. Wang, J. He and X.-H. Bu, *Small*, 2019, **15**, 1903410.
32. R.-Z. Zhang, L.-L. Lu, Z.-H. Chen, X. Zhang, B.-Y. Wu, W. Shi and P. Cheng, *Chemistry – A European Journal*, 2022, **28**, e202200401.
33. B. Geng, F. Yan, X. Zhang, Y. He, C. Zhu, S.-L. Chou, X. Zhang and Y. Chen, *Advanced Materials*, 2021, **33**, 2106781.
34. L. Krause, R. Herbst-Irmer, G. M. Sheldrick and D. Stalke, *Journal of Applied Crystallography*, 2015, **48**, 3-10.
35. A. Altomare, G. Cascarano, C. Giacovazzo and A. Guagliardi, *Journal of Applied Crystallography*, 1993, **26**, 343-350.
36. G. M. J. A. C. S. C. S. C. Sheldrick, 2015, **71**, 3-8.
37. L. Farrugia, *Journal of Applied Crystallography*, 1999, **32**, 837-838.
38. A. Spek, *Journal of Applied Crystallography*, 2003, **36**, 7-13.
39. Y. Xie, J. Cai, Y. Wu, Y. Zang, X. Zheng, J. Ye, P. Cui, S. Niu, Y. Liu, J. Zhu, X. Liu, G. Wang and Y. Qian, *Advanced Materials*, 2019, **31**, 1807780.
40. A. Govind Rajan, J. M. P. Martirez and E. A. Carter, *ACS Catalysis*, 2020, **10**, 11177-11234.
41. F. Li, X. Wang, X. Zou, Y. Tao, S. Yue, X. Chen and X. Lu, *International Journal of Electrochemical Science*, 2019, **14**, 8097-8109.
42. S. Singh, M. Yadav, D. K. Singh, D. K. Yadav, P. K. Sonkar and V. Ganesan, *New Journal of Chemistry*, 2022, **46**, 13422-13430.
43. Y. Wang, Z. Liu, H. Liu, N.-T. Suen, X. Yu and L. Feng, *ChemSusChem*, 2018, **11**, 2724-2729.

List of Publications

1. Synthesis and Investigation of Magnetic Properties of Rod Shaped Micron Sized Ni_4 and Co_2Ni_2 Cluster based MOFs.
   Debal Kanti Singha, Shams Sohel Islam, **Chhatan Das**, Niyaz Ahmed KC, Ramesh Chandra Nath, Partha Mahata
   ***Z. Anorg. Allg. Chem*. 2021, 647, 1939–19**.
2. *Cd-Based Coordination Polymer Using a Bioinspired Ligand: Studies Toward Turn-On Luminescence-Based Sensing and Schottky Diode Behavior through Device Fabrication.
   Chhatan Das, Vishwas D. Patel, Dhritiman Gupta, and Partha Mahata
   ***Cryst. Growth Des.* 2022, 22, 12, 7050–7061.**
3. *Differential Supercapacitor and Schottky Diode behaviours in Two New Isostructural Coordination Polymers Based on Redox Active Metal Ions.
   Chhatan Das, Subhrajyoti Debnath, Vishwas D. Patel, Dhritiman Gupta, Anjan Banerjee and Partha Mahata
   ***CrystEngComm*, 2023, 25, 6343-6353.**
4. *Isolation of a Cd-based Coordination Polymer Containing Mixed Ligands: Time and Temperature Dependent Synthesis, Sulfonamide Antibiotics Detection and Schottky Diode Fabrication.
   Chhatan Das, Vishwas D. Patel, Dhritiman Gupta, and Partha Mahata
   ***Inorg. Chem.* 2024, 63, 8, 3656–3666.**
5. *Solvent-Assisted Post Synthetic Metal-Ion Metathesis of Cd(II) With Cu(II): Catalytic Properties of a Cd-Based Crystalline Network Materials with Enhanced Stability and Gas Uptake.
   Chhatan Das, Arunava Misra, Mohabul Alam Mondala and Partha Mahata
   [Under revision in *Dalton Trans.*]

6. *Unlocking Enhanced Hydrogen Evolution with Bimetal-Organic Framework: A Synergistic Approach.
   Chhatan Das, Pappu Naskar, Anjan Banerjee and Partha Mahata
   [Communicated]

7. Stabilization of Cd^{2+} in Pentagonal Bipyramidal Coordination in a Mixed-Ligand based Coordination Polymer: Differential Luminescence Response towards Sulfonamide-Antibiotics and Trinitrophenol.
   Priyanka Manna, **Chhatan Das**, and Partha Mahata
   [Communicated]

***These works are included in this thesis.**